Technische Universität München


Excellence Cluster Universe

# The galaxy baryon cycle: environment, star-formation, and black hole feedback.

Alice Concas

Vollständiger Abdruck der von der

Fakultät für Physik der Technischen Universitätt München zur Erlangung des akademischen Grades eines

**Doktors der Naturwissenschaften (Dr. rer. nat.)**

genehmigten Dissertation.

Vorsitzende/-r: Prof. Dr. Björn Garbrecht

Prüfende/-r der Dissertation:

1. Prof. Dr. Elisa Resconi
2. Prof. Dr. Shawn Bishop

Die Dissertation wurde am 14.06.2018 bei der Technischen Universität München eingereicht und durch die Fakultät für Physik am 09.07.2018 angenommen.

*To Adriano and Graziella.*

"The most beautiful experience we can have is the mysterious. It is the fundamental emotion which stands at the cradle of true art and true science. Whoever does not know it and can no longer wonder, no longer marvel, is as good as dead and his eyes are dimmed."

*Albert Einstein*

"I am a passenger
And I ride and I ride
I ride through the city's backside
I see the stars come out of the sky
Yeah, they're bright in a hollow sky
You know it looks so good tonight

I am a passenger
I stay under glass
I look through my window so bright
I see the stars come out tonight
I see the bright and hollow sky
Over the city's ripped-back sky
And everything looks good tonight

Singin' la-la-la-la-la-la-la-la
La-la-la-la-la-la-la-la
La-la-la-la-la-la-la-la, la-la

Get into the car
We'll be the passenger
We'll ride through the city tonight
See the city's ripped backsides
We'll see the bright and hollow sky
We'll see the stars that shine so bright
The sky was made for us tonight"

*Iggy Pop, The Passenger*

# Contents

# List of Figures

# List of Tables

# Chapter 1

# Introduction

## 1.1 Voyage through the Universe: the Galaxies.

We have come a long way before to understand the nature of the mysterious and fascinating diffuse bright objects in the night sky, the "nebulae". For long time the scientists was debating about the nature of these objects, wondering if they was a particular type of gas clouds inside our Milky Way (MW) or if they was MW likes objects, composed by several stars and gas whose distance made impossible to solve individually. Only in the 1920's, Edwin Hubble, observing the Cepheid stars in the Andromeda nebula, confirmed the extragalactic nature of the "nebulae" (Hubble, 1925). Not long after, these objects took the name of "galaxies". This was the birth of the "extragalactic astronomy ".

As galaxies continued to be discovered over the years it became clear that they come in two basic types: elliptical (or early type, ETGs) which are predominantly spheroidal and spiral (or late type, LTGs) which exhibit a disc of stars, usually with spirals arms (see the Hubble original morphological scheme illustrated in Fig. 1.1). Today we know that $\sim$2 trillion galaxies inhabit our Universe (Conselice et al., 2016) and their bimodality concerns several other physical parameters including the age of their stellar populations, their chemical abundances, the radial profiles, integrated or central colors and total luminosity or stellar mass. The existence of a well-defined bimodality in the galaxy population suggests the need for a physical process or a combination of processes that trigger, regulate and eventually quench the star formation into the galaxy. The physical mechanisms that removes gas from a galaxy and/or prevent gas from condensing into new stars, commonly known as "quenching" mechanisms, are not yet fully understood. Unmasking the identity of the quenching processes is key to advancing our understanding of how galaxies form and evolve in the cosmic time.

In the first chapter I first provide a brief overview of observational evidences of the galaxy bimodality e their dependence on the cosmic time, in a new era of big surveys (Sec.1.2). In Sec.1.3 I present a brief introduction to galaxy formation in the cosmological framework, including dark matter accretion, internal and external feedback. I discuss the main processes responsible to regulate the star formation in the galaxies, focusing on the

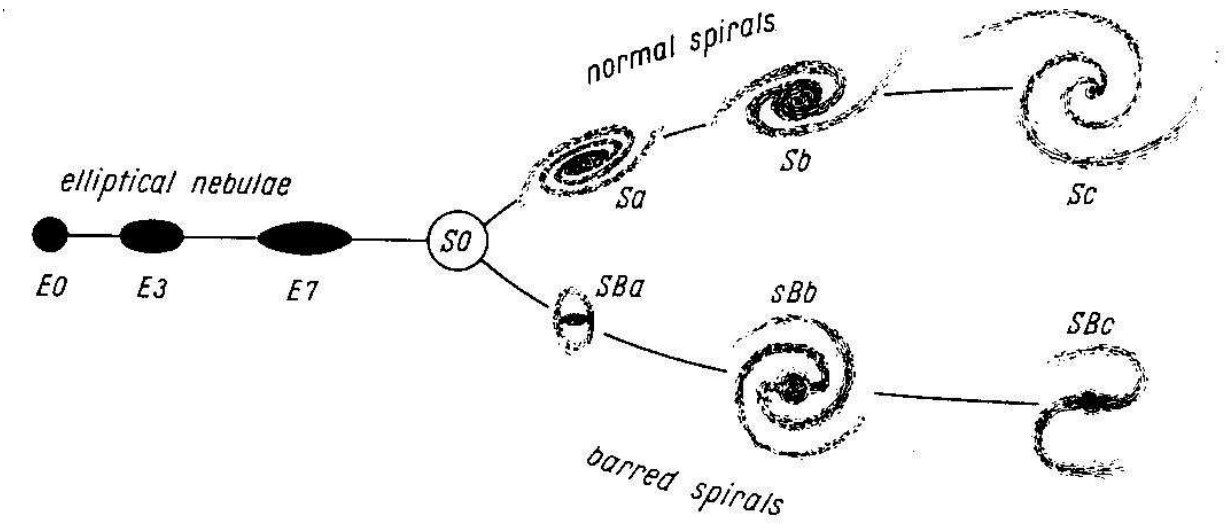


Figure 1.1: Morphological galaxy classification scheme proposed by Edwin Hubble Hubble (1936), also know as "Hubble tuning fork". The galaxies are classified according with their single-color morphological properties as elliptical galaxies (E, left side); lenticular (S0) galaxies or intermediate bulge+disc systems, and spiral galaxies subdivided into barred (SBa, SBb, SBc, bottom right) and non-barred (Sa, Sb, Sc, top right). Figure from Hubble (1936).

negative and positive feedback doe to the star-formation activity, the presence of the Active Galactic Nuclei (AGN) in the center, and, finally, the impact of the environment in the galactic evolution. In Sec.1.4 I discuss the observational probes used in this thesis, focusing on the role of optical emission and absorption lines used to (i) investigate the presence of outflowing ionized and neutral gas and, (ii) to study the effect of the dust and gas cold reservoir in local galaxies. Finally, I outline the structure and main goals of this Ph.D. thesis in Sec. 1.5

## 1.2 The observational perspective

With the advent of the large photometric and spectroscopic surveys at any redshift, the galaxy formation and evolution study has entered a new era of unprecedented statistical power. In the local Universe, in particular, the Sloan Digital Sky Survey (SDSS) revolutionised and is still significantly improving our knowledge of the galaxy properties and their evolution. Thanks to the SDSS statistics, indeed, it was possible to identify the existence of a well-defined galaxy bimodality that goes beyond the old distinction between elliptical and spiral galaxies. Such bimodality extends to a large variety of galaxy properties, including colours, star formation activity, morphology and clustering. In this section I analyse the main observational evidence of such bimodality to highlight our current knowledge of the galaxy properties and to, then, review the physical processes that can cause them.

### 1.2.1 The galaxy population bimodality

#### Morphology and colours

The first galaxy classification started with the single-colour morphological properties proposed by Hubble in the 1920s (as shown in Fig. 1.1, see also Lundmark 1926, 1927). The so called Hubble tuning fork distinguishes between late type galaxies (LTG) with a spiral morphology and early type galaxies (ETG), dominated by the central spheroidal component. The spiral region is divided in two sections depending on the presence of a central bar in addition to the bulge. In both spiral regions the sequence goes from pure disk galaxies, with no central bulge (right end side of Fig. 1.1), towards systems with increasing bulge component (S0 galaxies), to finish with pure elliptical galaxies with no disk, which might differ for ellipticity (left hand side of Fig. 1.1).

After the first qualitative and visual classification proposed by Hubble, galaxies have been quantitatively classified into different types on the basis of their surface brightness profile since the second half of last century. De Vaucouleurs in 1948 proposed the first distinction between a centrally cuspy profile for ETGs, the so called de Vaucouleurs profile, and an exponential profile for LTG with a prominent disk. Later on, Sèrsic in the 1963 generalized such profile to obtain a general model to quantitatively define the light distribution of galaxies, the so called Sèrsic profile:

$$\log\left[\frac{I(r)}{I(R_e)}\right] = -b_n\left[\left(\frac{r}{R_e}\right)^{1/n} - 1\right], \tag{1.1}$$

where $I(r)$ id the intensity at radius $r$ along the semi-major axis in linear flux units per unit area, and $I_e$ is the intensity at the effective radius $R_e$ that enclosed half of the total light from the model (e.g. Sérsic, 1963; Ciotti, 1991). The parameter $b_n$ is related to the Sèrsic index $n$ and is equal tol to $1.9992n - 0.3271$. The de Vaucouleurs profile is a particular case of the Sèrsic profile with Sèrsic index $n = 4$. Such model fits well the light distribution of spheroidal galaxies and bulges. The light distribution of the disk dominated LTGs are better fitted by an exponential profile with $n = 1$. In a general case, the galaxy light profile is well reproduced by two components: an exponential disk and a Sèrsic profile with high Sèrsic index in the central part. More recent attempts of morphological classification provide, indeed, a decomposition of the galaxies in their disk and bulge components and classify galaxies according to the ratio of luminosity or stellar mass contained in the bulge with respect to the total light or mass of the galaxy. Such ration is usually called $B/T$, where $B$ indicates the bulge component and $T$ the total galaxy light or stellar mass (see for example Simard et al. 2011).

The morphological bimodality is accopanied by a substantial color bimodality , as visible in the colour-absolute magnitude (CM, or colour-stellar mass) plane (e.g. Strateva et al., 2001; Blanton et al., 2003; Baldry et al., 2004, 2006; Schawinski et al., 2014). As illustrated in the color-stellar mass diagram based on SDSS data (Fig. 1.2), two sequences are generally identified in this plane: the blue cloud in the low mass regime and the red sequence which dominates at high masses, while the intermediate region, the so-called

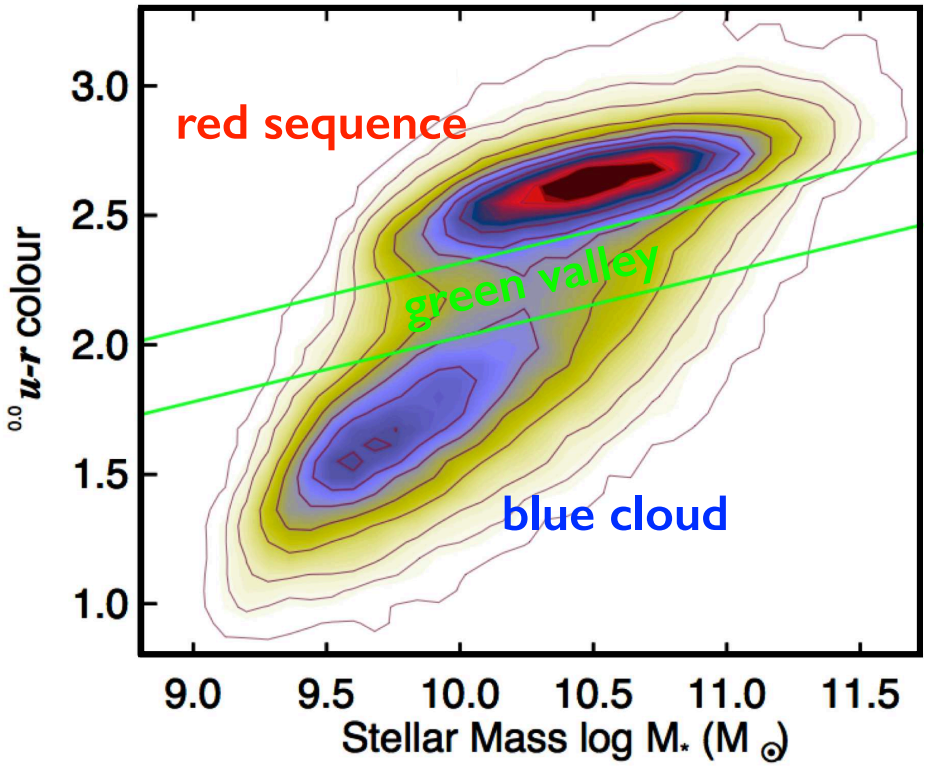


Figure 1.2: The u-r colour-mass diagram for a roughly mass-limited sample of local star forming galaxies drown from the SDSS. The green lines show the green valley between the red sequence and the blue cloud. Figure adapted from Schawinski et al. (2014).

green valley, is scarcely populated (Schawinski et al., 2014). The color bimodality mostly mirror the morphology bimodality. Indeed, blue galaxies are mostly LTGs, spirals and irregulars with recent star formation activity, while the red sequence is dominated, as expected, by red ETGs with little or no star formation (e.g. Schawinski et al., 2014). The less populated valley is dominated by intermediate type galaxies, which are interpreted as in morphological transformation from a spiral to a spheroidal morphology.

Although powerful, the use of the CM, or colour-stellar mass diagram has some limitations. Indeed, galaxy colours are the results of other galaxy properties and it is very difficult to disentangle which of them or which combination of them is making a galaxy red rather than blue. For example, while the presence of a large population of massive young stars can induce very blue colours and indicate recent star formation, the presence of the central super-massive black-hole (SMBH) might ionized the surrounding medium as well leading to a similar UV radiation. On the other end, while a very red color can point to the prevalence of a population of low mass red stars, indicating no star formation, a large dust content or a very high metallicity might lead to the same galaxy colour. Thus, a much more powerful way to look at the galaxy bimodaly, is to investigate directly other galaxy properties, such as their star formation activity, their dust content and their metallicity.

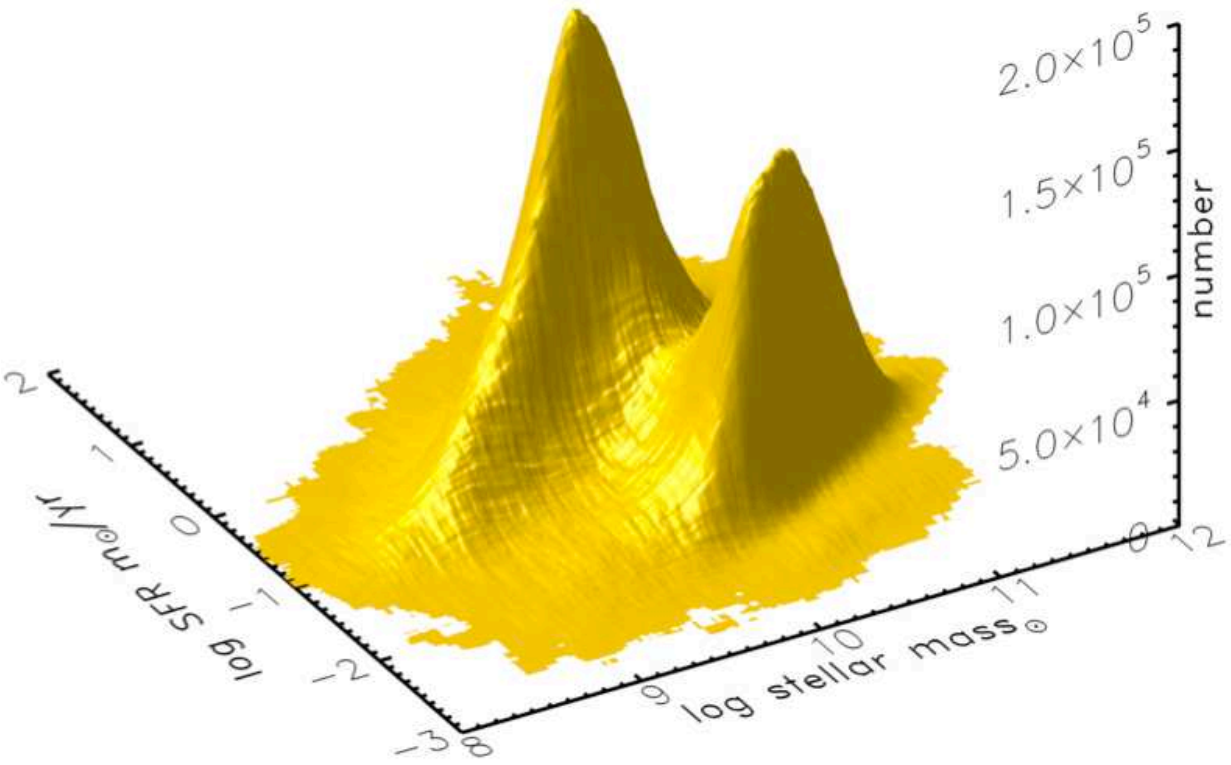


Figure 1.3: The 3D SFR-stellar mass relation for local star forming galaxies in the SDSS DR7 database. The third dimension is the number of galaxies in SFR-stellar mass bins. The two prominent peaks, one for star-forming galaxies and one for the quenched ones, are clearly shown. The tightly correlation between the SFR and M⋆ at high SFRs got the designation of Main Sequence (MS) of star-forming galaxies. The galaxies lying above the MS are the starburst galaxies. Note that for the quenched galaxies the SFR estimates are only an upper limit. In this plot is applied the volume correction. From Renzini & Peng (2015).

### The galaxy star formation activity

Among all galaxy properties, one of the most interesting is the ability or efficiency of galaxies in forming stars. Indeed, understanding what is driving the efficiency of such mechanism is the key to understand how galaxies assemble their mass and how and why they stop doing it to move from being very star forming, blue LTG to red and dead ETG.

Recent advances show that the color bimodality is driven by a substantial bimodality in the galaxy star formation activity. Indeed, by looking at the star formation rate- stellar mass (SFR-$M\star$) plane it is immediately visible that star forming galaxies tend to cluster around a tight relation, while red galaxies are confined in a cloud at much lower star formation rate. The star forming galaxy relation is known as the Main Sequence, and it is in place from redshift $\sim 0$ up to $\sim 4$ (MS; e.g., Brinchmann et al., 2004; Noeske et al., 2007; Elbaz et al., 2007; Daddi et al., 2007; Pannella et al., 2009; Magdis et al., 2010; Schreiber et al., 2015).

The SFR increases with the stellar mass ($M\star$) as a power law, $SFR \propto \mathrm{M}\star^{\alpha}$, with an intrinsic scatter of about 0.2-0.3 dex for moderate to relatively low stellar mass galaxies (Whitaker et al., 2015; Speagle et al., 2014). Measurements of the slope $\alpha$ vary widely in the literature, ranging between $0.6 - 1.2$ (see summary in Speagle et al. 2014). The observed relation suggests that prior to the shutdown of star formation, galaxy star formation histories are predominantly regular and smoothly declining on mass-dependent timescales (see also Heavens et al. 2004), rather than driven by stochastic events like major mergers and starbursts. However, Ilbert et al. (2015) suggest that the scatter of the relation is not constant but it increases as a function of stellar mass, at least up to $z \sim 1.4$, reflecting a larger variety of star formation histories for the most massive galaxies.

Several studies suggest also that the relation is not a power law but it exhibits a curvature with a flatter slope at the high-mass end with respect to the low mass regime (Whitaker et al., 2015; Schreiber et al., 2015; Lee et al., 2015; Tomczak et al., 2016) though bending is not found in other studies (e.g., Speagle et al., 2014; Rodighiero et al., 2014).

More recently Renzini & Peng (2015) proposed two different definitions of the MS: the ridge line connecting the peak of the 3D number density distribution of galaxies over the log(SFR)-log($\mathrm{M}_\star$) plane, or of the similar 3D distribution where the $z$ coordinate is given by the product of the number of galaxies times their SFR. The 3D distribution of Renzini & Peng (2015) based on SDSS data is shown in Fig.1.3. The two MS definitions give nearly parallel relations in the SDSS galaxy spectroscopic sample at $z < 0.085$ with slope $0.76 \pm 0.06$ over the stellar mass range $10^8 - 10^{10.5} M_\odot$, without any particular bending as in Whitaker et al. (2014) (see also Magnelli et al., 2014).

In the SFR-$\mathrm{M}_\star$ plane, well below the MS locus, there is a second highly populated region, characterized by low level of SF activity, as seen in Fig. 1.3. This locus is populated by poorly star forming galaxies with an extremely low specific star formation rate, defined as the ratio of the SFR and the galaxy stellar mass. Such galaxies are defined as *"quiescent"*, *"quenched"* or also *"passive"* galaxies, since they are not actively forming stars. Similarly to the CM diagram, the region between the MS and the passive region is scarcely populated by galaxies with an intermediate level of SFR. Such galaxies are interpreted and in a phase of transition between the MS to the passive region or simply as systems with a lower efficiency in forming stars with respect to the MS galaxies (see Ilbert et al., 2015. In the following we will indicate as "quenching" processes all the physical mechanism that might directly or indirectly stop the formation activity in a galaxy and let it move from the MS region to the "quenched" galaxy cloud.

As already highlighted in the CM diagram for blue and red galaxies, also star forming and quiescent galaxies provide different contribution at different stellar masses. Most of the works in the literature are in agreement in finding that the massive end of the galaxy stellar mass function (GSMF) is dominated by red, passive galaxies, while blue star-forming galaxies dominate the low-mas end (e.g. York et al., 2000; Pozzetti et al., 2007, 2010; Baldry et al., 2004; Ilbert et al., 2010, 2013; Muzzin et al., 2013). This bimodality holds up to very high redshift z$\sim$ 0 out to z$\sim$ 4, when the universe was only 1.5 Gyr old (Muzzin et al., 2013; Ilbert et al., 2013). An example of the redshift evolution of the GSMF is shown in Fig.1.4, for the global, the star-forming and, quiescent population, as found by Ilbert et al.

(2013).

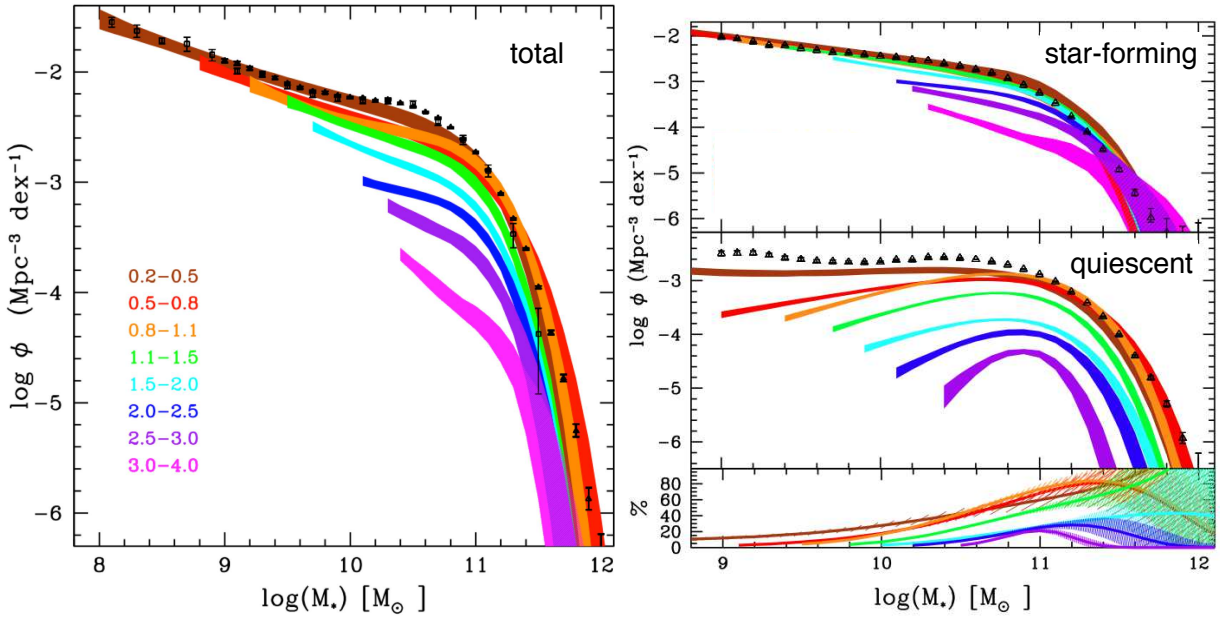


Figure 1.4: Galaxy stellar mass function at $0 < z < 4$ for a sample of 220,000 galaxies (left panel) and, for the star-forming and the quiescent population (right top and middle panel respectively). The bands correspond to the 68% confidence intervals at each redshift, including estimated uncertainties in the derived stellar masses. The squares and open triangles correspond to the local estimates by Baldry et al. (2012) and Moustakas et al. (2013), respectively. The right bottom panel shows the percentage of quiescent galaxies as a function of stellar mass in the same redshift bins. From Madau & Dickinson (2014), adapted from Ilbert et al. (2013).

### The environmental dependence

A plethora of studies starting form the '30s revealed the existence of a correlation between galaxy Hubble type and the local density of galaxies. Hubble & Humason (1931), Abell (1965) and, Oemler (1974) found that the low density field is largely composed of late type galaxies, while the densest regions of clusters of galaxies are predominantly hosting early types. This dichotomy has been, then, generalized by Dressler in 1980 as a fundamental correlation called the morphology-density relation. Indeed, by studying 55 clusters of galaxies, Dressler (1980) showed that the fraction of elliptical (E) and S0 galaxies increases rapidly with increasing galaxy density towards the center of the cluster (see Fig.1.5), while the fraction of spiral galaxies exhibits the opposite trend. More recent results based on the SDSS data confirmed that in the local Universe most star forming, blue, late type galaxies reside in low density environments, while the cores of massive galaxy clusters are galaxy graveyards full of massive spheroidal systems that are dominated by old stellar populations

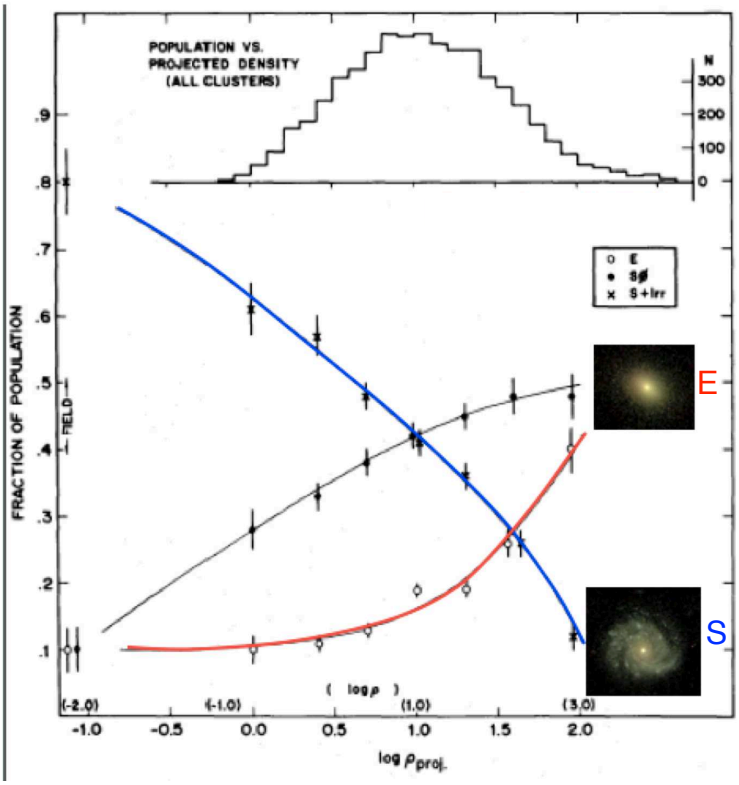


Figure 1.5: The fraction of Elliptical (E, in red), S0 (in black), and Spiral+Irregular (S+Irr, in blue) galaxies as a function of the local projected density in galaxies Mpc$^{-2}$. The data shown are for clusters galaxies and for galaxies in the field (only the first point for each type on the left of the plot). The upper histogram shows the number distribution of the galaxies in bins of projected density. E and S0s tend to populated regions of high galaxy density, while Ss tend to be in low galaxy density environment. From Dressler (1980), adapted from http://burro.case.edu/Academics/Astr222/Galaxies/Intro/properties.html.

(e.g. Lewis et al., 2002; Gómez et al., 2003; Balogh et al., 2004; Kauffmann et al., 2004; Hogg et al., 2004; Blanton et al., 2005; Baldry et al., 2006). Much of the debate centers on whether the morphology-density relation arises early on during the formation of the galaxies, or whether it might be caused by the environments itself.

A recently proposed way to study the relation between galaxy population and environmental conditions is the analysis of the ongoing star formation (SF) in galaxies of different environments (see, e.g., Christlein & Zabludoff, 2005). The SF rate (SFR) is an important measure of the evolutionary state of a galaxy, and a sensitive indicator of the environmental interactions. Previous studies of cluster galaxy SFRs have sometimes reached conflicting conclusions. The SFRs of cluster galaxies have been found to be reduced (Kennicutt, 1983; Bicay & Giovanelli, 1987; Kodaira et al., 1990; Moss & Whittle, 1993a; Abraham et al., 1996; Balogh et al., 1998; Koopmann & Kenney, 1998; Hashimoto et al., 1998; Gavazzi et al., 2002; Pimbblet et al., 2006), comparable (Kennicutt et al., 1984; Donas et al., 1990;

Gavazzi et al., 1991, 1998; Biviano et al., 1997; Moss & Whittle, 2005; Popesso et al., 2007), or in some case enhanced (Moss & Whittle, 1993b; Bennett & Moss, 1998) relative to the SFRs of field galaxies of the same classes. However, cluster and group galaxies tend to be gas poor in the local Universe. Haynes & Giovanelli (1984) provided the very first quantitative determination of the amount of atomic gas content in dense environment showing that cluster galaxies are characterized by a deficiency of HI with respect to isolated galaxies. The difference is even more striking when only relaxed clusters are considered in the comparison (Giovanelli & Haynes, 1985). More recently Catinella et al. (2013) used the HI gas mass retrieved in the GASS survey and find a significant lower gas mass fraction in group and cluster galaxies with respect to systems inhabiting less massive dark matter host halos.

Several cluster-related environmental processes can affect the galaxy gas content and, thus, SFRs of galaxies. Some processes mainly affect the gaseous content of a galaxy, such as the ram-pressure stripping (Gunn & Gott, 1972; Kenney et al., 2004; van Gorkom, 2004), re-accretion of the stripped gas (Vollmer et al., 2001), turbulence and viscosity (see, e.g., Quilis et al., 2001), and starvation/strangulation (Larson et al., 1980). Gravitational processes, which affect both the gaseous and the stellar properties of a galaxy, range from low-velocity tidal interactions and mergers (see, e.g., Mamon, 1996; Barnes & Hernquist, 1996; Conselice, 2006), to high-velocity interactions between galaxies and/or clusters (Moore et al., 1998, 1999; Struck & Smith, 1999; Mihos, 2004). Despite a number of recent studies of nearby and distant clusters, it is not yet clear which of these processes, if any, are dominant.

Peng et al. (2010) analysed such possibility by distinguishing the relative importance of internal versus external processes in driving the evolution of galaxy colours as proxy of their star formation activity. While internal processes are defined as strictly related to the galaxy stellar mass, morphology and central super-massive black hole activity, the external processes are purely related to the galaxy environment and its evolution. Peng et al. (2010) conclude that the environmental effects might play a role mostly in recent epoch, below $z \sim 1$, while the earlier phase of galaxy formation and evolution is dominated by internal processes.

### 1.2.2 Cosmic Star Formation History

The cosmic star formation history (CSFH) is one of the most fundamental observables of our Universe. It provides the star formation activity per comoving volume of the overall galaxy population as a function of time. The current epoch represents a fairly stable and peaceful period of such history. However, we know that the Universe was once a much more violent place, with stars being formed at a much higher rate than is seen around us today. Indeed, the most recent and comprehensive study of the CSFH presented by Madau & Dickinson (2014) confirms that after a rising phase before $z \sim 2$, the CSFH reaches a plateau or a peak between $1 < z < 2$ (see left panel of Fig. 1.6). After such active early epoch, the overall star formation activity of the Universe drops down quickly and it decreases by on order of magnitude until the current epoch. What causes such

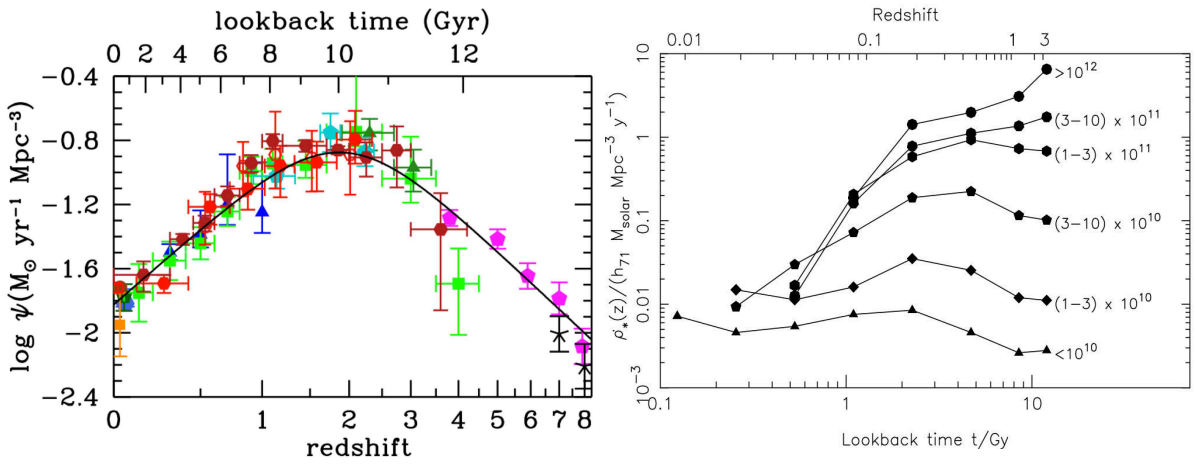


Figure 1.6: *Left panel*: The history of cosmic star formation from UV and FUV rest-frame measurements. The key epoch of galaxy formation is at z$\sim$ 2, when the CSFH density peaks. From Madau & Dickinson (2014). *Right panel*: Galaxy mass downsizing (Heavens et al., 2004). Massive galaxies tend to form earlier and their contribution to the CSFH drops more rapidly than low mass galaxies. For clarity the curves are offset vertically by 0.5 log units, except for most massive galaxies which are offset by an additional 1.0 log factor. The plot is also called "fossil record" of SDSS galaxies and it is obtained from time-tagging stelalr populations in nearby galaxies.

dramatic drop in the last 10-8 Gyrs of the Universe is still a debated issue. Nevertheless, nearly all observational and theoretical studies point to a direct relation to the rise of the galaxy bimodality highlighted in the previous sections.

As shown by Heavens et al. (2004) (see right panel of Fig. 1.6), galaxy with a different final stellar mass in the local Universe might have a quite different star formation history and so provide a very different contribution to the CSFH at different redshift. Galaxies with a final stellar mass of $\sim 10^{10}$ $M_{\odot}$ tend to have a very flat star formation history with a rather constant SFR across cosmic time. As the stellar mass increases, the galaxy star formation histories get steeper and steeper with the local most massive galaxies at $\sim 10^{12}$ $M_{\odot}$ exhibiting significant peak of star formation in the early Universe at $z > 2-3$ (Heavens et al., 2004; Juneau et al., 2005; Gruppioni et al., 2013). These mass dependence evolution is known as "galaxy downsizing", which indicates that most massive galaxies tend to form earlier with respect to the low mass counterpart (Thomas et al., 2010; Concas et al., 2017). Since in the local Universe most massive galaxies tend to be red ETGs with no star formation in high density environment and low mass galaxies tend to be blue and very active LTG in the field, it is clear that there is a direct link between the observed galaxy population dichotomy in terms of morphology, colours, star formation activity and environment and the shape of the CSFH. Understanding what are the physical processes responsible to lead to the overall quenching of the star formation activity in galaxies and their morphological transformation, if any, is still at the core if the galaxy evolution study and it is one of the main goals of this thesis.

## 1.3 The theoretical approach: from cosmology to baryon structures

### 1.3.1 Cosmological contest

The past three decades saw the rise of a "concordant" cosmological model of our expanding universe. Such a model, called Λ cold dark matter model, ΛCDM, is based on two fundamental assumptions. First, the distribution of matter in the universe is homogeneous and isotropic on sufficiently large scales (Cosmological Principle proposed by Milne 1933). Second, the large-scale structure of the universe is essentially determined by gravitational interaction and can be described by general relativity. Tree main components of this model are: the baryonic matter (which forms the visible Universe), the cold dark matter (matter that interacts only through gravity) and dark energy (Λ). The mass-energy budget of the today Universe requires that only $\sim 4\%$ of the total mass is made by ordinary baryonic matter, $\sim 26\%$ is made by dark matter, and $\sim 70\%$ is in form of dark energy (Planck Collaboration et al., 2016b).

The first finding of COBE of very small fluctuations in the temperature of the microwave background radiation, and its interpretation in terms of slight variations of the gravitational potential at the surface of last scattering, is a remarkable confirmation of the general theoretical framework of 'gravitational instability' for cosmic structure formation (Smoot et al., 1992). According to this theory, the early universe was almost perfectly smooth except for tiny density variations with respect to the average background density and related tiny velocity perturbations with respect to the Hubble expansion. Since slight density enhancements induce a slightly stronger gravitational attraction on the surrounding matter, they start to accrete material from its surroundings as long as pressure forces are not sufficient to counteract this infall. In this way the overdensity becomes even more overdense, and their gravitational influence even stronger. The denser it becomes the more it will accrete, resulting in an instability which can ultimately cause the collapse of a density fluctuation to a gravitationally bound object. The size and mass of the object is of course dependent on the scale of the fluctuation. For example, galaxies are thought to have formed out of fluctuations on a scale of $\sim 0.5^{-1}$Mpc, while clusters of galaxies have emerged out of fluctuations on a larger scale of $\sim 4^{-1}$Mpc. The formation of voids affects in the same general scheme, having grown out of primordial underdensities in the matter distribution. Once a fluctuation grows larger than $\delta > 1$, nonlinear effects become important. The perturbation decouples from the underlying expansion of the Universe and forms a gravitationally bound virialised structure known as a dark matter halo (Gunn & Gott, 1972). Such scenario has been confirmed and better tuned by the more recent WMAP and the Planck satellite results (Bennett et al., 2003; Planck Collaboration et al., 2016a,b)

In the ΛCDM scenario, the structure formation happens through a hierarchical or "bottom-up" build-up of structure, where small dark matter halos form first and then merge into larger structures. A simple scheme of this structure formation scenario is given

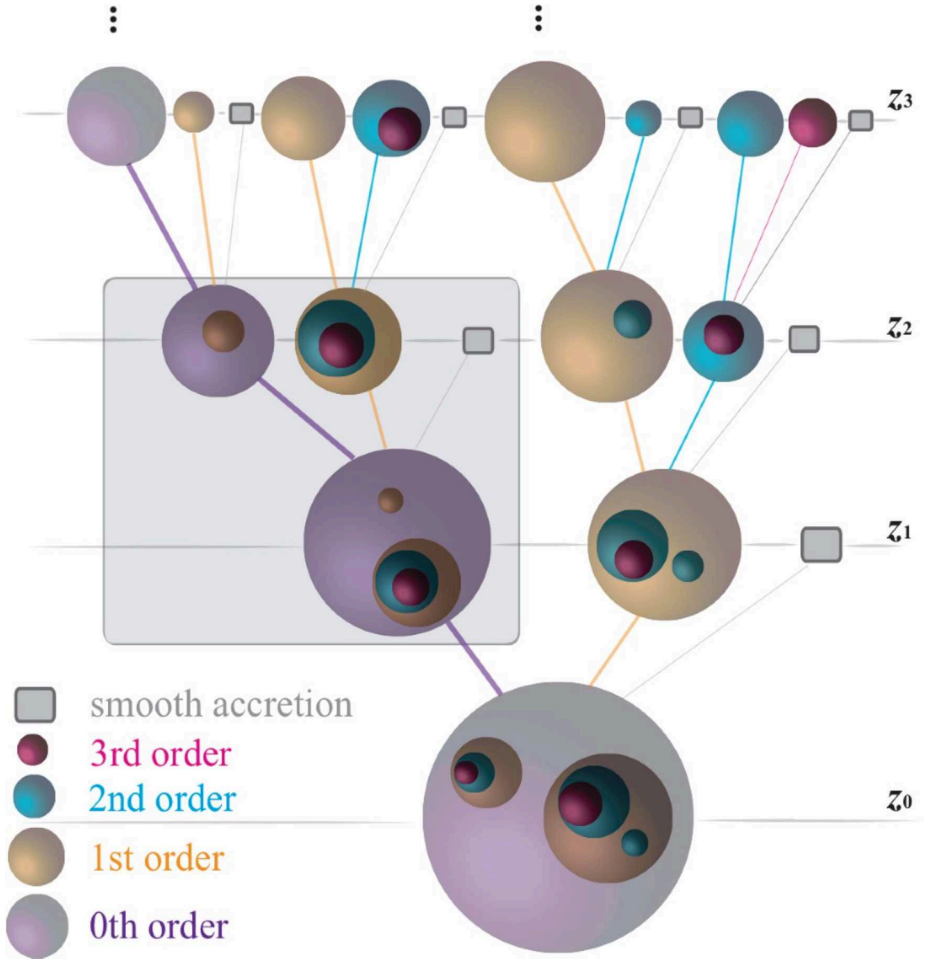


Figure 1.7: Illustration of a schematic merger tree, showing the assembly history of dark matter halo in discrete time steps. The redshift decreases from top $z_3$ to bottom $z_0$ (the time increase in the opposite direction). The big purple sphere at the bottom is the host halo at redshift $z = z_0$. The left branch illustrate the assembly history of the main or "zeroth-order" progenitors (purple spheres). They accrete "first-order" progenitors (yellow spheres), which end up as (first- order) sub-haloes at $z = z_0$. These, in turn, increase the "second-order" progenitors and end up as (second-order) sub-haloes at $z = z_0$, etc. At $z = z_0$, the 1st, 2st, and 3rd- order haloes are satellites (or sub-haloes) of the main 0th order host halo. The size of each sphere is proportional to the mass of the halo. The large shaded box shows a descendant halo plus its single-time-step progenitors. The small boxes indicate the smooth accretion (i.e., not part of any halo or progenitors haloes with masses below the mass resolution in the merger tree model). From Jiang & van den Bosch (2014).

in Fig. 1.7, where the growth of a halo is proposed as a "merger three". The galactic scale dark matter halos collapse first. Smaller halos hosting low mass galaxies merge to form more massive galaxies, that then merge as well to form bigger systems as galaxy clusters, which merge themselves to form the so called superclusters. Depending on their location in

the final dark matter halo, galaxies can be classified as "central" or "satellite". All galaxies form at the center of their own dark matter halo as central systems and become satellite as the time goes once their host halo merge into a larger halos, as shown in Fig. 1.7. The galaxy hosted by the most massive halo remains the central galaxy of the final halo. While, the galaxies located in the sub-haloes become satellites. The sub-haloes (smaller haloes or 1st, 2st, and 3rd- order haloes in Fig. 1.7), orbits withing the "zeroth-order" progenitor (purple spheres in Fig. 1.7).

### 1.3.2 Baryons Structures

Due to the success of the ΛCDM scenario in reproducing the large scale structure distribution, more and more works focused on smaller structures in order to embed galaxy formation into the hierarchical picture. In the hierarchical merging scenario, galaxies end up as spirals or ellipticals depending on the details of their merger history (e.g. Fig. 1.7). In particular, typical elliptical galaxies form through two channels: either the "wet" mergers of intermediate-mass gas-rich disks or through "dry" mergers of gas-poor early type galaxies (e.g., Kauffmann et al., 1996; Baugh et al., 1996; De Lucia et al., 2006; Scarlata et al., 2007). As a result, the model predicts that the number of the high mass galaxies should decrease with increasing redshift (that is, decreasing age) in favour of the number of smaller systems.

While the key physics of gas cooling and merging are now thought to be modeled with reasonable accuracy (e.g., Benson et al., 2001; Yoshida et al., 2002; Voit et al., 2002), other physics crucial to establishing the shape of the luminosity function or the stellar mass function remain poorly understood. The main uncertainty is reproducing the stellar mass distribution of galaxies is the metal pollution or the star formation feedback needed to regulate the formation of dwarf galaxies, and hence reconcile the rather shallow slope of the faint end of the observed luminosity and stellar mass function with the relatively steep mass function of dark matter halos. In addition, all current models of galaxy formation, based either on hydrodynamical simulations (Pearce et al., 2001; Kay et al., 2002) or semi-analytic techniques (e.g., Kauffmann et al., 1999; Somerville & Primack, 1999; Cole et al., 2000), exhibit strong gas cooling in the central regions of groups and clusters. This leads to the formation of extremely bright galaxies, which are never seen in reality, unless some additional suppression of the gas cooling is assumed.

This is why in the last decades a lot of effort has been devoted in finding the physical mechanisms able to regulate the star formation activity both at low and high stellar mass regime. Such "quenching" process might act in two distinct way: *i)* either by limiting the cold gas supply to galaxies and so lead to the progressive shut-down of the SFR after the gas reservoir exhaustion, or *ii)* by actively removing the gas from the galaxy and so stopping any star formation process. Following the nomenclature proposed by Peng et al. (2010), the first set of processes is directly linked to the galaxy environment and it is defined as **"environmental quenching"** or **"external quenching"**. The second set is, instead, related to the galaxy's stellar mass (including **SF efficiency**, and **AGN feedback**) and it is called **"mass"** or **"internal quenching"**.

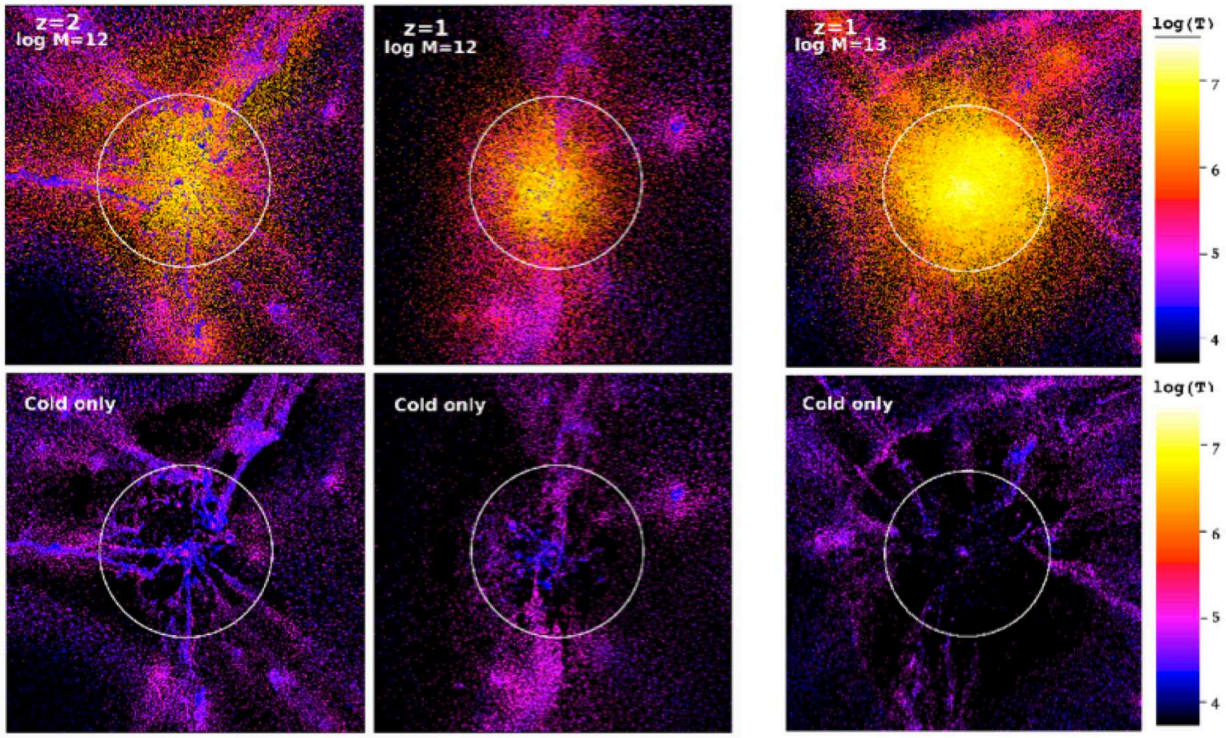


Figure 1.8: Temperature (T) snapshots of a cosmological ΛCDM simulation from Kereš et al. (2009), for gas in a groups with $M_{halo} = 1.1 \times 10^{12}$ $M_{\odot}$ at z = 2 and, z=1 in the left and middle panels and, in a group with $M_{halo} = 9 \times 10^{12}$ $M_{\odot}$ at z = 1, in the right panels. The box regions show the gas in a region $1h^{-1}$ Mpc (comoving) on a side and $1h^{-1}$ (comoving) in projected depth in the left and middle panels and, $2h^{-1}$ Mpc (comoving) on a side and $2h^{-1}$ (comoving) in projected depth in the right panels. The virial radius is shown as the circles. Upper panels show all gas particles. The middle panels show only the gas with $T < 10^5$ K with the same color scale.

### External or Environmental quenching

The classical models of galaxy formation predict that galaxies form from the collapse of overdense regions of matter: baryons are captured by the gravity of galaxy-sized dark matter halo and they are heated by continuous shocks until it forms an isotropic and spherical halo in hydrostatic equilibrium at virial temperature (White & Rees, 1978; White & Frenk, 1991). According to the mass accretion theory, there is a clear dichotomy on the way galaxies can accrete gas to sustain their star formation process, the so called "cold" and "hot" accretion modes (Katz et al., 2003; Kereš et al., 2005, 2009; Birnboim & Dekel, 2003; Dekel & Birnboim, 2006; Dekel et al., 2009). Such dichotomy is purely dictated by the dark matter host halo mass. In low mass halos at masses below $10^{12-12.5}$ $M_{\odot}$, the central galaxy acquires the cold gas through cold streams of gas penetrating the halo directly from the cosmic web. This accretion is expected to dominate the global growth of all galaxies at high redshifts (z> 2) and the growth of low-mass star-forming galaxies in

the low-redshift Universe.

In group- and cluster-sized halos with masses above $10^{12-12.5}$ $M_\odot$, the intra-group (IGM) and intra-cluster (ICM) medium is shock-heated at the virial temperature of $10^6 - 10^7$ K during the gravitational collapse. Such high temperature disrupt the streams of cold gas which are no longer able to penetrate the dark matter halos and reach the central galaxy. The accretion can happen only via cooling of the hot ICM and IGM (Dekel & Birnboim, 2006). As shown in Fig. 1.8, filamentary structures of cold mode accretion exist at high redshift ($z = 2$ left panels), they directly feed the central galaxy, but progressively decrease at lower redshifts ($z = 1$, middle panels) and, at higher virial masses (right panels, see also Birnboim & Dekel 2003; Dekel & Birnboim 2006; Kereš et al. 2009).

The transition from a cold gas accretion regime in low mass dark matter halos, to the hot accretion in the massive halos, naturally leads to the observed dichotomy between disky, gas rich star forming galaxies in the field and the spheroidal, gas poor, red and dead galaxies in groups and clusters of galaxies. However, from the observational point of view, although there is indication of a HI deficiency in group and cluster galaxies, the statistics is not sufficient to confirm a direct effect of the environment on the galaxy gas reservoir (Verdes-Montenegro et al., 2001; Gavazzi et al., 2005; Catinella et al., 2013; Popesso et al., 2015).

### Internal quenching

The simplistic scenario provided by the transition from cold to hot accretion mode is made more complex by the interplay between the accreted material into the halo and feedback produced by the galaxy itself. In the current paradigm of galaxy formation, two main "internal" processes are advocated to swipe away the gas supply, and/or to prevent the hot gas from cooling down and eventually fall onto the galaxy to feed its star formation activity: (1) the active galactic nuclei (AGN), and (2) the star formation activity (SF) itself.

It is commonly recognized that the observationally determined galactic stellar mass function and the theoretically determined halo mass function (assuming the ΛCDM cosmology presented in Section 1.3) have divergent behaviors at both the high- and low-mass ends ( left panel of Fig. 1.9). The differing slopes at both high and low masses indicate that star formation is less efficient in these regimes. According to the most accredited galaxy formation models, from the semi-analytical (SAM) ones to the more recent mass-abundance-matching models, in the central galaxies, the efficiency in converting the gas fraction into stars reaches a maximum at halo mass $\sim 10^{12}$ $M_\odot$ (see right panel of Fig. 1.9) with only $\sim 20$ % of their baryons currently locked up in stars (see for example Croton et al., 2006; Guo et al., 2011 based on the Millennium Simulation, and Moster et al., 2010; Behroozi et al., 2010; Yang et al., 2012 among the mass-abundance-matching models). As clearly shown in the right panel of Fig.1.9, the efficiency drops down steeply towards both sides of this mass threshold (e.g., Madau et al., 1996; Baldry et al., 2008; Conroy & Wechsler, 2009; Guo et al., 2010; Moster et al., 2010, 2013; Behroozi et al., 2010, 2013). Above and below this threshold, the models need feedback to reproduce the semi-empirical curve.

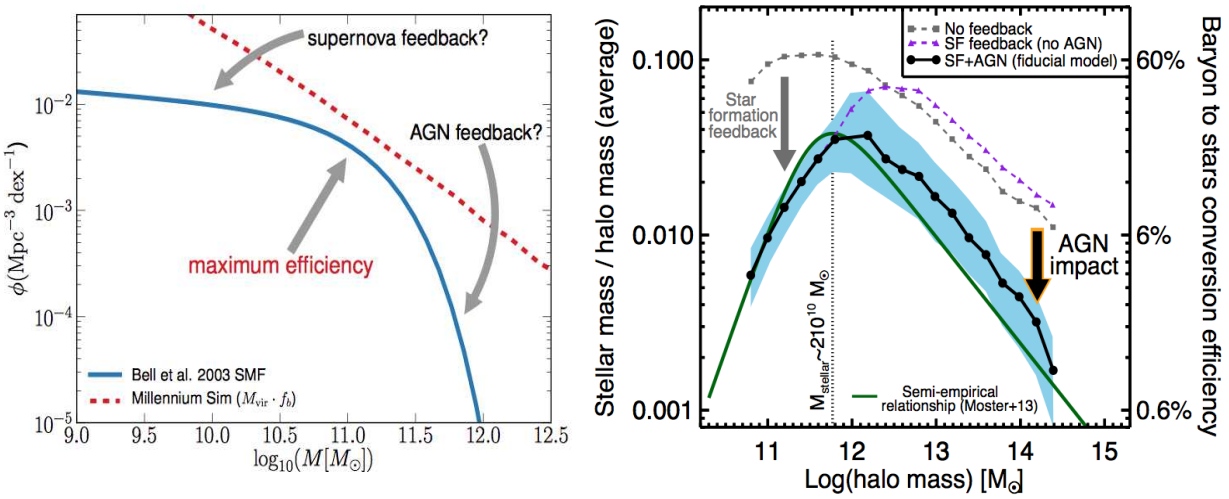


Figure 1.9: *Left panel*: Galaxy baryonic mass function (blue solid line, observed by Bell et al., 2003b) compared to the mass spectrum of cold dark matter halos of the Millennium Simulation (red dashed line). The halo mass function is scaled with the cosmological baryonic fraction $f_g = 0.163$ in order to demonstrate the maximum possible stellar mass content as a function of halo mass. The differing slopes at both high and low masses indicate that star formation is less efficient in these regimes. At low masses, this is commonly attributed to the formation and evolution of massive stars. While at high masses energy injection from central SMBH. Figure from Mutch et al., 2013. *Right panel*: The ratio of stellar to halo masses as a function of halo mass for a semi-empirical relationship (green line from Moster et al., 2013), and for three runs of simulation (with only SF feedback, only AGN feedback and without feedback, Somerville et al., 2008). The efficiency of converting the gas reservoir into stars reaches a maximum at dark halo masses $\sim 10^{10.2}$ $M_\odot$. Above and below this threshold limit the models need feedback to reproduce the semi-empirical curve. Figure from the recent review of Harrison (2017).

At low masses, the efficiency reduction is commonly attributed to the formation and evolution of massive stars. A combination of effects such as supernovae explosions and stellar winds in actively star-forming regions, can heat and/or remove the gas from the galaxy via large-scale outflows (e.g. Chevalier, 1977, Murray et al., 2005b and Hopkins et al., 2014). This reduces the availability of this material to fuel further star formation episodes, hence temporarily stalling in situ stellar mass growth. From a theoretical point of view, two main scenarios for star formation-driven feedback are propose: (1) one linked to the kinetic energy, the so called energy-driven feedback (see Chevalier, 1977; Chevalier & Clegg, 1985b; Leitherer et al., 1992; Springel & Hernquist, 2003; Veilleux et al., 2005) and, (2) the momentum-driven feedback related to the momentum injection into the interstellar medium (ISM, Murray et al., 2005b).

According to the first scenario, the kinetic energy released by supernova explosions and, by stellar winds from OB and Wolf-Rayet stars, plays the most important role in prevent and self-regulate star formation. This feedback mechanism is subject to the thermalisation

efficiency of the energy deposited into the ISM: such efficiency may vary, but it is believed to be around 1-10% (Chevalier, 1977; Murray et al., 2005a; Thornton et al., 1998; Mac Low & Ferrara, 1999). If the kinetic energy from SNe and stellar winds is efficiently transfer to the gas cloud motion, it can drive strong and large-scale outflows (Chevalier & Clegg, 1985a). This process can be important at high SFR, where the kinetic energy injected by SN ejecta and by stellar winds into the ISM is quite strong.

In the momentum-driven scenario, the momentum transferred by the UV radiation from young and massive stars to dust and the momentum injected by supernova explosions, dominate the feedback mechanism (Murray et al., 2005a). This process can be effective on driving galactic winds even when radiative losses are high, because momentum cannot be radiated away (Murray et al., 2005a). However, in order to be effective, this feedback mechanism requires particular ISM conditions, such as large optical depths to infrared radiation (Davé et al., 2011; Hopkins et al., 2011), as well as collisional coupling of gas and dust in the wind (Murray et al., 2005a; Davé et al., 2011). For these reasons, momentum-driven outflows may be most effective at launching cold and dense gas in dusty star-forming galaxies.

A natural outcome of these models is that star forming-driven outflows are more important, at fixed SFR, in low mass galaxies residing in less massive dark matter halos, where the gas can escape from their shallower gravitational wells (Dekel & Silk, 1986; Springel & Hernquist, 2003; Davé et al., 2011). I will return to a discussion of the observational evidence of galactic outflows in Section 1.4.

At high halo masses, the situation is more complicated. The energy released by supernovae or injected by stellar photoionisation is not sufficient to overcome the dark matter gravitational potential. More powerful outflows are required to let the gas escape from the deeper galaxy potential well. The energy and radiation generated by accretion onto the massive black hole (BH), in the most massive galaxies, exceeds the binding energy of the gas by a large factor (see Fabian, 2012 for a complete review). Therefore, energetic feedback from active galactic nuclei (AGN) is believed to provide an important and effective mechanism to eject the gas away through powerful winds, stop the growth of the galaxy and stifle accretion onto the BH (Di Matteo et al., 2005; De Lucia et al., 2006; Croton et al., 2006; Hopkins et al., 2006; Bower et al., 2006; Hopkins et al., 2014; Henriques et al., 2017).

Several empirical results, come out in the last two decades, and suggest an intimate connection between the super-massive black holes (SMBH thereafter) and their host-galaxies properties. These relations argue that SMBH and galaxies are linked in an evolutionary manner, which appear incredible because there are nine orders of magnitude difference in the physical size scale, equivalent to the difference between the size of a coin and the Earth (Harrison, 2014). As shown by Magorrian et al. (1998), and than confirmed by several authors (e.g. Marconi & Hunt, 2003, Kormendy & Ho, 2013), the SMBHs masses ($M_{BH}$) correlate with the masses of their host bulges. Two year later, this relation was followed by the correlation between $M_{BH}$ and the stellar velocity dispersion of the bulge (e.g. Ferrarese & Merritt, 2000 and Heckman et al., 2004), and with bulge luminosity (see Kormendy &

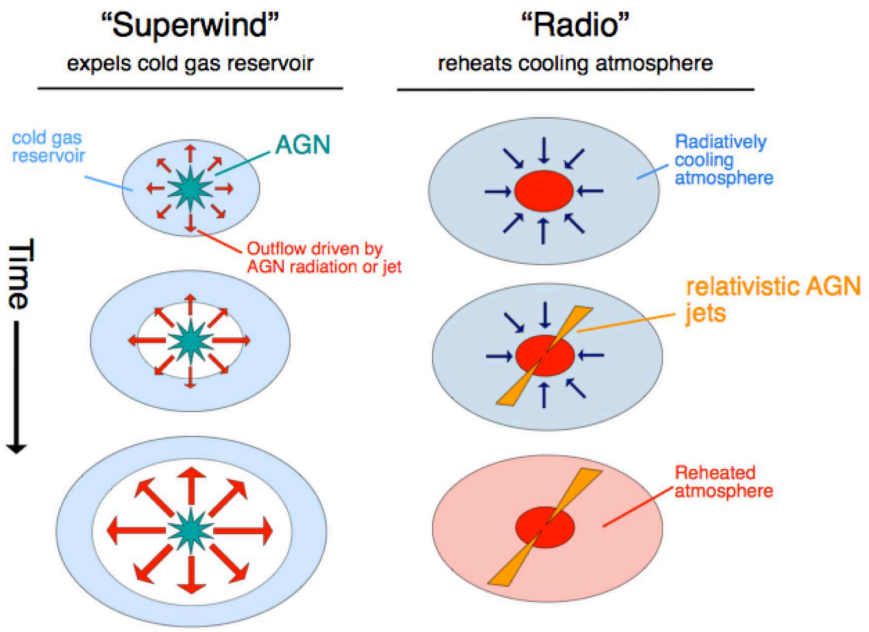


Figure 1.10: Schematic diagrams to illustrate the two main modes of AGN outflows: "superwind or "radiative" mode outflows such as those found in luminous AGNs (mass accretion rates $\gtrsim 1\%$ of the Eddington limit) and "radio or "maintenance" mode outflows such as those found in low-excitation AGNs (low Eddington ratios AGNs). Figure from Alexander & Hickox (2012).

Ho, 2013 for a comprehensive review). Other indication about a link between the physical drivers of BH growth and stellar mass assembly, is also demanded by the apparent similarity of the CSFH (discussed in Sec. 1.2.2) and the luminosity density of AGN as a function of redshift (Boyle & Terlevich, 1998; Franceschini et al., 1999). Both star formation and black hole accretion history follow similar general trends and peak around $z \sim 1-2$ and then decline rapidly towards the present day (e.g. Madau & Dickinson, 2014).

These lines of evidence guided in the last decade most of the developments of the galaxy formation models within the ΛCDM paradigm of structure formation shown in Section 1.3. In other words, the AGN activity and, in particular, its feedback, became the second fundamental ingredient of galaxy evolution in addition to the merger activity. Indeed, in many semi-analytic calculations one of the most adopted assumptions, to put it in a simply way, is that the gas-rich galaxy merging may trigger major starbursts, account for the formation and growth of SMBH and lead to the formation of elliptical galaxies (Sanders et al., 1988; Hopkins et al., 2008).

Different mechanisms have been proposed to explain AGN feedback processes depending on the energy released by black hole accretion: the so called "quasar","superwind" or "radiative" mode, and the "radio", "jet" or "maintenance" mode (see Fig. 1.10). The "radiative" mode operates in a typical galactic bulge when the accreting rate of SMBH is close to the Eddington limit (mass accretion rates $\gtrsim 1\%$ of the Eddington limit, Harrison,

2017). It is associated with wide-angle outflows, driven by the radiative output of the AGN, which can expel most of the gas in the host galaxy (e.g., King & Pounds, 2015).

Powerful winds have been invoked to quench the growth of both the BH and spheroidal component of common galaxies and explain the tight BH-spheroid mass relation (e.g., Di Matteo et al., 2005; Hopkins et al., 2008). These winds are purported to inhibit star formation in the merger remnants, and to create a population of red gas-poor ellipticals, thereby explaining the bimodal color distribution observed in large galaxy surveys (e.g., Kauffmann et al., 2003a).

In contrast mechanical energy injection is sometimes called "radio or "jet mode and is associated with low Eddington ratios (e.g., Merloni & Heinz, 2007; McNamara & Nulsen, 2012; Best & Heckman, 2012; Heckman & Best, 2014). This radio-mode feedback is used to quench the SF and BH activity in massive cluster galaxies through powerful jets. These assumptions are able to fix most of the "defects" of galaxy formation models, such as the shape of the galaxy luminosity function and "downsizing" of the cosmic star formation history (Croton et al., 2006; Somerville et al., 2008). The substantial success in explaining a variety of observations enjoyed by these semi-analytic models created a large consensus on the central role of AGN feedback in driving the galaxy evolution and, thus, on the existence of a substantial co-evolution between AGN and host galaxy. However, these results are obtained with the implementation of **ad hoc feedback** able to stop the star formation of the host galaxy and the BH growth. Therefore, feedback is arguably at the same time the strength of the current paradigm of galaxy formation but also the principal uncertainty.

## 1.4 The methodology

The focus of this thesis is to understand if and how internal and external processes might affect the galaxy star formation activity and lead to the observed galaxy bimodality in the local Universe. To this aim, we apply a well defined methodology to study, in particular, the occurrence of galactic wind in local galaxies and to estimate their effect on the galaxy properties. A different method is used, instead, to study the effect of different environmental processes on the galaxy appearance. For both purposes we perform an in depth analysis of spectroscopic data by using few spectral absorption and emission features observable in the rest-frame optical wavelength range of local galaxies.

In this section we first describe the spectral features used in the studies of internal and external processes performed in this thesis. We also detail the method used in the analysis of such features and describe the state of the art of the current studies. For the analysis of ionized and neutral gas outflows we use, in particular, the [OIII]$\lambda$5007 Å emission, and NaD $\lambda\lambda$5890,5896 Å absorption features, respectively, as main gas winds indicators. For the study of the effect of the environment on the galaxy gas content we use the so called Balmer decrement, which is given by the flux ratio of the H$\alpha$ and H$\beta$ Balmer lines. Such ratio, as detailed in the following section, is an indicator of the galaxy dust content. We first describe the electron transitions from which such lines are generated.

### 1.4.1 Electron transitions

According to quantum mechanics, atoms and electrons can be fully described by a so-called wave function. The wave function, also called atomic orbital, is described completely by four quantum numbers: the principal quantum number ($n$), the orbital angular momentum quantum number ($l$), the magnetic quantum number ($m_l$), and the electron spin quantum number ($m_s$). The principal quantum number, $n$, describes the energy of an electron or, in other words, the principal electron shell or energy level in which the electron is located. $n$ can be any positive integer, so $n = 1, 2, 3, 4, 5....$ The innermost or first principal shell, $n = 1$, is called ground state or lower energy state. When an electron is excited, it gains energy and it may jump to an other shell. The second quantum number or orbital angular momentum $l$ determines the shape of an orbital, and it can take values between 0 and $n-1$. For historical reason, each $l$ value is associated to a particular letter, as it is shown in Tab. 1.1. The choice of letters originates from the original system of categorizing spectral lines as "sharp", "principal", "diffuse" and "fundamental" (or "fine"), based on their observed fine structure.

| $l$ number | 0 | 1 | 2 | 3 | 4 |
|---|---|---|---|---|---|
| $l$ letter | $s$ | $p$ | $d$ | $f$ | $g$ |

Table 1.1: Values and historical letters of the orbital angular momentum $l$.

The magnetic quantum number $m_l$ specifies the orientation in space of an orbital of a given energy $n$ and shape $l$. This number divides each $l$ into $2l + 1$ individual orbitals which hold the electrons. $m_l$ can have the integer values between $-l$ and $+l$. Finally, the spin quantum number $m_s$ specifies the orientation of the spin axis of an electron and may have an upward spin, $m_s = +1/2$ or a downward spin, $m_s = -1/2$.
The distribution of electrons among the orbitals of an atom is called the electron configuration. The electrons are filled in according to a scheme known as the Aufbau principle (from German, meaning "building up"), which corresponds to increasing energy of the subshells without violating the Pauli principle[1]. The electron configuration of an atom is commonly written in an abbreviated form in which the orbitals occupied by the electrons are indicated by their principal number $n$ and their $l$ letter, with the number of electrons in the subshell indicated by a superscript, x ($nl^x$). As an example, for the hydrogen atom, the electron configuration in the state of lower energy is written as $1s^1$, $n = 1$, $l = 0 = s$ and $x = 1$ electron. For more complicated atoms or ions with more than a single electron, the Coulomb interaction between the electrons is more complicated. In these cases, the different quantum states can be notated with the capital letters: $^{2S+1}L_J$, where S is the spin quantum number, J is the total angular momentum quantum number and L is the orbital quantum number. L has standard labels for each value, the first of which are: "**S**"

[1]The Pauli Exclusion Principle states that, in an atom or molecule, no two electrons can have the same four electronic quantum numbers. As an orbital can contain a maximum of only two electrons, the two electrons must have opposing spins, $m_s = +1/2$ or $-1/2$

(for L=0),"**P**" (for L=1), "**D**" (for L=2), etc. The values of L and S are determined by the sum of the corresponding individual quantum numbers of the outer electrons (that are set by the orbitals that they are located in and their spins). Each combination of L and S results in a different energy level and, in the case where the total spin angular momentum $(2S+1) > 1$, $J$ can assume the values of $J = |L - S|$, so $J_1 = L + 1$, $J_2 = L - 1$, $J_3 = L$. In the case of the $O^{2+}$ ion, the lower energy level is the $^3\mathbf{P}$ configuration, where the two outermost electrons are in the $n = 2$, $l = 1$ orbital and have $S = 1$, so $(2S + 1) = 3$, $L = 1$ and and there are three possible values of $J = 0, 1, 2$. Another way to indicate the placement of electrons is an orbital diagram, in which each orbital is represented by a square, and the electrons as arrows pointing up or down (indicating the electron spin).

### 1.4.2 The [OIII] and NaI D spectral features

The strong [OIII] emission line at $\lambda\lambda$4959, 5007 Å was observed for the first time by Sir William Hugging in the Draco planetary nebula (NGC 6543). He showed that nebulae have not a spectrum of unresolved stars, as he expected, but they have bright emission lines at 4959 and 5007 Å. For a long time this line pair, also known as $N_1$ and $N_2$, was attributed to a new element, called "nebulium". The mystery of the origin of these lines was settled by Bowen in the 1928. He showed that the arcane "nebulium" lines observed in the spectra of several nebulae were to be explained as "forbidden" transitions in the doubly ionized oxygen ion, $O^{+2}$ ( http://laserstars.org/spectra/Nebulium.html).

The oxygen atom in the presence of a strong radiation field can lose two electrons and become a $O^{2+}$ ion (6 electrons). This condition occurs quite often in the inter stellar medium. The lowest energy electron configuration for this ion is shown in Fig. 1.11, and correspond to $1s^2 2s^2 2p^2$ $^3\mathbf{P}$. Collisions between free electrons and ions can excite this low energy level of the $O^{2+}$ ions. The radiation transitions from the excited levels have very small transition probabilities (of the order of $10^{-2}$ and $10^{-3}$ for the line transition at 5007 and 4960 Å, respectively) compared with ordinary lines, but in a low density regime of typical astrophysical nebulae, collisional de-exitation is even less probable (Osterbrock & Ferland, 2006). For this reason, almost every excitation leads to emission of a photon, producing a typical "forbidden" emission line spectrum, which is quite difficult to reproduce under terrestrial laboratory conditions. In the particular case of the $O^{2+}$ ion in the $2p^3$ configuration, the exited levels $^1\mathbf{S}_0$ and $^1\mathbf{D}_2$ decay to the the ground $^3\mathbf{P}$ level producing the oxygen emission lines at $\lambda$4363, 4959 and 5007 Å (see left panel of Fig. 1.12).

Forbidden lines disappear above a certain critical density, for the [OIII] line at $\lambda$5007 and 4959 Å the value is $n_c = 6.8 \times 10^5$ cm$^{-3}$ for gas temperature $T = 10000$ K (Osterbrock & Ferland, 2006).

The Na I D radiative transition arises from the neutral sodium atoms at temperatures T < 1000K. The ionization potential of the sodium is only 5.1 eV, corresponding to a wavelength of $\sim$ 2420 Å. This implies that the photons that ionize Na I are in the near-UV and that sodium is mainly shielded from ionizing radiation by dust. This sodium doublet is therefore a primarily probe of the dusty warm atomic phase and the cold molecular phase

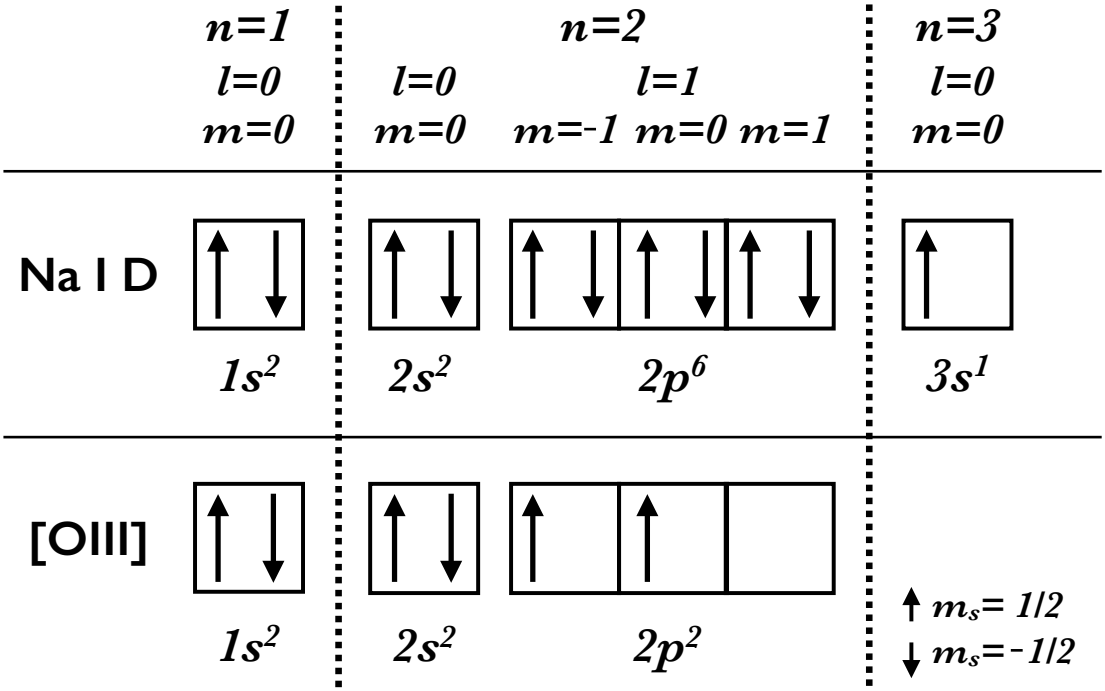


Figure 1.11: Ground level for the neutral sodium and the doubly ionized oxygen. The quantum numbers, $n$, $l$ and, $m_l$ are shown in the top. The electron spin quantum number $m_s$ is indicated with the arrows according with the legend. The Na I D have 11 electrons with the ground level configuration $1s^1\ 2s^2\ 2p^6\ 3s^1$. The $O^{+2}$ ion have 6 electrons with configuration $1s^2\ 2s^2\ 2p^2$.

(Spitzer, 1978).
The ground level configuration (state of lower energy) and corresponding diagram of the 11 electrons of the neutral sodium, $1s^1\ 2s^2\ 2p^6\ 3s^1$, are shown in Fig. 1.11. When the continuum photons, emitted by the stars, are absorbed by the neutral Na atoms, the external electron in the the ground-state configuration 3s goes into the excited energy levels of the 3p configuration composed by two states with total angular momentum j=3/2 and j=1/2 (spin-orbit effect). This transition indicated by the blue arrows in Fig.1.12 causes a doublet absorption line at $\lambda\lambda$5890,5896 Å. When the electrons in the 3p configuration decay spontaneously to the ground-state 3s, the photons are re-emitted (red arrows in Fig.1.12). For this reason, the NaI doublet can be observed both in absorption and in emission. This double process is caused by an electron jumping between the ground state and the first energy level in the Na atom, for this reason it is commonly called "resonant" line [2].

[2]A transition is resonant when a photon can be absorbed from the ground state and re-emitted to the same lowest level of the ground state, as for Lyman-alpha and the Na D $\lambda\lambda$5890,5896 Å transitions. A transition is non-resonant when the photon can be re-emitted to an excited level of a ground state that has multiple levels due to fine structure splitting.

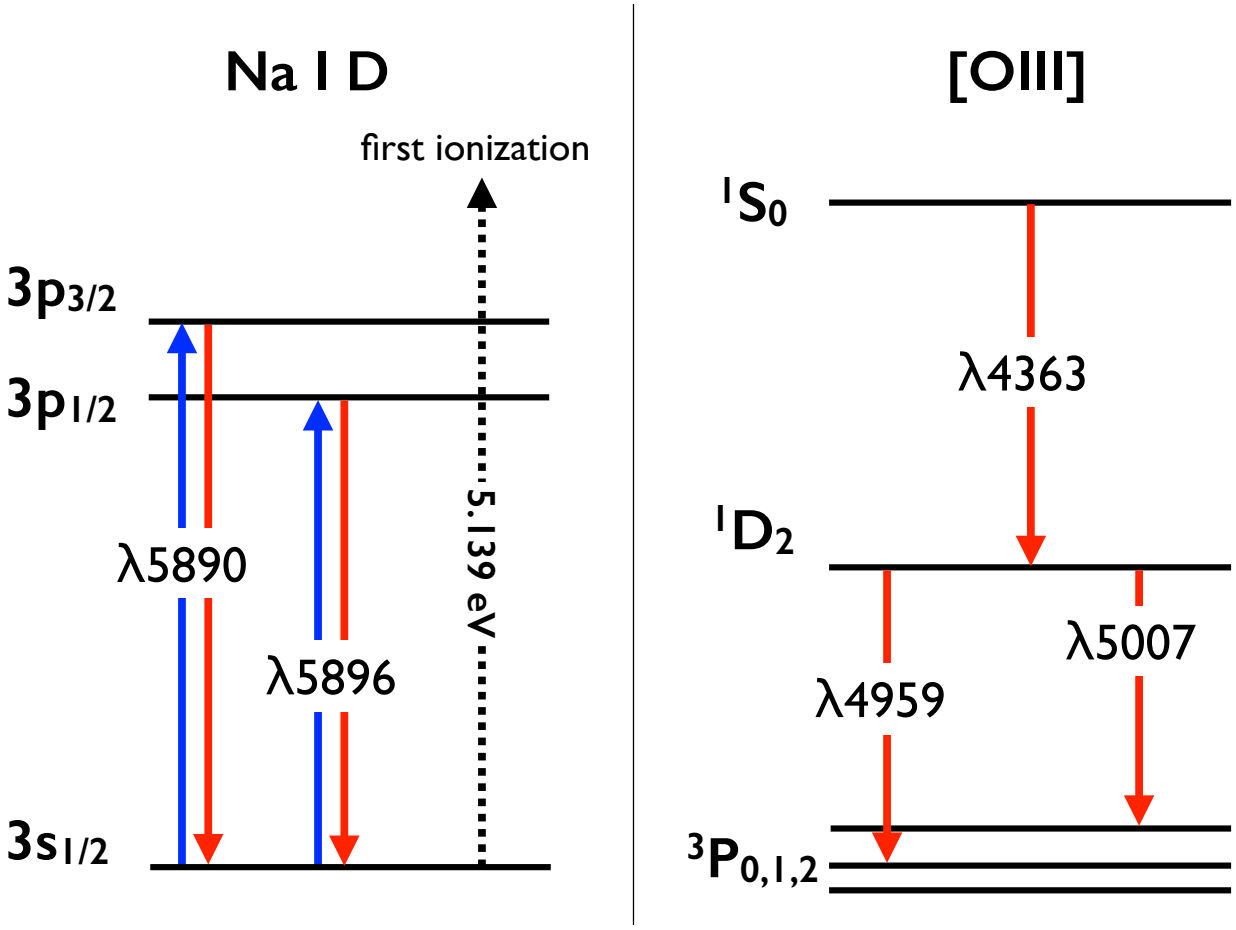


Figure 1.12: Energy-level diagram for the Na I doublet at $\lambda\lambda$5890,5896 Å and the [OIII] in the $2p^3$ configuration. Each transition shown is labeled by its rest wavelength (Å). Blue and red arrows indicate the transitions related to the absorption lines and emission lines, respectively. The Na I configuration is split into two energy levels that give rise to the Na I $\lambda\lambda$. They are both resonance-line transitions, i.e. those connected to the ground state.

### The line profile as indicator of galactic outflow

The most common method to identify outflows is through specific features in the profile of few emission and absorption lines. The best example of galactic outflow in this respect is given by the starburst galaxy M82 (Fig.1.13). This galaxy is the closest, brightest and best studied case of a starburst-driven outflow in the local Universe (see e.g., the recent review of Heckman & Thompson, 2017). The proximity of the system, at only D = 3.63 Mpc (Freedman et al., 1994; Gerke et al., 2011) in the M81 group and its disk inclination, $i = 80°$ (McKeith et al., 1995), make it particularly well-suited to observe the outflow along the minor axis. The first observational evidence for a galactic outflow in M82 dates back to the sixties (Lynds & Sandage, 1963) to the discovery of an extensive system of filamentary optical emission line gas extending to radii of several kpc from the central starburst out

Figure 1.13: Galactic wind in the prototypical starburst galaxy M82. The color- composite image was constructed by the Hubble Heritage team from B, V, I, and H$\alpha$ images obtained with the Hubble Space Telescope Advanced Camera for Surveys (Mutchler et al., 2007). The outflowing gas is visible as a bipolar cone of H$\alpha$ emission (red) extending along the galaxy minor axis. Figure from Chen et al., 2010.

along the minor axis (see Fig. 1.13 and Heckman & Thompson, 2017). While the most detailed studies of the M82 outflow have focused on the hot and warm-ionized phases, multi-wavelength observations reveal that a plethora of different phases are present and, disclosed the multiphase nature of galactic winds. Indeed, the outflowing gas is observed across the full electromagnetic spectrum, ranging from X-ray energies (Schaaf et al., 1989; Strickland & Heckman, 2009) to warm, ionized gas traced by visible-wavelength features such as H$\alpha$ (McKeith et al., 1995; Westmoquette et al., 2009) to atomic HI and molecular gas (Seaquist & Clark, 2001; Walter et al., 2002; Salak et al., 2013; Leroy et al., 2015; Martini et al., 2018). Kiloparsec-scale regions well out of the M82 disk are characterized by double emission-line profiles (see Fig. 1.14) with line splitting of 200-600 km/s (e.g., Heckman et al., 1990). Such ionized material probably lies along the surface of an expanding bubble or outflowing biconical structure (Heckman et al., 1990).

However, mapping outflows in emission, such as for M82 is difficult at larger galactic

distances, because the emitting gas inherently has a very low surface brightness. Nonetheless, several studies have detected emission signatures from outflows in galaxies beyond the local universe (Genzel et al., 2011; Newman et al., 2012a; Förster Schreiber et al., 2014). Currently, rest-frame UV and optical spectroscopy use three types of emission signatures to map the extent of outflows: the nebular, resonant, and non-resonant emission lines. A transition is resonant when a photon can be absorbed from the ground state and re-emitted to the same lowest level of the ground state, as for Lyman-alpha and the Na D $\lambda\lambda$5890,5896 Å transitions. A transition is non-resonant when the photon can be re-emitted to an excited level of a ground state that has multiple levels due to fine structure splitting. In this study we focus on nebular and resonant emissions, in particular.

The first type of emission signature (nebular lines) from outflows can appear as a broad component in nebular emission lines such as H$\beta$, H$\alpha$, [OII] and [OIII]. Broad components are regularly seen in local ultra-luminous infra-red galaxies (ULIRGs, e.g., Soto & Martin, 2012; Arribas et al., 2014; García-Burillo et al., 2015) and more recently in normal star-forming galaxies (Wood et al., 2015). Emission from resonant metal lines, such as NaD, may be observed as P-cygni profiles (e.g., Prochaska et al., 2011; Erb et al., 2012; Rupke & Veilleux, 2015; Scarlata & Panagia, 2015). The relative strength between the (mostly) blue-shifted absorption and (mostly) redshifted emission dictates whether the signature appears as a traditional P-cygni profile or as emission "infilling".

This technique allows to observe galactic outflows, similar to those observed in M82, in nearly all highly active star-forming galaxies at all cosmic epochs (see Veilleux et al. 2005 and Erb 2015 for a comprehensive overview) and usually the wind is associated to the galaxy SF activity itself (e.g. Heckman et al., 1990; Pettini et al., 2000; Shapley et al., 2003; Rupke et al., 2002, 2005a,b; Martin, 2005, 2006; Steidel et al., 2010; Hill & Zakamska, 2014). Yet, the effect of the global effect of the outflow on the galaxy properties is still hotly debated (Steidel et al., 2010; Chen et al., 2010; Martin et al., 2012a; Rubin et al., 2014).

Similarly, massive and fast outflows driven by the central AGN activity are observed at low (e.g. Feruglio et al., 2010; Villar-Martín et al., 2011; Rupke & Veilleux, 2011, 2013; Greene et al., 2012; Mullaney et al., 2013; Rodríguez Zaurín et al., 2013) and high redshift (e.g. Maiolino et al., 2012; Tremonti et al., 2007; Brusa et al., 2015; Perna et al., 2015; Cresci et al., 2015). At low redshift, Mullaney et al. (2013) found a clear sign of AGN-driving outflows in sample of 24,000 optically selected Type 1 and Type 2 AGN, drawn from the SDSS. They observed a prominent blueshifted and broader [OIII]$\lambda$5007 emission line (left panel of Fig. 1.15). By performing multi-component fitting to the optical emission line profiles of the stacked spectra, Mullaney et al. (2013) identified a narrow Gaussian component at the systemic velocity of the galaxy and a very broad and blue-shifted component with a FWHM of 1000 km/s (see left panel of Fig. 1.15). By using the optical integral field unit (IFU) observations of sixteen TYPE 2 AGN selected from the Mullaney et al. (2013) parent sample, Harrison et al. (2014) demonstrated that the [OIII] emission line feature is due to a complex kilo-parsec scale outflows, extended over $\geq 6-16$ kpc (Fig. 1.15, Fig. 1.16).

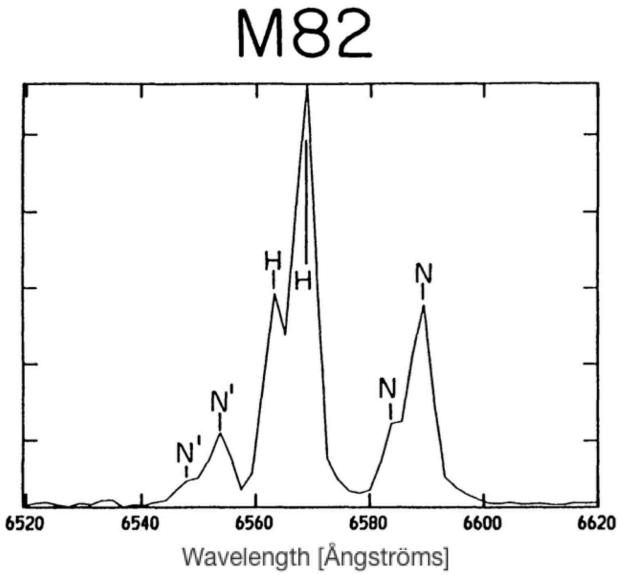


Figure 1.14: Example of double-peaked emission line profiles in the prototypical M82 galaxy. Each components in the [NII]$\lambda$6548, H$\alpha$, and [NII]$\lambda$6584 line profile are indicated by N', H, and N, respectively. Figure from Heckman et al., 1990.

Despite the increasing number of these observational evidence, it is still difficult to establish if and how the AGN driven outflow is affecting the host galaxies properties. As suggested by Cresci & Maiolino (2018), there is no clear evidence for a cause-effect relationship between the presence of the outflow and the suppression of the star formation activity of the host galaxy (see also Woo et al., 2017). Indeed, the AGN feedback is observed both to enhance ("positive feedback") or quench ("negative feedback") the SF activity of the host galaxy (e.g. Cresci et al., 2015; Maiolino et al., 2017; Cresci & Maiolino, 2018 and Harrison, 2017, for a review).

However, most observational evidence for both SF and AGN induced outflows have been based so far on relatively small samples of particular category of galaxies (e.g. Greene & Ho, 2005; Mullaney et al., 2013 for optically-selected AGN, Chen et al., 2010 for star-forming galaxies without AGN contribution) leading to strong selection biases. Indeed, what it is still lacking is a complete investigation of (*i*) the incidence of such outflows in the bulk of the galaxy population, (*ii*) the impact that they might have on the galaxy SF activity and, (*iii*) the identification of the main powering mechanism, such as star formation and/or AGN.

All these aspects are fully explored in this thesis through the investigation of outflow signatures in a large sample of SF and AGN dominated galaxies spectra in the local Universe (see Chapter 3 and 4).

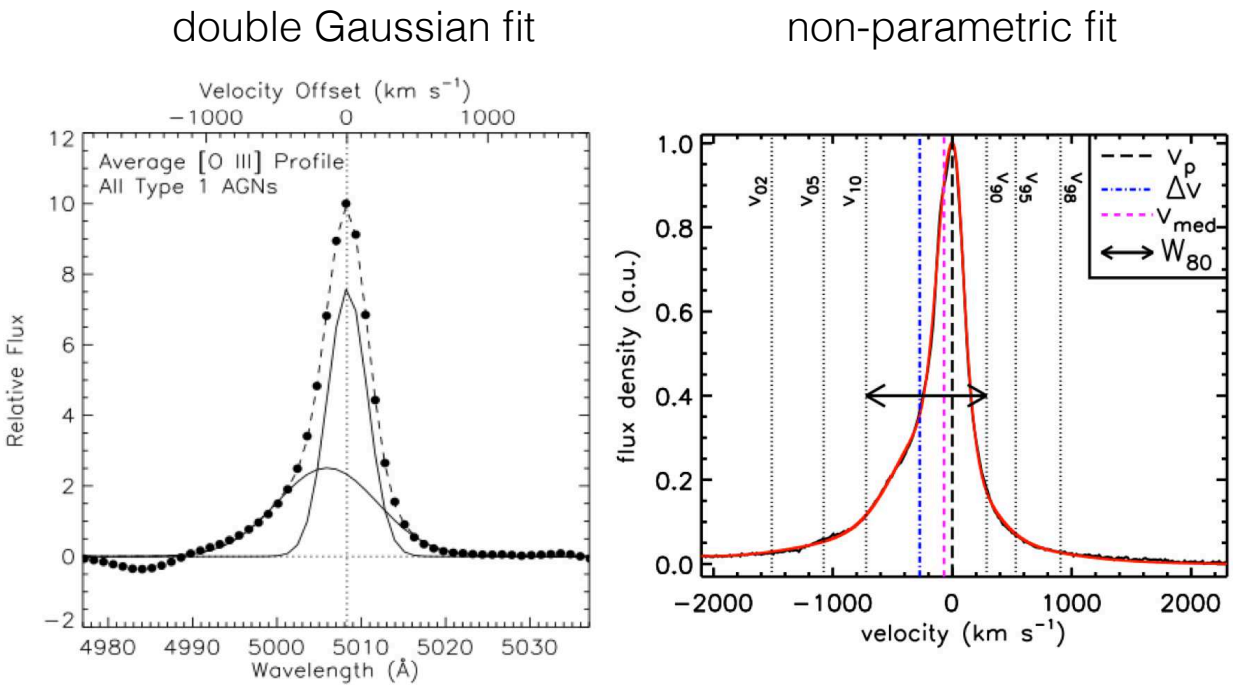


Figure 1.15: Examples of spatially integrated spectra in the [OIII] reagion for a Type 1 and Type 2 AGN, left and right panels, respectively. *Left panel*: Average [OIII] profile of $\sim 10,000$ Type 1 AGNs from Mullaney et al. (2013). This profile shows a strong blue wing ( or blueward asymmetry) that is well modelled by a broad (i.e. FWHM= 851km/s) second Gaussian component that is offset from the narrower component (i.e. FWHM = 335 km/s) by 148 km/s. The flux contained within the broader component represents $\approx 45\%$ of the total line flux. The fit produced by combining these two components is shown by the dashed line. *Right panel*: Example of spatially integrated [OIII] emission-line profile (black curve) and fit (red curve) from the Harrison et al. (2014) Type 2 AGNs sample. Also in this case, the line profile is asymmetric with clear blue wings. The vertical dotted lines show different percentiles to the flux contained in the overall emission-line profile (from left to right: 2nd; 5th; 10th; 90th; 95th and 98th) The long-dashed line shows the velocity of the peak flux density ($v_p$). The vertical short-dashed line shows the median velocity ($v_{med}$) and the dot-dashed line shows the velocity offset of the underlying broad wings ($\Delta v$). The arrow indicates the line width that contains 80% of the flux ($W_{80}$). Figures adapted from Mullaney et al. 2013 and Harrison et al., 2014.

### 1.4.3 Balmer decrement as tracer of dust content.

The Balmer series is the name given to a series of spectral lines of the hydrogen atom. They are produced by electron transitions that involve the energy level with principal quantum number n=2; from higher levels down to n=2 (n=3−∞ to n=2), emission lines and, from n=2 to higher levels (n=2 to n=3−∞), absorption lines. The two emission Balmer lines used in this thesis are H$\alpha$ at $\lambda = 6563$ Å, produced by the transitions from n=3 to n=2

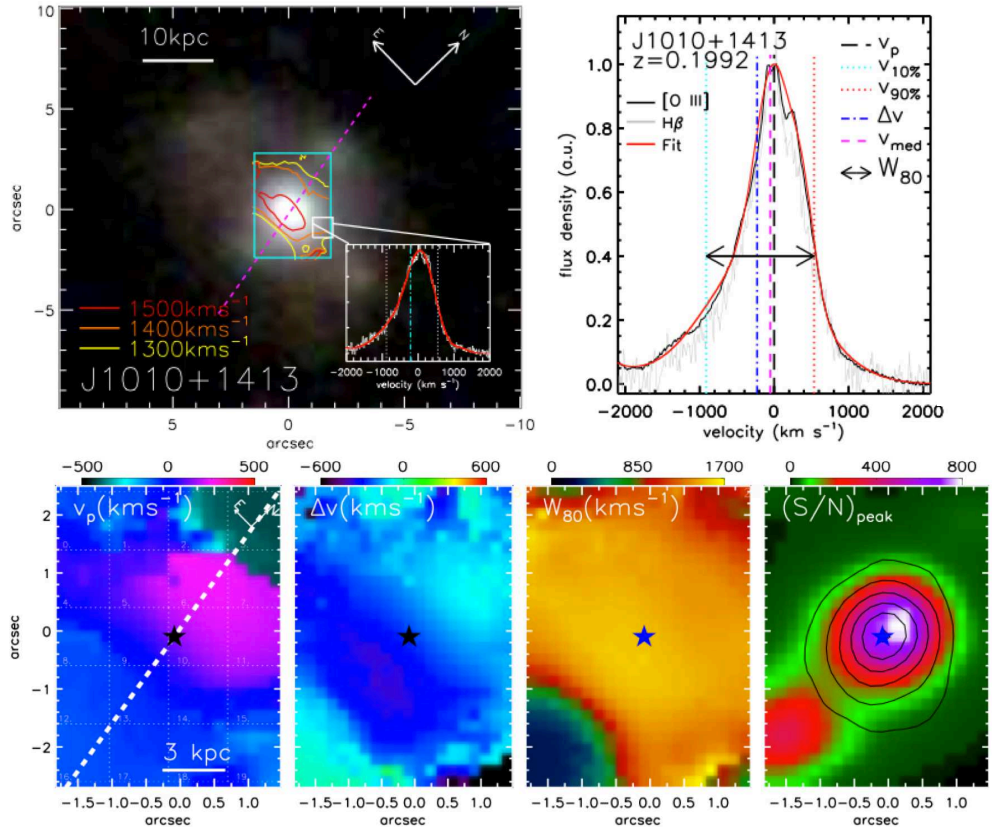


Figure 1.16: Example of ionized galactic outflow in a Type 2 AGN local J1010+1413 galaxy. *Top left panel*: Three colour (g, r, i) SDSS image. The cyan box shows the field-of-view of GMOS-IFU observations. The contours show values of $W_{80}$ (velocity width of the line that contains 80% of the emission-line flux) and highlights the spatial distribution where the [OIII] emission-line profiles are broadest. The dashed line shows the kinematic major axis. It is also shown an example [OIII] emission-line profile extracted from the highlighted spatial region (white box). *Top right panel*: Galaxy-integrated [O III]$\lambda$5007 emission-line profile (black curve) extracted from the full field-of-view of the IFU (cyan box in the top left panel). Zero velocity corresponds to the redshift and the spectrum has been normalised to the peak flux density. The solid red curves indicate the best fit to the emission-line profile. The vertical dashed and dotted lines correspond to the non-parametric velocity definitions showed in Fig. 1.15. The H$\beta$ emission-line profile is shown in gray. *Bottom panels*: From left to right the [OIII] emission-line peak ($v_p$), velocity offset of the broad emission-line wings ($\Delta v$), line width ($W_{80}$) and, signal-to-noise ratio of the peak flux density (S/N) at each pixel are show. The dashed line indicates the kinematic major axis. The stars in each panel show the position of the peak of this continuum emission. Figure adapted from Harrison et al., 2014.

and, H$\beta$ at $\lambda = 4861$ Å produced by the transitions from n=4 to n=2.

The Balmer emission lines in the interstellar medium arise predominantly from the re-

combination and subsequent cascade of electrons to the n = 2 level of hydrogen. During re-combination, an electron is captured into an excited state and the electron consequently cascades down the energy levels. The photons emitted during this process are normally called "recombination lines. The atomic structure of hydrogen is well understood by the quantum theory. For this reason the strength of the emission line fluxes can be well determined if the radiation field ionizing the hydrogen gas is known (see Dopita & Sutherland, 2003 and Osterbrock & Ferland, 2006 for more details). The relative fluxes of the resulting hydrogen emission lines, such as H$\alpha$/H$\beta$, is known as Balmer decrement. The intrinsic values of the Balmer decrement has been theoretically predicted in two particular cases, namely Case A and Case B (see Osterbrock & Ferland 2006). As extensively explained by Osterbrock & Ferland (2006), Case A assumes that an ionized nebula is optically thin to all Lyman emission lines (emission from n=1 in the hydrogen atom), while, in the Case B, the nebula is optically thick to all Lyman lines greater than Ly$\alpha$ line. In other words, in Case A, the Ly energetic photons can escape the region, contrariwise, in Case B such photons are absorbed and re-emitted as higher order lines, such as H$\alpha$ and H$\beta$ lines. In the real astronomical emission lines regions, the situation lie between these two extremes.

| T | 5,000K | 10,000K | 20,000K |
|---|---|---|---|
| Case A | 3.10 | 2.86 | 2.69 |
| Case B | 3.05 | 2.87 | 2.76 |
| $n_e$ | $10^2$ cm$^{-3}$ | $10^4$ cm$^{-3}$ | $10^6$ cm$^{-3}$ |
| Case B (5,000K) | 3.041 | 3.001 | 2.918 |
| Case B (10,000K) | 2.863 | 2.847 | 2.806 |
| Case B (20,000K) | 2.747 | 2.739 | 2.725 |

Table 1.2: Balmer decrement, H$\alpha$/H$\beta$ predicted by Case A and Case B, for 3 different temperatures in low density limit and Case B in 3 different number density (values from Osterbrock & Ferland, 2006).

For comparison, in Table 1.2 we show the line ratio assuming the two idealized cases, A and B. The relative fluxes of H$\alpha$ and H$\beta$ lines do not show a strong variation between Case A and Case B. Thus, the Balmer decrement should be roughly the same in all planetary nebulae, irrespective of the local gas temperature and density. However, this is not what is observed. Interstellar reddening produced by micron-sized dust particles selectively dims shorter-wavelength, bluer light more than it does longer-wavelength, redder light, leading to Balmer line ratios that differ systematically from the theoretical predictions. A planetary nebula lying behind a cloud of interstellar dust will be observed to have the intensity ratios H$\alpha$/H$\beta$ more than 2.86. The more dust, the greater the disparity between the observed and theoretical Balmer decrements. Turning this concept around, from the size of the discrepancy between observed and theoretical Balmer decrements, it is possible to infer the amount of interstellar reddening, and therefore, dust, between us and a given planetary nebula.

In chapter 5, we will show how the observed Balmer decrement can be used to study

the dust and the mount of molecular gas content in galaxies in particular as a function of the environment.

### The dust-to-gas mass ratio and the correlation with the molecular mass

The baryonic content of a galaxy exists in a range of states, from cold molecular gas to diffuse hot gaseous haloes. However, it is still quite unclear how the gas is distributed in galaxies and how the gas reservoir varies as a function of other galaxy properties.

The atomic gas content of galaxies can be traced using the 21cm line of HI, and integrated HI masses are now available for large samples of galaxies from HI-selected surveys such as the HI Parkes All Sky Survey (HIPASS; Barnes et al., 2001) and the Arecibo Legacy Fast ALFA survey (ALFALFA; Haynes et al., 2011) and targeted surveys such as the GALEX Arecibo SDSS Survey (GASS; Catinella et al., 2010), which has a uniform gas fraction limit rather than a gas mass limit.

The cold molecular gas is mostly composed of H2, but given its lack of transitions that can be excited at low temperatures, molecular gas measurements are mostly done using CO (carbon monoxide) as a proxy for H2. Single-dish CO surveys have generally been targeted but for inhomogeneous samples (e.g., Braine et al., 1993; Boselli et al., 1997). A notable exception here is the CO Legacy Data base for the GASS survey (COLDGASS; Saintonge et al., 2011) which obtained CO observations for galaxies from the GASS survey.

These methods are powerful but they have the major drawback of being extremely time-consuming. Alternative methods have been proposed to infer gas content in galaxies. These can be roughly divided into two classes: methods that make use of scaling relations to infer gas content, and those that measure gas content using a less direct tracer than CO. The former class are generally based on the good correlation between galaxy colour and the ratio of HI mass to B-band luminosity (Roberts, 1969; Bothun, 1984). This technique was used by Bell et al. (2003a) to infer a baryonic mass function for the low-redshift, $z < 0.2$, Universe. Similarly Kannappan (2004) and Zhang et al. (2009) have provided relations between colour and HI gas fractions which can be applied to large samples of galaxies. This has the advantage of being easy to apply to large samples of objects (e.g., Kauffmann et al., 2010; Zhang & Buta, 2012). A similar technique in this class is to invert the empirically found relationship between SFR and gas surface density, the Kennicutt-Schmidt (K-S) relation (Kennicutt, 1998 and references therein). This requires an estimate of the SFR which is then used to infer a gas mass (e.g., Tremonti et al., 2004; Erb et al., 2006; Puech et al., 2010). These relations, however, do not allow to study the variation of the gas mass content as a function of the galaxy star formation activity and to understand if the process that regulates the availability of gas to the galaxy is also responsible for the quenching of the SF activity itself.

The second class of methods aims, instead, to infer gas content via a tracer of gas content. The most widely used technique in this class is to make use of dust emission to infer gas content, building on the observation by Boulanger et al. (1985) that a comparison of IRAS and HI maps implied that dust is a reliable tracer of cold gas. It has been used to estimate gas content in the Milky Way (e.g., Dame et al., 2001), and in nearby galaxies by

a number of authors (e.g., Israel et al., 1996; Israel, 1997, 2005; Leroy et al., 2009; Boquien et al., 2013) and it has been extended to sub-mm observations (James et al., 2002) and more recently to Herschel data (e.g., Eales et al., 2010, 2012; Roman-Duval et al., 2010). These models depend on dust properties, such as the emissivity and temperature, and on the typical beam sizes for sub-mm and far-IR observations which are considerably larger than the resolution obtained in the optical.

In this thesis we will make use of an alternative method. Indeed, we will use the Balmer decrement as a proxy of the galaxy dust content and we will investigate the correlation between the Balmer decrement and the molecular gas mass available in the xCOLD GASS sample (Saintonge et al., 2017) in order to estimate the molecular gas mass for an unprecedented large sample of galaxies in the local Universe. The aim of this analysis is to investigate if there is a direct link between the availability of cold gas to galaxies and the environment where they live.

## 1.5 This Thesis

### 1.5.1 Thesis Outline

The main aim of this work is to identify the mechanism responsible for driving the suppression of the star formation activity in galaxies and lead to the substantial galaxy bimodality in the local Universe. Two main aspects of the quenching scenario are put under examination, the so called "internal quenching", related to the effect of the AGN and SF feedback, and, the "external quenching" due the effect of the environment on galaxy evolution. With respect to the "internal processes", we investigate the presence of galactic winds in the bulk of the galaxy population in the local Universe. We study the occurrence of multiphase outflows as a function of several galaxy properties, their nature, either SF or AGN driven, and its effect in the SF quenching. In the second part of this work, we focus on the effect of the environment in regulating the galaxies gas reservoir and so its star formation activity.

The thesis is structured as follows:

- **In Chapter 2**, I present the dataset used in this work. I describe in detail the overall properties of our major dataset, the spectroscopic Sloan Digital Sky Survey (SDSS). This includes a significant sample of optical spectra of local ($z< 0.3$) passive, star-forming and starburst galaxies. I introduce the main physical galaxy properties which are used in the analysis, as stellar mass, different SFRs measures and galaxy structural parameters, emission line fluxes and environmental definition in which our galaxies live.

- **In Chapter 3**, a sample of galaxies drawn from SDSS is used to look for evidence of galactic winds in the local Universe. I show, in particular, how we use the forbidden [OIII]$\lambda$5007 emission line as a tracer of ionizing gas outflows. I describe the method used to extract and analyze the kinematic of the oxygen in our stacked spectra. I show how the line profile changes as a function of the galaxy stellar mass and SFR

and how it relates to the particular photoionization mechanisms: star-formation (SF) or Active Galactic Nuclei (AGN) activity. Finally, I conclude by discussing the implications of our results for the role of AGN feedback as quenching mechanism in the present day Universe.

- **In Chapter 4**, I present a comprehensive study of the interstellar Na I $\lambda$5890, 5895 (NaD) resonant lines in the optical galaxy spectrum to look for cold-gas outflows in the local Universe. The dependence of cold galactic winds on the galaxies position in the SFR-$M_\star$ plane is investigated. I show the properties of the NaD line in galaxies with high SFR, in particular relating the absorption NaD line profile shape with the galaxy geometry in galaxies with different ionization mechanisms: AGN and SF. I compare the kinematics of the neutral gas with the kinematics of the ionized gas as traced by the [OIII]$\lambda$5007 emission line. The implication of our main findings are then discussed in the framework of the galaxy SF quenching.

- **In Chapter 5**, I describe a new empirical way to use the dust reddening as a probe of the ISM molecular hydrogen gas mass in galaxies. By using a sample of 333 nearby galaxies with CO(1-0) measurements from the IRAM-30m telescope, we investigate the connection between the dust reddening and the cold gas reservoir. In particular, I show how the dust reddening, measured by the H$\alpha$-H$\beta$ emission line ratio, correlates with the total CO line luminosity ($L_{CO}$) and total molecular gas mass $M_{H2}$.

- **Chapter 6** presents our study concerning the role of environment in regulating the amount of gas reservoir and so quenching the star formation activity of central massive galaxies in the SDSS sample at z$<$ 0.3. I show the comparison between different SFR indicators and, the impact that such indicators produce in the definition and characterization of the local Main Sequence of star-forming galaxies (MS). Than, the environmental dependence of the galaxy MS is explore. Finally, I use the empirical Balmer decrement- molecular mass relation, presented in Chapter 5, to estimate the molecular mass for an unprecedented number of galaxies ($\sim$ 160,000). We investigate how the molecular gas mass fraction, $f_{H2} = M_{H2}/M\star$ varies as a function of several global galaxy properties such as galaxy stellar mass, host halo mass ($M_{halo}$), and location in SFR-M$\star$ diagram. We conclude by discussing the implications of our results on the role of the environment in regulating the galaxy cold gas reservoir ans so the its SF activity.

Finally, a summary of the main results of this work and prospects for future research are presented **in Chapter 7**.

### 1.5.2 List of the papers

Portions of this work have appeared (or are to appear) in the following papers:

- *'Light breeze in the local Universe'*, **Concas A.**, Popesso, P., Brusa M., Mainieri V., Erfanianfar G. and, Morselli L., 2017, A&A, 606, A36
  Abstract: ' We analyze a complete spectroscopic sample of galaxies (∼600,000 ) drawn from Sloan Digital Sky Survey (SDSS, DR7) to look for evidence of galactic winds in the local Universe. We focus on the shape of the [OIII]$\lambda$5007 emission line as a tracer of ionizing gas outflows. We stack our spectra in a fine grid of star formation rate (SFR) and stellar mass to analyze the dependence of winds on the position of galaxies in the SFR versus mass diagram. We do not find any significant evidence of broad and shifted [OIII]$\lambda$5007 emission line which we interpret as no evidence of outflowing ionized gas in the global population. We have also classified these galaxies as star-forming or AGN-dominated according to their position in the standard BPT diagram. We show how the average [OIII]$\lambda$5007 profile changes as a function of the nature of the dominant ionizing source. We find that in the star-forming dominated source the oxygen line is symmetric and governed by the gravitational potential well. The AGN or composite AGN\star-formation activity objects, in contrast, display a prominent and asymmetric profile that can be well described by a broad Gaussian component that is blue-shifted from a narrow symmetric core. In particular, we find that the blue wings of the average [OIII]$\lambda$5007 profiles are increasingly prominent in the LINERs and Seyfert galaxies. We conclude that, through the identification of strong bulk motion as traced by the warm ionized gas, in the low-redshift Universe, "pure" star-formation activity does not seem capable of driving ionized-gas outflows, while, the presence of optically selected AGN seems to play a primary role. We discuss the implications of these results for the role of the quenching mechanism in the present-day Universe.'

- *'Two-Face(s): ionized and neutral gas winds in the local Universe.'*, **Concas A.**, Popesso, P., Brusa M., Mainieri V., Thomas D., 2018, arXiv:1710.08423, submitted to A&A, under review.
  Abstract: 'We present a comprehensive study of the interstellar NaI $\lambda$5890, 5895 (NaD) resonant lines in a complete spectroscopic sample of $\sim 600,000$ galaxies drawn from Sloan Digital Sky Survey (SDSS, DR7) in order to look for cold-gas outflows in the local Universe. This is the first time that doppler blue-shifts of the NaD absorption feature have been investigated as a tracer of cold gas kinematics (T $<$ 1000 K) with a statistically significant sample that includes passive, star-forming and starburst galaxies. Individual galaxy spectra are stacked in bins of stellar mass (M$\star$) and star formation rate (SFR) and the dependence of galactic winds, with respect to the galaxies position in the SFR-$M\star$ plane is investigated. While in most cases the interstellar medium (ISM) absorption and emission lines are fixed at the galaxy systemic velocity, at the higher SFR tail (SFR$>$ $12.5 M_{\odot} yr^{-1}$), we find evidence of blue-shifted NaD absorption profiles (by more than instrumental resolution, 70 km/s),

which we interpret as evidence of neutral outflowing gas. We explore the properties of the ISM in these galaxies with high SFR, in particular relating the absorption NaD line shape with the galaxy geometry in galaxies with different ionisation mechanisms: Active Galactic Nuclei (AGN) and star-formation. We find that: a) the ISM NaD absorption lines show a clear transition from a strong disk-like component, perfectly centered to the systemic velocity, in the edge-on system (inclination $i > 50°$ of the disk rotation axis), to an outflow, blue-shifted, component in face-on galaxies ($i < 50°$); b) these trends are observed in galaxies classified as "purely" star-forming and AGN dominated objects. In addition to this, we compare the kinematics of the neutral gas with the kinematics of the ionized gas as traced by the [OIII]$\lambda$5007 emission lines. We find that, in these high SFR galaxies, the perturbations of the [OIII] emission line are present only in AGN or composite AGN/star-forming systems, consistent with Concas et al. (2017). In our AGN sample, the presence of the oxygen line perturbation is independent to the stellar disk inclination: in both the face-on and edge-on systems, the velocity associated with the broad and blue-shifted gaussian component is $\sim 125 \pm 45$ km/s, velocity dispersion of $\sim 460 \pm 30$ km/s and a mean maximum velocity of $\sim -1042 \pm 106$ km/s. In conclusion, we find that, in the local Universe, galactic winds show two faces which are related to two different ejection mechanisms, namely the neutral outflowing gas phase related to the star formation rate along the galaxy disk and the ionized winds related to the AGN feedback.'

- *'The main sequence of star forming galaxies I. The local relation and its bending.'*, Popesso, P., **Concas A.**, Morselli L., Rodighiero G., Schreiber C., Renzini A., Cresci G., Belli S., Erfanianfar G., Mancini C., Inami H., Dickinson M., Ilbert O., Pannella M., Elbaz D., 2018, submitted to A&A, under review.
  Abstract: 'By using the WISE mid-infrared and H$\alpha$ star formation rate (SFR) indicators in a local galaxy sample we study the Main Sequence (MS) of star forming galaxies and the distribution of galaxies around it at stellar masses larger than $10^{10}$ $M_\odot$. The slope of the relation strongly depends on the combination of SFR indicators and on the method used to identify the MS. In all cases, the local MS shows a bending at high stellar masses with respect to the slope obtained in the low mass regime. However, the significance of the flattening depends on the indicator of the MS location. While the distribution of galaxies in the upper envelope of the MS is consistent with a log-normal distribution, the lower envelope shows an excess of galaxies, which increases as a function of the stellar mass but varies as a function of the SFR indicator used in the analysis. The scatter of the best log-normal relation fitting the upper envelope of the distribution, increases with stellar mass from $\sim 0.3$ dex at $10^{10}$ $M_\odot$ to $\sim 0.45$ at $10^{11}$ $M_\odot$. Beyond this stellar mass limit the location of the MS and the shape of the SFR distribution in the MS region vary significantly as a function of the SFR indicator, becoming very uncertain. We find that the increase of the B/T ratio along the MS is not quantitatively sufficient to explain the bending of the relation towards higher masses. In addition, at masses above $10^{10.5}$ $M_\odot$, where the MS shows the most significant bending and a larger scatter, the MS is dominated

by central galaxies of group and cluster sized halos. We argue that the MS bending in this region could be due to the regime of cold gas starvation induced by the hot halo environment and maintained by the central black hole radio mode feedback. Instead, the increase in scatter could be a consequence of the larger spread of star formation histories of central group and cluster galaxies with respect to lower mass galaxies at the center of low mass halos.'

- *'The impact of the environment on the gas reservoir.'*, **Concas A.** & Popesso, P., 2018 in preparation.
  Abstract: 'We explore the impact of the environment on regulate the molecular gas reservoir and star formation activity in local (z< 0.3) massive central galaxies (stellar masses larger than $M\star > 10^{10}$ $M_\odot$). We use the $L_{CO}$-$M_{H2}$-BD relation (presented in Chapter 5) to estimate the molecular mass, $M_{H2}$, for an unprecedented number of galaxies ($\sim$ 160,000 ) drawn from Sloan Digital Sky Survey (SDSS, DR7). Whit the exquisite statistics of our sample, we are able to quantify the variation of the molecular gas fraction, $f_{H2} = M_{H2}/M\star$, in the SFR-M$\star$ plane. We find that $f_{H2}$ anticorrelate with stellar mass above, below and along the Main Sequence (MS) of star forming galaxies, according with precedent very low statistic results. By using the halo mass catalog of Yang et al. (2007), we classify our galaxies according to the environment in witch their live, characterized by the host dark matter halo mass. We find that $f_{H2}$ decreases with the increase of the halo mass. The central galaxies in low dense environment tend to be more gas rich to respect the galaxies located in high mass halos. Such lack of cold gas supply above the $10^{12-12.5}$ $M_\odot$ halo mass threshold might limit the fuel for the galaxy SF process and so lower the galaxy SFR, leading to the MS bending observe in previous section. All our finding indicate that the environment play a pivotal role on regulate the cold gas reservoir and so quench the SF activity in central massive galaxies.'

In addition to the work presented in this thesis, the author has also contributed to the following papers during the period of its PhD:

- *'On the robustness of the Hβ Lick index as a cosmic clock in passive early-type galaxies'*, **Concas A.**, Pozzetti L., Moresco M., Cimatti A., 2017, MNRAS, 468, 1747

- *'Bulges and discs in the local Universe. Linking the galaxy structure to star formation activity'*, Morselli L., Popesso, P., Erfanianfar G., **Concas A.**, 2017, A&A, 597, A97

- *'The Main Sequence of star forming galaxies II. A non evolving sequence in slope and scatter from $z \sim 0$ to 2.5'*, Popesso P., Morselli L., **Concas A.**, Schreiber C., Renzin A., Rodighiero G., Cresci G., Belli S., Erfanianfar

G., Mancini C., Inami H., Dickinson M., Ilbert O., Pannella M., Elbaz D., 2018, submitted to A&A

# Chapter 2

# Data sample

This chapter gives an overview of the different data set used in this thesis. I first describe the overall properties of the major dataset, the galaxy optical spectra of the Sloan Digital Sky Survey (SDSS). Such spectroscopic sample offers an exquisite statistics to study the galaxies properties in local Universe. After that, I introduce the ancillary catalogues used to extend the informations of our spectroscopically selected galaxies in different wavelength range, from the UV to the IR and radio band. Finally, I focus on the main data products such emission line fluxes, stellar masses (M$\star$), different star-formation rate (SFR) indicators, galaxies structural parameters (inclination and bulge over disc ratio), and environmental definition in which our galaxies live.

## 2.1 The Sloan Digital Sky Survey

The Sloan Digital Sky Survey (SDSS) is one of the most ambitious and successful survey in the history of astronomy. By producing both imaging and spectroscopic surveys over a large area of the northern sky, the SDSS currently provides the most comprehensive picture of galaxies in the low-redshift Universe (see the galaxy distribution across the redshift in Fig. 2.1). Over the last couple of decades of operations (SDSS-I, 2000-2005; SDSS-II, 2005-2008; SDSS-III 2008-2014 and the current SDSS-IV 2014-2020) it obtained deep, 35,000 square degrees of images, covering a unique footprint of 14,055 square degrees of sky. The survey uses a dedicated 2.5-m f/5 modified Ritchey-Chrtien telescope located at Apache Point Observatory, in south east New Mexico. The telescope is described in detail in Gunn et al. (2006).

The imaging survey operates the instrument in a drift scan mode. The camera collects photometric imaging data in 5 photometric bands (u, g, r, i and z) centered at (3540, 4770, 6230, 7630 and 9130 Å).The filter system, described by Fukugita et al. (1996), spans the entire optical range from the atmospheric ultraviolet cutoff in the blue to the sensitivity limit of silicon in the red. A detailed description of the imager and the camera sensitivity can be found in Gunn et al. (1998) and in the recent Doi et al. (2010).

Objects are detected in the imaging survey, classified as extended sources and, used to

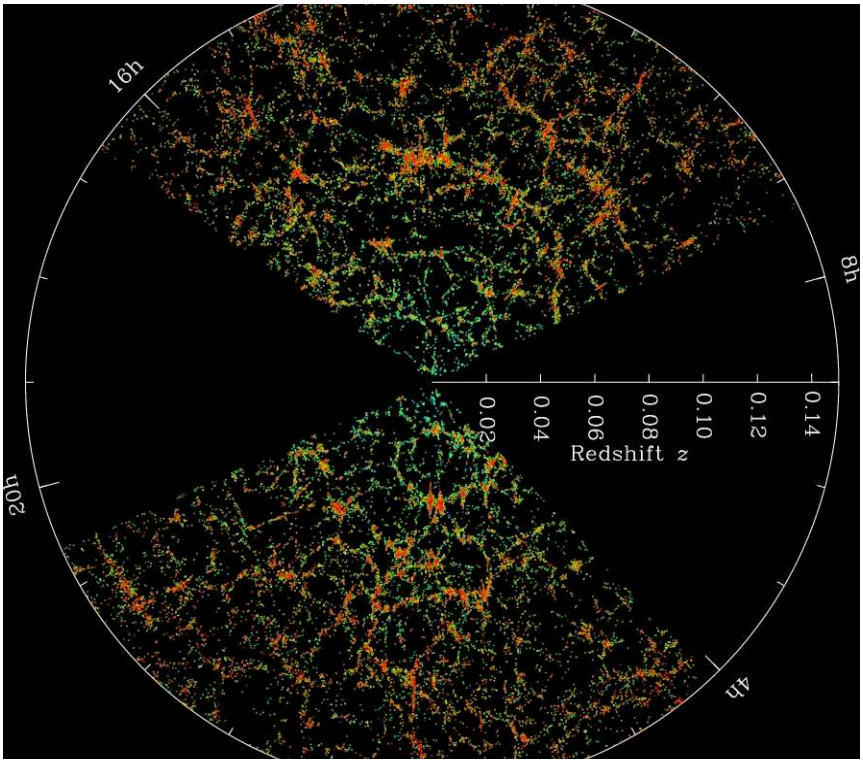


Figure 2.1: Large scale structure in the northern equatorial slice of the SDSS main galaxy redshift sample. The galaxies are color-coded by g-r color. Credit: M. Blanton and the Sloan Digital Sky Survey.

select, in a uniform way, different classes of objects whose spectra will be taken. During the years the SDSS uses two spectroscopic instrument: the SDSS spectrograph, used in SDSS-I, -II and in the SEGUE surveys and the new BOSS spectrograph for used in the SDSS-III BOSS survey. The spectrograph parameters and description for both the instruments can be found at http: //www.sdss.org/dr12/spectro/spectro_basics/. In SDSS, spectra for many objects are taken simultaneously. This is possible by using a plate-cartridge system infrastructure. The spectrograph is connected by fiber optic cables to an aluminum disk, namely "plate", placed in the focal plane of the telescope. Each plate, with holes drilled at the position of the sources to be observed, corresponds to a specific patch of the sky. An example of the overplay of the SDSS imaging (with galaxies and quasars) and corresponding holes in the plate are shown in Fig. 2.2, left panel. Each area in the sky requires its own unique plate.

During the day the plates are plugged with fibres and mounted onto a cartridge. At the night, each selected cartridge is attached to the telescope focus and all the spectra, 640 (for the SDSS spectrograph and 1000 with the BOSS spectrograph) at a time, are observed with a total integration time of 45 - 60 minutes depending on observing conditions. A 3D representation of the 1000 sources observed with a plate and their distances based on the SDSS measured redshifts is shown in the right panel of Fig. 2.2. Spectra are extracted

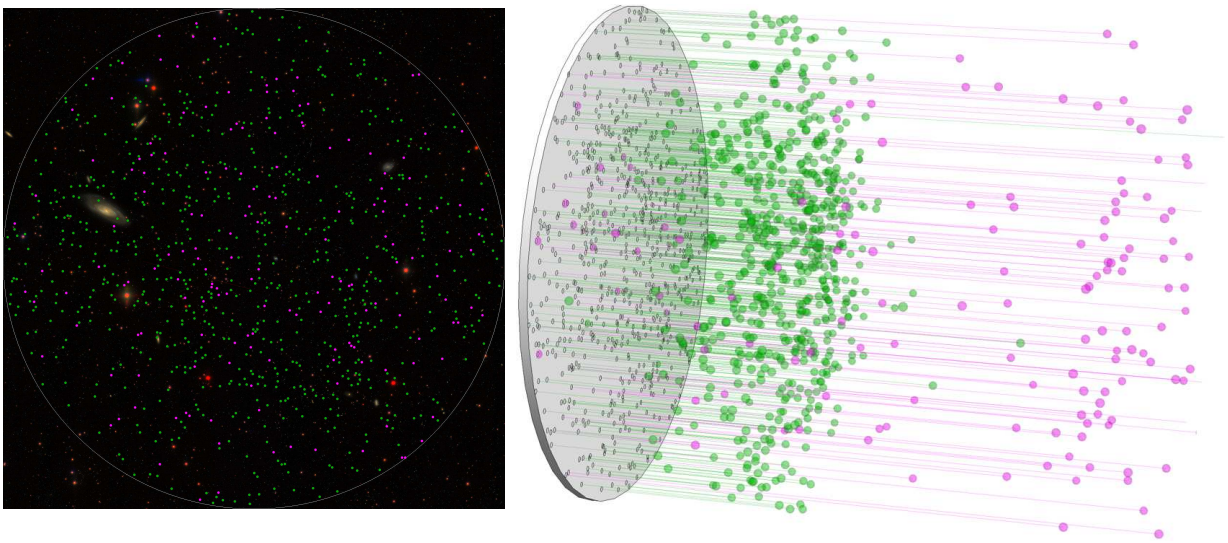

Figure 2.2: Example of a SDSS, BOSS plate. *Left panel*: Overlay of the SDSS imaging and coloured points corresponding to the holes in the plate (green for the galaxies and magenta per quasars). *Right panel*: 3D representation of the distances to these objects (galaxies and quasars) based on their SDSS measured redshifts. Credit: David Kirkby for the SCIENCE BLOG FROM THE SDSS ( http: //blog.sdss.org/2014/09/19/sdss−plates/).

and calibrated in wavelength and flux.

The fibers are located at the focal plane via plug plates constructed for each area of sky. The fiber diameter is 0.2 mm (3" on the sky), and adjacent fibers cannot be located more closely than 55" on the sky. Tests of the redshift accuracy using observations of stars whose radial velocities are accurately known show that the SDSS radial velocity measurements for stars have a scatter of about 3.5 km/s. We use, in particular, objects included in the Main Galaxy Sample (MGS, Strauss et al., 2002) which have Petrosian magnitude $r < 17.77$ and redshift distribution extending from 0.005 to 0.30, with a median z of 0.10.

The spectroscopic sample analyzed in this thesis is drawn from SDSS-II to the seventh data release (DR7, Abazajian et al., 2009). This spectroscopic catalog containing $\sim 930,000$ galaxy spectra. The wavelength coverage of the spectrograph is continuous from 3800 to 9200 Å. The instrumental resolution is $R \equiv \lambda/\delta\lambda \sim 1850 - 2200$ with a mean dispersion of 69 km $s^{-1}$. An example of the galaxy spectrum provided by this release is shown in Fig. 2.3.e Further details concerning the seventh data release can be found at http://www.sdss.org/dr7/ and in Abazajian et al. (2009).

### 2.1.1 The MPA-JHU dataset

In this work we make use of emission lines, SFRs and stellar masses ($M\star$) measurements taken from the MPA-JHU catalog[1]. The data are produced by a collaboration of researchers

[1]http://www.mpa-garching.mpg.de/SDSS/DR7/

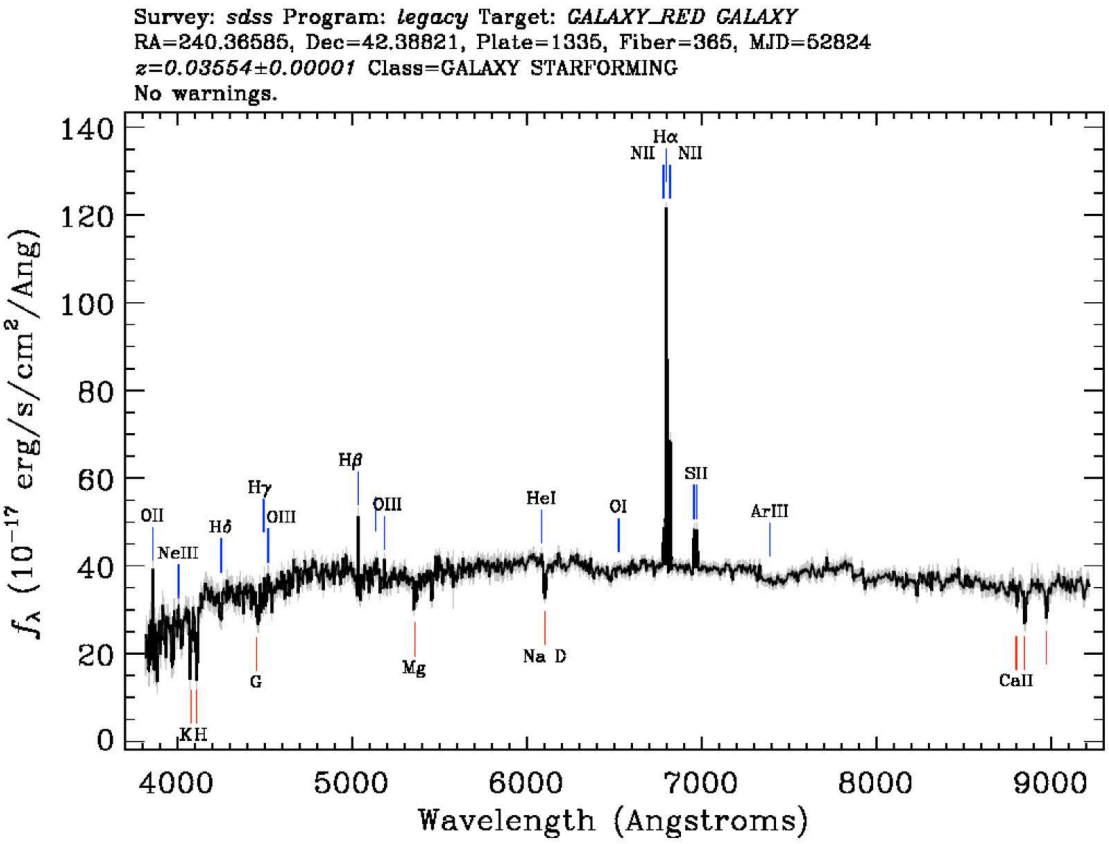


Figure 2.3: Example of optical galaxy's spectrum used in this thesis, drawn from Sloan Digital Sky Survey seventh data release (DR7, Abazajian et al., 2009). The wavelength coverage of the spectrograph is continuous from 3800 to 9200 Å, with an instrumental resolution of $R \equiv \lambda/\delta\lambda \sim 1850 - 2200$ and a mean dispersion of 69 km s$^{-1}$. The main emission and absorption lines are highlighted in the figure by the blue and red lines, respectively. Figure from: http://skyserver.sdss.org

from the Max Planck for Astrophysics (MPA) and Johns Hopkins University (JHU). The team is made up of Stephane Charlot, Guinevere Kauffmann, Simon White, Tim Heckman, Christy Tremonti and Jarle Brinchmann.

The emission lines are estimated from the spectra using the procedure developed and outlined by Tremonti et al. (2004), which is optimised for use on SDSS galaxy spectra. This consists in performing a non-negative least-squares fit of the emission-line-free regions of the observed spectrum, using a set of theoretical spectral energy distribution (SED) template broadened to the observed velocity dispersion. The template spectra are computed by using stellar population synthesis models from Charlot & Bruzual (in prep., CB08)[2] correspond to 30 instantaneous-burst models of different ages and metallicities. Once the fitted spectrum is subtracted from the observed spectrum, the residuals can be fitted to Gaussian-broadened emission-line templates. The method assumes a single broadening width for all the Balmer lines, and another independent width for all the forbidden lines. The strength of each line is fitted independently to obtain each flux and corresponding error.

The $M\star$ are obtained from a fit to the SED by using the SDSS broad-band optical u,g,r,i,z photometry (Kauffmann et al., 2003a; Salim et al., 2005). The fits are made to a large grid of models from Bruzual & Charlot (2003), BC03, spanning a large range in star formation histories. For each model a likelihood is calculated from $\chi^2$. The likelihood of all models is then marginalised onto the mass axis and a likelihood distribution for the mass is obtained. The magnitudes are corrected for emission lines by assuming that the relative contribution of emission lines to the broad-band magnitudes is the same inside the fiber as outside. See Kauffmann et al. 2003a, Salim et al. 2005 and the MPA-JHU web site[3] for details.

The SFR measurements are based on the Brinchmann et al. (2004) approach. The H$\alpha$ emission line luminosity is used to determine the SFRs for the star forming galaxies, as classified in the BPT diagram (Baldwin et al., 1981). For all other galaxies, either AGN or non emission line galaxies, the SFRs are inferred by D4000-SFR relation (e.g. Brinchmann et al. 2004 figure 11 and Kauffmann et al. 2003a). The SFR estimates based on H$\alpha$ flux are corrected for dust extinction on the basis of the Balmer decrement. All SFR measurements are corrected for the fiber aperture following the approach proposed by Salim et al. (2007). Both the stellar masses and SFR are computed by assuming a Kroupa initial mass function (IMF, Kroupa 2001).

### 2.1.2 The WISE dataset

The GALEX-SDSS-WISE Legacy Catalog (GSWLC, Salim et al. 2016) is obtained by cross-matching the SDSS spectroscopic catalog with the GALEX UV and WISE database in additional to SDSS and 2MASS photometric information. It contains physical properties of ∼700,000 galaxies with SDSS redshifts at $0.01 < z < 0.30$. GSWLC contains galaxies

[2]The spectra are available as part of the GALAXEV package, which is can be obtained from http://www2.iap.fr/users/charlot/bc2003/index.html.

[3]https://wwwmpa.mpa-garching.mpg.de/SDSS/DR7/Data/stellarmass.html

within GALEX footprint, regardless of a UV detection, altogether covering 90% of SDSS. We use, in particular, the subsample with medium-deep GALEX observations of $\sim 1500$ s exposure (GSWLC-M), which covers 49% of the SDSS area. This is done to combine relatively deep UV observations and high statistics. Indeed, the "deep" catalog (GSWLC-D) samples only 7% of the SDSS area, resulting in a rather poor statistics. GSWLC utilizes WISE observations at 22$\mu$m (WISE channel W4) to determine SFRs independently of the UV/optical SED fitting. The depth of WISE observations over the sky is not uniform, but is still much more uniform than GALEX depth, and essentially covers the entire sky without gaps. The average $5\sigma$ depth in the W4 channel if 5.4 mJy.

The mid-IR SFRs in GSWLC are estimated from the total IR luminosity (8-1000 $\mu$m) by interpolating the luminosity-dependent IR templates of Chary & Elbaz (2001) so that they match the 22 $\mu$m flux. The IR luminosity are tested using Dale & Helou (2002) templates, which do not have an associated luminosity, but the IR SED shape-luminosity dependence is imposed from empirically calibrated relations of Marcillac et al. (2006). The agreement is excellent with a scatter of 0.02 dex. To obtain mid-IR SFRs from IR luminosity, Salim et al. (2016) use a simple conversion given by Kennicutt (1998), adjusted to Chabrier IMF using the 1.58 conversion factor:

$$\log SFR = \log(LIR) - 9.996 \tag{2.1}$$

where SFR is in $M_\odot/yr$ and the $L_{IR}$ in $L_\odot$. The GSWLC provides also an estimate of stellar masses, SFRs and dust attenuations derived via SED fitting from the UV to the mid-IR data. The SED fitting is performed using the state-of-the-art UV/optical SED fitting technique code CIGALE (Noll et al., 2009).

### 2.1.3 The H-ATLAS *Herschel*/SPIRE dataset

Bourne et al. (2016) provide the Data Release I catalog of multiwavelength associations to the H-ATLAS sources detected in the 5 *Herschel* bands at 100 and 160 $\mu$m with PACS and 250, 350 and 500 $\mu$m with SPIRE over an area of $\sim 150$ deg$^2$. The IR sample is described in Valiante et al. (2016). Namely the 250 $\mu$m detections are used as priors for the source extraction in the remaining *Herschel* bands. Thus, the H-ATLAS catalog is a 250 $\mu$m selected catalog. The Valiante et al. (2016) catalog includes 120230 sources in total, with 113995, 46209 and 11011 sources detected at $> 4\sigma$ at 250, 350 and 500 $\mu$m, where the $1\sigma$ level is 7.4, 9.4 and 10.2, mJy, respectively. Bourne et al. (2016) provide a cross-match with SDSS, GALEX, 2MASS and WISE photometry and with the SDSS and GAMA spectroscopic catalogs. We use the subsample of H-ATLAS DRI catalog with spectroscopic counterpart at $z < 0.085$.

In this thesis, the total IR luminosity is estimated from the far-IR data as follows. We use all the available far infrared data-points, with the addition of the WISE 22 $\mu$m data point, when available, to compute the IR luminosities integrating the best spectral energy distribution (SED) template in the range 8-1000 $\mu$m. To this aim we use two different sets of templates to check the model dependence. We use the Main Sequence (MS) and

starburst (SB) templates of Elbaz et al. (2011) and the set of Magdis et al. (2014). All templates provide infrared luminosities extremely consistent to each other with a rms of 0.05 dex.

### 2.1.4 Structural parameters: Simard et al. (2011) dataset

Galaxy structural parameters for 1,123,718 galaxies from the Legacy area of SDSS DR7 are provided from the bulge/disc decomposition of the Simard et al. (2011) catalogue. Simard et al. (2011) performed a two-dimensional, point-spread-function-convolved, bulge+disk decompositions in the g and r bandpasses. Bulge and disk photometric errors remain below 0.1 mag down to bulge and disk magnitudes of g $\approx$ 19 and r$\approx$ 18.5. Four different decomposition procedures are investigated which make improvements to sky background determinations and object deblending over the standard SDSS procedures that lead to more robust structural parameters and integrated galaxy magnitudes and colors, especially in crowded environments. The most reliable procedure included the following three important steps:

1. GIM2D-based sky background level determination, from GIM2D code (Simard et al., 2002);

2. SExtractor object deblending;

3. Simultaneous bulge+disk decomposition in g and r.

They also used three different fitting models: (i) a pure Sèrsic model (see Section 1.2.1 in Chapter 1); (ii) an exponential disc plus De Vaucouleurs bulge (Sèrsic index $n = 4$); and (iii) an exponential disc plus free Sèrsic (free $n$) bulge model. The most appropriate model for a given galaxy is determined by the F-test probability. All three catalogs provide several measured structural parameters, rest-frame magnitudes, and colors. In this thesis we make use of the bulge over total magnitude values, B/T, and disk inclination, i. See Simard et al. (2011) for more details.

### 2.1.5 Environment: Yang et al. (2007) dataset

Yang et al. (2007) provide the Data Release I of the galaxy's group catalog in a magnitude limited redshift survey of galaxies drawn from the Sloan Digital Sky Survey (SDSS DR4). They used a modified version of the halo-based group finder developed by Yang et al. (2005) to the New York University Value-Added Galaxy Catalogue (NYU-VAGC; see Blanton et al. 2005), which is based on SDSS DR4 Adelman-McCarthy et al. 2006) and on the updated version based on DR7 (Abazajian et al., 2009) [4]. See Yang et al. (2007) for more details on the changes and improvements in the group finder algorithm. As detailed in Yang et al. (2005, 2007), the group-finder algorithm associate the galaxies according to their common dark matter haloes. Note that the halo masses are only available for halos

[4]http://gax.sjtu.edu.cn/data/Group.html

with $M_{halo} > 10^{11.5}$ $M_{\odot}$ (Yang et al., 2007), because this is the lower limit of the stellar mass-halo mass calibration provided in that work. For isolated galaxies at stellar masses below the calibration limit, we associate an halo mass upper limit of $10^{11}$ $M_{\odot}$. In the first step, a combination of two methods is used to identify the centers of potential groups and to estimate their characteristic luminosity. Using an iterative approach, the adaptive group finder then uses the average mass-to-light ratios of groups, obtained from the previous iteration, to assign a tentative mass to each group. This mass is then used to estimate the size and velocity dispersion of the underlying halo that hosts the group, which in turn is used to determine group membership in redshift space. Finally, each individual group is assigned two different halo masses: one based on its characteristic luminosity and the other based on its characteristic stellar mass. Applying the group finder to the SDSS DR4, they obtain 301,237 groups in a broad dynamic range, including systems of isolated galaxies. They also used detailed mock galaxy catalogs constructed for the SDSS DR4 to test the performance of the group finder in terms of completeness of true members, contamination by interlopers, and accuracy of the assigned masses. In particular, the algorithm was applied to three galaxy samples constructed from the SDSS DR4 galaxy catalog: sample I, which only contains galaxies with measured redshifts from the SDSS; sample II, which also contains those SDSS galaxies for which redshifts are available from alternative sources (mainly from the 2dFGRS); and sample III, which also includes galaxies which due to fiber collisions do not have a measured redshift, but which have been assigned the redshift of their nearest neighbor. The result is a total of 295,992, 301,237, and 300,049 groups from samples I, II, and III, respectively, and each group is assigned two values for its halo mass based on the ranking of either the characteristic luminosity or the characteristic stellar mass of its member galaxies. The final catalogue provide several properties of the group catalog, in this thesis, we make use of the: dark matter halo mass of the group in which our galaxies live and their classification as a central or satellite galaxies, according with their mass and luminosity.

# Chapter 3

# Ionized gas winds in the local Universe

*This chapter is adapted from Concas et al. 2017, A&A , 606, A36*

## 3.1 Abstract

We analyze a complete spectroscopic sample of galaxies (∼600,000 ) drawn from Sloan Digital Sky Survey (SDSS, DR7) to look for evidence of galactic winds in the local Universe. We focus on the shape of the [OIII]$\lambda$5007 emission line as a tracer of ionizing gas outflows. We stack our spectra in a fine grid of star formation rate (SFR) and stellar mass (M$\star$) to analyze the dependence of winds on the position of galaxies in the SFR versus M$\star$ diagram. We do not find any significant evidence of broad and shifted [OIII]$\lambda$5007 emission line which we interpret as no evidence of outflowing ionized gas in the global population. We have also classified these galaxies as star-forming or AGN-dominated according to their position in the standard BPT diagram. We show how the average [OIII]$\lambda$5007 profile changes as a function of the nature of the dominant ionizing source. We find that in the star-forming dominated source the oxygen line is symmetric and governed by the gravitational potential well. The AGN or composite AGN\star-formation activity objects, in contrast, display a prominent and asymmetric profile that can be well described by a broad Gaussian component that is blue-shifted from a narrow symmetric core. In particular, we find that the blue wings of the average [OIII]$\lambda$5007 profiles are increasingly prominent in the LINERs and Seyfert galaxies. We conclude that, through the identification of strong bulk motion as traced by the warm ionized gas, in the low-redshift Universe, "pure" star-formation activity does not seem capable of driving ionized-gas outflows, while, the presence of optically selected AGN seems to play a primary role. We discuss the implications of these results for the role of the quenching mechanism in the present-day Universe.

## 3.2 Introduction

As fully described in Chapter 1, the most striking feature of the history of our Universe is a drastic decrease in the star-formation activity of the galaxy population by almost an order of magnitude over the last 10 Gyr, after a phase of high and rather constant activity (e.g., Lilly et al., 1996; Madau et al., 1998; Madau & Dickinson, 2014, for a comprehensive review). Which process or which combination of processes, leading to the so called "quenching" of the star formation activity, causes such a decrease is still a matter of intensive debate. It is apparent that identifying the quenching process(es) is crucial to establishing a complete view of how galaxies evolve across cosmic time.

According to the most accredited galaxy formation models, from the semi-analytical (SAM) ones to the more recent mass-abundance-matching models, in the central galaxies, the efficiency in converting the gas fraction into stars reaches a maximum at halo mass $\sim 10^{12}$ $M_{\odot}$ with only $\sim 20$ % of their baryons currently locked up in stars (see for example Croton et al., 2006; Guo et al., 2011 based on the Millennium Simulation, and Moster et al., 2010; Behroozi et al., 2010; Yang et al., 2012 among the mass-abundance-matching models). The efficiency drops down steeply towards both sides of this mass threshold (e.g., Madau et al., 1996; Baldry et al., 2008; Conroy & Wechsler, 2009; Guo et al., 2010; Moster et al., 2010, 2013; Behroozi et al., 2010, 2013). There is an overall agreement, from the theoretical point of view, that below halo masses of $10^{12}$ $M_{\odot}$, the decreasing SF efficiency is likely to be due to gas eating and removal associated with the star-formation activity. Indeed, galactic winds driven by the energy and momentum imprinted by massive stars to the surrounding ISM, are believed to be sufficiently energetic to eject the gas away from the galaxy potential well and quench the star formation (see for instance Chevalier, 1977 for energy-driven outflows, Murray et al., 2005b for momentum-driven outflows, and to Hopkins et al., 2014 for effect of multiple stellar feedback in cosmological simulations). Above stellar masses of $10^{12}$ $M_{\odot}$, instead, more powerful outflows are required to let the gas escape from the deeper galaxy potential well. The energy and radiation generated by accretion onto the massive black hole (BH), in the most massive galaxies, exceeds the binding energy of the gas by a large factor (see Fabian, 2012 for a complete review). Therefore, energetic feedback from active galactic nuclei (AGN) is believed to provide an important and effective mechanism to eject the gas away by powerful winds, stop the growth of the galaxy and stifle accretion onto the BH (Di Matteo et al., 2005; De Lucia et al., 2006; Croton et al., 2006; Hopkins et al., 2006; Bower et al., 2006; Hopkins et al., 2014; Henriques et al., 2017).

However, although these models are very successful in reproducing a large variety of observational evidence, in particular, the evolution of the stellar mass function (e.g., Henriques et al., 2017), they still lack a clear observational confirmation. Indeed, a lot of effort has been made in the last decade from the observational point of view to observe the presence of such outflows at any mass scale and to study their effect on the evolution of the galaxy star-formation activity to identify a possible relation of cause and effect.

Steidel et al. (2010) observe blue-shifted Lyman-$\alpha$ emission in most of the star-forming (SF) galaxy population at redshift $\sim$2 and associate such emission line disturbance to

star-formation-induced outflow (see also Erb, 2015 for different emission line study). At somewhat lower redshift, but in a large redshift window ($0.5 < z < 1.5$), Martin et al. (2012a) use UV rest-frame absorption features to identify blue-shifted components as indication of outflow and find evidence of outflowing material in massive, highly star-forming galaxies (see also Rubin et al., 2014 for similar studies).

Powerful AGN-driven outflows have recently been observed both at low (e.g., Feruglio et al., 2010; Villar-Martín et al., 2011; Rupke & Veilleux, 2011, 2013; Greene et al., 2012; Mullaney et al., 2013; Rodríguez Zaurín et al., 2013; Cicone et al., 2014) and high redshift (e.g., Maiolino et al., 2012; Tremonti et al., 2007; Brusa et al., 2015; Perna et al., 2015; Cresci et al., 2015). However, it is not clear yet if the AGN feedback, in the form of galactic flows, is a specific property of the bulk of the AGN population or if it concerns only a subclass of these objects (Brusa et al., 2015). In addition, it is unclear if they cause a quenching or an enhancement of the galaxy SF activity (e.g., Cresci et al., 2015).

Furthermore, new observations are revealing the ubiquity of SF-induced outflows in very actively star-forming galaxies at all cosmic epochs (see Veilleux et al., 2005 and Erb, 2015 for a comprehensive overview). They are usually associated with energetic starburst phenomena (e.g., Heckman et al., 1990; Pettini et al., 2000; Shapley et al., 2003; Rupke et al., 2002, 2005a,b; Martin, 2005, 2006; Hill & Zakamska, 2014), while their impact in the normal star-forming galaxies (Chen et al., 2010; Martin et al., 2012a; Rubin et al., 2014; Cicone et al., 2016) and their global effect on the baryon cycle is still debated (Steidel et al., 2010).

These studies have traditionally been carried out with relatively small samples of galaxies. The availability of large spectroscopic data sets such as the SDSS (York et al., 2000), allows us to dramatically extend such studies in size. Significant improvement has recently been made in this regard (e.g., Greene & Ho, 2005; Chen et al., 2010; Mullaney et al., 2013; Cicone et al., 2016). However, all these resent works have only focused on a particular category of galaxy. For example, the optically-selected AGN in Mullaney et al. (2013) and Greene & Ho (2005) and the star-forming galaxies without AGN contribution in Chen et al. (2010) and Cicone et al. (2016).

The aim of this work is to explore the global proprieties of galactic winds in the local Universe *a)* by analyzing their incidence in the galaxy population, *b)* by identifying the powering mechanism: star formation, AGN or a mixed contribution of the two, and *c)* by clarifying what impact they might have on the galaxy SF activity. For this purpose we investigate the outflow signatures in a large sample of optical spectra at redshift $z < 0.3$, drawn from the Sloan Digital Sky Survey (SDSS; Abazajian et al., 2009), by using the ionized gas as traced by the [OIII]$\lambda$5007 emission line. The [OIII]$\lambda$5007 emission line is one of the strongest features in the rest-frame optical 1D spectrum of both active star-forming and AGN-dominated galaxies. This line is produced through a forbidden transition emitted by low-density and warm gas (T$\sim 10^4$K, see Chapter 1 for more details). Thus, any disturbed kinematic, such as a broadening and asymmetry of the [OIII] line, is only due to the presence of strong bulk motions of ionized interstellar gas (e.g., for local galaxies Heckman et al. 1990; Veilleux et al. 1995; Lehnert & Heckman 1996; Soto et al. 2012; Westmoquette et al. 2012; Mullaney et al. 2013; Rodríguez Zaurín et al. 2013; Bellocchi

et al. 2013; Rupke & Veilleux 2013; Liu et al. 2013; Harrison et al. 2014; Zakamska & Greene 2014; Cazzoli et al. 2014; Arribas et al. 2014; Cicone et al. 2016, and at high redshift Shapiro et al. 2009; Newman et al. 2012b; Harrison et al. 2012; Cano-Díaz et al. 2012; Genzel et al. 2014; Förster Schreiber et al. 2014; Brusa et al. 2015; Perna et al. 2015; Carniani et al. 2015). Also, [OIII]$\lambda$5007 emission is expected to lie in spectral regions free from strong stellar atmospheric absorptions. In this respect, it is expected that the [OIII]$\lambda$5007 emission line can be used with great success to identify or confirm galactic winds. We explore how the emission line profile changes as a function of key physical parameters: stellar mass, SFR, and primary photoionization processes (SF, AGN). In doing so, we analyze both the presence of a second broader Gaussian component and non-parametric variation of the line-profile.

This work is organized as follows. In Section 4.3, we present our sample selection and physical properties. In Section 4.4, we describe the method used to extract and analyze the [OIII]$\lambda$5007 emission line from our stacked spectra. We present and discuss the main results in Section 6.3.2 and finally we summarize our findings in Section 4.6. Throughout this chapter, we assume the following cosmological parameters: $H_0 = 70$ km s$^{-1}$ Mpc$^{-1}$, $\Omega_M = 0.3$ and $\Omega_\Lambda = 0.7$.

## 3.3 Data sample

### 3.3.1 SDSS spectra

The galaxy sample analyzed in this chapter is drawn from the Sloan Digital Sky Survey, (SDSS, York et al., 2000). As fully described in the Chapter 2, we use the spectroscopic catalog containing $\sim 930,000$ spectra belonging to the seventh data release (DR7, Abazajian et al., 2009). We use only objects included in the Main Galaxy Sample (MGS, Strauss et al., 2002) which have Petrosian magnitude $r < 17.77$ and redshift distribution extending from 0.005 to 0.30 , with a median z of 0.10. The spectra cover a wavelength range from 3800 to 9200 Å. They are obtained with 3″ diameter aperture fibers that, in the adopted cosmology, corresponds to $\approx 0.31 - 13.36$ kpc for the redshift range $z = 0.005 - 0.3$. The instrumental resolution is $R \equiv \lambda/\delta\lambda \sim 1850 - 2200$ with a mean dispersion of 69 km s$^{-1}$. Further details concerning the DR7 spectra can be found at http://www.sdss.org/dr7/.

### 3.3.2 Star-formation rates and stellar masses

We adopt the star formation - stellar mass plane (hereafter SFR-$M\star$) in order to classify galaxies in their fundamental properties. In order to define the position for each galaxy in the SFR-$M\star$ plane, we use the SFR and $M\star$ measurements taken from the MPA-JHU catalog[1]. As illustrated in Chapter 2, the stellar masses are obtained from a fit to the spectral energy distribution (SED) by using the SDSS broad-band optical photometry (Kauffmann et al., 2003a). The SFR measurements are based on the Brinchmann et al.

[1]http://www.mpa-garching.mpg.de/SDSS/DR7/

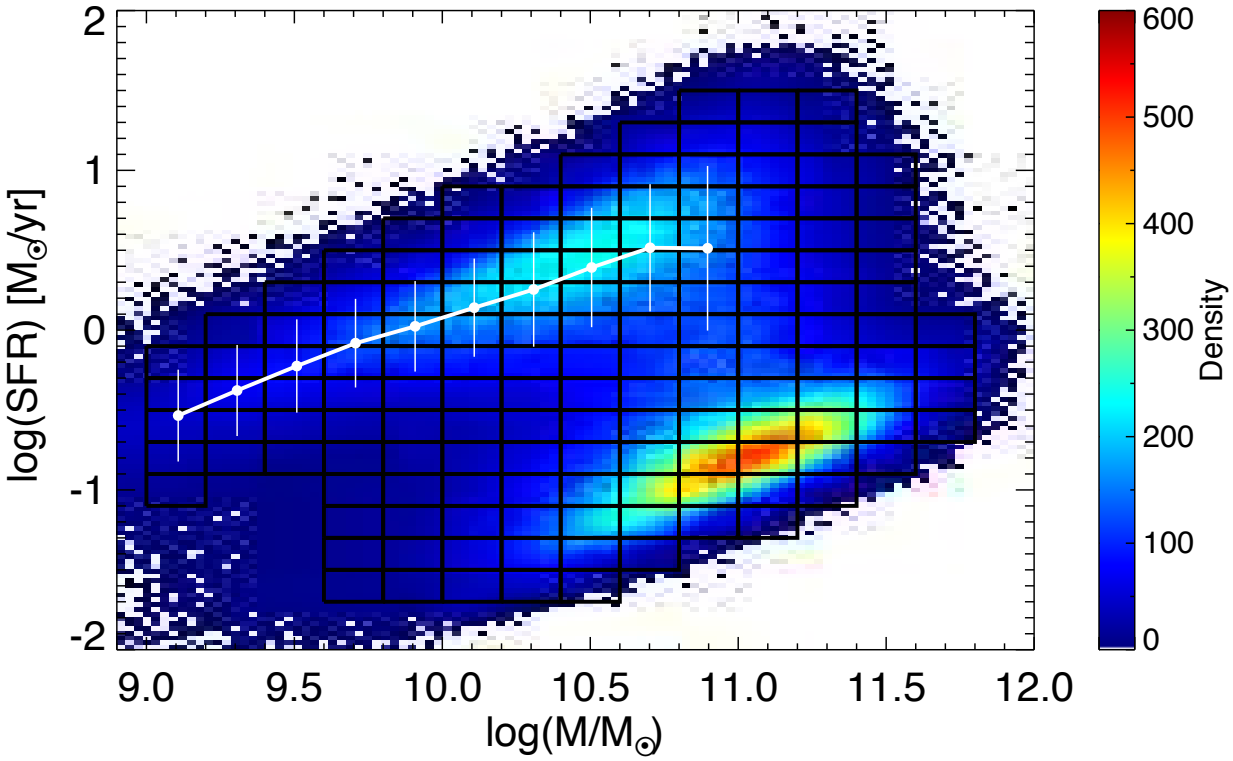


Figure 3.1: SFR-$M\star$ plane for DR7 SDSS galaxies. The black boxes represent the fine grid used for the stacking of the total sample.The white line shows the position of the so-called "main sequence" (MS) of star−forming galaxies. The MS is computed as the mode and the dispersion of the SFR distribution in stellar mass bins following the example of Renzini & Peng (2015).

(2004) approach. They use the H$\alpha$ emission line luminosity to determine the SFRs for the star-forming galaxies. For all other galaxies, which have emission lines contaminated by AGN activity or unmeasurable emission lines, the SFRs are inferred by D4000-SFR relation (e.g., Kauffmann et al., 2003a). All SFR measurements are corrected for the fiber aperture following the approach proposed by Salim et al. (2007).

We apply a stellar mass cut at $\log(M/M_{\odot}) \geq 9.0$ to limit the incompleteness in the low-mass regime (see also Morselli et al., 2017). In this way, we ended up with a global sample of $\sim$ 600000 galaxies.

The galaxy sample is shown in the SFR-stellar mass plane in Fig.6.9. The color-code accords with the number density of galaxies per bin of SFR and stellar mass. We overplot also the main sequence of star forming galaxies (MS hereafter) estimated as the peak (mode) of the distribution in the star forming galaxy region, similarly to Renzini & Peng (2015).

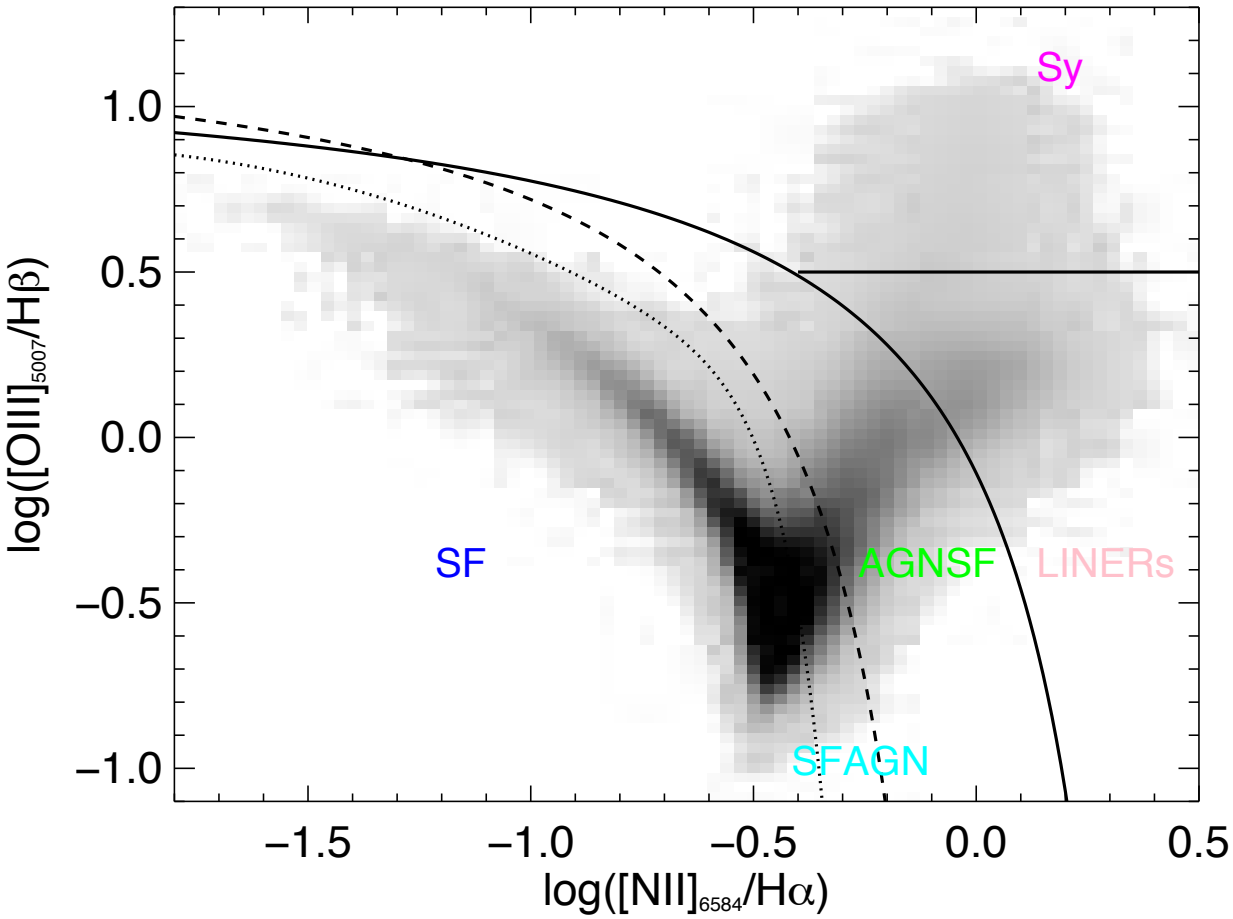


Figure 3.2: The distribution of the galaxies in our sample in the BPT line-ratio diagram. The solid curve is the theoretical demarcation of Kewley et al. (2001) , that separates star-forming galaxies and composites from AGN. The dashed (Kauffmann et al., 2003b ) and dotted Stasinska et al. (2006) curves indicate the empirical division between composite SF-AGN and AGN-SF and the pure star-forming galaxies, respectively (see text for more details). The horizontal line at log ([OIII]/H$\beta$) = 0.5 is the demarcation criteria between TYPE 2 (or Seyfert, Sy) and LINERs galaxies showed in Kewley et al. (2006).

### 3.3.3 BPT classification

Emission line diagnostic diagrams are a powerful way to probe the nature of the dominant ionizing source in galaxies. Baldwin, Phillips, & Terlevich(1981, BPT), and after them, Veilleux & Osterbrock (1987) demonstrate that it is possible to distinguish normal star-forming- from AGN-dominated galaxies by considering two pairs of emission lines ratios. The MPA-JHU catalog also includes, for each single spectrum, the flux measurements of [OIII]$\lambda$5007, H$\beta$, H$\alpha$ and [NII]$\lambda$6584 emission lines. As showed in Stasinska et al. (2006), the galaxies that lie on the left side of the Kauffmann et al. (2003b) demarcation line also include objects that have an AGN contamination. In order to better segregate the

| subsample | number | percent | N Bins |
|---|---|---|---|
| TOT | 621990 | 100% | 148 |
| SF | 128258 | 20.6% | 88 |
| SF-AGN | 46081 | 7.4% | 81 |
| AGN-SF | 69421 | 11.2% | 119 |
| LINERs | 34640 | 5.6% | 99 |
| TYPE 2 | 10679 | 1.7% | 77 |
| unClass | 332911 | 53.5% | 132 |
| TYPE 1 | 10548 | | 1 |

Table 3.1: Basic data of the subsamples discussed in the text. The TYPE 1 AGN come from the Mullaney et al. (2013) classification.

purely star forming galaxies from AGN hosts, we refine the BPT classification of our sample instead of using the selection criteria performed by Brinchmann et al. (2004). By using the two optical line ratios:[OIII]$\lambda$5007/H$\beta$ and [NII]$\lambda$6584/H$\alpha$, then, we define new galaxy subsamples on the basis of the prevalence of different photoionization processes. All galaxies with no or very weak emission lines ($S/N < 4$) are not classified in the BPT diagram and we refer to these objects as "unClass" (332911 galaxies, 53.5% of the total sample). For the lines with $S/N > 4$ (289079 galaxies, 46.5% of the total sample), we adopted the following classes of emission line nebulae:

**SF** Pure star-forming galaxies, objects with emission line ratio below the Stasinska et al. (2006) curve (128258 galaxies, 20.6% of the total sample).

**SF−AGN** The objects whose emission lines are due primarily to star formation activity but that also have a second minor component due to AGN presence; they are located between the Stasinska et al. (2006) and Kauffmann et al. (2003b) demarkation lines (46081 galaxies, 7.4% of the total sample).

**AGN−SF** The composite transition region objects that lie inside the region defined by Kauffmann et al. (2003b) and Kewley et al. (2001) curves (69421 galaxies, 11.2% of the total sample).

**TYPE 2 (or Seyfert galaxy, Sy) AGN and LINERs** All the objects located above the diagnostics outlined of Kewley et al. (2001) and separated in Seyfert galaxies and low−ionization nuclear emission−ine regions (LINERs) with the demarcation criteria shown in Kewley et al. (2006), $\log([OIII]/H\beta) = 0.5$ (34640 and 10679 galaxies, 5.6% and 1.7% of the total sample for LINERs and TYPE 2, respectively).

The corresponding diagnostic diagram is shown in Fig. 3.2. We split the total sample into six classes: SF, SF−AGN, AGN−SF, LINERs, TYPE 2 and unClass (cf. Table 4.1). In Fig. 3.3 we report the contour levels at 25%, 50%, and 75% of the distribution for the six BPT classes, labeled in different colors, in the SFR-$M\star$ plane.

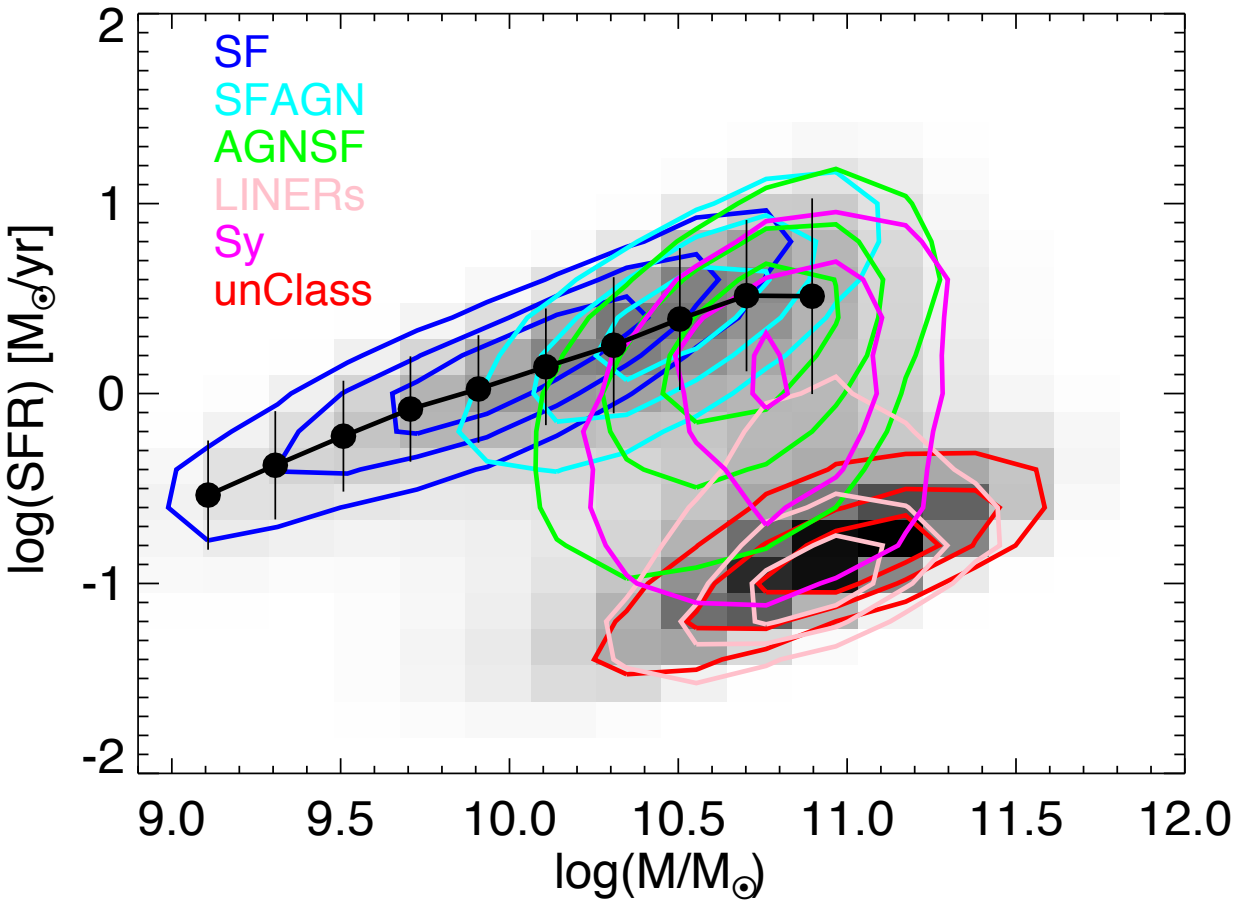


Figure 3.3: Location of SF, SF−AGN, AGN−SF, LINERs, TYPE 2 (or Sy) and unClass galaxies in the SFR-$M\star$ plane. From outside to inside, the contours encompass 25, 50, and 75 per cent of the data points. The black line shows the mode and dispersion of the MS.

Throughout this chapter we also compare the above BPT classes with all the SDSS TYPE1 AGN defined in Mullaney et al. (2013) (cf. Table 4.1, see Section 2.4 in Mullaney et al., 2013 for more details). Due to the dominating AGN contribution, a measurement of the SFR and stellar mass derived from the spectra and optical broad band photometry is not available for this class of galaxies. Therefore, they cannot be placed in the SFR-stellar mass plane.

## 3.4 Method

In this section, we describe how we measure the properties of the [OIII]$\lambda$5007 emission line.

### 3.4.1 Stacked spectra

The auroral [OIII]$\lambda$5007 emission line can be very faint and typically undetectable in most SDSS galaxy spectra. To reduce the contribution of random fluctuations in the measured flux and then improve the signal-to-noise ratio (SNR) we perform our analysis in stacked optical spectra. In particular, we use the median stacked spectra taken from Concas et al. in prep. In brief, we divide the SFR-$M\star$ parameter space into small bins, shown in Fig.6.9. The boundaries of this grid, together with the abundance of sources per bin, are chosen to provide a fine sampling of the SFR-$M\star$ plane and at the same time to have good statistics in each bin. We adopt bins of $\Delta \log(M/M_{\odot}) = 0.2$ and $\Delta \log(SFR) = 0.2$ dex for the total sample and larger bins for the analysis of the individual BPT classes, where the statistics is reduced. We request a minimum of 50 galaxies in each bin. The galaxy spectra are first corrected for the foreground Galactic reddening using the extinction values from Schlegel et al. (1998) then they are transformed from vacuum wavelengths to air and shifted to the rest frame. We normalize each spectrum to the stellar continuum with the mean flux from 6400 Å to 6450 Å, where the spectrum is free of strong emission and absorption lines. Finally, the rest-frame spectra in each bin are stacked together to produce a single median spectrum. We obtain 148 galaxy-stacked spectra for the total sample and 88, 81, 119, 99, 77, 132 and 1 for the subclasses described in section 3.3.3 (SF, SF−AGN, AGN−SF, LINERs, TYPE 2, unClass and TYPE 1 respectively). The different numbers of stacked spectra between the total sample and the subsamples is due to the fact that towards the quiescent region less and less galaxies can be classified in the BPT diagram. In such a region of the SFR-M$\star$ plane, we analyze the [OIII]$\lambda$5007 profile only in the stacked spectrum of the total sample. As mentioned in the previous section, for the TYPE 1 AGNs, the SFR and M$\star$ measurements are not available from the optical spectra and broad band photometry. In this case we collect all the single TYPE 1 spectra in one single stacked spectrum.

The error of the stacked spectra is obtained through a bootstrapping analysis. The statistical error obtained in this way depends on the number of spectra used in the stacking analysis in each bin. However, we check that the error is very stable from the most populated bins ($\sim$ 4000 galaxy spectra) to the less populated ones (50 galaxies).

### 3.4.2 Fitting the stellar continuum

In order to also reliably measure the weak emission lines emitted by the ionized gas, the stellar continuum must be properly removed. To this end, we use the penalized pixel-fitting (pPXF) algorithm, which is a publicly available IDL code, developed by Cappellari & Emsellem (2004) to find the best fit stellar continuum and separate the nebular emission lines

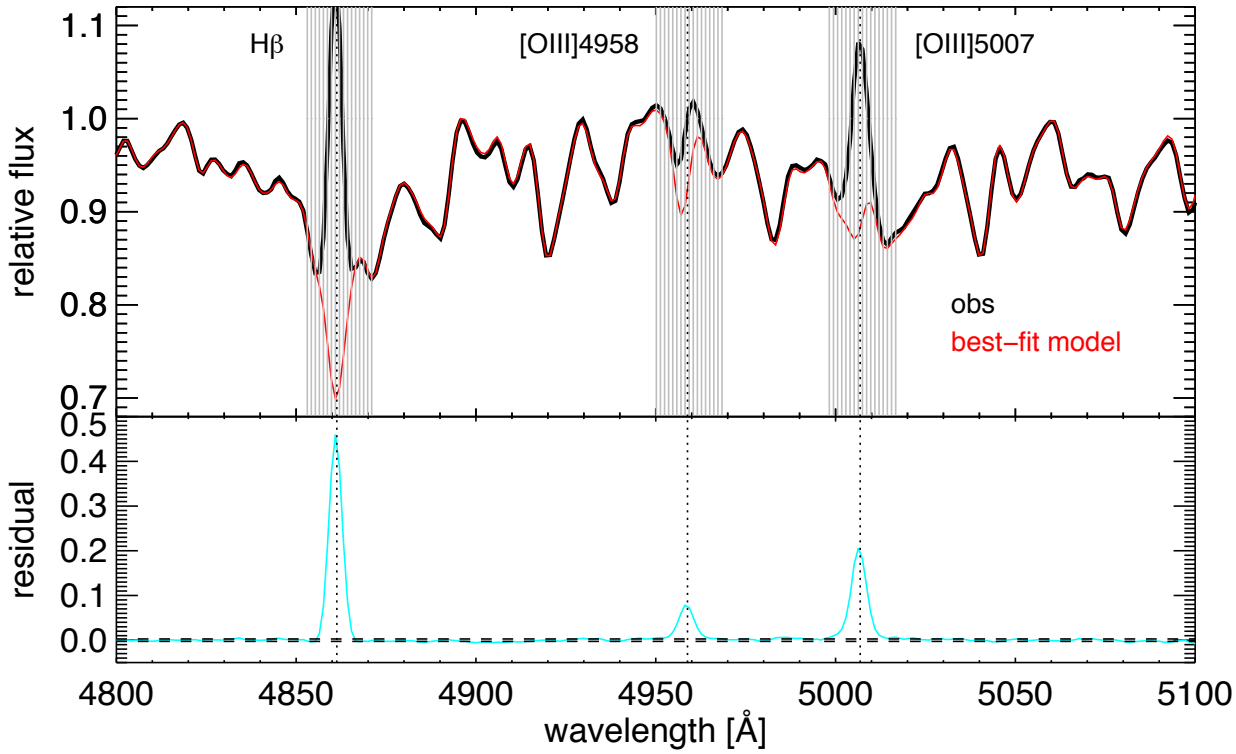


Figure 3.4: Example of our continuum fit and subtraction performed for the stacked spectrum with SFR=$10^{0.2} M_{\odot} yr^{-1}$ and $M\star = 10^{10.5} M_{\odot}$. The top panel shows the observed stacked spectrum (black line) and our best-fit stellar continuum model (red line). The light-gray-shaded regions indicate the wavelength range where the H$\beta$, [OIII]$\lambda$4959 and [OIII]$\lambda$5007 emission lines are located. The bottom panel shows the residual spectrum (cyan line) and the level of fluctuations in the fit residuals (dashed line).

in each stacked spectrum. In brief, pPXF is able to parameterize the line-of-sight velocity distribution (LOSVD) through a Gauss-Hermite expansion of the absorption-line profile by fitting the stellar continuum with a linear combination of simple stellar population (SSP) input model spectra. In the pPXF analysis, we adopt a library of template spectra based on the stellar population models from Bruzual & Charlot (2003), hereafter BC03. BC03 models are available at a resolution of 3 Å FWHM in the wavelength range between 3200 and 9500 $\AA$, which is very similar to the one of SDSS spectra ($\approx 1800-2000$ between 3800 and 9200 Å). Our templates include a simple stellar population with ages $0.01 \leq t \leq 14$ Gyr and four different metallicities, $Z/Z_{\odot} = 0.2, 0.4, 1, 2.5$ by assuming a Chabrier (2003) initial mass function (IMF). We perform the pPXF analysis for each stacked spectrum in the wavelength range : $[4800, 5050]$ Å, where the H$\beta$, [OIII]$\lambda$4959, 5007 emission lines are located. The results are a best-fit stellar continuum. For each galaxy bin, we subtract the best-fit stellar continuum from the observed stacked spectrum. This 'residual' spectrum is used for any analysis of [OIII]$\lambda$5007 emission line features. An example of the fitting procedure result is shown in Fig. 3.4, which shows the very good agreement of the observed

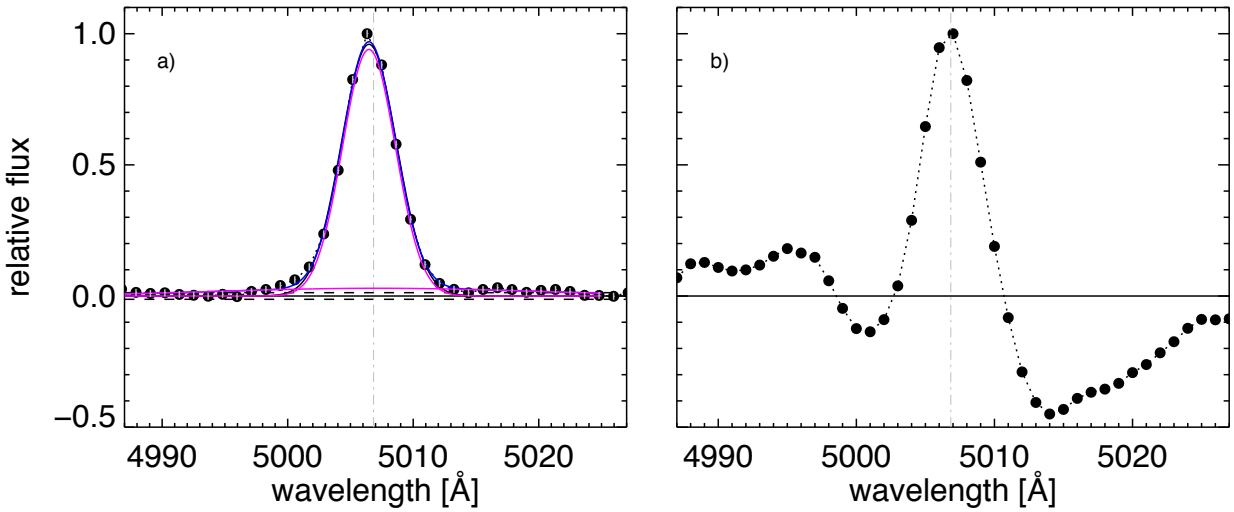


Figure 3.5: Average [OIII]$\lambda$5007 profile of the galaxy subsample with SFR=$10^{0.2} M_{\odot} yr^{-1}$ and $M\star = 10^{10.5} M_{\odot}$. In panel a) we show the emission line derived with our method, obtained with the fit and remove of the stellar continuum by pPXF algorithm (see the text for more details). In panel b) we show the emission line for the same SFR and $M\star$ galaxies obtained by the continuum-subtracted spectra provided by the SDSS pipeline as shown by (Mullaney et al., 2013). Our method is more efficient at modeling and removing the stellar features in the proximity of the [OIII] line. The black symbols are the observed flux. The magenta lines illustrate the two-Gaussian component and the blue curve shows the combined fit. The level of scatter in the residuals of our fit is shown with the horizontal dashed lines. The vertical gray line marks the rest-frame position of the [OIII] line.

and the model continuum over a large wavelength range in the [OIII] emission line region. In order to check the stability of the fitting procedure and to estimate the error of the residual spectrum, we apply a bootstrapping technique by performing the fit on the sample of bootstrapped stacked spectra in each SFR-stellar mass bin (see previous paragraph). The stability of the procedure is confirmed by the fact that the error of the residual spectrum is consistent or only slightly larger (at maximum 30%) with respect to the error of the stacked spectra. As an example, the panel a) of Fig. 3.5 shows the residual spectrum in the [OIII]$\lambda$5007 emission line region. The quality of our continuum fit is guaranteed by the low level of fluctuations in the fit residuals (dashed lines in Fig. 3.5). The error of the residual spectrum is then used to estimate the SNR of the emission line in the residual stacked spectra.

For comparison, we also show the result of the continuum subtraction method applied by Mullaney et al. (2013) (Fig. 3.5, panel b). They use, in particular, the single continuum subtracted spectra provided by the SDSS pipeline. While this method turns out to be reasonable for AGN spectra where the emission line has a very high SNR with respect to the continuum, it is not applicable to galaxy spectra with lower SNR emission lines, as in the case considered here.

### 3.4.3 Measuring [OIII]$\lambda$5007 emission line profiles

We analyze the oxygen line shape with two different approaches: a) By fitting the line with a single and a double Gaussian to identify a possible second broader component with respect to the systemic one, and b) by adopting a non-parametric analysis. The two methods are complementary. The first one allows us to separately study the various components that determine the observed line, while the second procedure is independent to the particular fitting function and is relatively insensitive to the quality of the data (see Perna et al., 2015, Zakamska & Greene, 2014, Liu et al., 2013).

#### Profile fitting

We fit the [OIII] line profile in the residual spectrum with one and two Gaussian components by using an IDL MPFIT fitting code. In both cases we fit the line center, width and amplitude.

The single Gaussian fit allows us to estimate the global line width, $\sigma_{[OIII]}$ , and the SNR of the line. The observed $\sigma_{obs}$ of the line is the convolution of the real width of the emitted line and the instrumental resolution. To remove the instrumental effects, we correct the $\sigma_{obs}$ with $\sigma_{[OIII]} = \sqrt{\sigma^2_{obs} - \sigma^2_{inst}}$, where $\sigma^2_{inst}$ is the instrumental dispersion. For SDSS data, the $\sigma_{inst}$ change as a function of wavelength, and it varies with the location of the object on the plate and the temperature on the night of the observations. Therefore, in order to use the correct $\sigma_{inst}$ for all our stacked spectra, we use the instrumental resolution measured for each single spectrum from the ARC lamps provided by the MPA-JHU group ($\sigma_{ARC}$). The final $\sigma_{inst}$ applied in each stacked spectrum is the median value of the singles $\sigma_{ARC}$. The mean $\sigma_{inst}$ in the [OIII] wavelength range for our sample is $\sim 60$ km s$^{-1}$.

The double Gaussian fit allows us to estimate the significance of a second component and its line profile. We take the double Gaussian profile as the best fit for the [OIII] line profile when it leads to a reduction of the reduced $\chi^2$ value by more than 30%. This is to avoid a misidentification of a second component when the double Gaussian fit provides two Gaussian components with consistent width and center and different amplitude. Indeed, in this case the sum of the two Gaussian would lead anyhow to a single Gaussian component. We check that a reduction of the $\chi^2$ value by at least 30% is a good threshold to distinguish the need of a double Gaussian fit.

We check the reliability of our multi Gaussian fit by using an additional statistical criterion. To avoid overfitting and allow for the correct number of Gaussian used in each [OIII] line fit, we employed the Bayesian Information Criterion (BIC, Liddle, 2007): BIC= $\chi^2 + p * \ln(n)$ , where $\chi^2$ is the chi squared of the fit, $p$ is the number of free parameters (3 and 6 for one and two Gaussian components, respectively) and $n$ is the number of flux points used in the fit. We measured the BIC value by using the one single Gaussian fit and the double Gaussian fit. The model with the smallest value of the BIC was chosen as the preferred model for the data. We find that the BIC method is perfectly in agreement with the previous method. In the following section, we discriminate between a single or double Gaussian fit on the basis of the BIC.

When the double Gaussian fit is retained as the best fit, we use it to estimate a) the SNR of the second component to check its significance, b) to compare the flux percentage of the second component with respect to the systemic contribution, c) to estimate the velocity shift of the centroid with respect to the systemic redshift, and d) to estimate the line width of the second and systemic component.

The errors on all measured quantities are obtained with a bootstrapping technique. The fit is repeated on the bootstrapping sample (see previous paragraph) to obtain the distribution of all measured quantities, and hence the dispersion as an estimate of the error.

**Non-parametric analysis**

To have a model-independent measurement of emission line profiles, we also apply a non-parametric approach. This approach is commonly used in AGN outflow studies (Liu et al., 2013; Rupke & Veilleux, 2013; Zakamska & Greene, 2014; Harrison et al., 2014; Brusa et al., 2015; Perna et al., 2015). Briefly, we construct the cumulative flux of the line as a function of velocity: $F(v) = \int_{-\infty}^{v} f(v')\,\mathrm{d}v'$, in the observed spectrum without using any particular fitting function. Then, we describe the velocity width, asymmetry and the wings prominence of the [OIII] line by using the following non-parametric quantities:

1. **Velocity width**. The velocity width, $W80$ , is the velocity range that encloses 80% of the total flux. It is defined by $W80 = v90 - v10$, where $v90$ and $v10$ are the velocities at which 90% and 10% of the line flux accumulates, respectively. For a purely Gaussian velocity profile the $W80$ is proportional to the standard deviation ($\sigma$) and full width at half maximum (FWHM), as shown in the following equation, $W80 = 2.563 \times \sigma = 1.088 \times$FWHM. Values of $W80$ are given in km s$^{-1}$.

2. **Asymmetry**. The dimensionless parameter $R = ((v95 - v50) - (v50 - v05))/(v95 - v05)$ gives a measure of the asymmetry of the velocity profile relative to the median velocity. In a perfectly symmetric profile R is $R = 0$

3. **Line wings**. The prominence of the line wings in the profile is the non-parametric analog of the kurtosis, with $r9050 = W90/W50$, where $W90$ and $W50$ are the width comprising 90% and 50% of the flux, $W90 = v95 - v05$ and $W50 = v75 - v25$. In a Gaussian profile $r9050$ is equal to 2.4389 and the $r9050$ increases in profiles with more extended wings.

The error on each of the quantities is estimated, as in the previous case, via bootstrapping analysis. Each quantity is measured in the bootstrapping sample related to each residual spectrum in order to estimate the dispersion of the distribution as a measure of the error. This is done, in particular, to check if each quantity deviates more than $3\sigma$ from the value corresponding to a Gaussian distribution with the same width of the observed line. For this purpose, we use the measure of the global line width estimated with the single Gaussian line profile, as explained in the previous paragraph.

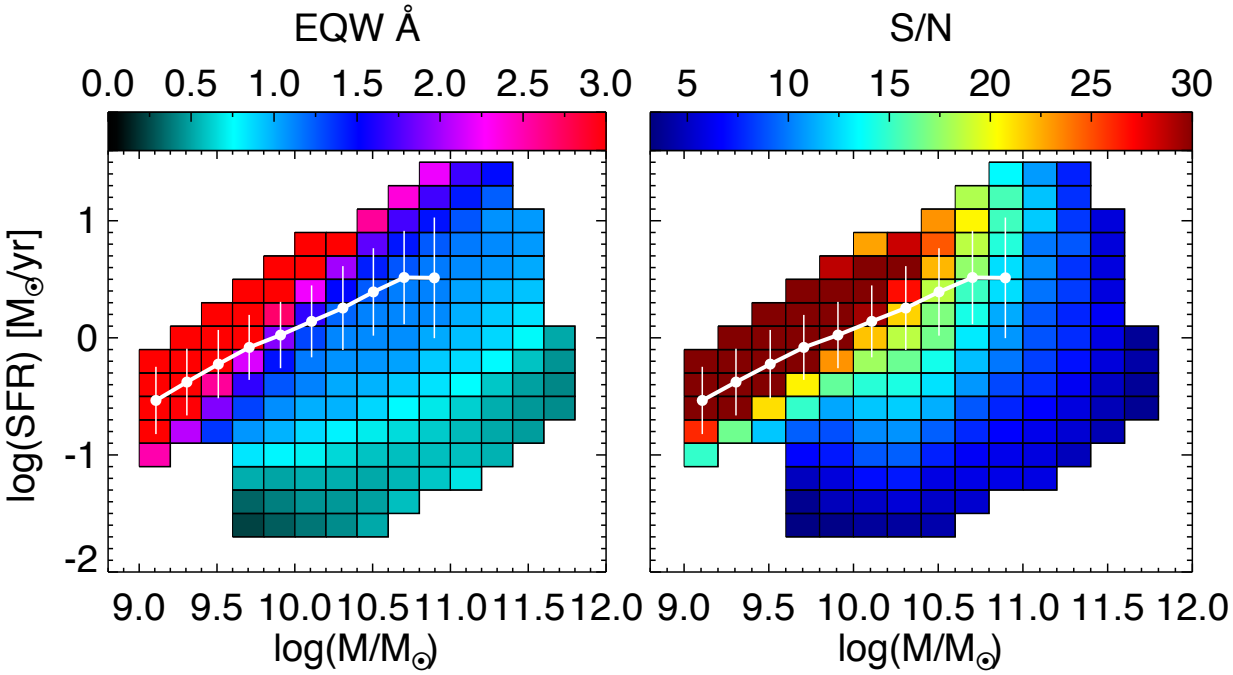


Figure 3.6: EQW (left panel) and total line-signal-to-noise ratio, SNR (right panel) in the SFR-M⋆ diagram for the total sample. The white line shows the mode and dispersion of the MS. The galaxy bins with total emission line SNR $< 8$ are plotted in gray.

## 3.5 Results

In this section we first show our results for the total sample (621990 galaxies), then we focus on the results obtained for the six BPT classes: SF, SF−AGN, AGN−SF, LINERs, TYPE2 AGNs (289079 galaxies) and unClass (332911 galaxies). We also show the comparison with the TYPE1 AGN sample of Mullaney et al. (2013) (10548 galaxies). See Tab. 4.1 for percentage values and number of stacked spectra in each sample.

### 3.5.1 [OIII] line in the global sample

We analyze the line flux and shape of the total sample, stacked in 148 median spectra (see Section 3.4.1), as a function of position in the SFR-M⋆ diagram. Fig. 3.6 shows the distribution of the [OIII]$\lambda$5007 equivalent width (EQW, left panel) and corresponding signal-to-noise ratio (SNR, right panel), of the total emission line in the SFR-M⋆ plane. As expected, the MS region is populated by the higher EQW values and higher SNR, while towards the passive region, the line is intrinsically weak, with EQW $\leq 1$ Å and low SNR, SNR$\leq 8$. In order to ensure a robust and accurate measurement of the total emission line shape, we impose a SNR limit on the [OIII] line of 8. The stacked spectra with [OIII] line detected with SNR ¿ 8 are 94, which correspond to 366133 galaxies. The median spectra

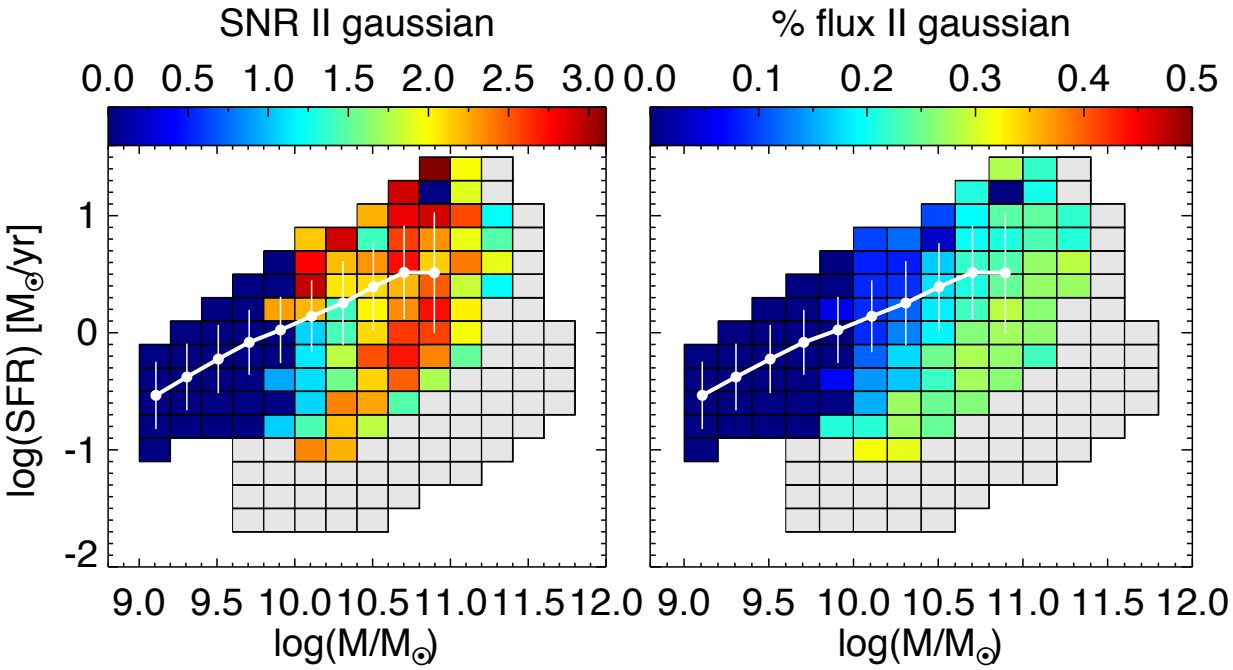


Figure 3.7: Signal-to-noise ratio, (SNR) and flux enclosed in the second broader Gaussian component (left and right panel) in the SFR-M⋆ diagram for the total sample. The white line shows the mode and dispersion of the MS. The galaxy bins with total emission line SNR $< 8$ are plotted in gray.

with a low SNR level (54, obtained from 255857 single galaxies) are preferentially unClass objects, mainly located in the quiescent region, as can be seen from the distribution of different BPT classes in Fig. 3.3. In the remaining figures here, all bins with total emission line SNR $< 8$ are plotted in gray and are not considered in the analysis.

We use the results of the best Gaussian fit, single or double, to check the significance of the second Gaussian component. When a single Gaussian turns out to be the best fit, we set the SNR of the second component to zero. When the best fit is provided by a double Gaussian, we estimate the SNR of the second component as the ratio between the flux encapsulated in this component and the noise in the region of the line profile. This is done in each bin of the SFR-stellar mass plane. The left panel of Fig. 3.7 shows the SNR of the second Gaussian component, while the right panel shows the percentage of flux encapsulated in it. Despite the very high SNR of the global [OIII] line (Fig. 3.6 right panel), the second broad Gaussian component is only marginally detected with a SNR$\sim$2.5-3 at masses above $\sim 10^{10} M_{\odot}$ and in a large range of SFR (Fig. 3.7 left panel). Al lower masses, the [OIII] line is perfectly consistent with a single Gaussian and no additional component is needed to fit the line profile. The flux encapsulated in the second broad component, though, is less than 10% most of the MS region, with the exception of the highest mass bins, where it reaches a value of 20%; it reaches a similar percentage (20-25%) in the valley between the MS and the quiescent region also.

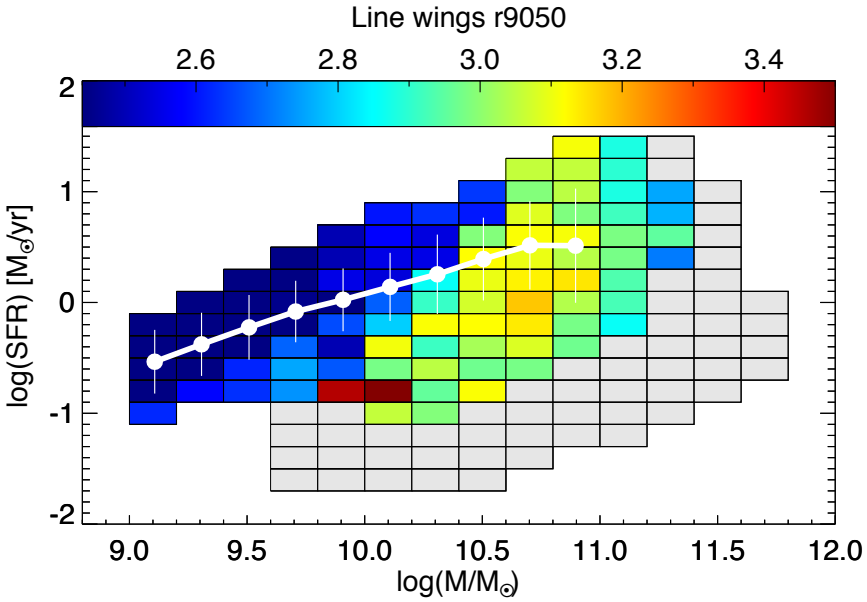


Figure 3.8: Prominence of the line wings $r9050$ in the SFR−M⋆ diagram for the total sample. The white line shows the mode and dispersion of the MS. The bins below M⋆ = $10^{10.5}$ M⊙ have $r9050$ values consistent with 2.44 within $3\sigma$. The galaxy bins with total emission line SNR $< 8$ are plotted in grey.

This is also confirmed by the non-parametric analysis. The values of the line wings parameter, $r9050$, as a function of the position in the SFR-M⋆ plane, is shown in Fig. 3.8. The $r9050$ parameter is consistent with the value of a Gaussian function ($r9050 \sim 2.44$) along and around the MS relation, up to stellar masses of $10^{10.5} M_{\odot}$. The kurtosis is exceeding, with poor significance ($\sim 2\sigma$), the Gaussian value up to values of $2.9 - 3$ in the mass range $10^{10.5-11}$ $M_{\odot}$, where the percentage of flux encapsulated in the broader component is of 20-25%. For comparison, the kurtosis of a Lorentzian profile, with strong wings, is 6.31. In all bins, the [OIII] line appears to be symmetrical, with typical $R$ values always consistent with 0 within $3\sigma$ of significance.

Fig. 3.9 shows the distribution of the line width in the SFR-M⋆ plane, estimated either with the dispersion $\sigma_{[OIII]}$ and the analogous non-parametric $W80$ (right and left side, respectively). We observe a progressive increase in the line width with the galaxy stellar mass M⋆ , irrespective of SFR. This is expected since the [OIII] emission traces the galaxy potential well. We compare the value of $\sigma_{[OIII]}$ in any bin of the plane with the mean galaxy velocity dispersion, estimated from the absorption features due to the stellar component provided by the MPA-JHU public catalog. The left panel of Fig. 3.10 shows that at high stellar masses, the ratio between $\sigma_{[OIII]}$ and the galaxy velocity dispersion is consistent with 1. Only at lower masses ($< 10^{10.5}$ $M_{\odot}$) does the ratio increase to higher values. However in this region, none of the previous indicators (flux enclosed in the second broader component, asymmetry $R$ or the kurtosis $r9050$) show signature of a non Gaussian line profile. Thus, we ascribe such an increase to two factors: a) the galaxies in this region

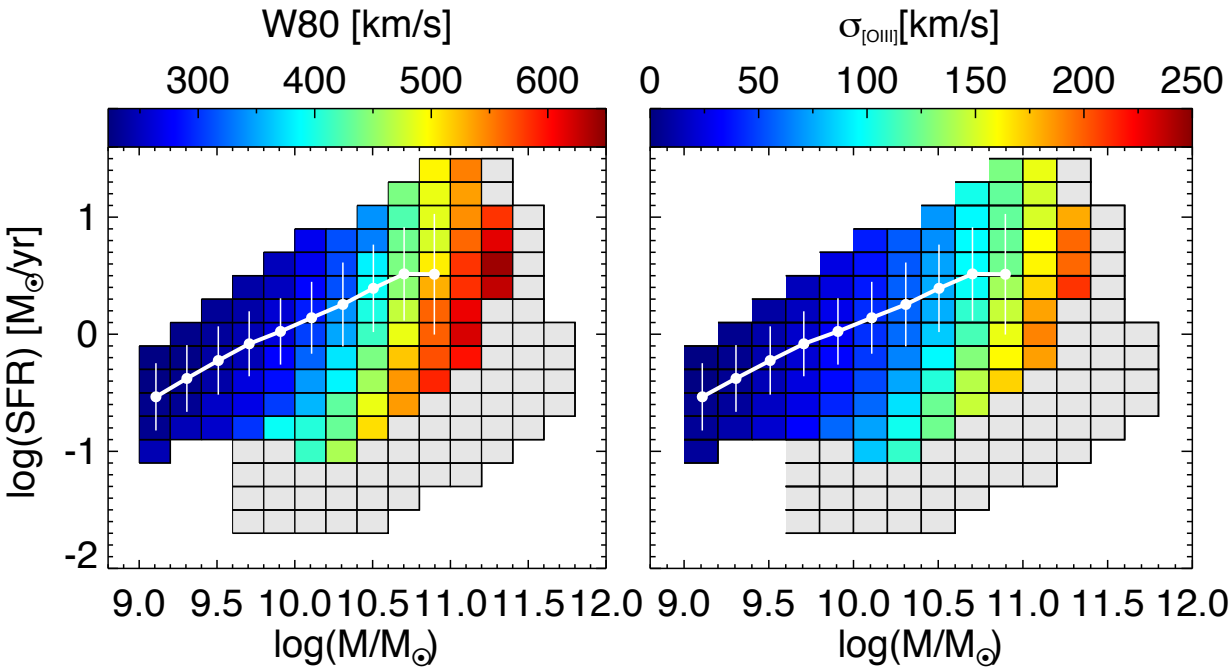


Figure 3.9: Non-parametric $w80$ and $\sigma_{[OIII]}$ (left and right panels, respectively) in the SFR-M$\star$ diagram for the total sample. The white line shows the mode and dispersion of the MS.

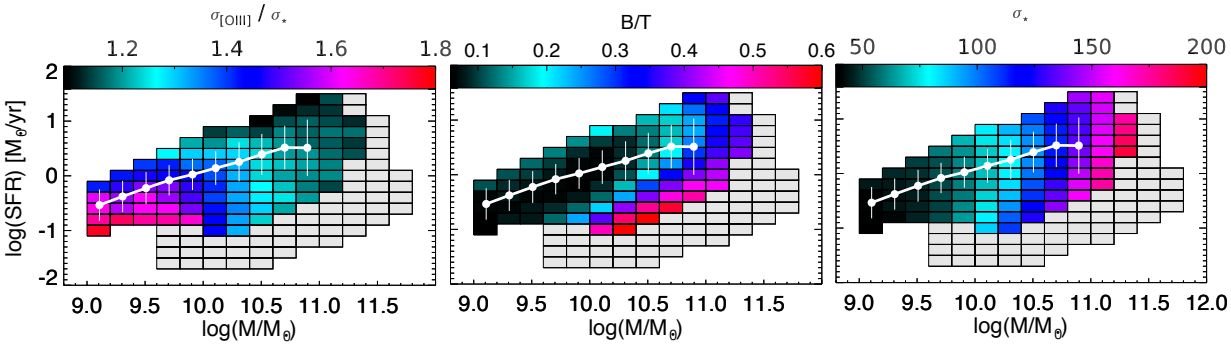


Figure 3.10: *Left panel*: $\sigma_{[OIII]}/\sigma_\star$ in the SFR-M$\star$ plane. At high stellar mass, the gas kinematics follows the velocity dispersion of the stellar component. *Central panel:* B/T median values in the SFR-M$\star$ diagram. The bulge-disk decomposition is taken from the Simard et al. (2011) catalog. We use the values calculated with the r filter. *Right panel*: $\sigma_\star$ distribution in the SFR-M$\star$ plane. At low stellar masses the $\sigma_\star$ is below to the instrumental resolution. In all panels, the white line shows the mode and dispersion of the MS.

tend to be pure disks, as shown by the mean B/T of $\sim 0.1$ as derived from Simard et al. (2011, central panel of Fig. 3.10), thus the gas could show a different kinematics than the stellar component; b) in this region of the diagram, the MPA-JHU public catalog provides values of the stellar velocity dispersion lower than the SDSS resolution of 70 km s$^{-1}$, which we assume to be a lower limit (see right panel of Fig. 3.10).

Thus, we conclude that there is only marginal evidence for a broad component in the [OIII]$\lambda$5007 emission line profile and only in a specific locus of the SFR-stellar mass plane. When detected, such a component is centered at the systemic redshift and there is no evidence of a blueshift, as indication of wind, as for the more symmetrical profiles of TYPE 2 AGNs shown in Mullaney et al. (2013). Most of the MS region is well represented by galaxies with [OIII] profile well fitted by a single Gaussian component with no asymmetry and with low kurtosis values. Only at high masses ($10^{10.5} - 10^{11} M_{\odot}$) do we observe a marginally higher kurtosis and therefore the presence of line wings. However, for these galaxies, we do not find an excess of the line [OIII] width with respect to the galaxy velocity dispersion provided by the stellar component. Indeed, only a small percentage of the [OIII] flux is encapsulated in the wings. This indicates that likely a low percentage of the gas in these galaxies is moving away in a very low velocity wind.

### 3.5.2 Trends with AGN and SF activity

The absence of significant outflow signature in the global population does not exclude the possibility that strong winds might be observed in specific classes of objects. In order to investigate this possibility, in this section we analyze the [OIII] line profile in the BPT subclasses, and so as a function of different ionization sources. As described in Section 4.3 we split our sample into: SF, SF−AGN, AGN−SF, LINERs, TYPE 2, and unClass galaxies. We perform a first analysis on the stacked spectra of each subclass and then we study the stacked spectra as a function of the position in the SFR-M$\star$ plane for each subclass separately.

Fig. 3.11 shows our multicomponent emission line fit to the stacked [OIII] line profile of each subclass. It is immediately apparent, that the significance of a second broad and slightly blueshifted component is remarkably increasing with the increase of the AGN contribution. While the star forming galaxy population shows a symmetric Gaussian [OIII] line profile, the increase of the nuclear activity in the SF-AGN and AGN-SF leads to the raise of significant line wings. LINERs, TYPE 2, and TYPE 1 AGN, in particular, also show a more prominent and slightly blueshifted broader component (characterized by a velocity dispersion of $470.1 \pm 110.0$, $363.1 \pm 14.0$ and $363.1 \pm 14.0$ km s$^{-1}$, respectively) with respect to the systemic velocity ($\Delta V$ ¡ 70 km s$^{-1}$) and corresponding negative values in the asymmetry parameter (R). The flux enclosed in the second Gaussian component goes from 0% in the SF galaxies to 48% in the TYPE 1 AGN, consistently with the result obtained for the TYPE 1 in Mullaney et al. (2013), as shown in Fig. 3.12.

The study of the [OIII] line profile of the individual BPT classes as a function of the location in the SFR-stellar mass plane shows the following aspects:

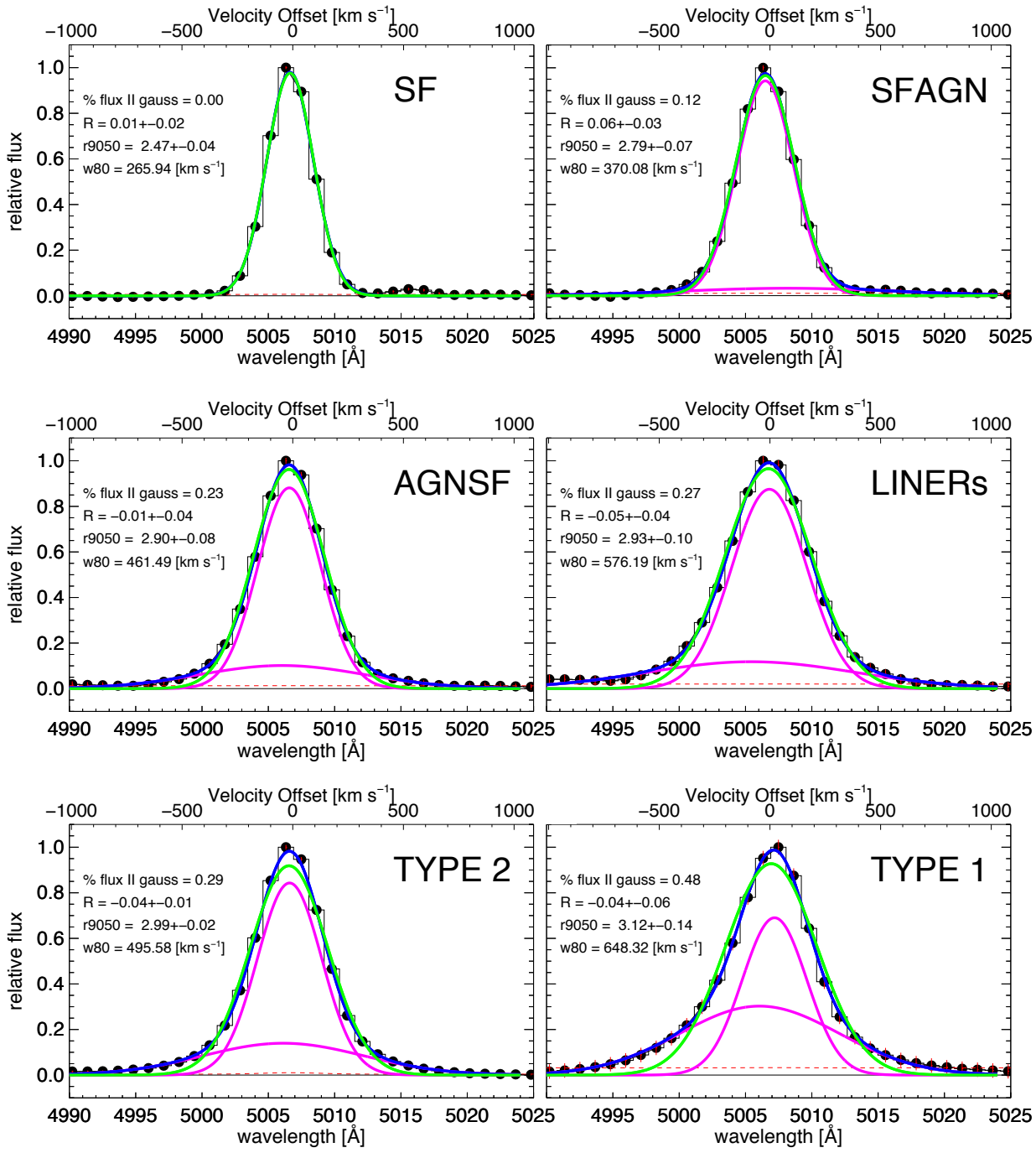


Figure 3.11: Emission-line profile fits to composite spectra in different classes of photoionization processes: SF, SF−AGN, AGN−SF, LINERs, TYPE 2 and TYPE 1. The black symbols are the observed flux. The flux errors, in each point, are shown in red. The green line shows the single-Gaussian fit. The magenta line illustrates the two-Gaussian component and the blue curve shows the combined fit. The level of scatter in the residuals of our fit is shown with the horizontal dashed red lines. The significance of a second broad and blue-shifted component (magenta curves) is remarkably increasing with the increase of the AGN contribution. In each panel we show the derived values of flux enclosed in the second broader Gaussian component, asymmetry $R$, prominence of the line wings $r9050$ and $w80$.

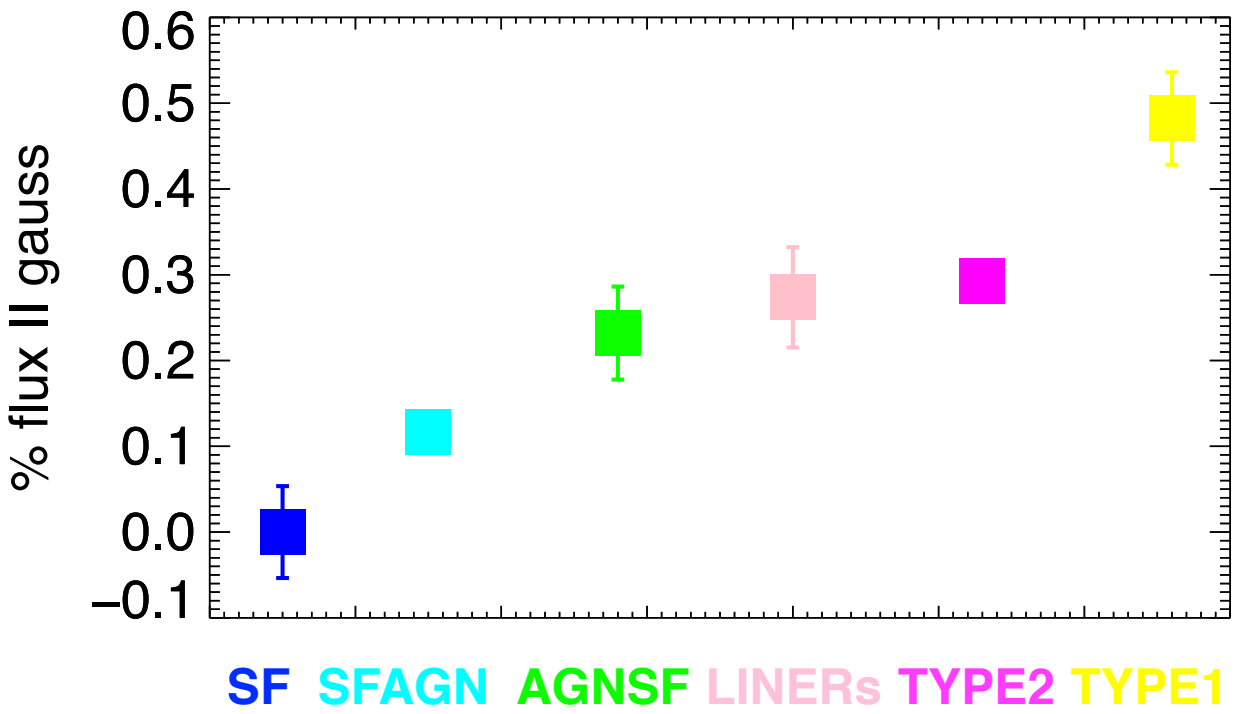


Figure 3.12: Mean values of the flux percentage enclosed in the second Gaussian component for all the BPT classes: SF,SF-AGN, AGN-SF, LINERs, TYPE 2 and TYPE 1. The flux increases with the increase of the AGN contribution. The error bars show the dispersion around the mean values.

- SF galaxies, dominating the MS region up to masses of $10^{10} M_{\odot}$, are characterized by a purely Gaussian [OIII] line profile with no evidence of a second broader component. This is confirmed by the fitting procedure and by the non-parametric method that indicates values of asymmetry and line wings consistent with the Gaussian values within $1.5\sigma$.

- SF galaxies with a small contribution from the central AGN (SF-AGN) show evidence of a second broader component only at the $2\sigma$ level. Such galaxies, as shown in Fig. 3.3, are mainly located in the MS region at stellar masses $> 10^{10} M_{\odot}$.

- galaxies with a dominating AGN contribution (AGN-SF) show evidence of a second broader component at more than $3\sigma$ only on and above the MS.

- LINERs and TYPE2 galaxies show a high SNR ($> 3$) second broader component independently of their location on the SFR-stellar mass plane. We refer to Fig. 3.3 for their distribution in the plane.

- the results are confirmed by the non-parametric method. The analysis of the asymmetry R shows that for the SF object, the line tends to be symmetrical (R$\sim 0$) while in the LINERs and TYPE 2, we observe R$\sim -0.1$, consistent with the results of Zakamska & Greene (2014) for a sample of SDSS obscured quasars.

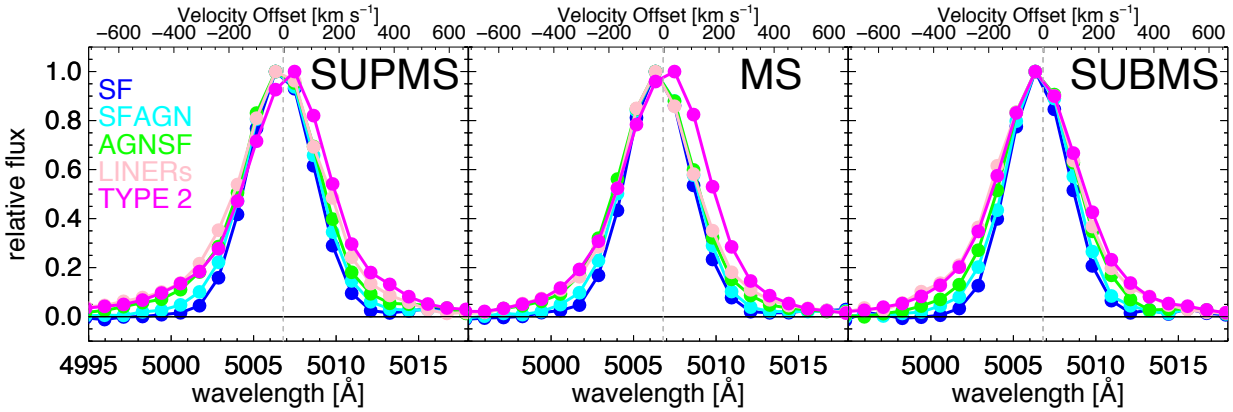


Figure 3.13: Variation of the observed [OIII] emission line profile as a function of the SF and AGN contribution for galaxies located in different SFR bins. In the left, middle, and right panels we show the galaxy bins located above (SUPMS), inside (MS) and below (SUBMS) the MS, respectively, with $\Delta$SFR=0.4, 0.0 and −0.4 dex. The galaxy bins shown have M$\star = 10^{10.5}$ M$\odot$. The [OIII] emission line appears at any M$\star$ and SFR.

An example of the AGN effect on the [OIII] line profile is shown in one mass bin above (left panel), on (central panel) and below (right panel) the MS in Fig. 3.13.

The location of the AGN-SF, LINERs, and TYPE2 AGNs perfectly matches the location of the plane where we observe in the global population a line wings value slightly larger than the Gaussian value. This is also confirmed by the BPT analysis applied to the stacked spectra, as a function of the location in the SFR-stellar mass plane. As shown in Fig. 3.14, SF-AGN are preferentially located at high SFR and stellar masses, while AGN-SF and LINERs dominate the valley between the MS and the quiescent region. Indeed, after removing such galaxies from the global sample, the value of the line wings parameter becomes consistent with the Gaussian value all over the plane. This indicates that the deviation from the pure Gaussian behavior observed in Fig. 3.8 is due to galaxies dominated by the AGN contribution. In turn, this suggests that, if the second broader component is interpreted as an indication of galactic wind, such wind is likely driven by the AGN, while SF does not seem capable of driving any wind at any mass or SFR value.

In order to better compare the [OIII] line width with respect to the galaxy velocity dispersion in the different subclasses, we show in Fig. 3.15 the [OIII] line width measured by the standard deviation $\sigma_{[OIII]}$ as a function of stellar velocity dispersion $\sigma_\star$ for all the ionization classes: SF, SF−AGN, AGN−SF, LINERs, and TYPE 2. Given that the median instrumental resolution of SDSS spectra is $\sim$ 70 km s$^{-1}$ we restrict the analysis to the bins with $\sigma_\star$ above this limit. For clarity, we collect our $\sigma_{[OIII]}$ values in bins of $\sigma_\star$, with $\Delta\sigma_\star = 20$ km s$^{-1}$. The different ionization sources are indicated with different colors as labeled in the figure. At fixed $\sigma_\star$, we find that the velocity dispersions measured for the ionized gas increases with the increase of the AGN activity from the 'pure' SF to the TYPE 2 galaxies.

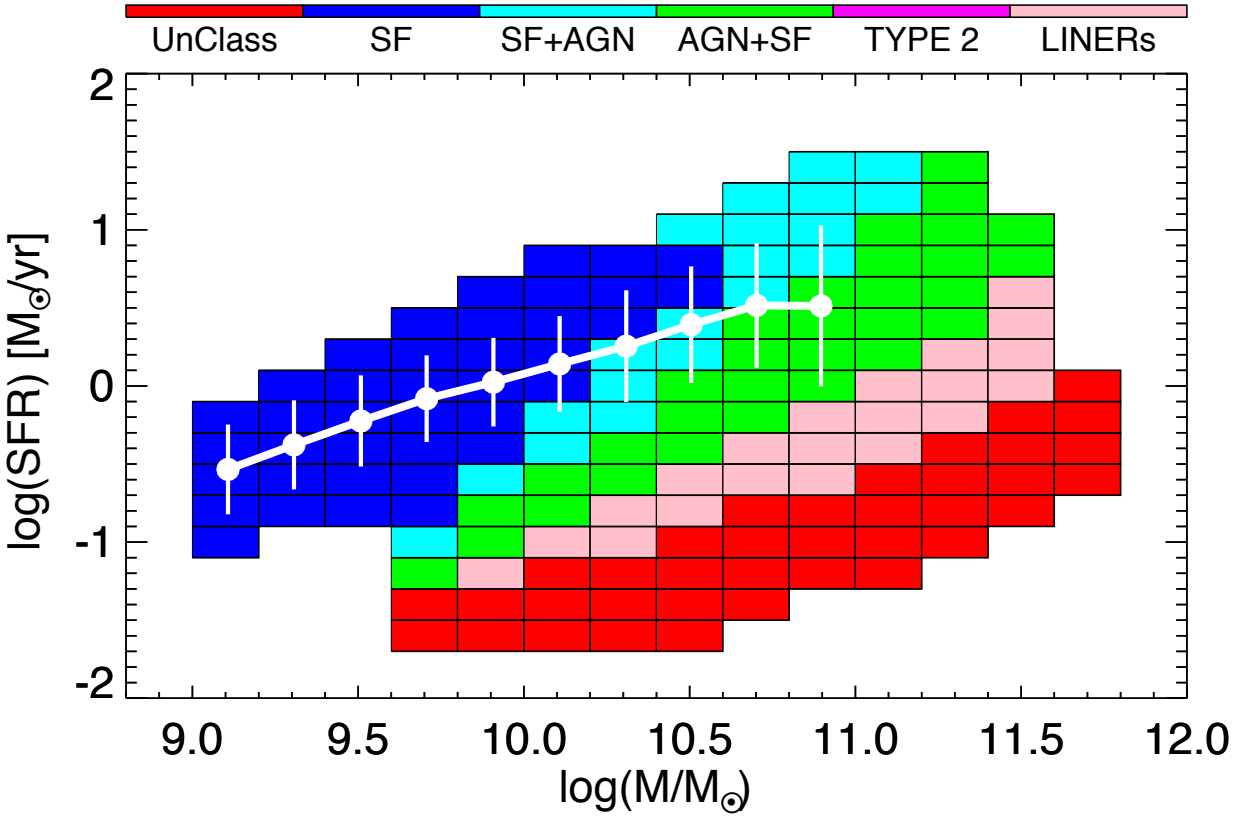


Figure 3.14: BPT classification for the total sample in the SFR−M⋆ plane.

As mentioned in section 3.3.3, the unClass subsample includes a large amount of galaxies (53.5% of the total sample) that are impossible to classify individually using the BPT diagram. In order to take into account this large fraction of galaxies, we decided to perform the BPT analysis in the median stacked spectra. Following the approach of Concas et al. in prep. we used a combination of the publicly available codes pPXF (Cappellari & Emsellem, 2004) and GANDALF (Sarzi et al., 2006) to fit and remove the stellar continuum and to derive emission line fluxes of the four emission lines used in the BPT diagram (i.e., H$\beta$, [OIII]$\lambda$5007, [NII], H$\alpha$). As expected, the majority of the stacked spectra show very weak emission lines. These galaxies are mainly located in the so-called quiescent region as shown in Fig.3.3. At higher SFR values, all the unClass stacked spectra show all the four emission lines (H$\beta$, [OIII]$\lambda$5007, [NII] and H$\alpha$) with S/N$>$ 4 to classify them in the BPT diagram. We verified that these galaxies follow the same trend shown by the rest of the sample. The prominence of the second broader component increases in parallel to an increase of the nuclear activity contribution, as we can see by the increase of velocity dispersion of the ionized gas with respect to the increase of AGN activity at any stellar velocity dispersion (see triangles in Fig.3.15).

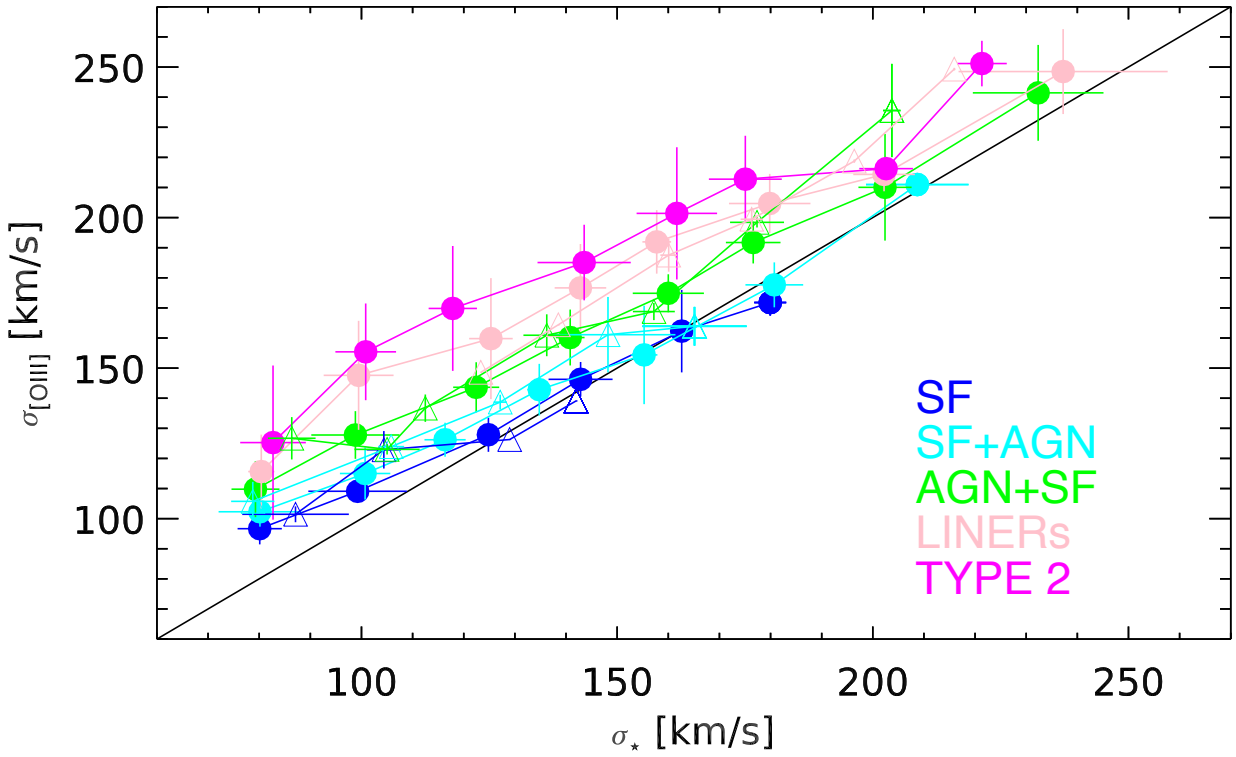


Figure 3.15: $\sigma_{[OIII]}$ plotted against $\sigma_\star$ MPA-JHU mean values for the five ionization classes (SF, SF−AGN, AGN−SF, LINERs and TYPE 2). We show the median and dispersion values of $\sigma_{[OIII]}$ and $\sigma_\star$ in bins of $\sigma_\star$, with $\Delta\sigma_\star = 20$ km s$^{-1}$. Filled symbols are the objects in the main SF, SF−AGN, AGN−SF, LINERs, and TYPE 2 subsamples. Open triangles are the unClass objects. The solid black line denotes $\sigma_{[OIII]} = \sigma_\star$.

## 3.6 Discussion and conclusions

In this work we investigate the presence of galactic winds in a large spectroscopic sample of $\sim 600,000$ local galaxies drawn from the spectroscopic SDSS DR7 database. In particular, we use the deviation of the forbidden [OIII]$\lambda$5007 emission line profile from a Gaussian as a proxy for the galactic winds. We use the spectral stacking technique to increase the SNR of the spectra and to determine how the average [OIII]$\lambda$5007 profile changes as a function of the key galaxy physical parameters, such as SFR and M$\star$. We also explore how the line profiles relate to the particular photoionization mechanisms: SF or AGN activity. We analyze the oxygen emission line profile by performing a line fit and a non-parametric analysis. Our main results can be summarized as follows:

- In the global galaxy population, we find no evidence of a second Gaussian broader component in most of the SFR-stellar mass plane. A marginal detection, at the $\sim 2\sigma$ level, is obtained only at stellar masses $> 10^{10.5} M_\odot$ in a large range of SFR. This is confirmed by the observation of a line width parameter slightly larger (again at the $\sim 2\sigma$ level) than the value predicted for a pure Gaussian line profile in the same

region of the plane. The line profile appears to be always symmetric, even when a second broader component might contribute. The flux percentage enclosed in the broader component, when detected, is approximately 10% in most of the plane and reaches values of 20-25% at very high masses and SFR and in the valley between the MS and the quiescent region.

- The comparison of the line width of the [OIII] with the velocity dispersion obtained from the absorption stellar features reveals a good agreement in most of the plane, indicating that the [OIII] traces the underlying galaxy potential well as the stellar component. Only in few very low SFR and stellar mass bins do we observed a disagreement, that we ascribe to spectral resolution issues and differences in the stellar and gas kinematics in purely disk galaxies.

- The analysis of the [OIII] line profile as a function of the BPT classification reveals that for the "pure" SF galaxies, the ionized interstellar gas traced by the [OIII]$\lambda$5007 line never appears to be outflowing. The line profile is perfectly fitted by a single Gaussian without need for a second component. This holds in all the regions of the SFR-stellar mass plane dominated by SF galaxies, such as the MS.

- The significance of a second broader Gaussian component increases with a clear trend with the increase of the AGN contribution to the galaxy spectrum, with a maximum for the AGN TYPE1 of Mullaney et al. (2013). The flux enclosed in the second component rises steadily from 0% in pure SF galaxies to $\sim$48% in the TYPE1 AGNs.

- The analysis of the [OIII] line profile of each BPT class in the SFR-stellar mass diagram shows that galaxies with an increasing AGN contribution occupy preferentially the region of the diagram where the global population shows a marginal deviation from the Gaussian line profile: at high mass and SFR and in the valley between the MS and the quiescent region. If AGN hosts are removed from the global sample, such deviations disappear in any locus of the SFR-stellar mass digram. The preferential location of AGN hosts, distinguished in different BPT classes, is also analyzed by performing the BPT analysis on the stacked spectra. We clearly observe a preferential location of galaxies in the diagram as a function of their nuclear activity. In particular, SF-AGN galaxies occupy the region at high stellar mass and SFR, while AGN-SF and LINERs are located preferentially in the valley between the MS and the quiescent region.

- The comparison of the velocity dispersion obtained from the [OIII] line width with the velocity dispersion derived from the absorption features imprinted by the stellar component shows that the ionized gas traces the galaxy potential well as the stellar component for the pure SF galaxies. The ratio between the two velocity dispersions increases with the increase of the AGN contribution at any bin of stellar velocity dispersion. This, once again, confirms the role of the AGN contribution in leading to a larger [OIII] line width, and so to the presence of winds, independently of the galaxy mass or SFR.

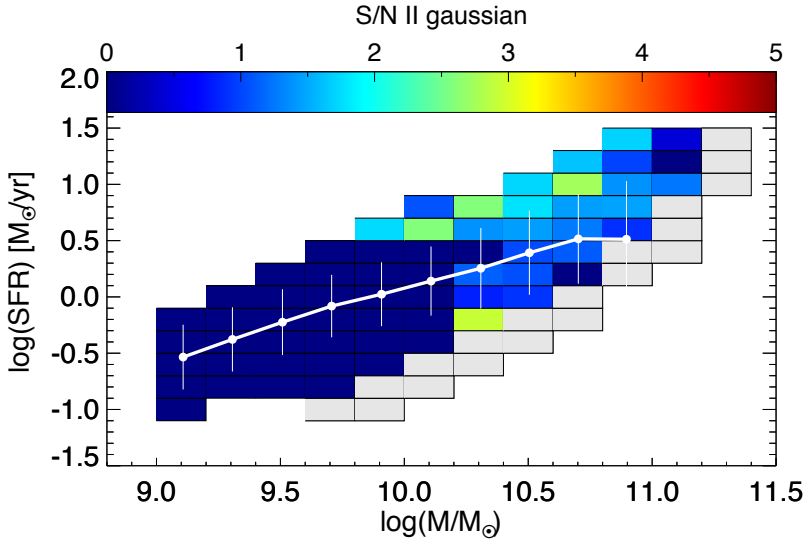


Figure 3.16: SNR of the second broader Gaussian component for the "HII" galaxy sample in the SFR-M$\star$ diagram. The white line shows the mode and dispersion of the MS. At high SFR and M$\star$ the SNR shows a slight increase. The galaxy bins with total emission line SNR $< 8$ are plotted in gray.

Our results clearly indicate that, when using the low-density ionized gas emission lines as wind indicators, the SF activity itself, in the local Universe, is not capable of driving galactic winds at any value of the instantaneous SF rate or stellar mass. We point out that this outcome is not directly in disagreement with previous findings of outflow signatures in SF galaxies with much higher levels of SF activity, as ULIRGS or high redshift MS star forming galaxies (e.g., Heckman et al., 1990; Pettini et al., 2000; Shapley et al., 2003; Rupke et al., 2002, 2005a,b; Martin, 2005, 2006; Hill & Zakamska, 2014). Indeed, such systems exhibit SFR level at least one order of magnitude higher than the level of activity in the local average star forming galaxies. Thus, we cannot exclude that star formation might be capable of driving outflow when feedback is sufficiently energetic to induce motion. Our results indicate, however, that, at the level of activity observed in the local Universe, SF feedback is not capable of inducing significant gas bulk motions. A direct comparison with a similar sample of galaxies at higher redshift, and so with a higher level of SF activity, must be carried out to determine the SF threshold, above which SF might eventually lead to systematic galactic winds.

This result, however, contrasts the findings of Cicone et al. (2016), who detect signatures of ionized outflows in local SDSS star forming galaxies at high SFR. They also find an increase of the line width with increasing SFR at fixed mass, and interpret this as evidence of SF driven outflow. We ascribe such discrepancy to the differences in the sample selection. Cicone et al. (2016) analyze a sample of $\sim 160,000$ local star forming galaxies classified in the BPT diagram according to Kauffmann et al. (2003b). As shown in Stasinska et al. (2006), these selection criteria may introduce a significant bias in the SF galaxy sample, due to the inclusion of a large percentage of systems with an AGN contribution. This

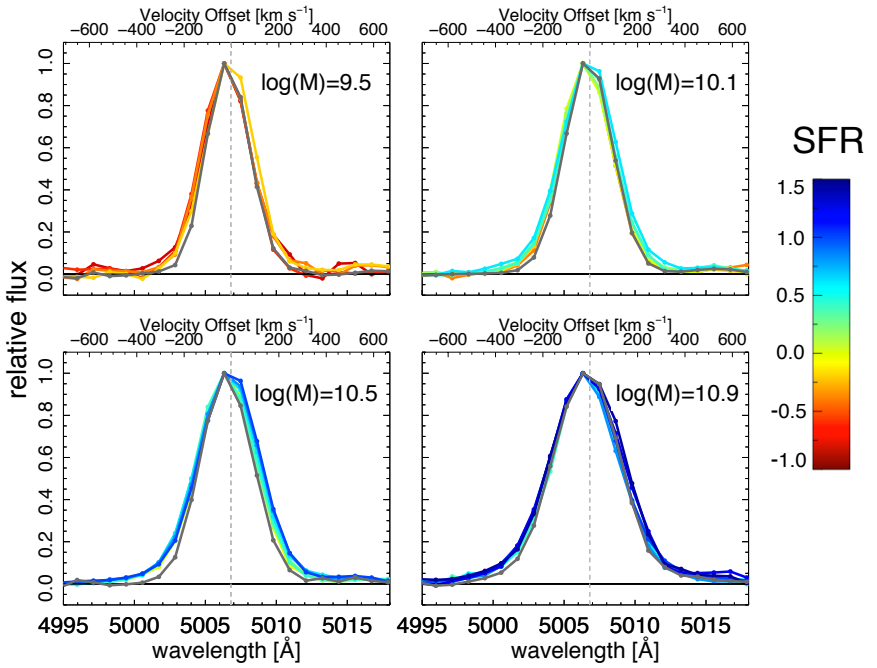


Figure 3.17: Comparison in four different stellar mass bins of the observed [OIII] line profile of pure SF (gray curves) and SF-AGN galaxies (color curves) in the HII sample, classified according to the BPT classification of Stasinska et al. (2006). The line profile of the pure SF galaxies does not change as a function of the SF level. For this reason, in each mass bin, we only show a single curve concerning one level of SFR. The line profile of the SF-AGN galaxies tends to increase in width at increasing SFR as indicated by the several curves color-coded as a function of the SFR.

effect may be particularly strong at high SFRs where the number of composite SF−AGN is high. In order to investigate this issue, we perform our analysis on the "HII"' sample of star forming galaxies as defined in Cicone et al. (2016). As Cicone et al. (2016), we do not find any significant broad second Gaussian component for the galaxies located at low SFR and M⋆, while we note a weak increase of this second component ($\sim 10\%$ of the total line flux, $\sim 2\ \sigma$ level) at SFR$\geq 1\ M_{\odot}/yr$ and stellar masses M⋆ $\geq 10^{10} M_{\odot}$ (Fig. 3.16). However, by classifying the Cicone et al. (2016) "HII" sample with the Stasinska et al. (2006) BPT classification, as done for our sample, we see (Fig. 3.17) that

- pure SF galaxies consistently show a pure Gaussian profile with constant width at fixed stellar mass;
- SF−AGN galaxies show a more prominent second Gaussian component, although of low significance ($< 2\sigma$), a larger width with respect to pure SF galaxies of the same mass and SFR, and an increase of the width with increasing SFR at fixed stellar mass.

We, thus, conclude that the effect observed by Cicone et al. (2016) is likely due to the contamination by systems with an AGN contribution. The larger width of the [OIII]

profile at high SFR in such galaxies could be due to availability of a large quantity of cold gas, which favors at the same time the SF activity and accretion onto the central black hole, eventually leading to stronger BH feedback. We also point out that the transition between pure SF galaxies and AGN-contaminated galaxies takes place in the region of the diagram that starts to be dominated by bulgier sources (see central panel of Fig. 3.10). This is a further indication that the central activity might be a bias in the analysis performed by Cicone et al. (2016).

Our results confirm the role of AGN feedback in leading to galactic wind, at least of ionized gas, in the local Universe. This result is in agreement with many recent findings in a large redshift window. At low redshift, we find very good agreement with the results of Mullaney et al. (2013), that observe a prominent blueshifted and broader Gaussian component in addition to the systemic one for TYPE 1 and TYPE 2 AGNs. Our analysis extends this result to a lower level of nuclear activity also. While the use of the fiber SDSS spectra does not allow us to have any spatial information on the origin and the location of the wind, by using the optical integral field unit (IFU) observations of sixteen TYPE 2 AGN selected from the Mullaney et al. (2013) parent sample. Harrison et al. (2014) demonstrate that this particular [OIII] emission line feature is due to the kiloparsec scale outflows, extended over $\geq 6 - 16$ kpc.

At higher redshift, Harrison et al. (2016) find a high prevalence of extreme ionized gas velocities in high-luminosity X-ray AGN. Moreover, Brusa et al. (2015) and Cresci et al. (2015) show that in X-ray-bright AGN, the nuclear activity can lead to very powerful winds, of the order of $\sim 1000$ km s$^{-1}$, also in the molecular gas.

We point out that, on average, we do not observe such large velocity shift or line width. The observed average velocity shift with respect to the systemic redshift is below the SDSS instrumental resolution $\Delta V < 70$ km s$^{-1}$, and the line width of the second Gaussian component is only of the order of 350-400 km s$^{-1}$ also in the BPT classes, which include an AGN contribution. Thus, rather than galactic wind, the overall population of AGN hosts in the local Universe undergo a phase of light "breeze". This difference might arise for two reasons: a) Bright X-ray AGNs are rare objects in the local Universe, thus, the average velocity shift and line width is dominated by sources with a lower level of nuclear activity and feedback; b) we are observing a final phase of the wind, which was more powerful in the past due to the higher nuclear activity of the central AGN.

Since the AGN hosts are located in the high-mass region of the SFR-stellar mass diagram at stellar masses M$\star \geq 10^{10.5} M_{\odot}$, and are thus likely to be in dark matter halos larger than $10^{12-12.5} M_{\odot}$, such velocities are at least one order of magnitude lower than the escape velocity from the galaxy. Therefore, the gas entrained in the wind is very unlikely to be capable of escaping the galaxy potential well.

Thus, we conclude that, through the identification of strong bulk motion as traced by the warm ionized gas, at least in the local Universe, the AGN activity is likely the only mechanism capable of driving galactic winds. However, given the velocity of such winds, the gas in this scenario is not capable of escaping from the galaxy and thus affecting the galaxy gas content and SF activity.

# Chapter 4

# Neutral gas winds in the local Universe

*This chapter is adapted from Concas et al. 2018a, submitted to A&A, under review.*

## 4.1 Abstract

We present a comprehensive study of the interstellar NaI $\lambda$5890, 5895 (NaD) resonant lines in a complete spectroscopic sample of$\sim 600,000$ galaxies drawn from Sloan Digital Sky Survey (SDSS, DR7) in order to look for cold-gas outflows in the local Universe. This is the first time that doppler blue-shifts of the NaD absorption feature have been investigated as a tracer of cold gas kinematics (T $<$ 1000 K) with a statistically significant sample that includes passive, star-forming and starburst galaxies. Individual galaxy spectra are stacked in bins of stellar mass (M$\star$) and star formation rate (SFR) and the dependence of galactic winds, with respect to the galaxies position in the SFR-M$\star$ plane is investigated. While in most cases the interstellar medium (ISM) absorption and emission lines are fixed at the galaxy systemic velocity, at the higher SFR tail (SFR$> 12.5 M_{\odot} yr^{-1}$), we find evidence of blue-shifted NaD absorption profiles (by more than instrumental resolution, 70 km s$^{-1}$), which we interpret as evidence of neutral outflowing gas. We explore the properties of the ISM in these galaxies with high SFR, in particular relating the absorption NaD line shape with the galaxy geometry in galaxies with different ionisation mechanisms: Active Galactic Nuclei (AGN) and star-formation. We find that: a) the ISM NaD absorption lines show a clear transition from a strong disk-like component, perfectly centered to the systemic velocity, in the edge-on systems (inclination $i > 50^{\circ}$ of the disk rotation axis), to an outflow, blue-shifted, component in face-on galaxies ($i < 50^{\circ}$); b) these trends are observed in galaxies classified as "purely" star-forming and AGN dominated objects. In addition to this, we compare the kinematics of the neutral gas with the kinematics of the ionized gas as traced by the [OIII]$\lambda$5007 emission lines. We find that, in these high SFR galaxies, the perturbations of the [OIII] emission line are present only in AGN or composite AGN/star-forming systems, consistent with Concas et al. (2017) (see Chapter 3). In our

AGN sample, the presence of the oxygen line perturbation is independent to the stellar disk inclination: in both the face-on and edge-on systems, the velocity associated with the broad and blue-shifted Gaussian component is $\sim 125 \pm 45$ km/s, velocity dispersion of $\sim 460 \pm 30$ km/s and a mean maximum velocity of $\sim -1042 \pm 106$ km/s. In conclusion, we find that, in the local Universe, galactic winds show two faces which are related to two different ejection mechanisms, namely the neutral outflowing gas phase related to the star formation rate along the galaxy disk and the ionized winds related to the AGN feedback.

## 4.2 Introduction

As fully described in Chapter 1, in the past 10 Gyr, after a phase of high and rather constant star formation activity, the Universe has undergone a drastic decline in the star formation activity of the galaxy stellar population by almost an order of magnitude (e.g. Lilly et al., 1996; Madau et al., 1998; Madau & Dickinson, 2014, for a comprehensive review). The physical mechanisms that removes gas from a galaxy and/or prevent gas from condensing into new stars, commonly known as quenching mechanisms, are not yet fully understood. Unmasking the identity of the quenching processes is key to advancing our understanding of how galaxies form and evolve in the cosmic time.

The most accredited galaxy formation models indicate that, in central galaxies, defined as the most luminous and massive galaxies in the dark matter halo, the efficiency of converting the gas reservoir into stars reaches a maximum at dark matter halo masses $\sim 10^{12}$ $M_\odot$ (see for example Croton et al., 2006; Guo et al., 2011 based on the Millennium Simulation, and Moster et al., 2010; Behroozi et al., 2010; Yang et al., 2012 among the mass abundance matching models). Galaxies with both lower and higher mass than this mass threshold are less efficient at forming stars (e.g. Madau et al., 1996; Baldry et al., 2008; Conroy & Wechsler, 2009; Guo et al., 2010; Moster et al., 2010, 2013; Behroozi et al., 2010, 2013). Below halo masses of $10^{12}$ $M_\odot$, the theoretical models predict that the decrease in efficiency of converting gas into stars is due to the formation and evolution of massive stars. A combination of effects such as supernovae explosions and stellar winds in actively star-forming regions, can remove the gas from the galaxy via large-scale outflows (see Chevalier, 1977, Murray et al., 2005b and Hopkins et al., 2014 respectively for energy-driven outflows, momentum-driven outflows and for effect of multiple stellar feedback in cosmological simulations).

At high masses (halo masses $> 10^{12}$ $M_\odot$), the deeper galaxy potential well requires more energetic sources to expel the gas from the galaxy. In most massive galaxies, the energetics generated by the growth of the massive central black hole (BH) exceeds the binding energy of the gas by a large factor (see Fabian, 2012 for a complete review). Therefore, energetic feedback from active galactic nuclei (AGN) is believed to provide an effective mechanism to eject the gas away from the galaxy via powerful winds, which suppress the star formation through lack of fuel (Di Matteo et al., 2005; De Lucia et al., 2006; Croton et al., 2006; Hopkins et al., 2006; Bower et al., 2006; Hopkins et al., 2014; Henriques et al., 2017). However, despite the ability of these models in predicting a large variety of observational

evidence, such as the evolution of the stellar mass function (e.g. Henriques et al., 2017), a clear consensus regarding which kind of feedback processes dominate as a function of luminosity and cosmic epoch is poignantly lacking. Over the past 20 years, several efforts have been made to observe the presence of such winds at different redshift and mass scales, and to study their effect on the evolution of the host galaxy.

Galactic SF-induced outflows are believed to be "ubiquitous" in highly active star-forming galaxies at all cosmic epochs (see Veilleux et al., 2005 and Erb, 2015 for a comprehensive overview), usually associated with energetic starburst phenomena (e.g. Heckman et al., 1990; Pettini et al., 2000; Shapley et al., 2003; Rupke et al., 2002, 2005a,b; Martin, 2005, 2006; Steidel et al., 2010; Hill & Zakamska, 2014). Yet, their effect on normal star-forming galaxies (Chen et al., 2010; Martin et al., 2012a; Rubin et al., 2014) and their global impact on the baryon cycle is still hotly debated (Steidel et al., 2010).

Energetic outflows driven by AGN winds are observed at low (e.g. Feruglio et al., 2010; Villar-Martín et al., 2011; Rupke & Veilleux, 2011, 2013; Greene et al., 2012; Mullaney et al., 2013; Rodríguez Zaurín et al., 2013; Concas et al., 2017) and high redshift (e.g. Maiolino et al., 2012; Tremonti et al., 2007; Brusa et al., 2015; Perna et al., 2015; Cresci et al., 2015). Despite the increasing number of these observational evidence, it is still difficult to establish which AGN properties is driving the outflow and what is the effect on the host properties and evolution (e.g. Mullaney et al., 2013; Brusa et al., 2015). In addition, it is not clear yet if the AGN feedback can enhance ("positive feedback") or quench ("negative feedback") the SF activity of the host galaxy (e.g. Cresci et al., 2015; Maiolino et al., 2017 and Harrison, 2017, for a review).

Most observational evidence, for both SF and AGN induced outflows, have been based so far on relatively small samples of particular category of galaxies (e.g. Greene & Ho, 2005; Mullaney et al., 2013 for optically-selected AGN, Chen et al., 2010 for star-forming galaxies without AGN contribution) leading to strong selection biases. As a first attempt to perform such study in an unbiased sample, in Concas et al. (2017), we use the Sloan Digital Sky Survey (SDSS; Abazajian et al., 2009) spectra to investigate the incidence of outflows as ionized gas in the SFR-$M_\star$ plane (see Chapter 3). Such analysis shows that the [OIII] emission line profile does not exhibit any signature of outflow in normal SF galaxies. Instead, the outflow signature becomes more and more prominent with the incidence of the AGN contribution.

It is now well established that the galactic winds are complex multi-phase phenomena, observed in neutral, ionized, and molecular gas phase in both SFGs (e.g. Heckman et al., 1990; Pettini et al., 2000; Shapley et al., 2003; Veilleux et al., 2005; Rupke et al., 2005a,b; Chen et al., 2010; Martin et al., 2012a; Rubin et al., 2014; Bordoloi et al., 2014; Erb, 2015) and AGN dominated objects (e.g. Rupke et al., 2005c; Förster Schreiber et al., 2014; Feruglio et al., 2010, 2015; Sturm et al., 2011; Harrison et al., 2014; Cimatti et al., 2013; Liu et al., 2013; Villar-Martín et al., 2011; Zakamska & Greene, 2014; Genzel et al., 2014; Perna et al., 2017b; Brusa et al., 2015, 2016; Talia et al., 2017; Concas et al., 2017). However, there is no general framework capable to explain the relations between the different wind phases and their respective statistical incidents. In a recent work, Rupke et al. (2017), by studying a sample of 10 nearby Type 1 quasars, showed that only 70% have ionized

outflows, 80% have neutral outflows, and 50% have both, while Perna et al. (2017b) found a completely different incidence rate for 563 less luminous AGNs at z< 0.8 (Type 1 and 2 sources). The authors show that only 40% of the sample exhibit signatures of ionized outflows and signatures of neutral outflow are found only in one target (< 1% of the sample). It is important, therefore, to investigate the incidence of the different winds phases, their correlations and the dependence of the outflow properties as a function of different galaxy properties in an unbiased and statistical sample.
In this chapter, by using a large sample of optical spectra at redshift $z < 0.3$, drawn from the SDSS, we extend the analysis of the ionized gas wind showed in Chapter 3 (and Concas et al. (2017)) by exploring the main kinematic proprieties of the *neutral* interstellar medium (ISM). Specifically, we focus on the study of the interstellar neutral gas as traced by the NaI $\lambda$5890, 5895 (NaD) resonant lines, which provide an unambiguous wind signature of blue-shifted absorbing material in front of the continuum source (e.g. Heckman et al., 2000; Rupke et al., 2002, 2005a,b,c; Schwartz & Martin, 2004; Martin, 2005; Rupke & Veilleux, 2015; Cazzoli et al., 2016; Rupke et al., 2017). Our main goal is to characterize the kinematics of the neutral outflows and investigate 1) how they are related to the host galaxy properties, such as SFR, stellar mass and galaxy geometry, 2) identify the main triggering mechanism: star formation, AGN or a mixed contribution of the two effects, and 3) explore if there is a difference between this cool neutral gas and the warmer ISM tracer by the [OIII]$\lambda$5007 emission line in the same galaxies.

This chapter is organized as follows. Firstly, we describe our sample selection and physical properties in Section 4.3. The details of the method of creating stacked spectra and measuring the NaD line profile are described in Section 4.4. We present and discuss the main results in Section 4.5 and finally we summarize our findings in Section 4.6. Throughout this chapter, we adopt the following $\Lambda$CDM cosmology with $H_0 = 70$ km s$^{-1}$ Mpc$^{-1}$, $\Omega_M = 0.3$ and $\Omega_\Lambda = 0.7$

## 4.3 The Data

As fully described in Chapter 2, the dataset used in the present study is based on the Sloan Digital Sky Survey, (SDSS, York et al., 2000) spectroscopic catalog, data release 7 (DR7, Abazajian et al., 2009). In particular, we analyze objects drawn from the Main Galaxy Sample (MGS, Strauss et al., 2002) which have Petrosian magnitude $r < 17.77$ and redshift distribution spanning $0.005 < z < 0.30$. The spectra are obtained with $3''$ diameter fibers, that cover a wavelength range from $3800 < \mathring{A} < 9200$, with an instrumental resolution of $R \equiv \lambda/\delta\lambda \sim 1850 - 2200$ and a mean dispersion of 69 km s$^{-1}$ pixel$^{-1}$. See http://www.sdss.org/dr7/ for more exhaustive details concerning the DR7 spectra.

Throughout this chapter, we make use of the $M\star$ and SFR measurements taken from the MPA-JHU catalogue [1]. Briefly, the stellar masses were estimated by fitting the broad-

[1] http://www.mpa-garching.mpg.de/SDSS/DR7/

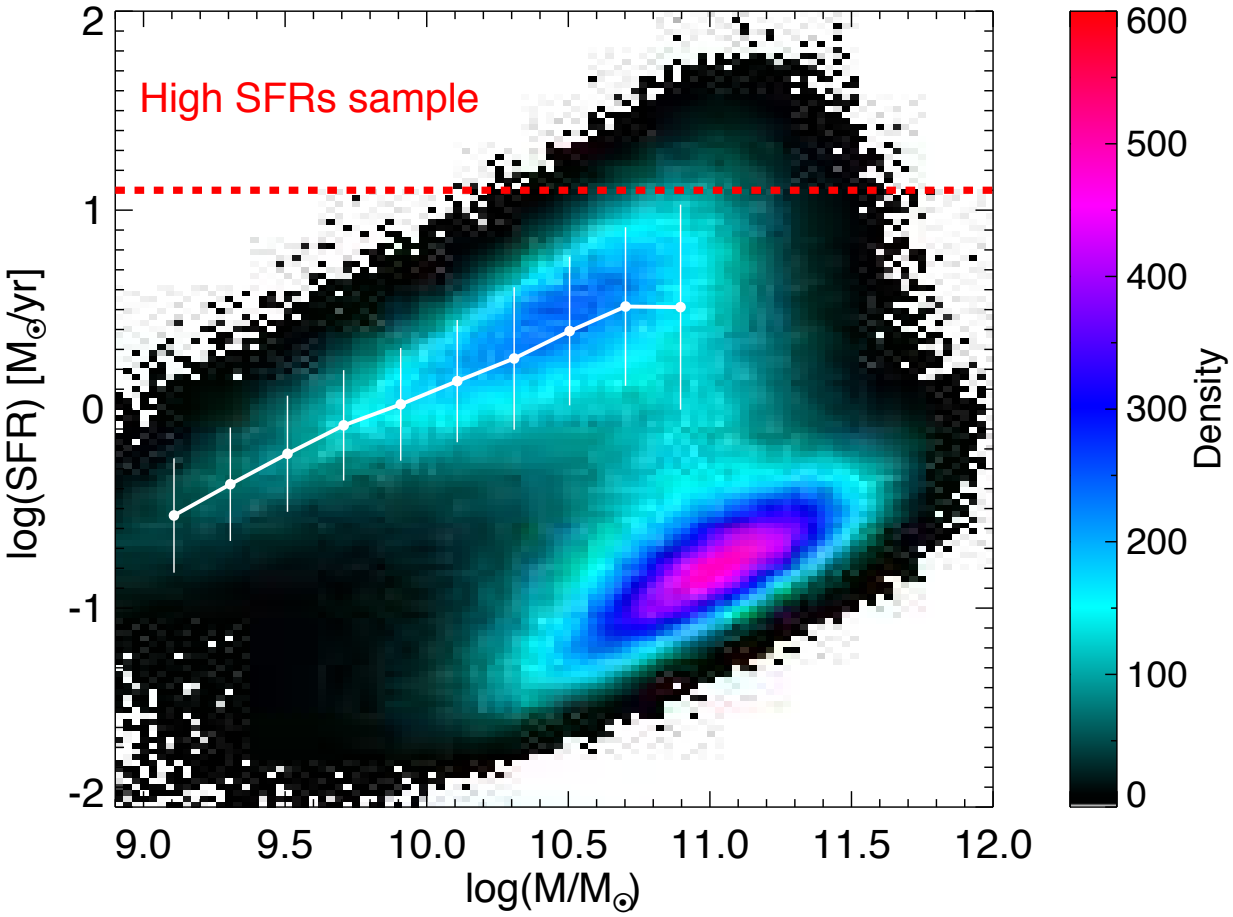


Figure 4.1: SFR-$M\star$ plane for DR7 SDSS galaxies. The white line shows the position of the so-called "Main-Sequence" (MS) of star−forming galaxies. The MS is computed as the mode and the dispersion of the SFR distribution in stellar mass bins following the example of (Renzini & Peng, 2015). The dashed red line divides the galaxies with high SFRs that shows blue-shifted Na D lines.

band optical photometry (Kauffmann et al., 2003a) and the SFR measurements are based on the Brinchmann et al. (2004) procedure. The H$\alpha$ emission line luminosity is used to determine the SFRs for the star forming galaxies and the D4000-SFR relation (e.g. Kauffmann et al., 2003a) for all galaxies that have emission lines contaminated by AGN activity or not measurable emission lines. All SFR measures are corrected for the fiber aperture as described by Salim et al. (2007). We restrict the selection to galaxies with stellar mass $\log(M/M_{\odot}) \geq 9.0$, to limit the incompleteness in the low mass regime. In this way, we ended up with a global sample of $\sim 600000$ galaxies.

The MPA-JHU catalog also includes, for each single spectrum, the flux values of several emission lines. In order to distinguish normal star-forming from AGN dominated galaxies, according with the Baldwin, Phillips, & Terlevich(1981, BPT) diagnostic diagram, we use two optical line ratios: [OIII]$\lambda$5007/H$\beta$ and [NII]$\lambda$6584/H$\alpha$. Following Concas et

al. (2017) we define new galaxy subsamples on the basis of the prevalence of different photoionization processes: SF, SF−AGN, AGN−SF, LINERs and TYPE 2, respectively 20.6%, 7.4%, 11.2%, 5.6% and 1.7% of the total sample (see Chapter 3 for more details). In this chapter the LINERs and TYPE 2 galaxies are classified together as AGN galaxies. All the galaxies with no or very weak emission lines ($S/N < 4$), 53% of the total sample, are not classifiable using the BPT diagram and we call these objects "unClass". However, as is done in Concas et al. (2017), also the "unClass" galaxies are taken into account in our analysis. We refer the reader to Concas et al. (2017) for more details.

Throughout this chapter, we made use of the galaxy structural parameters taken from the bulge/disk decomposition of Simard et al. (2011) catalogue (hereafter, S11). The S11 catalogue provides an estimate of its bulge and disk magnitudes, inclination and the global bulge-to-total flux ratio (B/T) for $\sim 1.12$ million galaxies in the SDSS.
We refer to this sample hereafter as Sample C17, containing $\sim 600,000$ galaxies which corresponds to the galaxy sample presented in Chapter 3 and in Concas et al. (2017, hereafter C17). The galaxy sample is shown in the SFR-stellar mass plane in Fig.6.9. The color code is according to the number density of galaxies per bin of SFR and stellar mass. We overplot also the Main Sequence of star forming galaxies (MS hereafter), estimated as the peak (mode) of the distribution in the star forming galaxy region, similarly to Renzini & Peng (2015).

### 4.3.1 ISM NaD in galaxy spectra

In this work we focus on the NaI doublet at $\lambda\lambda$5890,5896 Å resonant lines in the rest-frame optical galaxy spectra. As fully described in Chapter 1, this radiative transition arises from the neutral sodium atoms at temperatures T < 1000 K. The transition which gives rise to the doublet is from the ground-state configuration 3s to the energy levels of the 3p configuration composed by two states with total angular momentum j=3/2 and j=1/2 (spin-orbit effect). The continuum photons emitted by the stellar component are absorbed by the NaI atoms and are re-emitted when the electrons in the 3p configuration decay spontaneously to the ground-state. As a resonant line, the NaI doublet can be observed both in absorption and in emission.

To increase the low signal-to-noise ratio (SNR) of the NaD in the SDSS spectra, we apply a stacking procedure. However, due to the resonant nature of the NaD, absorption and emission can mix up in the stacking with the effect of compensating each or biasing the result. Thus, we first perform here an analysis of the distribution of NaD in absorption and emission in the SFR-$M\star$ plane to define the correct criteria for the stacking analysis.

It is now generally recognised that more than one process causes the formation of this sodium doublet in a galaxy spectrum, including 1) the absorption and re-emission of stellar radiation by the ISM as well as 2) the absorption of radiation produced in the stellar interiors by the most external gas layers (stellar contribution). Often the stellar absorption contribution can be very prominent, especially in the spectrum of cold stars (e. g. Rupke et al., 2005a; Chen et al., 2010). Before exploring the distribution of the ISM Na D of the single galaxy spectra, in the SFR-$M\star$ diagram we need to take into account

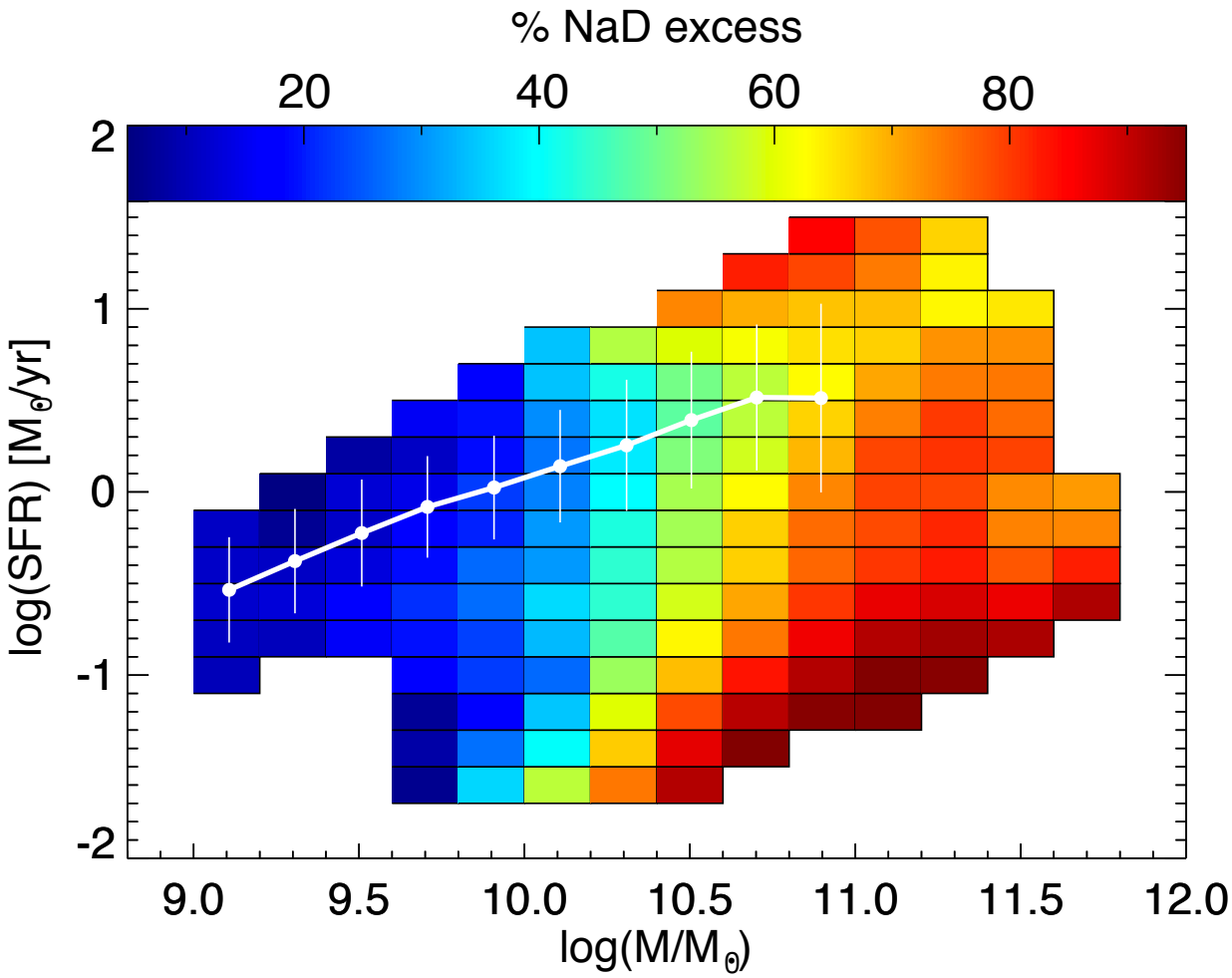


Figure 4.2: Percentage of the Na D excess (Na $D_{obs}$ > Na $D_{mod}$) objects, in the SFR-M⋆ diagram for the singles Na D measurements of MPA-JHU catalog (only object with SNR > 2 in the single observed Na D Lick measurements). The Na D excess objects dominate the high M⋆ region, while the number of the Na D deficiency (Na $D_{obs}$ < Na $D_{mod}$) galaxies increases at low stellar masses. The white line shows the mode and dispersion of the MS.

the stellar contribution. We did this preliminary check by using the informations provided in the MPA-JHU catalog[2], which furnish a measure of the Na D absorption-line strength parametrised by the Na D Lick index (as defined in Worthey et al., 1994). The catalogue include measurements of the Na D Lick index performed directly in the low signal to noise single spectrum, Na $D_{obs}$ and the respective error, Na $D_{obs\_err}$. In addition by fitting the observed spectra with a library of synthetic stellar populations templates, based on the population synthesis code of Bruzual & Charlot, 2003, also a best-fit stellar model for each single spectrum is catalogued (see the details of the fit procedure in Tremonti et al., 2004) along with the Lick index measure calculated in the stellar continuum model. By

[2]http://wwwmpa.mpa-garching.mpg.de/SDSS/DR7/SDSS_indx.html

comparing the Na $D_{obs}$ value and the respective synthetic Na $D_{mod}$, we can evaluate the Na D ISM contribution, defined as Na $D_{obs}$ − Na $D_{mod}$ in each single spectrum. In order to be unbiased from spurious results, we perform this preliminary analysis for the objects with an observed Lick index SNR > 2 (Na $D_{obs}$/ Na $D_{obs\_err}$ > 2, only the ∼ 47% of our C17 sample).

In agreement with previous works based in the SDSS galaxy spectra (e.g. Chen et al., 2010, Jeong et al., 2013), we find galaxies with a sodium excess, Na $D_{obs}$ > Na $D_{mod}$ (hereafter Na D excess) and galaxies with a weaker NaD absorption than in the stellar population models, Na $D_{obs}$ < Na $D_{mod}$ (hereafter Na D deficiency).

The distribution of the NaD excess objects in the SFR-$M\star$ plane is reported in Fig.4.2. We find that the two distinct distributions exist in this plane. The percentage of the Na D excess objects is prominent (∼ 80% of the higher SNR in the observed Lick index sample) at high stellar masses, roughly $M\star > 10^{10.5} M_{\odot}$, while at low mass regime, the Na D strength in the observed spectra is globally lower than expected in the stellar best-fit models. The nature of these discrepancies (Na D excess and deficiency) between the observed and theoretical Na D measurements is explored in detail in Section 4.5.

However, the bimodal distribution of the emission and absorption (Na D deficiency and excess, respectively) in our single NaD values allows us to perform the stacking analysis in the SFR-M⋆ plane with the caveat that the central region, at $M\star = 10^{10.5}$ $M_{\odot}$, is the most uncertain. However, at lower and higher masses, only less than 20% percent of contaminants in absorption and emission, respectively, can bias the results.

## 4.4 Method

In this section, we describe how we fit and remove the stellar absorption contribution and ionized emission lines and how we measure the properties of the ISM Na D resonant line in our stacked spectra.

### 4.4.1 Stacked spectra and stellar continuum fit

In order to improve the signal-to-noise ratio (SNR) of our single spectra and, at the same time, to connect the NaD feature to the galaxy properties (SFR, $M\star$, galaxy inclination and main ionization source), we stack together the optical spectra of the C17 Sample in bins of SFR and $M\star$ ($\Delta \log(M/M_{\odot}) = 0.2$ and $\Delta \log(SFR) = 0.2$ dex). Following the approach of C17, we obtain 148 galaxy stacked spectra in the C17 Sample (see the fine grid in Fig. 3.1 in Chapter 3).

We use a combination of the publicly available codes pPXF (Cappellari & Emsellem, 2004) and GANDALF (Sarzi et al., 2006) to find and remove the best fit stellar continuum and then simultaneously fits the nebular emission lines that can affect the Na D region. As in C17 we used the BC03 stellar library (Bruzual & Charlot, 2003) to produce a model of the stellar spectra that matches the observed line-free continuum in the wavelength range $3800 < \lambda < 6900$ Å. Any interstellar medium emission and absorption lines, including NaD,

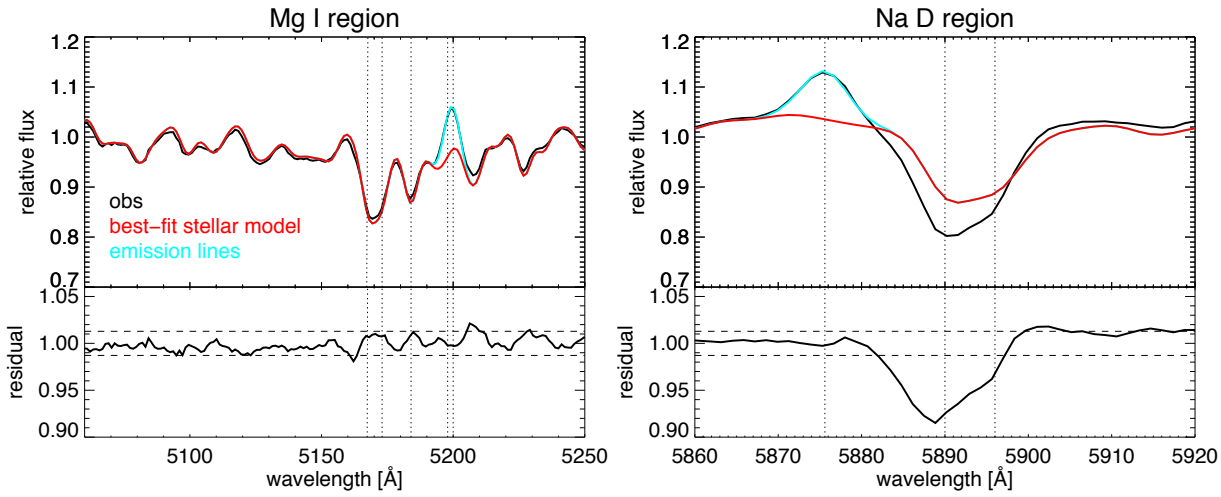


Figure 4.3: Example of our continuum fit and subtraction performed for the stacked spectrum whit SFR= $10^{1.4}$ $M_{\odot}yr^{-1}$ and $M\star = 10^{10.9}$ $M_{\odot}$ in the Mg I and Na D regions, left and right panel respectively. The observed stacked spectrum is shown with a solid black line, the best-fit stellar continuum model in red and the emission lines in cyan. The dotted lines indicate the stellar Mg I triplet at $\lambda\lambda$5167, 5173, 5184 Å the [NI]$\lambda$5198, 5200 Å emission lines, the He I $\lambda$5876 emission and the Na I doublet $\lambda\lambda$5890, 5896. The bottom panels shows the residual spectra (solid black line) and the level of fluctuations in the fit residuals (dashed line). The Mg I region is well reproduced by the stellar fit with residuals lower than the mean scatter. The Na D fit is affected by residuals from a blue-shifted extra absorption Na D component.

are ignored in our fit. Our templates include simple stellar population with ages $0.01 \leq t \leq 14$ Gyr, four different metallicities, $Z/Z_{\odot} = 0.2, 0.4, 1, 2.5$ and assume a Chabrier (2003) initial mass function (IMF).

As an example, Fig 4.3 shows the stellar continuum (red line) and emission line (cyan lines) fit and related subtraction (residuals in bottom panels) performed for one stacked spectrum in the regions near the Mg I (left panel ) and Na D (right panel). From this plot, we infer that our approach provides an excellent fit to the stellar continuum shape and nebular emission lines in the galaxy median spectra. In particular our stellar models are able to reproduce the expected stellar Mg I triplet at $\lambda$5167,5173,5185, which is known to be proportional to the stellar Na I D contribution in galaxy spectra (see Heckman et al., 2000; Rupke et al., 2002, 2005a and references therein); in the Mg I region the residuals are below the mean level of fluctuations in the total fit. The Na D fit is affected by residuals from a blue-shifted extra absorption Na D component.

After this procedure, the entire host stellar continuum and ionized emission lines (in particular the HeI$\lambda$5876 Å) are subtracted from the observed stacked spectrum. This "residual" spectrum (bottom right panel in Fig. 4.3) is used for any analysis of Na D line features. The error of the "residual" spectrum is obtained through bootstrap resampling methods showed in C17.

| subsample | number | percent | N Bins |
|---|---|---|---|
| Sample C17 | 621990 | | 148 |
| Starburst Sample TOT | 15,284 | 100% | |
| SF | 3735 | 24.4% | 1 |
| SF-AGN | 4196 | 27.4% | 1 |
| AGN-SF | 3912 | 25.6% | 1 |
| AGN | 872 | 5.7% | 1 |
| unClass | 2569 | 16.8% | 1 |
| TOT | 8772 | 100% | |
| i=[0-30] | 1684 | 19.2% | 1 |
| i=]30-40] | 1438 | 16.4% | 1 |
| i=]40-50] | 1769 | 20.2% | 1 |
| i=]50-60] | 1779 | 20.3% | 1 |
| i=]60-70[ | 1336 | 15.2% | 1 |
| i=[70-90] | 766 | 8.7% | 1 |

Table 4.1: Basic data about the subsamples discussed in the text. The C17 Sample consists of all the galaxies presented in C17. The galaxies with very high SFRs (SFR$\geq 12.5 M_{\odot}$/yr) are classified as Starburst Sample and split in different bins of ionization source and inclination (i).

### 4.4.2 Measuring the ISM NaD absorption line profiles

In our stacked spectra, the velocity structure of the NaD line is generally complicated; this resonant line shows absorption, emission, or a combination of two contribution across the galaxies physical parameters (as also found in the star forming galaxy spectra showed in Chen et al., 2010 and in the nearby quasars in Rupke & Veilleux, 2015; Rupke et al., 2017). To correctly quantify the centroid velocity and velocity dispersion of the Na D resonant line, a careful treatment of the absorption and emission lines is mandatory. Each stacked spectrum is fit with three distinct models using the IDL MPFIT fitting code.

**Model 1.** The first model, $one - free - doublet$ model, consists of a pair of Gaussians with a single kinematic component (as in previous works, e.g. Davis et al., 2012; Cazzoli et al., 2014, 2016). The four free parameters of the model are the line centroid of the strongest blue absorption in the doublet ($\lambda_1$), the line width ($\sigma_1$), the amplitude of the blue component ($A_{\lambda 5890}$), and the ratio between the amplitudes of the blue and red components ($A_{\lambda 5890}/A_{\lambda 5896} = \alpha$). The central blue wavelength of the Na D doublet (Na D $\lambda$5890), $\lambda_1$ is tied to define a single Doppler shift to respect the galaxy's systemic velocity (defined as the systemic redshift, $\lambda = 5890$ Å), $\Delta V_1$.The ratio between the two amplitudes, is limited to vary between an optically thin $\alpha$=2 and optically thick absorbing gas, $\alpha$=1 (Spitzer, 1978).
This approach allows us to characterise the kinematics of the global observed doublet

without introducing other model dependent parameters. However, some stacked spectra show complex profiles, that suggest the presence of an additional Gaussian pair, in emission or in absorption (e.g. Chen et al., 2010; Cazzoli et al., 2016). This is motivated by two main facts. First, the scattering processes that arise in the flowing material can produce a P Cygni-like profiles of Na D (see the analysis of the absorption and emission-line profiles for the Mg II $\lambda 2796, 2803$ doublet and Fe II multiplet at $\lambda 2600$ Å in cold gas wind models showed in Prochaska et al., 2011), characterized by blue-shifted absorption plus resonance line emission at roughly the systemic velocity.

To model both the P Cygni profile and the interstellar absorption or emission at the systemic velocity, we introduce a second pair of Gaussians at the $one - free - doublet$ model.
In particular we define two new models of double doublets: the $two - free - fix - doublet$ and the $two - free - doublet$, respectively, model 2 and 3.

**Model 2.** The $two - free - fix - doublet$ consist of two gaussian doublets: one fixed to the systemic velocity and one free to varies in the wavelength space. The model is described by: the line centroid of the two doublets ($\lambda_1$ and $\lambda_2$ ), the lines widths ($\sigma_1$ and $\sigma_2$), the amplitudes of the blue lines ($A1_{\lambda 5890}$ and $A2_{\lambda 5890}$) and the ratio $\alpha_1$ and $\alpha_2$. We note that often the $two - free - doublet$ leads to unphysical solutions, since the absorption or emission troughs are not well resolved. In order to not incur in this spurious results, the width of the second pair of Gaussians is constrained to the velocity dispersion of the nebular gas previously fitted to the H$\alpha$ emission line (this is similar to those assumed in previous studies e.g. Cazzoli et al., 2016 and Martin et al., 2012b by using the [OII] doublet). The model describe the observed line with five free parameters. As in the first model the flux ratio ($\alpha_1$ and $\alpha_2$) is set to vary between 1 and 2. The velocity of the outflowing gas is now expressed by the shift of the central blue wavelength ($\lambda_1$), $\Delta V_2$.

**Model 3.** The $two - free - doublet$ is equal to the model 2 but with both the doublets free to vary in the wavelength range (seven free parameters). In this way, also the non systemic red component (in emission or absorption) is well fitted. The blue-shift of the outflowing component is referred to $\Delta V_3$.

To avoid overfitting and allow for the correct number of Gaussian doublets used in each Na D line fit, we employ the the Bayesian Information Criterion (Liddle, 2007): $BIC = \chi^2 + p * \ln(n)$ , where $\chi^2$ is the chi squared of the fit, p is the number of free parameters and n is the number of flux points used in the fit. We measure the BIC value by using the three fitting methods described above, BIC1, BIC2 and BIC3, respectively. The model with the smallest value of the BIC is chosen as the preferred model for the data. We visually inspect each fit to evaluate the success of this procedure. According with this statistical method we use $\Delta V_1$, $\Delta V_2$ and $\Delta V_3$ and $\sigma_1$,$\sigma_2$ and $\sigma_3$ to quantify the blue-shift and the width of the outflowing component.

In order to estimate measurements uncertainties, the observed spectrum is perturbed

randomly accordingly with the observed SNR. We simulate, in this way, 1000 different realizations of the same observed spectrum. Than, we fit the new noisy spectra with our 3 methods. Each quantity ($\Delta V_1$, $\Delta V_2$ , $\Delta V_3$, $\sigma_1$,$\sigma_2$ and $\sigma_3$) is measured on all the new template spectra, the 68% confidence interval is adopted as a measure of the uncertainty.

As in Rupke et al. (2005b), we define a blue-shifted detection only if the difference between the velocity peak and the systemic velocity is $> 70$ km/s (instrumental resolution of our SDSS data). To better parameterize the blue wings of the neutral Na D velocities, we also provide a measure of the maximum velocity, $V_{max} = \Delta V - 2\sigma$ as defined for the absorption Na D component in Rupke & Veilleux (2015).

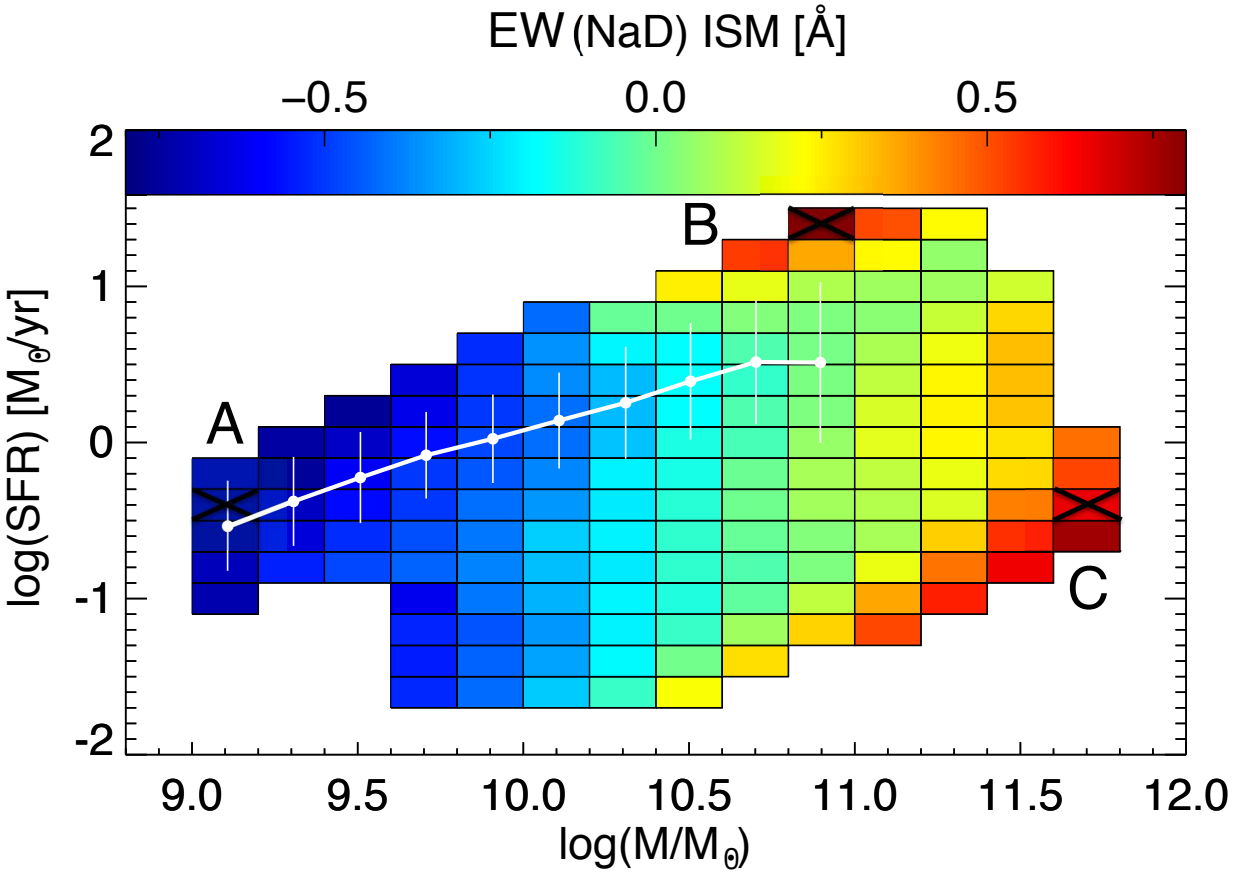


Figure 4.4: EW of the ISM NaD line, obtained after the stellar continuum subtraction, in the SFR-M⋆ diagram for the C17 Sample. Negative EW values correspond to a residual Na D emission, while positive values correspond to an absorption. The white line shows the mode and dispersion of the MS. As a example, we show the NaD line fit in Fig. 5 for the crossed Bins, A, B and C.

# 4.5 Results

## 4.5.1 NaD lines in the global sample

After subtraction of the stellar continuum, we measure the residual equivalent width, EW(NaD), in all the 148 stacked spectra of the C17 Sample. In Fig. 4.4 we show the EW(NaD) obtained for all stacked spectra in the SFR$-M\star$ parameter space. As found for the individual galaxies spectra in Section 4.3.1, we find that, also in the stacked spectra, the SFR-M$\star$ plane is populated by both positive and negative EW(NaD) values, which correspond to residual Na D in absorption and in emission, respectively. In particular, we observe three different regions in the plane in which the NaD shows high absolute EW.

At low stellar masses, $M\star < 10^{10.5}\ M_{\odot}$, we find NaI D in emission, which corresponds to having a more prominent NaD stellar absorption contribution than in the observed spectrum as it is shown in the left top panel of Fig. 4.5. Previous studies have reported the presence of sodium deficiency objects having Na D that are weaker than expected based on stellar population models that match the stellar continuum (e.g., Jeong et al. 2013). By using a similar galaxy subsample of low redshift galaxy, z$<$ 0.08, drawn from the SDSS, Jeong et al. (2013) found that most of their Na D deficient objects exist in local galaxies and are caracterized by strong emission-line in their optical spectra. Example of Na D emission line detection is also presented in few late-type galaxies by Bica & Alloin (1986).

At higher stellar masses, the EW(NaD) increases from negative to positive values (Fig. 4.4), with stronger SNR at very high SFRs and also in the quiescent region. In this high mass regime, in both very high and low SFRs, the observed NaD ISM absorption line shows an excess with respect to the stellar absorption models (positive EW(NaD)values in Fig. 4.4). The trends found are noticeable directly in the observed spectra of the left central and bottom panels of Fig.4.5, see the mismatch between the black observed spectrum and the best fit stellar model (in red).

We applied the Gaussian fit method described in Section 4.4.2 to all the 148 stacked spectra in order to derive the neutral gas kinematics, $\Delta V$ and $\sigma$, according the statistical criteria explained before.

For galaxies located at low stellar masses ($M_{\star} < 10^{10.5} M_{\odot}$) the NaD emission line is centered around the systemic velocity and well within the SDSS instrumental dispersion ($\sim 70$ km s$^{-1}$). An example of the NaD emission and its modelling with a centered sodium doublet is shown in the top right panel of Fig.4.5.

At higher stellar masses (M$\star > 10^{10.5} M_{\odot}$) and lower level of SFR, the residual Na D line shows a deeper absorption component with respect to the stellar contribution (positive values of EW(NaD) in Fig. 4.4). As an example, we report a quiescent stacked spectrum in the bottom left panel of Fig.4.5 (see the difference between the black observed spectrum and the red stellar model). By fitting this absorption extra line, (Fig.4.5 right bottom panel) we find that, also in this case the velocity of the line is consistent with the systemic velocity within the instrumental resolution.

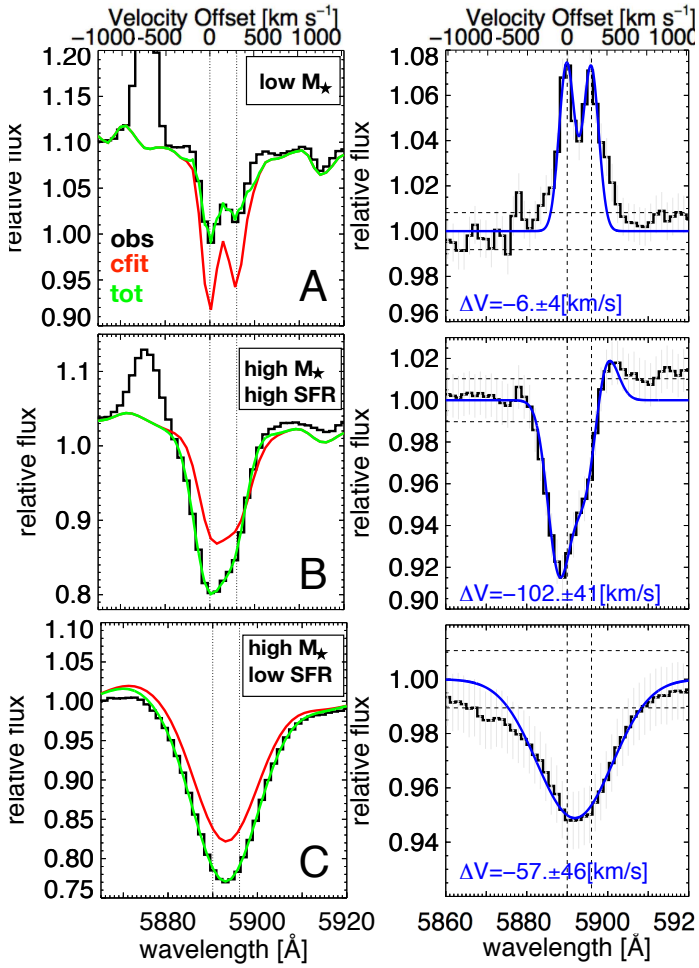


Figure 4.5: Examples of Na D fits in three different regions of the SFR-M$\star$ plane labeled in the plot: low stellar mass (M$\star$ < $10^{10.5}$ $M_\odot$, top panels, bin A in Fig. 4.4), high stellar mass and high SFR (M$\star$ > $10^{10.5}$ $M_\odot$ and SFR> $10^{1.1}$ $M_\odot$/yr, central panels, bin B in Fig. 4.4) and low SFR high stellar mass (M$\star$ > $10^{10.5}$ $M_\odot$, SFR< $10^{0.5}$ $M_\odot$/yr, bottom panels, Bin C in Fig. 4.4). The expected wavelengths of NaD are shown as vertical dashed lines. *Left panels*: continuum fits to the NaD region. The black histograms illustrate the observed stacked spectrum, the red line the best-fit stellar continuum and the green line shows our best-fit NaD combined fit, continuum plus ISM NaD. *Right panels*: Best-fit ISM NaD. The black histogram is the observed flux after the stellar continuum has been removed. The best-fit NaD lines and the velocity shift are shown in blue color in each panel. Only the high stellar mass and high SFR bin (central panel) shows a doppler blue-shift of the NaD absorption feature. In the others two regions the NaD line shows a zero-velocity line, below the instrumental resolution 70 km s$^{-1}$, both in emission (top panel) and absorption (bottom panel). The He I 5876 Å emission lines have been fit and removed.

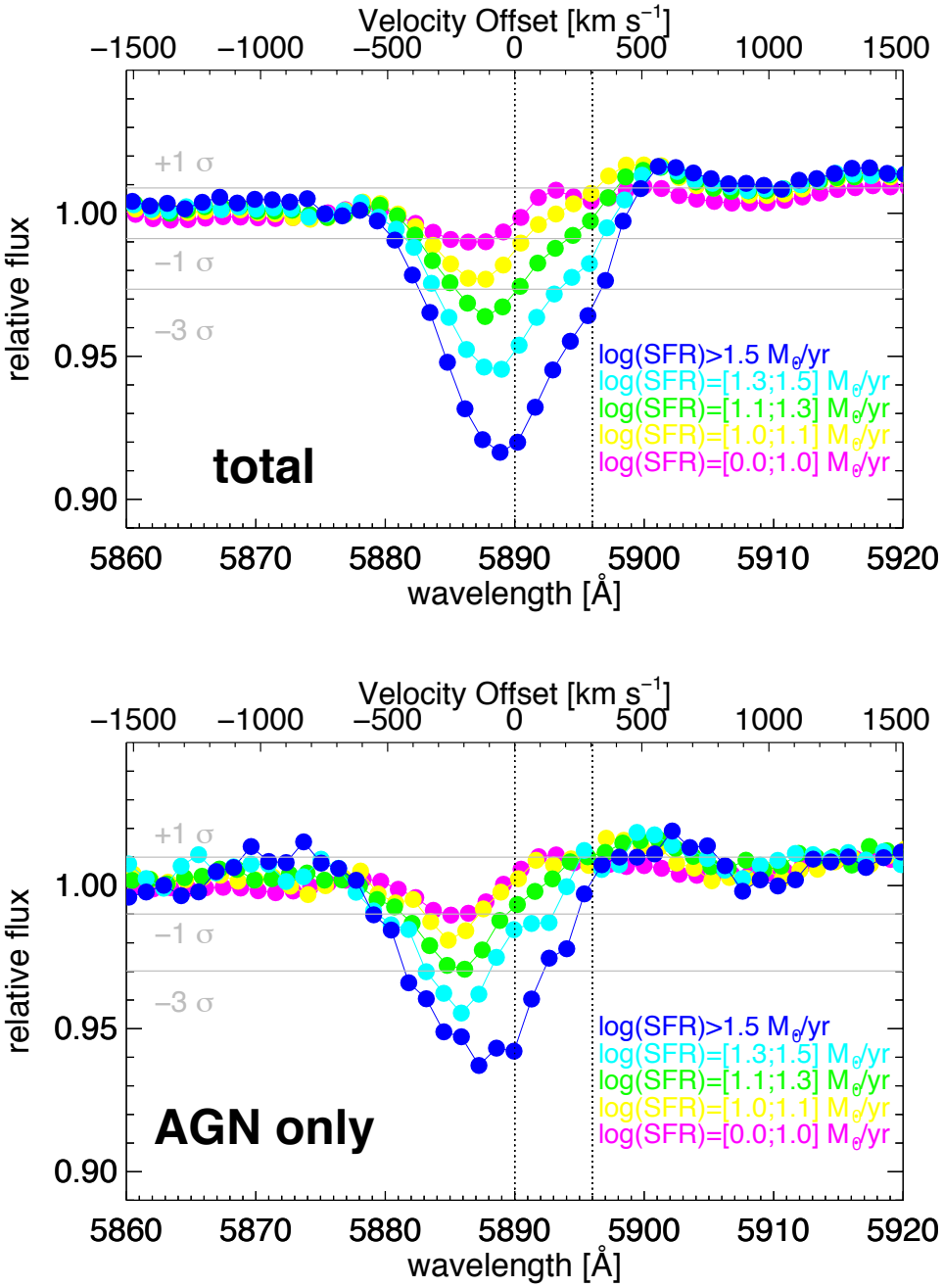


Figure 4.6: Variation of the ISM NaD resonant line profile as a function of the SFR for the galaxies with $M_\star > 10^{10.7}$ $M_\odot$ in the total sample (top panel) and in the AGN dominated objects (bottom panel). The intensity of the line increases with the increase of the SFR, from the magenta to the blue curves. Only the galaxies with SFR$\geq$ 12 $M_\odot$/yr show a blue-shifted NaD line, detected with good level of significance $> 3\sigma$ (or $\sim 3$ for the noisier AGN spectra). The AGN subsample shows the same trend observed in the total sample.

The origin of the Na D excess in the early-type galaxies has been strongly debated. A

possibility is that the absorption of the stellar light doe to the presence of extra neutral sodium atoms in the ISM. However the very low dust mass in the most massive local early type galaxies make the ISM the less probable explanation for our Na D excess. Another possibility is that the NaD excess is related to the extra sodium abundance in the stars. The discovery of the extra Na D and Mg b to respect the solar abundance in early-type galaxies is first reported by O'Connell (1976) and Peterson (1976). Then this finding is well confirmed by several studies (e.g. Carter et al., 1986; Alloin & Bica, 1989; Thomas et al., 2003; Worthey, 1998; Worthey et al., 2011). Finally, also a bottom-heavy stellar initial mass function (IMF) in the ETGs can produce a sodium excess in the galaxy spectrum. This possibility is explored in several studies (e.g van Dokkum & Conroy, 2010, 2012; Spiniello et al., 2012 and Parikh in prep.). However, these results are still a matter of debate. We point out that, the study of the Na D at the systemic velocity, whatever its origin, stellar (IMF or chemical abundance) and/or ISM, is well above the scope of this work.

If we finally focus on the massive ($M\star > 10^{10.7}$ $M_\odot$) late type SFR$>$ 1 $M_\odot$/yr) galaxies, as it shown in Fig.4.6 we find that only for galaxies with very high SFRs tail (stacked bins with SFR$\geq 12.5 M_\odot/yr$, green, cyan and blue curves in the figure), the Na D is statistically detected with good level of significance $> 3\sigma$ and the line velocity ($\Delta V$), appears to be blue-shifted with respect to the systemic velocity, $\Delta V \geq$ 100km s$^{-1}$.An example of our line fit, for galaxies with high SFR and high M$\star$, is reported in the middle right panel of Fig.4.5.

It is known that the AGN dominated objects (LINERs and TYPE 2 objects in our AGN subsample) are located at high stellar masses with a distribution that cover the entire plan in the SFR range, from the high SFR tail to the quiescent galaxies and the region in between (Leslie et al., 2016). In order to check if there is a correlation between the NaD results showed before for the total galaxy sample and the AGN activity, we investigate separately the AGN galaxy subsample. As shown in the bottom panel of Fig.4.6, also for this subsample, we find the same trend between the sodium shape and the SFR. The incidence of NaD blue-shifted line seems to be independent to the AGN presence in the galaxy host.

### 4.5.2 Cold winds in starburst galaxies

Based on the results shown in the previous Section, we analyse the galaxies located at high SFRs, in which there are clear signs of measurable blue-shifted interstellar Na D absorption lines. We select all the galaxies with SFR $\geq 12.5 M_\odot/yr$. We refer to this sub-sample as the starburst Sample, containing 15, 284 galaxies (see the cut in Fig. 4.1 and information in Tab. 4.1).

#### Trends with galaxy inclination

In order to study the wind geometry in our high star-forming galaxies we split the starburst Sample in six bins of inclination angle. Figure 4.7 illustrates the interstellar Na D

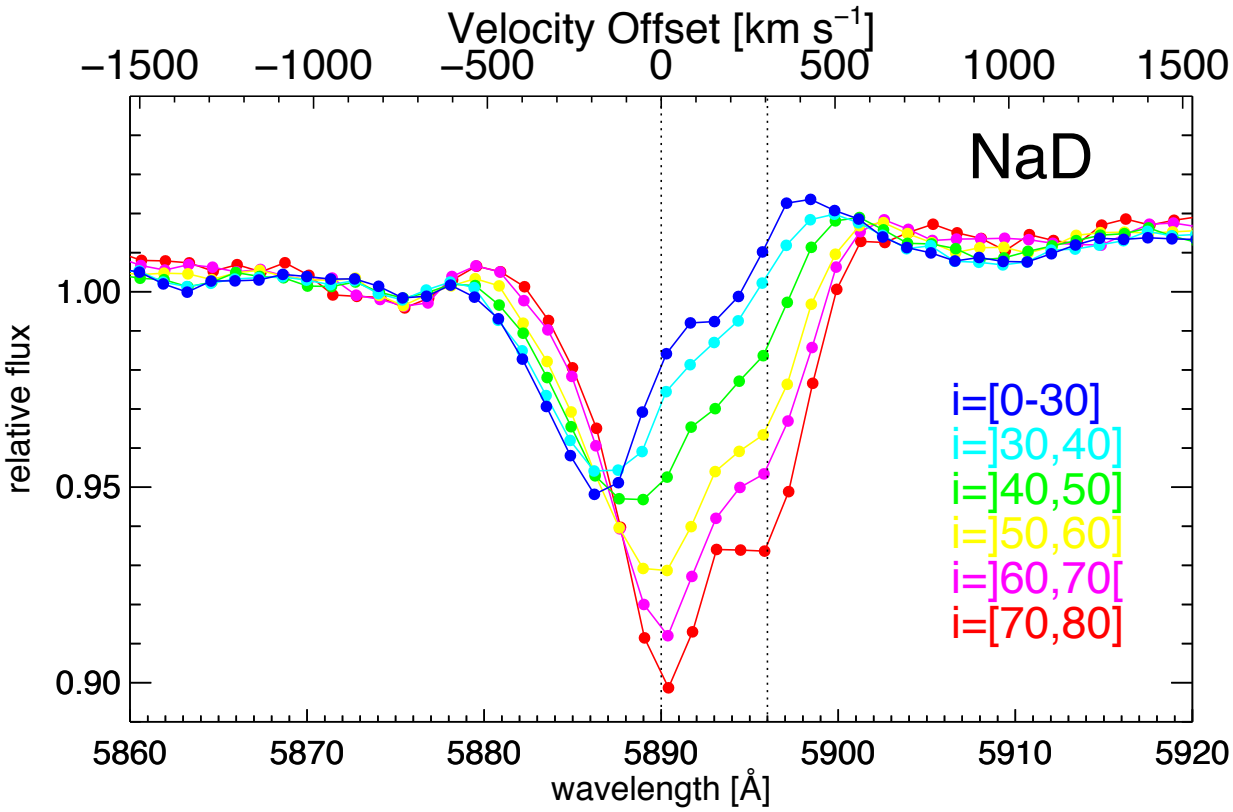


Figure 4.7: Variation of the ISM Na D line profile as a function of the galaxy's inclination for the galaxies with SFR≥ 12.5 $M_{\odot}$/yr including "pure" SF galaxies and galaxies with an AGN contribution. The line is centred to the systemic velocity in the edge-on sample (inclination $i > 50°$) and it shows a progressive blue-shift according with the decrease of the mean disk inclination. The maximum shift is reached by the face-on galaxies ($0° \leq i \leq 30°$, blue curve).

absorption profiles for composite spectra in six different inclination bins. We find a clear trend between the blue-shifted absorption profiles and the galaxy inclination: the neutral sodium line shows a transition from a strong disk-like component, perfectly centered to the systemic velocity, in the edge-on system (inclination $i > 50°$ of the disk rotation axis), to an outflow, blue-shifted, component in face-on galaxies ($i < 50°$). This result is perfectly consistent with the finding of Chen et al. (2010) for a subsample of star-forming galaxies.

A quantitative analysis of these six ISM Na D is performed according with the fit methods described in Section 4.4.2. Fig. 4.8 shows the mean velocity shift (top panel) and relative efficiency of the parameterized models, expressed by the BIC values (bottom panel), as a function of the disk orientation. We find that the Na D lines in galaxy samples with inclination bigger than 50° can be reproduced with a sample $one - free - doublet$ model, lower BIC value in model 1 (filled circles in the figure). The velocity of the line peak is consistent with the systemic velocity of the galaxy ($\Delta V \sim 0$ km s$^{-1}$). In the low inclination spectra, we find a very complicated Na D line structure. In particular, we

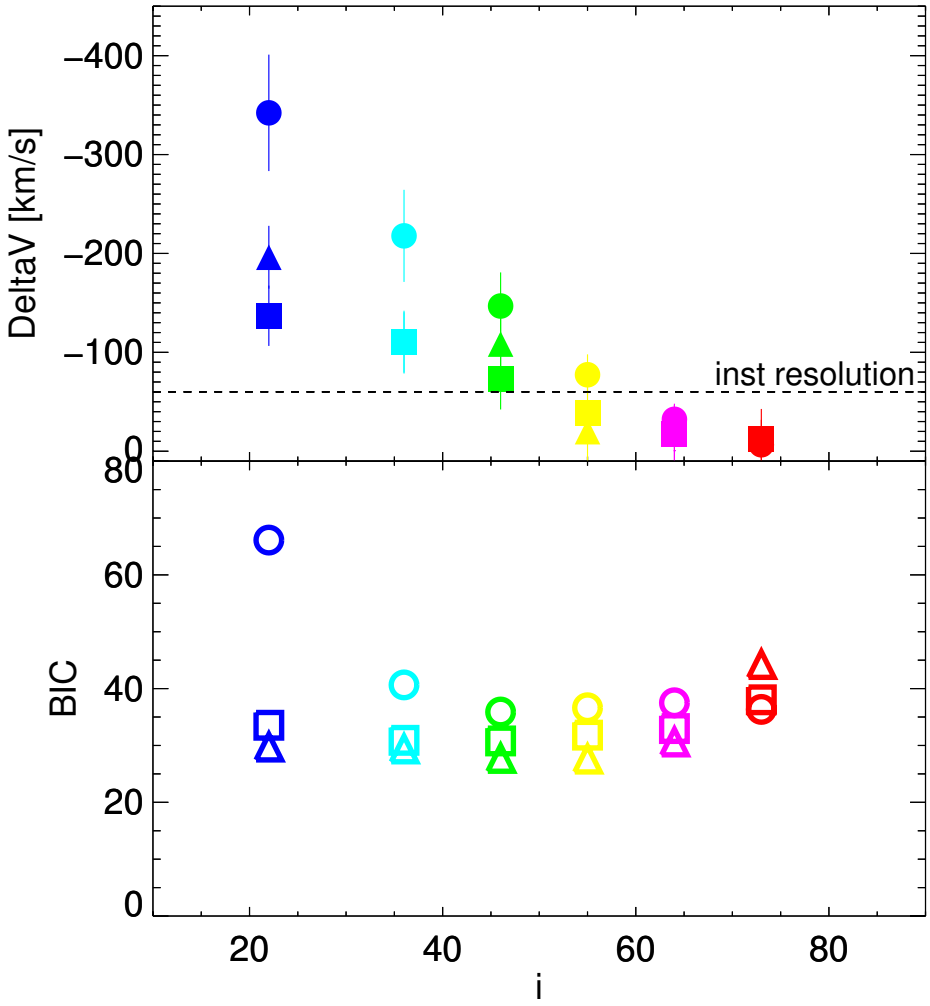


Figure 4.8: NaI D peak velocity and BIC values estimate with method 1, 2 and 3 (circles, squares and triangles, respectively) described in Section 4.4, for all the inclination subsamples described in Fig. 4.7. The velocity increases with the decrease of the disk inclination. The BIC associated with a single doublet component, model 1, is favorite only at large inclination values, while the methods 2 and 3 provide a better fit in the other cases.

find evidence for the presence of a blue-shifted absorption component and a line-emission at roughly the systemic velocity, consistently with the P-Cygny predictions showed in the cool gas wind models of Prochaska et al. (2011) (Monte Carlo radiative transfer techniques) for the Mg II and Fe II resonance lines and in the semi-analytical line transfer model of Scarlata & Panagia (2015). For these low inclination samples the methods 2 and 3 better reproduce the line shape, as it is showed in the Fig. 4.8 bottom panel by the low BIC values of 2 and 3. In the face-on galaxy sample the velocity of the line peak reaches a maximum value of $\Delta V \sim 200$ km/s and maximum velocity of $V_{max} \sim 460$ km s$^{-1}$.

Finally we find that the width of the outflowing component is quite stable for all the 3

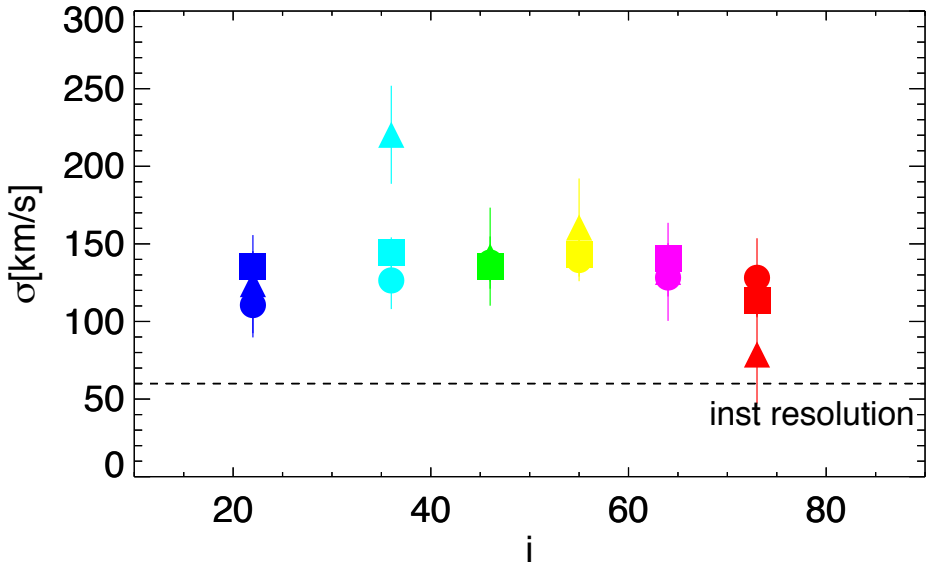


Figure 4.9: NaI D velocity dispersion of the outflowing component estimate with method 1,2 and 3 (circles, squares and triangles, respectively) described in Section 4.4, for all the inclination subsamples described in Fig. 4.7. The width of the outflowing component is quite stable for all the 3 methods adopted with a mean value of $\sigma \sim 130 \pm 30$ km s$^{-1}$.

methods adopted and in each inclination with a mean value of $\sigma \sim 130 \pm 30$ km s$^{-1}$ (see Fig. 4.9).

### Trends with AGN and SF activity

In order to investigate if the interstellar Na D shift is tied to a particular triggering mechanism, star formation end/or AGN activity, we split the starburst sample into subclasses based on their BPT classification (see Tab. 4.1 for the subsample informations). This allows us to characterise the sample by their distinct ionisation sources. We perform our analysis on the stacked spectra of each subclass: SF, SFAGN, AGNSF and AGN galaxies. We find that the trend with the galaxy inclination described in the previous section is present in all the ionization classes. In the left panels of Fig. 4.10, we report the NaD stacked spectra in two main inclinations bins: face-on (blue curves) and edge-on systems (magenta curves), with inclination ranges $i < 50°$ and $i > 50°$ respectively, for the "pure" SF and AGN galaxies. The face-on systems clearly show a NaD blue-shifted line while the edge-on samples are chaterized by a doublet perfectly located at the systemic $\lambda$ values. The average peak velocities computed in the samples with $i > 50°$ are all compatible with $\Delta V = 0$ km s$^{-1}$: we do not detect outflowing neutral Na D gas in the edge-on galaxies, in both SF and AGN dominated galaxies. The sodium line only appear to be more prominent in the edge-on systems compared to the lower inclination samples (see the magenta curves in the left panels of Fig. 4.10). This extra Na D absorption can be consistent with a stronger attenuation of the stellar light through the galaxy disk (disk self-absorption).

The NaD line in the face-on AGN galaxies samples appears to be slightly more blue-

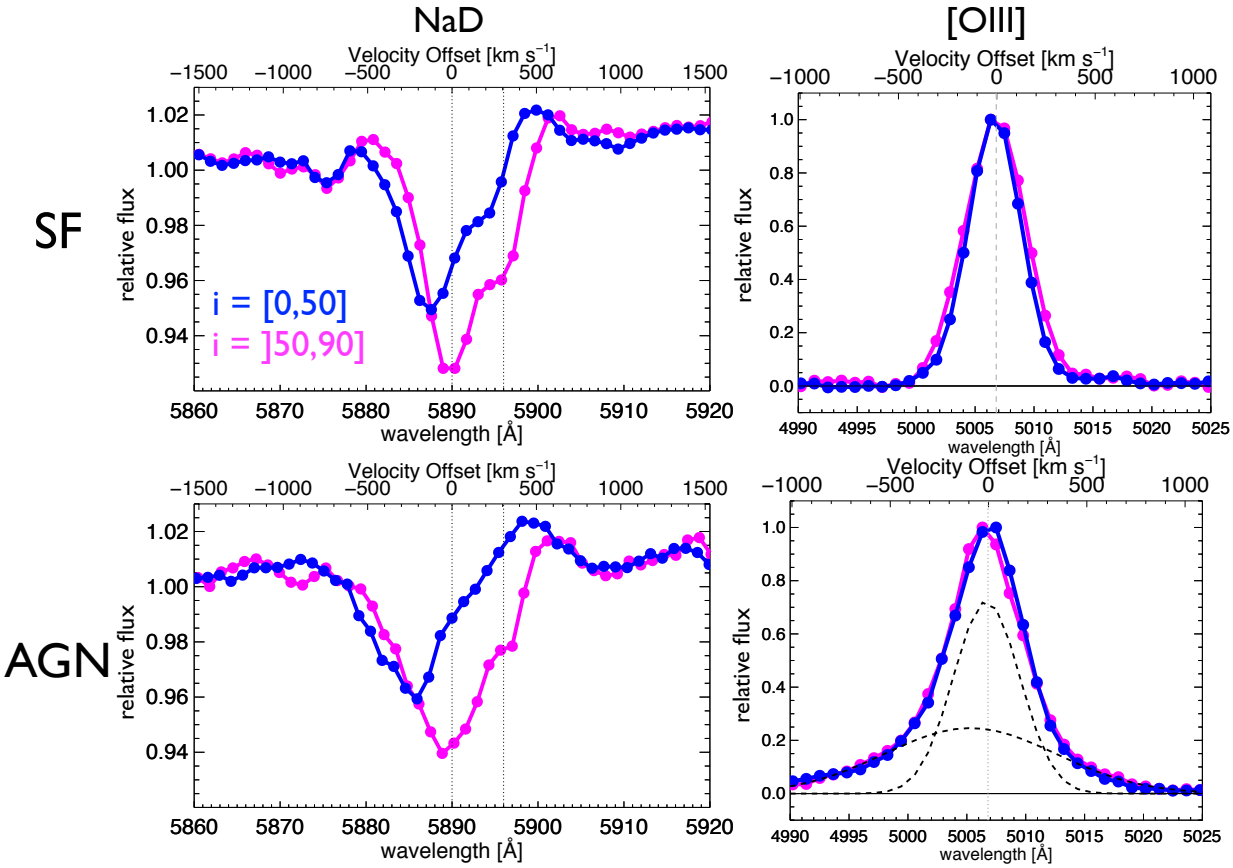


Figure 4.10: Na D and [OIII]$\lambda$5007 line profiles (left and right panels, respectively) for face-on and edge-on systems with inclination respectively $i = [0, 50]$ and $i = ]50, 90]$). The spectra are extracted from the "pure" SF galaxies (top panels) and for the AGN subsample (right panels). The Na D line shift clearly correlate with the galaxy inclination in both the SF and AGN dominated samples. The [OIII] emission line are independent to the galaxy inclination but shown a strong shape variation between the SF and AGN subsamples. In the oxygen AGN case,bottom right panel, the black dashed lines illustrate the two-Gaussian components, narrow and broad blue-shifted component, needed to best fit the data.

shifted than in the SF case. However, a more quantitative analysis shows that there is not a significant difference in the velocity shift in the face-on systems of all the ionization subsamples. The peak velocities values are all consistent within $1\sigma$ error with a mean value of $\Delta V \sim 200$ km s$^{-1}$ and a mean maximum velocity shift of $V_{max} \sim 480$ km s$^{-1}$. The results of our fits would indicate that there is no strong correlation between the evidence of neutral gas wind and presence of the central optically selected AGN.

### 4.5.3 Ionized winds in starburst galaxies

In this section we compare the presence of neutral, cold gas winds with respect to the ionized outflowing gas phase. In particular, we analyse the [OIII]$\lambda$5007 emission line in the same galaxy stacked spectra, showed in the previous sections: face-on and edge-on systems split in "pure" SF and AGN dominated objects. See the right panels of Fig. 4.10.

Similar to what was found in C17, also for the galaxies with higher SFR, we find that the purely star forming galaxy population, with no signature of AGN activity, shows an unperturbed symmetric Gaussian [OIII] line profile, while the AGN systems display a prominent and asymmetric line.

In order to quantify the blue wings contribution in the emission line, following the procedure described in C17, we model the [OIII]$\lambda$5007 with 1 and 2 Gaussian profiles. This approach allows us to decompose the emission oxygen line in the 2 different Gaussian components and to evaluate the presence of a second broad and blue-shifted component which we interpret as outflowing ionized gas wind. We do not find any evidence for a second broad and blue-shifted component in the "pure" SF samples, in both the face-on and edge-on systems. The oxygen line width increase from the SF samples, FWHM= $328.4 \pm 4.4$ km s$^{-1}$ and $376.5 \pm 7.2$ km s$^{-1}$ for the face-on and edge-on systems, to the broader AGN cases, characterized by a FWHM= $616.3 \pm 15.6$ km s$^{-1}$ and $656.2 \pm 19.2$ km s$^{-1}$ for the face-on and edge-on systems. For the AGN samples (both face-on and edge-on systems) we find a second broad and blue shifted gaussian component characterized by a velocity peak of $\sim 125 \pm 45$ km s$^{-1}$, velocity dispersion of $\sim 460 \pm 30$km s$^{-1}$ and a mean $V_{max} \sim -1042 \pm 106$ km s$^{-1}$ (see the line decomposition in Fig. 4.10).

Despite what we find for the neutral gas phase in the previous section (and clearly shown in the left panels of Fig.4.10), the [OIII] line shape does not depend on the galaxy disk inclination (right panels of Fig.4.10). In both the AGN (bottom right panel) and "pure" SF (top right panel) sample the oxygen line of the face-on systems perfectly overlaps with that of the edge-on subsamples. We check that this result is true for all the ionization classes, SF, SFAGN, AGNSF and AGN. The evidence of outflowing ionized gas in the AGN contaminated samples seems to be unconnected to the stellar disk geometry.

As a main result, by comparing the Na D resonant line shape and the [OIII] emission line in the same galaxy stacked spectra, we find a clear evidence of cold-gas outflows in face-on SF galaxies but any wind feature in the ionized gas counterpart traced by the [OIII]. In the AGN case, the cold-gas wind is observed in face-on systems together with the ionized counterpart regardless of the inclination angle.

In both neutral and ionized phase, the outflow velocity is relatively small, of the order of 200 and 500 km s$^{-1}$ for the peak velocity shift and the maximum velocity, respectively. We use the catalog of halo masses of Yang et al. (2007) to retrieve the mean halo mass of the pure SF and AGN. The region of the SFR-M$\star$ diagram considered here, at high stellar masses and SFR, is dominated at 60% by central galaxies of massive halos of $10^{12.5-13}$ M$_\odot$, whose escape velocity largely exceeds the outflow velocity observed here. Thus, we conclude that, on average, the outflowing gas will never escape the halo potential well.

Cazzoli et al. (2016) found very consistent results in the analysis of $\sim$ 50 local LIRGs and ULIRGs.

## 4.6 Summary and Conclusions

In this chapter we present the results of a study based on a statistically significant sample of passive, star-forming and starburst galaxies, drawn from the SDSS, to look for evidence of neutral galactic winds in the local Universe. We use, in particular, the doppler blue-shifts of the interstellar NaI $\lambda$5890, 5895 (NaD) resonant line as a tracer of cold gas outflows. The single SDSS spectra are stacked together in bins of SFR and M$\star$ to reach a much higher signal-to-noise ratio (SNR) than in the individual spectra and study the neutral gas wind occurrence as a function of the galaxy position in the SFR-M$\star$ diagram.

After carefully subtracting the stellar continuum, we find that galaxies at very high stellar masses M$\star > 10^{10.5} M_{\odot}$, in the passive and starburst regions show a clear residual sodium absorption component (see Fig. 4.4, 4.5 and, top panel in Fig. 4.6). While for passive galaxies this is found consistent with the systemic velocity of the galaxy, for starburst galaxies (at SFR $> 12.5 M_{\odot}/yr$), the residual component is clearly blue-shifted, by more than the instrumental resolution (70 km s$^{-1}$). In the former case it is still unclear whether the residual component is due to the ISM or to an extra sodium abundance in the stars or an effect of a bottom-heavy IMF in the ETGs. In the latter case, instead, the clear blue-shift suggests the presence of outflowing gas.

We find that the incidence of NaD blue-shifted line seems to be independent to the AGN presence in the galaxy host. The AGN population follows the same trend in the SFR-M$\star$ plane as the bulk of the galaxy population (see Fig.4.6).

We perform an in depth analysis of the galaxies in the starburst region (SFR $> 12.5 M_{\odot}/yr$) at very high mass to study the geometry of the outflow and to identify the most likely ejecting mechanism, SF and/or AGN feedback. We find that the ISM NaD absorption lines show a clear transition from a clear Gaussian doublet, perfectly centered at the systemic velocity in the edge-on systems (inclination $i > 50^{\circ}$ of the disk rotation axis), to an outflow, blue-shifted, component in face-on galaxies ($i < 50^{\circ}$, see Fig. 4.7). The velocity shift of $\sim$ 200 km s$^{-1}$ at the peak velocity and the maximum velocity shift is of $\sim$ 460 km s$^{-1}$ in the face-on galaxies, while it decreases to zero in edge-on systems. This would suggest that the outflow direction is perpendicular to the disk or it exhibits a large opening angle.

These trends are observed in galaxies in both "purely" star-forming and AGN dominated objects. These results would suggest that the blue-shifted Na D component is outflowing from the galactic disk and it is likely powered by the local star formation activity of the disk itself in both pure SF systems and AGN. This result is in agreement with Sarzi et al. (2016), who detect signature of neutral outflows only in objects dominated by central starburst or composite AGN/star-formation activity by using a sample of $\sim$500 SDSS galaxy spectra and FIRST radio emission (see also Perna et al., 2017a). Similar results are also recently showed by Nedelchev et al. (2017), that find a lower incidence of

cold gas winds in a sample of single SDSS Seyfert 2 galaxy with respect to the non active galaxy control sample.

In addition, in the face-on galaxies the Na D residual component profile is also characterized by a typical P-Cygni profile (see blue curve in Fig.4.7). According to the theoretical predictions of Prochaska et al. (2011) in Monte Carlo radiative transfer model and of Scarlata & Panagia (2015) in semi-analytical line transfer model, the P-Cygni profile can by interpreted as the overlap of the absorption component, created in the material between the galaxy and the observer, and the emission, produced by scattering photons into the line of sight. This particular feature is also consistent with recent integral field unit (IFU) observations of Na D resonant lines in low redshift QSO systems (e.g. Rupke & Veilleux 2015 and Rupke et al. 2017).

We compare the line profile of Na D residual component with the [OIII] line profile to check for the co-existence of neutral and ionized gas outflow. We find that, even at the highest SFRs, purely SF galaxies do not show evidence of outflow in the [OIII] profile, which is perfectly fitted by a single Gaussian component, consistently with the results showed in Chapter 3.

For the AGN population in the same highest SFR region, instead, the [OIII] emission line exhibits an asymmetric profile, consistent with the presence of an extra broad and blue-shifted component. Thus, we observe both neutral and ionized phase gas outflow only in the AGN population. This is in agreement with the results obtained by Rupke et al. (2005b), who found agreement between neutral and ionized wind kinematics only in Seyfert but not in starbursts systems.

However, the [OIII] line profile in the AGN population does not show any correlation with the galactic disk inclination (see bottom right panel of Fig.4.10). We argue that the geometry of the ionized phase wind, likely powered by the central black hole (BH), most likely depend on the BH accretion disk inclination, which does not depend on the inclination of the galactic disk on much larger scale. This is also consistent with the findings of Rupke et al. (2017) in luminous QSO.

We point out that our results do not exclude that strong neutral gas wind might be caused by BH feedback in powerful QSOs, as observed e.g. by Rupke et al. (2005a) and (Rupke & Veilleux, 2011, 2013, 2015). However, such systems are very rare objects in the Local Universe and they do not dominate the mean in the stacking analysis presented in this work. Thus, we conclude that for the AGN population, the ionised gas outflow traced by the [OIII] profile asymmetry is powered by the BH feedback, whereas the neutral gas outflow traced by the Na D profile is generating from the star forming disk.

The low outflow velocities (see Section 4.5.3) suggest that the neutral and ionized phases of the outflowing gas remain bound to the galaxy and likely fall back to the disk. These warm and cold "light breezes" observed in the SDSS galaxy spectra are consistent with the "gas circulation" scenario proposed by Fraternali & Binney (2006, see also Fraternali, 2017 for a review). In this scenario, the cold gas is driven out of the disk by SF feedback, mixes with the hot halo gas, and falls back to the disk in a ballistic fashion, creating a fountain cycle. Such gas circulation may sustain the SF activity for a long time since the hot, metal-poor, gas in the halo cools down to the disk after mixing with the cold,

metal-rich, fountain gas.

We do not find, however, any evidence of accreting gas in any of the analysed stacked spectra. This may be related to the low velocities of the inflowing material. For typical spiral galaxies, the fountain gas is expected to fall back at velocities of the order of 70 km $s^{-1}$ or less (as predicted by Fraternali & Binney, 2006 for NGC 891 and by Marasco et al., 2012 for the Milky Way), which are comparable to the velocity resolution of the SDSS spectra. Furthermore, as discussed by Fraternali (2017), the fountain gas could fall back at larger radii with respect to the location where the peak of the SFR density occurs. The 3" diameter fiber in the SDSS spectra does not allow us to sample the more external region of the galaxies. Finally, recent parsec-scale hydrodynamical simulations, including the presence of thermal conduction, showed that the efficiency of the fountain-driven gas accretion strongly decreases with increasing the virial temperature of the gas halo (Armillotta et al., 2016). This effect can by particularly important for our massive galaxies which reside in high-mass dark matter halos.

In conclusion, much higher spectral resolution observations and full spatial coverage are necessary to better understand the fate of the moderate outflowing gas observed here, put new constrain on gas circulation models, and improve our understanding of the galaxy baryon cycle.

# Chapter 5

# $L_{CO}$−$M_{H_2}$-Balmer Decrement relation

*This chapter is adapted from Concas & Popesso 2018, in preparation.*

## 5.1 Abstract

In this chapter, we propose a new methodology aimed at indirectly uncover the cold gas reservoir of star-forming galaxies. By using a sample of local massive galaxies drawn from the xCOLD GASS survey, we investigate the empirical correlation between the dust extinction and the total molecular gas mass. In particular, the ratio between the H$\alpha$ and H$\beta$ emission lines, the Balmer Decrement (BD), is used as a tracer of dust reddening in the optical galaxy spectra. This value is compared with the CO(1-0) line luminosity ($L_{CO}$) and the derived molecular mass ($M_{H2}$) for the same objects of the xCOLD GASS sample. We find a strong correlation between the two observables, BD and $L_{CO}$ and, between BD and $M_{H2}$, with a scatter of 0.33 and 0.34 dex, respectively. We test the correlation against galaxy inclination, metallicity, adopted $\alpha_{CO}$ conversion factor and galaxy size, to look for possible sources of scatter and bias. The slope and the scatter of the correlation do not depend on any of the considered parameters in our sample. The correlation disappear if the atomic gas phase is take in account. This is likely due to the fact that the region traced by the BD, the stellar disk, is much smaller than the HI disk, as a demonstration that the atomic hydrogen mass $M_{HI}$ mass is not tracing the star formation regions in local galaxies.

## 5.2 Introduction

Tightly connected, dust and gas are the key ingredients of star formation, which is governed by their complex, mutual interplay in the baryon cycle. Stars form in cold dense molecular clouds and, dust works as catalyst in transforming atomic hydrogen into molecular hydrogen (e.g., Wolfire et al. 1995). Dust is believed to be mainly produced in the envelopes of asymptotic giant branch (AGB) stars and, at the end of the life of massive

stars during the explosive Supernovae (SN) phase (see Dunne et al. 2011 for a short summary). Supernovae shocks, on the other hand, destroy dust grains, which can form again in the interstellar medium (ISM) by accretion processes. Dust absorbs the ultraviolet (UV) emission of young stars, allowing gas to cool and condense to form new stars. The dust and gas content of galaxies are linked to each other through metallicity, as shown in the local Universe (Draine et al., 2007; Leroy et al., 2011): the gas-to-dust mass ratio in the ISM increases as a function of metallicity. Dust has therefore been often adopted as a proxy to gas in absence of time-expensive, sub-millimeter spectroscopic cold gas observations in particular at high redshift (e.g. Magdis et al., 2012; Santini et al., 2014; Scoville et al., 2014; Genzel et al., 2015). The energy absorbed by dust at short wavelengths is re-emitted in the infrared (IR) and sub-millimeter (sub-mm) regimes, where the thermal emission of grains dominates the spectral energy distribution (SED) of galaxies (∼8-1000 $\mu$m). Dust emission is frequently used to trace the ongoing rate of star formation (e.g. Kennicutt, 1998; Nordon et al., 2010, 2012; Elbaz et al., 2011). As pointed out in the Chapter 1, the direct observation of the molecular gas through CO observations is extremely time-consuming. The largest homogeneous available sample of CO detected local galaxies is provided by the xCOLD GASS survey (Saintonge et al. 2017), which obtained single-dish observations with IRAM Plateau de Bure of $\sim$ 1000 local galaxies at stellar masses above $10^9$ $M_{\odot}$. The detection rate of the xCOLD GASS survey is less than 50% because the sample comprises non only star forming systems but also low SFR and quiescent galaxies. Although xCOLD GASS provide a fairly representative sample of the local galaxy population, the statistics is still too low to enable the study of the relation between molecular gas content and the environment. Indeed, only few of the xCOLD GASS galaxies, in particular at the high mass end, are located in massive host halos according to the host halo mass catalog of Yang et al. (2007). Similar approaches at higher redshift provide galaxy sample over a wide redshift window even more sparsely sampling the environment. For instance the PHIBBS survey (Tacconi et al., 2013) provided CO luminosities and molecular mass estimates for a sample of $\sim$ 100 galaxies over a very large time window, $0.7 < z < 2.2$. By using the dust-to-gas mass ratio approach to retrieve the gas mass, Cortese et al. (2012) combined Herschel photometry and multiwavelength data to build detailed SEDs of nearby galaxies from the Herschel Reference Survey (HRS; Boselli et al. 2010). In combination with radio data, these authors studied the dust-to-HI and dust-to-stellar mass ratios of their targets, finding that the former increases as a function of stellar mass, while the latter tends to decrease as a function of stellar mass. RemyRuyer et al. (2013) combined Key Insights on Nearby Galaxies A Far-Infrared Survey with Herschel galaxy sample (KINGFISH, Kennicutt et al. 2011) and other samples of nearby galaxies observed in the far-infrared bands with Herschel, including direct measurements of molecular gas mass, to study the gas/dust vs. metallicity relation over a 2 dex metallicity range. However, also in this case this approach suffers from the limitation that galaxy sample is not necessarily representative of all galaxy populations and metallicity dependencies play an important role both for dust-and CO-based masses. Similarly at high redshift several surveys use a single sub-mm continuum observations to scale them to dust or gas mass using known relations (e.g. Eales et al., 2012; Scoville et al., 2014); or characterizing the galaxy SED including the far infrared (FIR)

peak (e.g. Dale et al., 2012; Galametz et al., 2013). For instance, Scoville et al. (2014, 2015, 2017) applied a similar concept to the Rayleigh-Jeans (RJ) side of the SED of local and high-z galaxies. They suggested that gas masses can be measured using single-band sub-mm observations, adopting dust emissivities calibrated on Planck observations of the Milky Way. They applied this method to early ALMA observations of four small samples of galaxies at four different cosmic epochs. They found a clear reduction of the cold gas mass fraction along and across the Main Sequence (MS) of star-forming galaxies at any redshift to z$\sim$ 1 to z$\sim$4. More recently Brinchmann et al. (2013) proposed an alternative method to retrieve the galaxy dust mass based on the absorption rather than the emission due to the dust grains. Indeed, they use the extinction of several emission line fluxes in the rest-frame optical spectra of SDSS galaxies to indirectly constrain the dust mass. The main limitation of this approach is that it requires very high signal-to-noise emission lines in order to constraint the extinction models. In addition, due to the nature of the fitting procedure that requires a priori knowledge of the extinction law models, the results are necessarily model dependent.

In this work we apply a slightly different approach. Indeed, the main aim of this work is to retrieve the galaxy molecular mass to test how it varies along and across the Main Sequence of star forming galaxies and if the galaxy gas reservoir depends purely on the galaxy stellar mass or also on the environment. For such purpose we need a galaxy statistical sample large enough to probe all the environments at fixed stellar mass and a reliable method to retrieve the gas mass or the molecular mass. To this aim we use the most largely available and cheapest- in terms of observing time- indicator of galaxy dust content: the Balmer decrement. As explained in Chapter 1, the Balmer decrement is given by the ratio of the H$\alpha$ over H$\beta$ flux. Since the dust grains absorb preferentially at bluer wavelength, the H$\beta$ emission line is more extincted than the H$\alpha$ line. Thus, the Balmer decrement is a direct measure of dust extinction and so a proxy of the dust mass. A measure of the Balmer decrement is available nearly for all galaxies of the SDSS spectroscopic sample. Thus, it allows to have information on the dust content of a complete and statistically significant sample of galaxies in all environments.

In order to retrieve for the same sample the molecular mass, which is the fuel of the star formation process, our approach is to calibrate directly the Balmer decrement on the largest available sample of galaxies with known molecular mass, the COLD GASS sample (Saintonge et al., 2011) and its revised version the xCOLD GASS (Saintonge et al., 2017). In this chapter we study the correlation between the Balmer Decrement and the galaxy molecular mass. Such correlation will be used in the next chapter to adopt the Balmer decrement as a proxy for the molecular gas mass and study its dependence on the galaxy properties along and across the MS.

## 5.3 Data

### 5.3.1 The H$\alpha$ and H$\beta$ fluxes

As explained in Chapter 2, the emission line fluxes are taken from the revised version of the MPA-MJU catalog[1] adapted to the DR7 data release. The emission line fluxes are estimated after continuum removal. The spectral continuum is removed by fitting each galaxy spectrum with a set of sets of spectral energy distribution templates (from Charlot & Bruzual in prep. CB08 models) at the SDSS spectral resolution. After subtracting the best-fitting stellar population model of the continuum, any remaining residual is removed with a sliding 200 pixel median and fit the nebular emission lines. To recover also very weak nebular features, all emission lines are fitted simultaneously with Gaussians, requiring that all of the Balmer lines (H$\alpha$, H$\beta$, H$\delta$, and H$\gamma$) have the same line width and velocity offset (see for details Tremonti et al. 2004).

As discussed on the MPA-JHU website, and well explained by Groves et al. (2012), the listed errors of the MPA/JHU catalogue are formal, and likely underestimates. Following the approach of Groves and collaborators, we multiplied the uncertainty of the emission lines by the factors $f = 1.882$, to take into account continuum subtraction errors.

### 5.3.2 The CO molecular gas mass

The sample of galaxies analyzed in this work is taken from the extended CO Legacy Database for GASS survey (xCOLD GASS, Saintonge et al., 2017), designed to provide a picture of molecular gas across the local galaxy population. The original COLD GASS sample (Saintonge et al., 2011) was selected to have a flat distribution of stellar mass between $M\star > 10^{10} M_{\odot}$ and redshift $0.025 < z < 0.050$. The galaxies sample was selected randomly out of the complete parent sample of SDSS galaxies within the ALFALFA footprint matching these criteria, making it unbiased and representative of the local massive galaxy population. This first COLD GASS survey was followed by a second sample, namely COLD GASS-low, which extends the original sample down to stellar masses of $10^9$ $M_{\odot}$ in the same redshift window. The combination of the two samples provides xCOLD GASS (Saintonge et al., 2017). About half of the original COLD GASS and COLD GASS-low samples (532 systems) has a CO(1-0) detection or upper limit in the IRAM-30m telescope observations. The catalog also provide several global galaxies properties, as M$\star$ (from SDSS DR7 MPA/JHU catalog), SFR (from WISE + GALEX when detected in both data sets else from SED fitting, see Janowiecki et al. 2017) and, HI observations (from Catinella et al., 2018). See Saintonge et al. (2011, 2017) for a complete description of the sample selection, survey strategy and associated data.

The CO(1-0) data provide the CO line luminosity ($L_{CO}$) from which the total molecular gas mass, $M_{H2}$, are derived by using:

$$M_{H2} = \alpha_{CO} \times L_{CO}$$

[1] http://www.mpa-garching.mpg.de/SDSS/DR7/

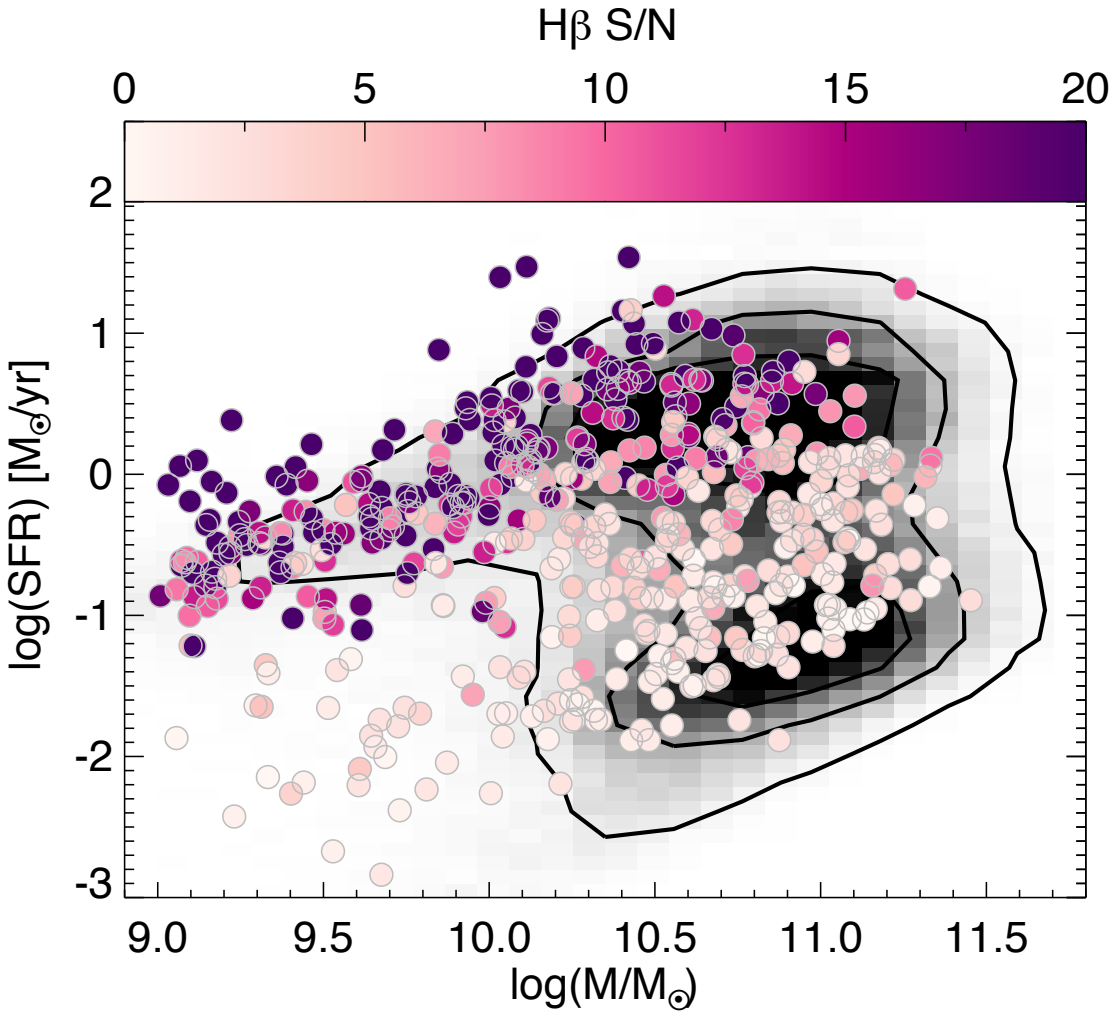


Figure 5.1: Distribution of xCOLD GASS sample in the SFR-M⋆ diagram, color-coded by H$\beta$ signal−to−noise ratio (S/N). The black contours show the overall SDSS population.

where $\alpha_{CO}$ is the CO−to−$H_2$ conversion factor, calculated with the function calibrated by Accurso et al., 2017. This conversion factor has a metallicity dependence and a second order dependence on the offset of a galaxy from the star-forming MS. In order to investigate if such dependences might induce any bias in the cross-correlation of the Balmer Decrement with the molecular gas mass, we perform the correlation separately between the Balmer decrement $L_{CO}$ and $M_{H2}$ and compare the scatter.

The galaxies with detected CO line are 63% of the sample (333 objects), while for the remaining galaxies only $L_{CO}$ and $M_{H2}$ upper limits are provided (see Saintonge et al., 2016, 2017).

The xCOLD GASS sample is cross matched with SDSS DR7 MPA-JHU emission lines catalog[2], witch provides the measurements of H$\alpha$ and H$\beta$ fluxes and related uncertainties

[2]https://wwwmpa.mpa-garching.mpg.de/SDSS/DR7/raw_data.html

necessary to evaluate the Balmer Decrement.

In Fig. 5.1 we illustrate the distribution of the xCOLD GASS sample in the SFR-M$\star$ plane. The points are color-coded as a function of the $H\beta$ signal to noise ratio (S/N). This is done because the $H\beta$ is weaker than $H\alpha$ and, thus, is causing most on the uncertainty of the Balmer decrement. The $H\beta$ is well observed in galaxies above and on the Main Sequence (MS) of star forming galaxies but it shows and lower and lower S/N at larger distances from the MS towards the quiescence region.

For the purposes of this study, we select only the galaxies with well detected emission line fluxes. After a selection in signal to noise in the H$\beta$ flux, (S/N$>$ 10), we end up with a final sample of 200 galaxies. 133 galaxies with low H$\beta$ flux, (S/N$<$ 10) are rejected to minimize the error in the final Balmer Decrement.

## 5.4 The Balmer decrement-$M_{H2}$ correlation

First, we study the correlation between the observed $L_{CO}$ versus the observed Balmer decrement. In the left panel of Figure 5.2 the line luminosities of the CO(1-0) line and the BD are compared. We find a strong correlation between the two observables. The Spearman rank correlation coefficient (Spearman, 1904) confirms the positive correlation, $\rho = 0.69$ with very high probability, $P > 99\%$. Note that the uncertainties on the BD are large, as they include the large of H$\beta$ emission uncertainty. We quantify the BD-$L_{CO}$ correlation by fitting a power law of the form :

$$\log(L_{CO}) = 6.2\pm1.7 \times \log(BD) + 4.1\pm1.1 \quad .$$

By using the molecular mass, $M_{H2}$, provided by the xCOLD GASS catalog, we find a positive correlation between BD and $M_{H2}$, confirmed by a Spearman correlation coefficient of $\rho = 0.64$ and with a probability of correlation above 99%. The best fit power law is given by:

$$\log(M_{H2}) = 4.2\pm2.0 \times \log(BD) + 6.3\pm1.3 \quad .$$

In both $L_{CO}$ and $M_{H2}$ cases, we find that the scatter of the correlation is 0.33-0.34 dex, respectively. This suggest that the inclusion of the metallicity dependent $\alpha_{CO}$ conversion factor to transform $L_{CO}$ into $M_{H2}$ is not a source of additional scatter. In order to understand what are the possible sources of scatter and to test the slope of the correlation against biases, we study the distribution of the residuals against several parameters such as the galaxy size and inclination. Indeed, the the BD is derived in the galaxy region sampled by the SDSS fiber, whose diameter is 3 arcsec. The CO molecular mass is derived over the entire physical region of the galaxy. If the system is significantly more extended that the fiber region, any gradient in the spatial dust distribution, for instance for the presence of a bulge component, would affect also the value of the BD. This is true for very nearby galaxies and for the most massive ones, which tend to be very extended. For this check we take as a measure of the galaxy size the $r50$ radius (the radius encapsulating 50% of the galaxy light) provided by the SDSS pipeline as a result of a de Vaucouleurs or exponential

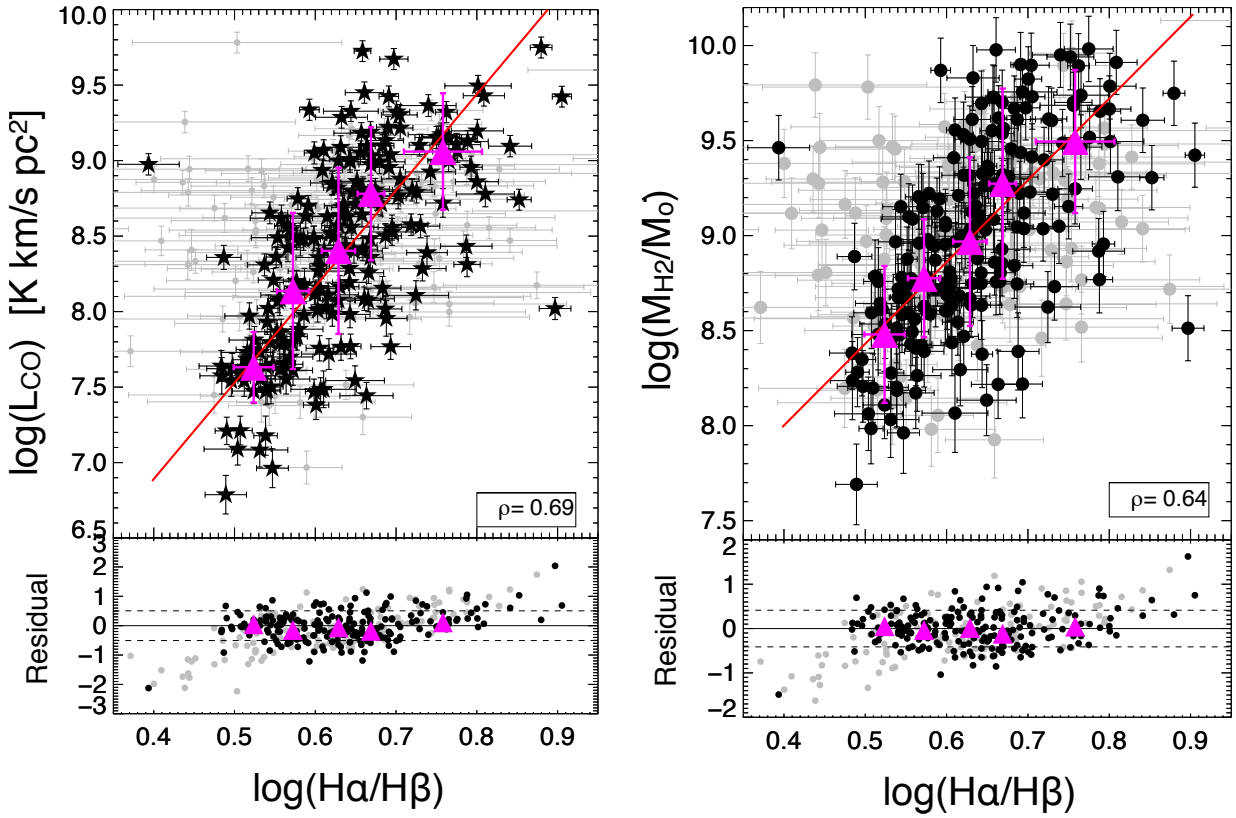


Figure 5.2: $L_{CO}$ and $M_{H2}$ plotted against H$\alpha$/H$\beta$ for 333 galaxies in original xCOLD GASS sample with detected CO(1-0) line flux, left and right respectively. The black and gray symbols are the galaxies with H$\beta$ observed with high and low S/N, S/N> 10 and S/N< 10, respectively. The magenta symbols show the medium values and dispersion in bins of H$\alpha$/H$\beta$. The red lines is the best linear log-log fits. Both the $L_{CO}$ and $M_{H2}$ clearly show a strong correlation with the H$\alpha$/H$\beta$ as indicate by the Spearman correlation coefficient ($\rho$) in the figure. The residuals are shown as a function of H$\alpha$/H$\beta$ in the lower panels.

profile fitting. We take into account also the galaxy inclination, because for very inclined galaxies the light has to pass through the entire disk before escaping, with a large probability of being absorbed by the disk itself. This could bias the BD towards higher values. The galaxy inclination measure is taken as well from the Simard et al. (2011) catalog. We do not test the effect of the galaxy metallicity, because the the scatter does not increase in the BD-$M_{H2}$ correlation with respect to the BD-$L_{CO}$ correlation. In addition, since the aim of the project is to study the variation of the molecular gas along and across the MS, we test the residuals around the best fit relation as a function of the galaxy specific SFR and the distance from the MS.

The results of such analysis are shown in Fig. 5.3. The two upper panels of the figure show the dependence of the residuals around the best fit relation as a function of $r50$ (left

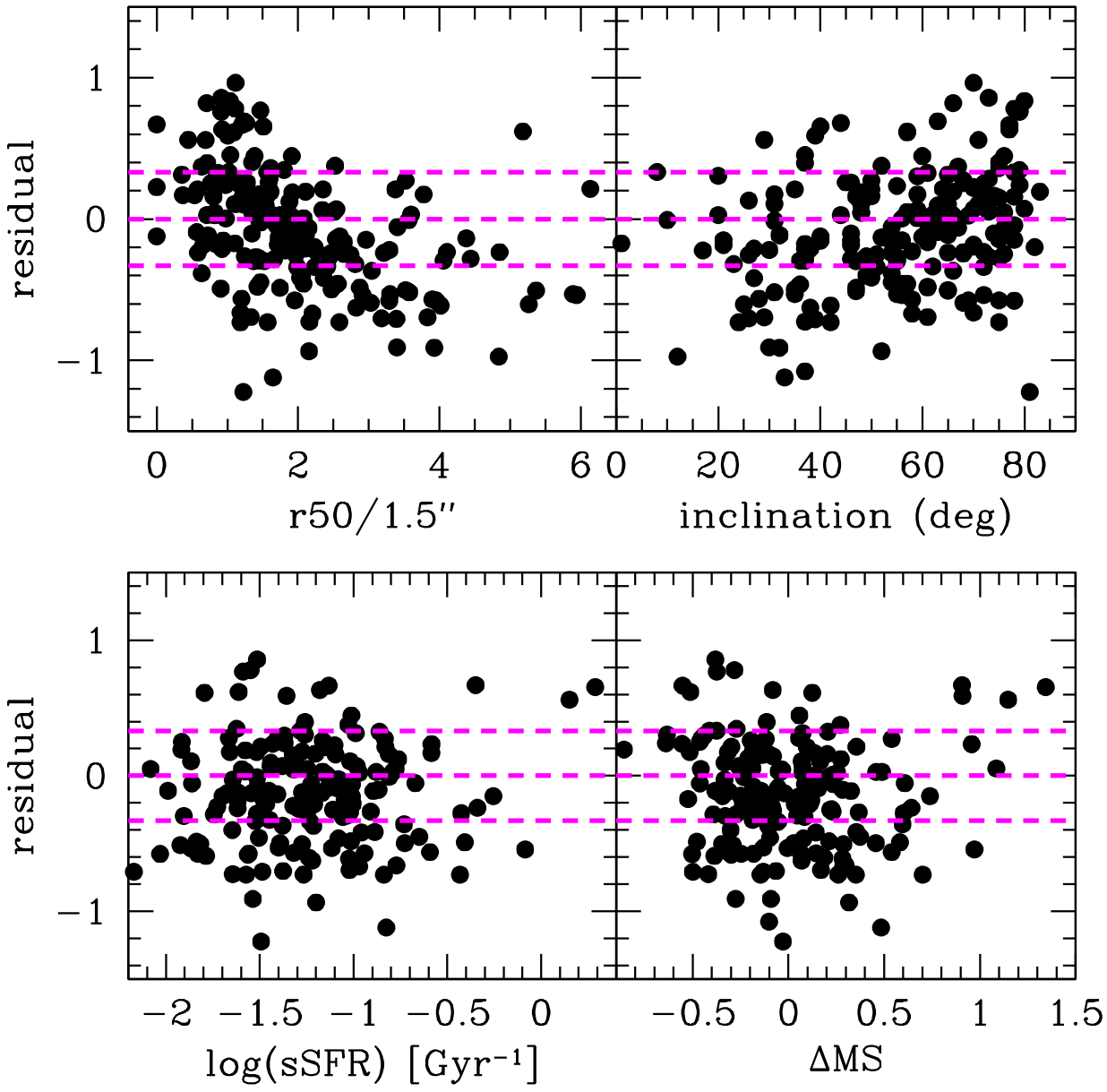


Figure 5.3: Residuals around the best $M_{H2}$-BD relation. The residuals are defined as the difference between the molecular mass derived from the *BD-$M_{H2}$* best fit relation and the observed CO derived molecular mass of the xCOLD-GASS galaxies. *Upper left panel*: relation between the residuals and the ratio between the galaxy r50 and the fiber radius of 1.5 arcsec. *Upper right panel*: relation between residuals and galaxy inclination as derived from Simard et al. (2011). *Bottom left panel*: relation between residuals and galaxy specific SFR (sSFR=SFR/M⋆). The SFR and stellar mass are taken from Salim et al. (2016). The SFR is based on WISE 22 $\mu$m flux. *Bottom right panel*: relation between the residuals and the distance from the MS of star forming galaxies. The MS is taken from Popesso, Concas et al. (2018, see next Chapter).

panel) and the inclination (right panel). In the former case, as expected, we see an anti-correlation, whereas very extended galaxies exhibit an underestimation of their molecular mass derived with the BD. This is likely due to the fact that the disk region is not sampled by the SDSS fiber region, whose emission is dominated by the central component. The Spearman correlation test gives a correlation coefficient of $-0.48$ with a probability of 98% of correlation. Such values are reduced to $-0.01$ and 30% if we considered only galaxies with r50 less than twice the fiber radius. No correlation is found, instead, with the galaxy inclination.

The bottom panels of the Fig. 5.3 show the relation between the residuals and the specific star formation rate ( sSFR=SFR/M$\star$, left panel) and the distance from the MS ($\Delta MS$, right panel). The SFR is based on the mid-infrared WISE 22 $\mu$m fluxes and it is taken from Salim et al. (2016). The distance from the MS is estimated by considering the MS provided by Popesso, Concas et al. (2018) in the local Universe (see next Chapter for more details). In none of the two cases we see a correlation, as confirmed also by the Spearman test. We conclude that the main source of bias in our estimate is just the selection effect due to the percentage of galaxy physical region sampled by the SDSS fiber aperture. Such criterion will be used in the next chapter for the selection of the galaxy sample.

## 5.5 The Balmer decrement-$M_{HI}$ correlation

For a subsample with observed atomic mass (105 galaxies), we consider also the relation between Balmer decrement and atomic gas mass ($M_{HI}$ from Catinella et al. 2018). First, one should consider that the molecular mass itself does not correlate well with the HI gas mass, as found in Catinella et al. (2013, 2018) This is due to the fact that the molecular gas mass is located mainly in the star forming region of the galaxy stellar disk, while the HI disk is much more extended (Catinella et al., 2018). Similarly the Balmer decrement does not correlate with the HI mass as shown in the left panel of Fig. 5.4. Finally, also the total mass fraction, give by the sum of the HI and H2 gas mass, does not show any correlation with the Balmer decrement, as shown in the right panel of Fig. 5.4.

## 5.6 Conclusions

We find a strong correlation between the observed Balmer decrement, measured by H$\alpha$ and H$\beta$ emission lines, and the observed CO(1-0) line luminosity, $L_{CO}$ and the derived molecular gas mass, $M_{H2}$. The scatter of the two correlation is the same, thus indicating that the metallicity dependence of the $\alpha_{CO}$ conversion factor is not an additional source of scatter. The main source of bias is, instead the selection effect due to the SDSS fiber aperture. Indeed, for very nearby extended galaxies, with the 3" fiber aperture sample only the very central region of the system, the Balmer decrement value is likely driven mainly by the central bulge component and it indicates a reduced dust extinction than in the

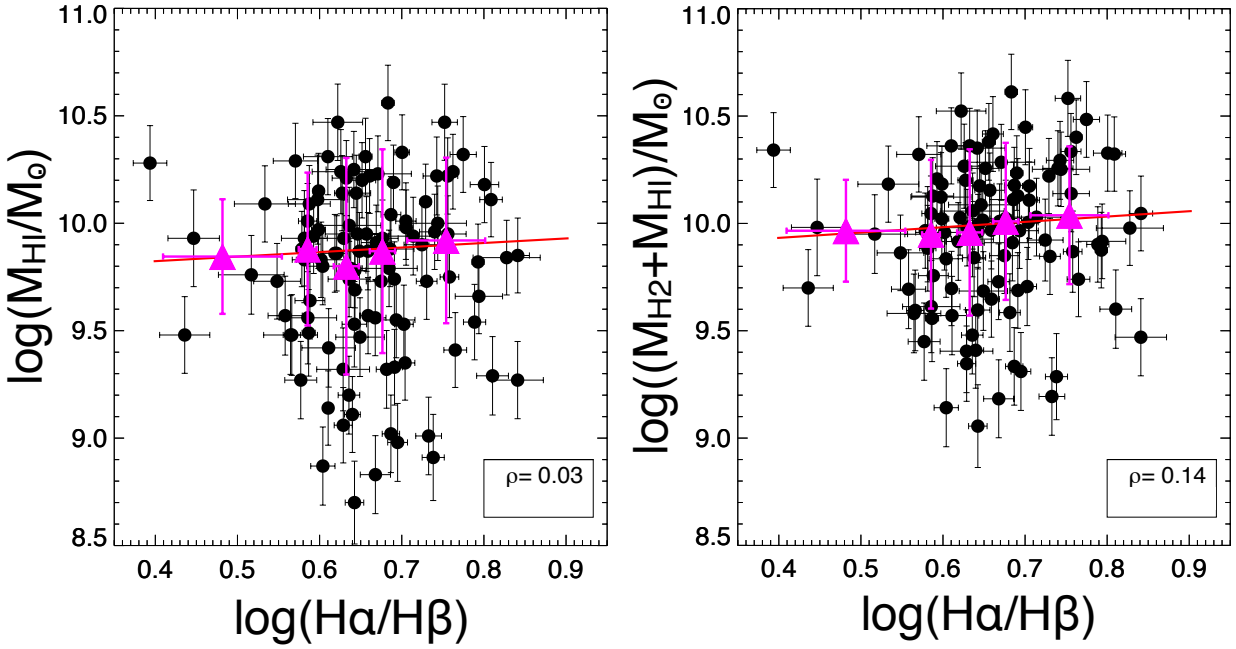


Figure 5.4: $M_{HI}$ and total gas mass ($M_{H2}$+$M_{HI}$) plotted against H$\alpha$/H$\beta$ for 105 galaxies in xCOLD GASS sample with molecular and atomic observations, left and right respectively. There is no correlation between BD and $M_{HI}$ and BD and total gas mass, $M_{H2}$+$M_{HI}$. The correlation coefficients ($\rho$) are given in the lower right corner. The symbols and colors as described in Fig. 5.2.

galaxy disk. In order to use the Balmer decrement as an unbiased proxy of the molecular gas mass, this method can be applied only to SDSS galaxies with $r50$ at least less than twice the fiber aperture radius. The residuals with respect to the best fit relation do not show any dependence of galaxy inclination, morphology, specific SFR and distance form the Main Sequence of star forming galaxies. Thus our method can be applied the variation of the molecular gas reservoir in big galaxies surveys, for which the BD is provided. The next chapter will focus on such analysis.

## Acknowledgements

This work made use of the xCOLD GASS IRAM-30m legacy survey (Saintonge et al., 2011, 2017). The authors acknowledge the members of the xCOLD GASS project for providing the data.

# Chapter 6

# Environmental quenching in the local Universe

*This chapter is adapted from Concas & Popesso 2018 in preparation, Popesso, Concas et al. (2018) submitted to A&A.*

## 6.1 Abstract

In this chapter we illustrate the analysis of the relation between star formation (SF) activity of local galaxies and their environment. This is done by relating the location of galaxies with respect to the Main sequence (MS) of star forming galaxies as a function of the environment, express through the host halo mass. By using the Balmer decrement-$M_{H2}$ correlation studied in the previous chapter, we investigate if the environment acts in reducing the availability of cold molecular gas, which is the fuel for the star formation process. We will first summarize the results of Popesso, Concas et al. (2018) on the bending of the MS in the local Universe and the increase of the scatter towards the high mass regime. We will highlight the role of the environment as a possible driver of the MS shape in particular towards high stellar masses. Furthermore, we will consider the distribution of the molecular gas mass in the SFR-M$\star$ plane and how the environment drives the decrease of the molecular gas fraction along the MS. We will discuss the gas starvation, induced by the fall of galaxies in the massive halos and the consequent inability of the hot corona to cool efficiently, might be the main mechanism for setting the molecular gas content in massive galaxies.

## 6.2 The Main Sequence of star forming galaxies.

In this section we briefly summarize the main results of Popesso, Concas et al. (2018). We investigate the slope and shape of the MS in the local Universe by using different dataset. In particular, we perform the analysis of the SFR distribution in the MS region for galaxies with masses above $10^{10} M_{\odot}$. Such distribution is used to define the MS location

and its scatter with different indicators. To this aim we use the most robust and reliable SFR indicators available, either the dust corrected $H\alpha$ based SFR, or the combination of the UV light emitted by young stars and the IR luminosity, accounting for the UV component absorbed and reprocessed by dust. In particular, we use two different samples: the SDSS spectroscopic sample, MPA-JHU dataset, with SFR based mainly on corrected $H\alpha$ SFR (Brinchmann et al., 2004) and the WISE sample matched to the SDSS sample of Salim et al. (2016), WISE dataset hereafter, with SFR based on WISE 22 $\mu$m data, when available, and dust corrected UV based SFR. To further check our results we use also the far infrared H-ATLAS *Herschel*/SPIRE based SFR of Valiante et al. (2016). The details of each dataset: MPA-JHU, WISE and H-ATLAS *Herschel*/SPIRE are widely described in Chapter 2.

To take into account different biases, either due to the infrared or the UV galaxy selection and the different SFR indicators, we perform the analysis with each catalog. In particular, we define the following subsamples:

- a) the MPA-JHU catalog (defined by its SFR indicators as "H$\alpha$+D4000" sample);
- b) the Salim et al. (2016, hereafter S16) sample with 22 $\mu$m WISE SFR, when available, and SFR from SED fitting for all WISE undetected galaxies (hereafter "WISE+SED fit" sample);
- c) the subsample of S16 limited to WISE detected sources at 22 $\mu$m, complemented with galaxies classified as star forming in the BPT diagram and with SFR derived from dust corrected H$\alpha$ in the MPA-JHU catalog (hereafter "WIRE+$H\alpha$" sample);
- d) the S16 sample with SFR based purely on SED fitting (hereafter "SED fit")
- e) the H-ATLAS sample (hereafter "SPIRE" sample).

In all cases we apply a redshift cut at $z = 0.085$ in order to ensure mass and SFR completeness down to $10^{10} M_{\odot}$ (see also Peng et al. 2010).

All SFR and stellar masses are converted to a Chabrier initial mass function (IMF, Chabrier 2003), when, necessary, for consistency.

We study the shape of the distribution of the residuals $\Delta MS = \log(SFR_{gal}) - \log(SFR_{MS})$ given by the distance from the SFR of the individual galaxy ($SFR_{gal}$) and the SFR on the MS at the mass of the galaxy ($SFR_{MS}$). In particular, we use as reference the MS relation of Renzini & Peng (2015). This is obtained as the peak of the SFR distribution in the $\log(SFR) - log(M\star)$ plane in the stellar mass range $10^8 - 10^{10.5}$ $M_{\odot}$, where the H$\alpha$ SFRs of the MPA-JHU sample dominate in number the MS region. Thus, we consider it an accurate estimate of the MS location in the low stellar mass regime. This approach allows us to verify if the MS is bending at higher stellar masses with respect to the best fit relation of the lower stellar mass regime.

Fig. 6.1 shows the distribution of the residuals $\Delta MS$ for the different galaxy samples considered here. In all cases the upper envelope is well fitted by a log-normal distribution (the black Gaussian in logarithmic scale in each panel). The red vertical line in each

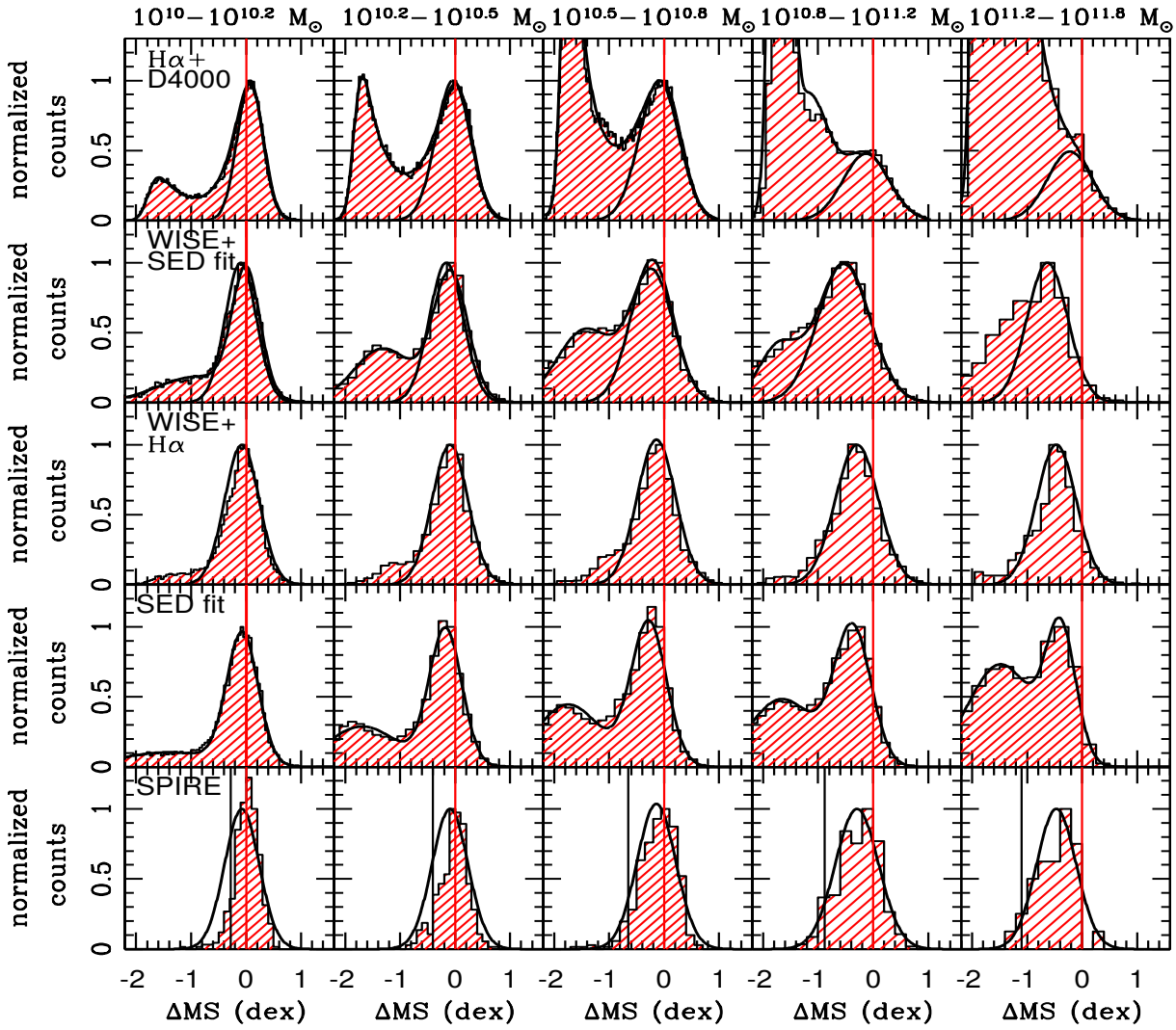


Figure 6.1: Distribution of the residual $\Delta MS$ around the MS in several stellar mass bins in the local Universe (red shaded histogram). The vertical red line, in all panels, shows the $\Delta MS = 0$ point corresponding to the MS location given by the linear relation of Renzini & Peng (2015). Each row shows the distribution based on different samples. From the top to the bottom we show the distribution of the residuals based on a) the MPA-JHU SFR and stellar mass estimates ("H$\alpha+D4000$"), b) the S16 sample with SFR based on WISE 22 $\mu$m data-point, when available, and SFR based on SED fitting elsewhere ("WISE+SED fit") c) the S16 subsample with SFR based on WISE 22 $\mu$m data-point, when available, and SFR based on dust corrected H$\alpha$ flux from MPA-JHU catalog for BPT classified SF galaxies ("WISE+H$\alpha$"), d) the S16 sample with SFR based on SED fitting only ("SED fit"), d) the H-ALTLAS 250 $\mu$m selected sample with SFR derived from far-infrared data ("SPIRE"). In the bottom row the black vertical line show the luminosity limit corresponding to the $5\sigma$ limit of the $250\mu$ selected sample of Valiante et al. (2016). The solid curve in each panel shows the best fit normal distribution in the log-log space. For the "H$\alpha + D4000$", "WISE+SED fit", and "SED fit" samples we show also the best fit curve of the whole distribution including the quiescence region. In all panels the distribution is normalized to the peak of the MS distribution.

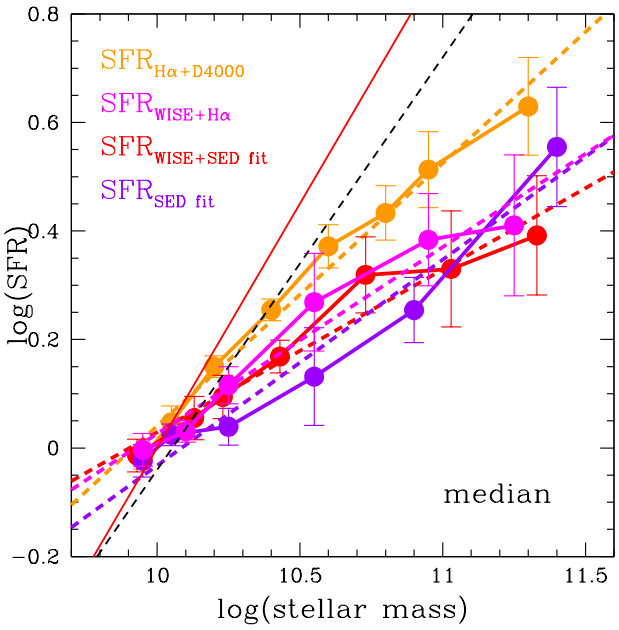


Figure 6.2: Location of the MS based on the *median* of the best fit log-normal distribution for the different samples. The dashed lines of different color show the best fit linear regression on each sample. The color code of points and lines is indicated in the figure. The black dashed line indicates the relation of Renzini & Peng (2015) the red line shows the relation of Peng et al. (2010).

panel shows the $\Delta MS = 0$ location corresponding to the value of the MS according to the log-linear relation of Renzini & Peng (2015). It is apparent that the peak of the $\Delta MS$ distribution is not consistent with 0 in all samples towards high stellar masses. The significance of the deviation, however, depends on the SFR indicator used for the analysis. In all cases, the peak of the distribution falls below 0 at least above $10^{10.5}$ $M_{\odot}$, suggesting that the MS location is bending towards lower values of SFR.

Fig. 6.2 shows the MS location for each sample based on the median SFR of the log-normal distribution, retrieved by fitting the upper envelope of the SFR distribution. The "H$\alpha$+D4000" and the S16 "WISE+$H\alpha$" samples agree within $1\sigma$ up to $\sim 10^{10.5}$ $M_{\odot}$. Above this threshold, in the "H$\alpha$+D4000" sample the peak of the distribution in the log-log space is less significant and it completely disappears at masses above $10^{11}$ $M_{\odot}$. This is mainly due to the fact that the "H$\alpha$+D4000" sample is completely dominated by the uncertain D4000 estimates of the SFR at high masses. The S16 "WISE+SED fit" and "WISE+$H\alpha$" samples show in all cases a clear peak in the MS locus at any stellar mass and with a more significant bending than with in the S16 "H$\alpha$+D4000" sample.

The median of the SFR distribution of the S16 "SED fit" sample lies below the other relations almost at any mass bin. We ascribe this discrepancy to the systematic underestimation of the SFR from SED fitting in the upper envelope of the MS (see for details Popesso, Concas et al. 2018).

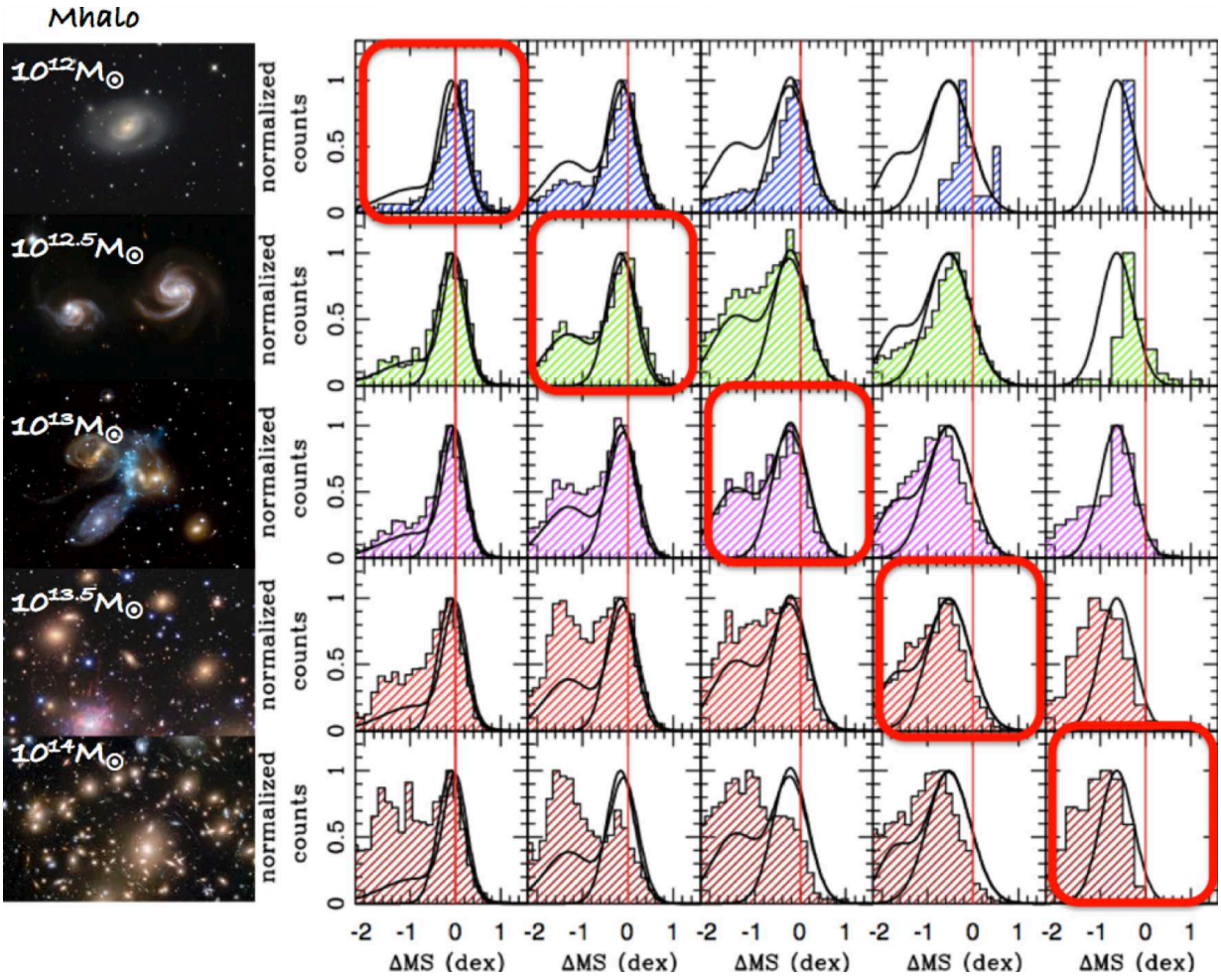


Figure 6.3: Distribution of the residual $\Delta MS$ around the MS in several stellar mass bins (horizontal axis) and as a function of the host halo mass (vertical direction). Each row shows the distribution in a bin of halo mass as retrieved in the Yang et al. (2007) catalog, from halo masses below $10^{12}$ $M_\odot$ for isolated galaxies to masses above $10^{14}$ $M_\odot$ in the galaxy cluster regime. The solid curve show the best fitting normal distribution of Fig. 6.1 found as a function of the stellar mass in the "WISE+ SED fit" sample.

We point that the observed bending is not affected by the excess of galaxies observed in the lower envelope of the MS towards high stellar masses. Indeed, the MS location is identified as the peak of the $\log(SFR)$ distribution which accurately found by fitting only the upper envelope of the relation.

By matching the "WISE+SED fit" sample with the halo mass catalog of Yang et al. (2007), we associate to each galaxy the value of the host halo mass and the classification as central and satellite galaxy. The halo mass catalog is described in Chapter 2. Note that the halo masses are only available for halos with $M_{halo} > 10^{11.5}$ M$\odot$ (Yang et al., 2007), because this is the lower limit of the characteristic stellar mass-halo mass calibration provided in

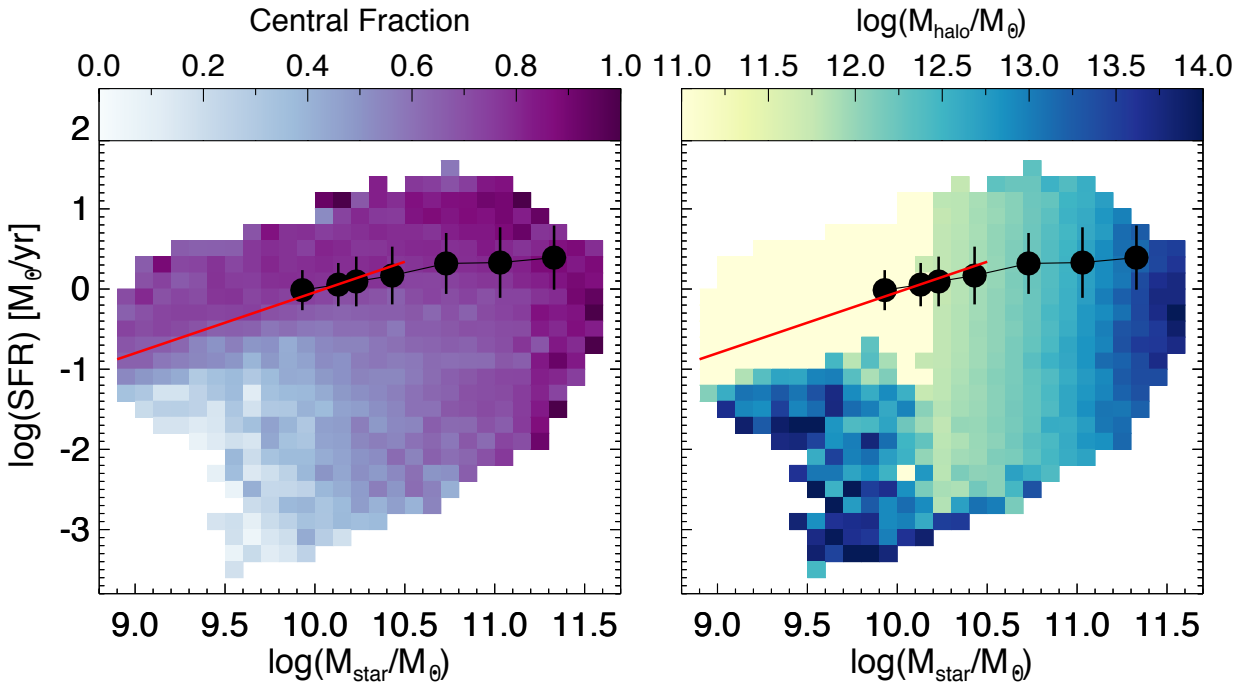


Figure 6.4: *Left panel*: SFR-M⋆ plane based on the S16 $WIDE + SEDfit$ sample, color coded as a function of the fraction of central galaxies identified in the host halo catalog of Yang et al. (2007). *Right panel*: same as the left panel but color coded as a function of the mean host halo mass in bin of SFR and M⋆ 0.1 dex × 0.2 dex wide. Also the host halo mass is retrieved by matching the Salim et al. (2007) catalog with the halo mass catalog of Yang et al. (2007). At very low masses (below $10^{10}$ $M_{\odot}$) dominate isolated galaxies in low mass halos for which only an upper halo mass limit is provided in the Yang et al. (2007) catalog. This is why in this region it is not possible to observe any halo mass gradient as at higher masses. In both panels the black points indicate the location of the local MS based on the median indicator while the red solid line shows the relation of Renzini & Peng (2015) at lower masses.

that work. To isolated galaxies at stellar masses below the calibration limit we associate a host halo mass upper limit of $10^{11}$ $M_{\odot}$.

In order to highlight the role of the environment defined by the halo mass value, we analyze the $\Delta MS$ distribution of the "WISE+SED fit" sample as a function of the host halo mass (see Fig. 6.3). As shown in Fig. 6.3, galaxies in low mass halos tend to be located in the upper envelope of the MS, while galaxies in massive halos favor lower SFR in the lower envelope of the distribution. This is particularly evident in the high stellar mass regime above $10^{10.5}$ $M_{\odot}$.

In addition, as shown in the right panel of Fig. 6.4, the mean host halo mass in the SFR-M⋆ plane is increasing along the MS with the stellar mass. This indicates that galaxies in massive halos dominate statistically the MS population at high stellar masses, thus shaping the MS in this mass regime. This is due to the fact that the vast majority

of galaxies are central galaxies (left panel of Fig. 6.4). In addition the stellar mass of the central galaxy and the host halo mass are strictly related by the known $\frac{M_{\star,cen}}{M_{halo}}$-$M_{halo}$ relation, where $M_{\star,cen}$ is the stellar mass of the central galaxy and $M_{halo}$ is the total mass of the host halo (Behroozi et al., 2013; Yang et al., 2009). It is worth to notice that the region where the MS is mostly bending above $10^{10.5}$ $M_{\odot}$ corresponds to host halo mass of $\sim 10^{12-12.5}$ $M_{\odot}$. Such mass range is considered to be the mass threshold for the transition between a regime of cold to hot accretion (Dekel & Birnboim, 2006; Kereš et al., 2009). In low mass halos, below $\sim 10^{12-12.5}$ $M_{\odot}$, the central galaxy is fed with cold gas by the gas streams coming from the cosmic filaments. In high mass halos, instead, the gas filling up the halo volume is shocked heated to the halo virial temperature during the gravitational collapse and the cold gas streams are no longer able to penetrate the halo and replenish the central galaxy of cold gas (Kereš et al., 2009). Such lack of cold gas supply above the $\sim 10^{12-12.5}$ $M_{\odot}$ halo mass threshold might limit the fuel for the galaxy SF process and so lower the galaxy SFR, leading to the observe bending.

To test this possibility we explore the relation between the molecular gas mass fraction of galaxies and the host halo mass.

## 6.3 The impact of the environment on the gas reservoir.

In order to relate the molecular gas mass fraction of galaxies to their environment, we take advantage of the $M_{H2}$-Balmer decrement relation presented in Chapter 5. This is used to convert the Balmer decrement value, provided by the MPA-JHU sample for most of the star forming galaxies, into molecular gas mass, $M_{H2}$. This approach has several advantages. First, it allows to keep the very high statistics of the SDSS DR7 sample, which is mandatory for environmental studies. Indeed, even the xCOLD GASS sample (Saintonge et al., 2017), which is the largest available with a reliable measure of the molecular gas mass, provides a limited number of less than 100 MS galaxies above $10^{10.5}$ $M_{\odot}$. This does not provide a statically significant sample once it is further divided in subsamples as a function of the host halo mass. Our approach, instead, allows to have a reliable estimate of the molecular gas mass, calibrated on the xCOLD GASS estimates, for a statistically significant sample of $\sim$ 160,000 galaxies, at $z < 0.2$ and stellar mass above $10^{10}$ $M_{\odot}$, for which the MPA-JHU catalog provides a measure of the Balmer decrement (see Chapter 2 for more details). In addition, since the MS is dominated by central galaxies, as shown in the previous section, we limits our analysis to the galaxies identified as central in the Yang et al. (2007) host halo mass catalog. We use this sample to quantify the variation of the molecular gas fraction ($f_{H2} = M_{H2}/M\star$) in the SFR-M$\star$ plane and as a function of the environment.

### 6.3.1 Sample and methodology

The main ingredients of our analysis are the galaxy stellar mass, M$\star$, and SFR to locate galaxies in the SFR-M$\star$ plane as a function of their distance from the MS, the H$\beta$ and

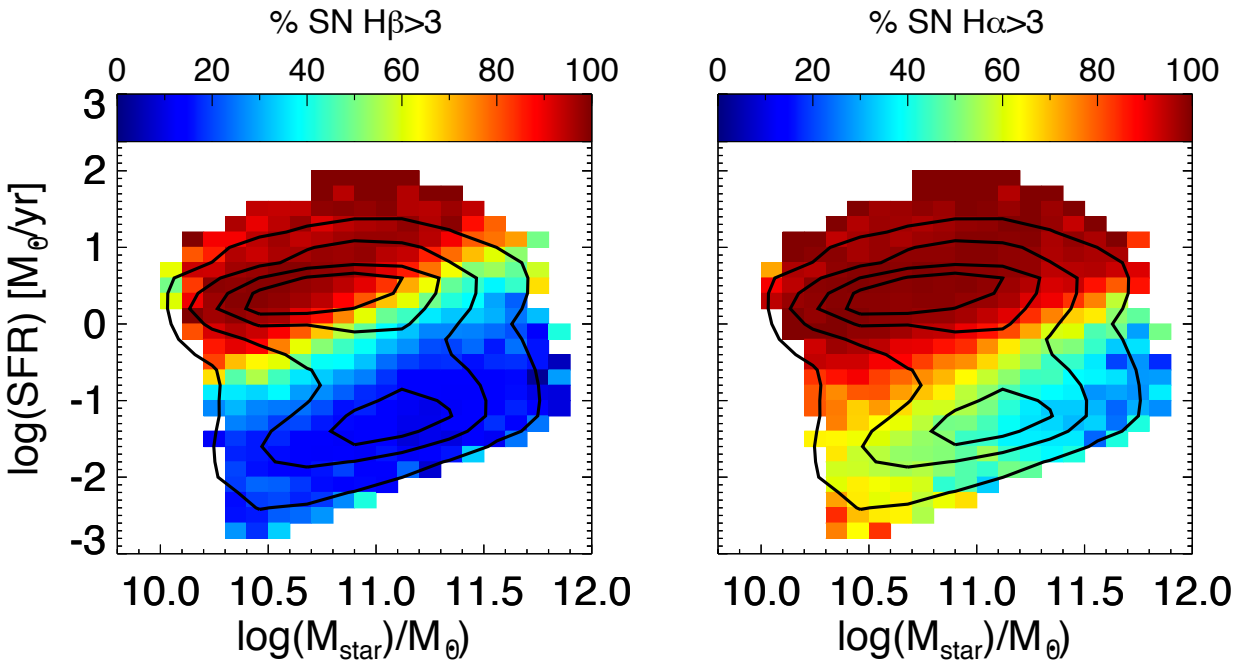


Figure 6.5: Percentage of central galaxies with well detected, signal-to-noise ratio, SN> 3, H$\beta$ (left panel) and H$\alpha$ (right panel), in the SFR-M$\star$ diagram. The Main Sequence of star forming galaxies and the region above it, are characterized by a high percentage of both Balmer emission line galaxies at high SN. From outside to inside the contours encompass 5, 25, 50 and 75 per cent of the data points.

H$\alpha$ line fluxes to estimate the Balmer decrement of individual galaxies and a measure of the galaxy environment. The reference sample is the "WISE+SED fit" sample described above and taken from Salim et al. (2016), whereas the stellar masses are derived via SED fitting and the SFR is based on the WISE 22 $\mu$m emission, when available, and otherwise on the SED fitting derived SFR (see Chapter 2 for a detailed description of sample and derived quantities). The environment is defined on the basis of the Yang et al. (2007) halo mass catalog as done in Popesso, Concas et al. (2018, see previous section and Chapter 2 for more details). Finally, the single Balmer line fluxes are taken from the MPA-JHU catalog [1] and are matched to the "WISE+SED fit" sample. As detailed in Tremonti et al. (2004), the observed SDSS spectra are first fitted by a combination of stellar population synthesis models from Charlot & Bruzual (in prep., CB08)[2], than, the emission line fluxes are obtained by a Gaussian fit to continuum-subtracted spectra. This procedure allows to correct the line fluxes for stellar absorption in both the H$\beta$ and H$\alpha$ region (see Chapter 2 for more details). The distribution of the galaxies percentage with a H$\beta$ and H$\alpha$ emission lines at signal-to-noise-ratio SNR $>$ 3, is shown in the left and right panel of Fig. 6.5,

[1] http://www.mpa-garching.mpg.de/SDSS/DR7/

[2] The spectra are available as part of the GALAXEV package, which is can be obtained from http://www2.iap.fr/users/charlot/bc2003/index.html.

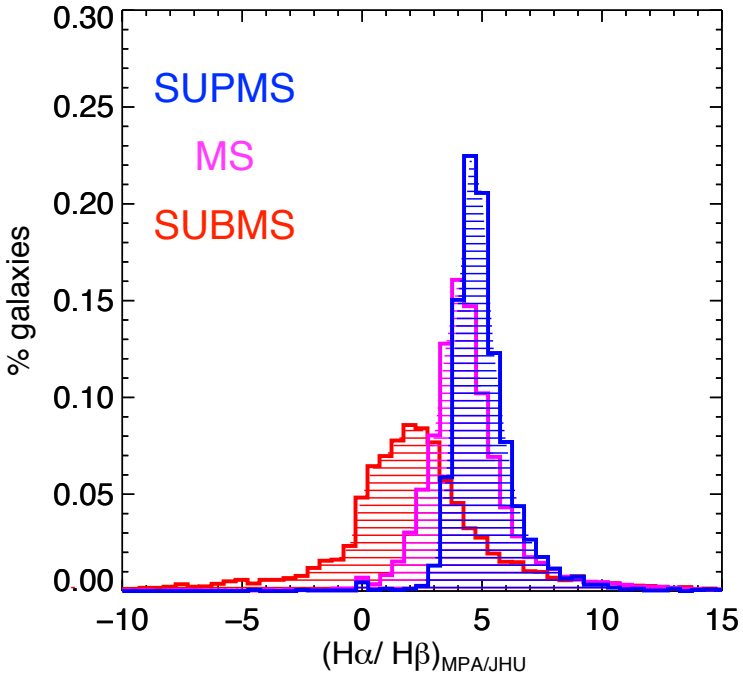


Figure 6.6: Distribution of the Balmer decrement in a small mass bin between $10^{11}$ and $10^{11.3}$ $M_{\odot}$ for three different galaxy population cells in the SFR-M$\star$ plane. We show the distribution of a cell above (blue histogram, SUPM), on (magenta histogram, MS) and below (red histogram, SUBMS) the MS.

respectively. Galaxies with high SNR in the H$\alpha$ line dominate the whole MS region, including the lower envelope, while the H$\beta$ exhibits a much lower SNR, which tends to be below 3 (no detection) towards the quiescence region. However, it must be noted that the H$\beta$ SNR tend to be low also in the MS region at the high mass end, where the MS is bending. This is mainly due to two facts. First, the H$\beta$ flux is less intense than the H$\alpha$ line as predicted by the atomic structure of hydrogen in the quantum theory (see the deep discussion in Sec. 1.4.3 in Chapter 1). Second, it might be more extincted by dust. For this reason the measure of such emission flux in the individual galaxy spectrum is more affected by noise than the H$\alpha$ emission.

To overcome this problem and obtain a reliable estimate of the Balmer decrement along and across the MS, we tackle the issue from a statistical point of view. Rather than considering individual galaxies, we considered population of galaxies, defined as a function of their location with respect to the MS and as a function of their halo mass. To this aim, we divide the SFR-M$\star$ plane in a grid of cells 0.2 dex wide in $\log(SFR)$ and $\log(\mathrm{M}\star)$ and we consider the mean Balmer decrement of the population in each cell of the grid. This approach is the same adopted for the analysis of the [OIII] emission line and the NaD absorption line profiles described in Chapter 3 and 4. As an example, we show the distribution of the Balmer decrement in a stellar mass bin at $10^{11} - 10^{11.3}$ $M_{\odot}$ and in three bin of SFR, namely above, on and, below the MS, see Fig. 6.6. As confirmed by a KS test,

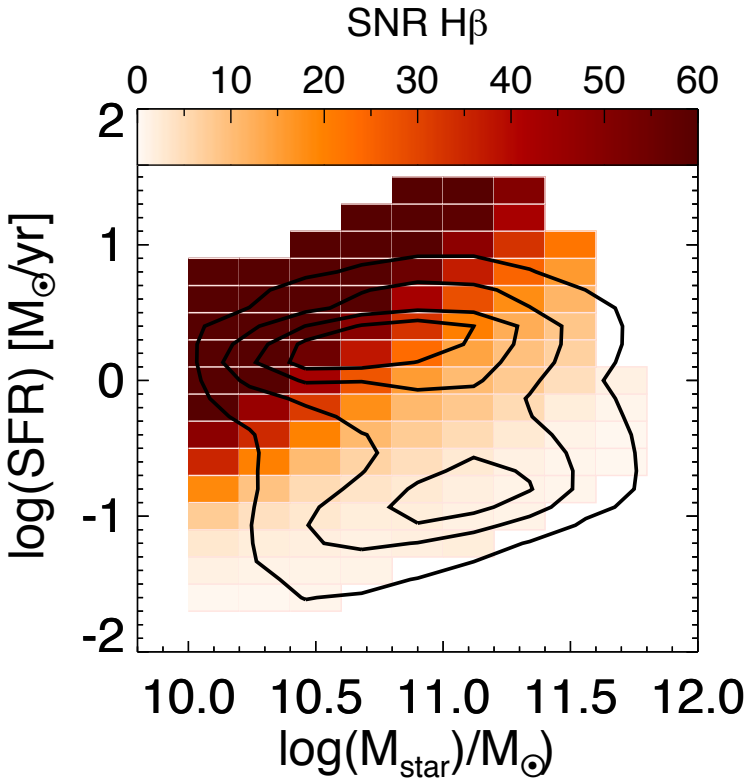


Figure 6.7: Signal-to-noise ratio, (SNR) of the H$\beta$ emission line calculated in the stacked spectra, in the SFR-M$\star$ diagram. The line is well detected (SNR$>$ 3) in the whole plane, except for the extreme region of passive galaxies. From outside to inside the contours encompass 5, 25, 50 and 75 per cent of the data points.

the three distribution are not drawn from the same parent distribution and their mean and median values different by few $\sigma$. This indicates that the method allows us to highlight differences in the mean Balmer decrement along and across the MS.

In order to check the reliability of the mean Balmer decrement estimated in this way, we perform also a stacking analysis of the spectra in each cell. As previously described in Chapter 3 Section 3.4.1 and Chapter 4 Section 4.4.1, we use a combination of the publicly available codes pPXF (Cappellari & Emsellem, 2004) and GANDALF (Sarzi et al., 2006) to fit and remove the stellar continuum and to derive H$\beta$ and H$\alpha$ emission line fluxes. We find that the H$\beta$ emission line fluxes retrieved in this way exhibit a very high SNR ($>$ 10) in the hole MS region, including its lower envelope (Fig. 6.7). In addition, the mean Balmer decrement retrieved from the individual galaxies distribution and the one derived from the stacked spectra are in very good agreement within the error bars.

The molecular gas mass is estimated for each galaxy by using the calibration between Balmer Decrement and $M_{H2}$ as described in Chapter 5 thorough the following equation:

$$\log(M_{H2}) = 4.2\pm2.0 \times \log(BD) + 6.3\pm1.3 \quad (6.1)$$

where BD is the Balmer decrement provided by the ratio of the H$\alpha$ and H$\beta$ fluxes. The

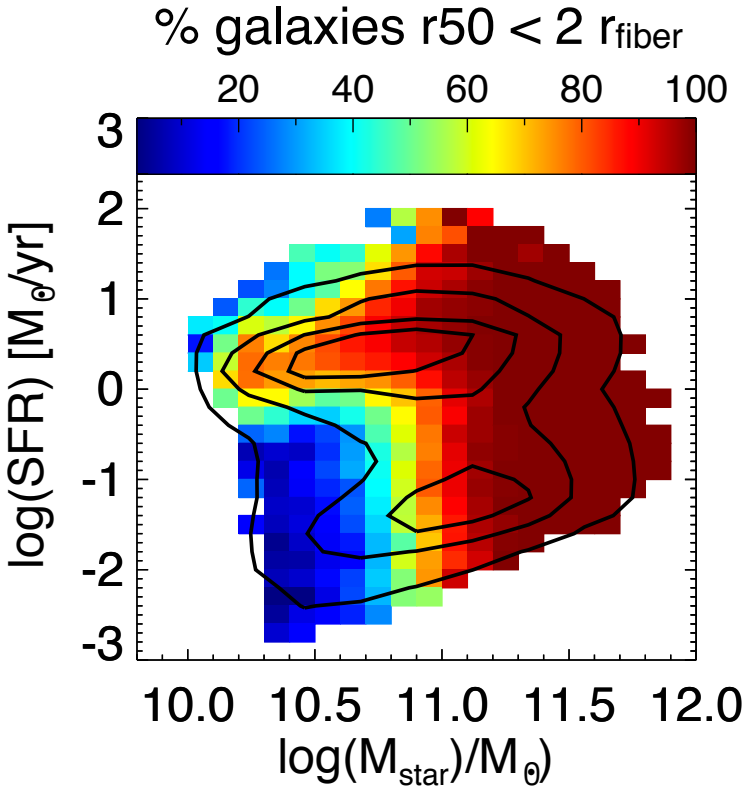


Figure 6.8: Percentage of galaxies completely sample, $r_{50} < 2 \quad r_{fiber}$ by the SDSS fiber, in the SFR-M$\star$ diagram. The galaxy size, estimate by the radius that contains the 50% of the galaxy light (in r band, $r_{50}$) is compare to the physical region sampled by the spectral fiber ($r_{fiber}$). Statistically, along the whole MS the galaxies are completely sample by the spectral fiber, the percentage of galaxies with $r_{50} < 2 \quad r_{fiber}$ is $> 70 - 80\%$. From outside to inside the contours encompass 5, 25, 50 and 75 per cent of the data points.

error on such estimate is calculated via error propagation of the Eq. 6.1.

As point out in the previous Chapter, the H$\alpha$ and H$\beta$ lines are derived in the galaxy region sampled by the SDSS fiber, whose diameter is 3 arcsec. In previous Chapter, we identify the limited area sample by the SDSS fiber as the main source of scatter in the Balmer decrement-$M_{H2}$ correlation. Indeed, as shown in Fig 5.3 in Chapter 5, for galaxies with a $r50$ (the radius encapsulating 50% of the total galaxy light) more than twice the fiber radius of 1.5", the Balmer decrement results too low for the observed molecular mass. This is due to the fact that the fiber area samples only the central galaxy region, where the presence of a poorly active or gas poor bulge component might bias the value of the Balmer decrement towards low level of dust reddening. For this reason we exclude all the galaxies with $r50 > 3$arcsec. As shown in Fig. 6.8 this does not affect the region of the MS peak, where most of the galaxies are fully sampled by the fiber area, but it affects the starburst region, well above the MS and the lower envelope of the MS at masses $10^{10} - 10^{10.5}$ $M_{\odot}$. This is due to two aspects. First, since the SDSS spectroscopic sample is a magnitude

limited sample, the higher the redshift the higher the absolute magnitude limit. Thus, the high stellar mass end is dominated by the most distant galaxies, whose apparent size is smaller than the fiber aperture. In addition, as shown in Morselli et al. (2018, in prep.), galaxies in the SB region tend to be more extended than the MS counterpart at fixed stellar mass. In order to avoid any bias in our analysis we keep only the cells of the SFR-M$\star$ grid where at least 70% of the galaxy population has $r50 < 3$arcsec. This limits our analysis to the region within $\pm 1$ dex from the MS at masses below $10^{10.5}$ $M_{\odot}$, while at larger masses we can consider the whole SFR range.

### 6.3.2 Results

In the following sections, we investigate how the molecular gas mass fraction, $f_{H2} = \mathrm{M}_{H2}/\mathrm{M}\star$, varies as a function of several global galaxy properties: stellar mass (M$\star$), host halo mass ($\mathrm{M}_{halo}$), and location in SFR-M$\star$ diagram. The purpose is to understand the role of environment, if any, in the bending of the MS towards high stellar masses (see Section 6.2).

To classify galaxies as a function of their position with respect to the MS, we split our sample in three galaxy subsamples, as follows:

- *(i)* the Main Sequence galaxy sample, MS hereafter, as the galaxies which reside between $\pm 1\sigma$ from the MS, as defined in Popesso, Concas et al. (2018) for the "WISE+SED fit" sample used for this analysis (see Section 6.2);
- *(ii)* the MS upper envelope, SUPMS hereafter, as the galaxies located above $1\sigma$ from the MS and,
- *(iii)* the MS lower envelope, SUBMS hereafter, as the galaxies located between 1 and $3\sigma$ below the MS.

We quantify the strength of any correlation between $f_{H2}$ and the different galaxy properties on the basis of the Spearman correlation coefficients ($\rho$, Spearman 1904).

#### Molecular gas fraction in the SFR-$M\star$ plane for central galaxies

The distribution of the central galaxies sample in the SFR-M$\star$ diagram is presented in Fig. 6.9, color-coded as a function of the Balmer Decrement value (left panel), and, as a function of the molecular hydrogen gas mass fraction, $\mathrm{f}_{H2}$ (right panel).

The H$\alpha$/H$\beta$ goes from the low values, $\sim 2-3$, expected in case of dust free HII regions, in the quiescent region of the passive non star forming galaxies, to higher values $\sim 5-5.5$ in more star-forming galaxies. Very massive star-forming galaxies in the upper MS envelope exhibit the highest values of H$\alpha$/H$\beta$, pointing to a very high level of dust reddening. However, when we use the derived molecular gas fraction, $f_{H2}$, we observe a clear anti-correlation with the stellar mass. As more clearly shown in Fig. 6.10, $f_{H2}$ of individual galaxies appears to clearly anti-correlate with the stellar mass for central galaxies, in all

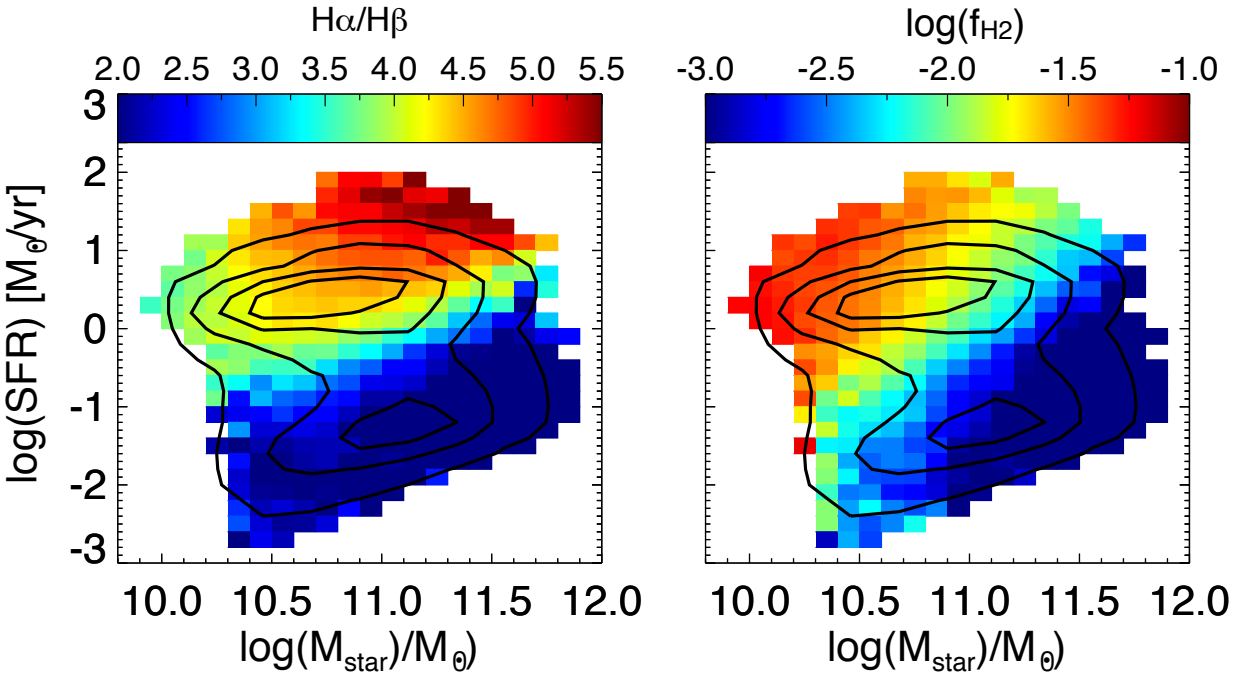


Figure 6.9: *Left panel*: Balmer Decrement, H$\alpha$/H$\beta$, in the SFR-M$\star$ diagram for our central galaxies. *Right panel*: Molecular gas mass fraction, f$_{H2}$, in the SFR-M$\star$ diagram for our central galaxies. From outside to inside the contours encompass 5, 25, 50 and 75 per cent of the data points.

galaxy subsamples, on, above and below the MS, respectively. This result is in good agreement with the previous scaling relations of Saintonge et al. (2017) obtained with the xCOLD GASS sample (512 galaxies). The correlation is stronger for the galaxies located above and along the MS subsamples, while is less pronounced in the SUBMS galaxies. This is confirmed by the Spearman correlation coefficient $\rho = -0.49$ for the SUPMS and MS samples and, $\rho = -0.22$ for the SUBMS galaxies. However, one should take into account that below the MS, most of the galaxies are low SNR emission line galaxies. This leads to very noisy estimates of the Balmer decrement and, in turn, of the molecular gas mass fraction.

Similarly, Fig. 6.11 shows the molecular gas fraction, $f_{H2}$, of individual galaxies as a function of the host halo mass. Also in this case we observe a significant anti-correlation in each sample with a similar value of the Spearman correlation of the $f_{H2}$-stellar mass relation. This is expected for central galaxies, because the central galaxy stellar mass is related to the host halo mass as explained in previous sections (e.g., Behroozi et al., 2010; Yang et al., 2012).

However, to obtain a more robust result, we estimate the mean $f_{H2}$ from the mean Blamer decrement in the cells of the SFR-$M\star$ grid, where at least 70% of the galaxy population is well sampled by the fiber aperture ($r50 < 3$ arcsec). We estimate $f_{H2}$ also from the Balmer decrement obtained from the stacked spectra in each cell. Fig. 6.12 shows

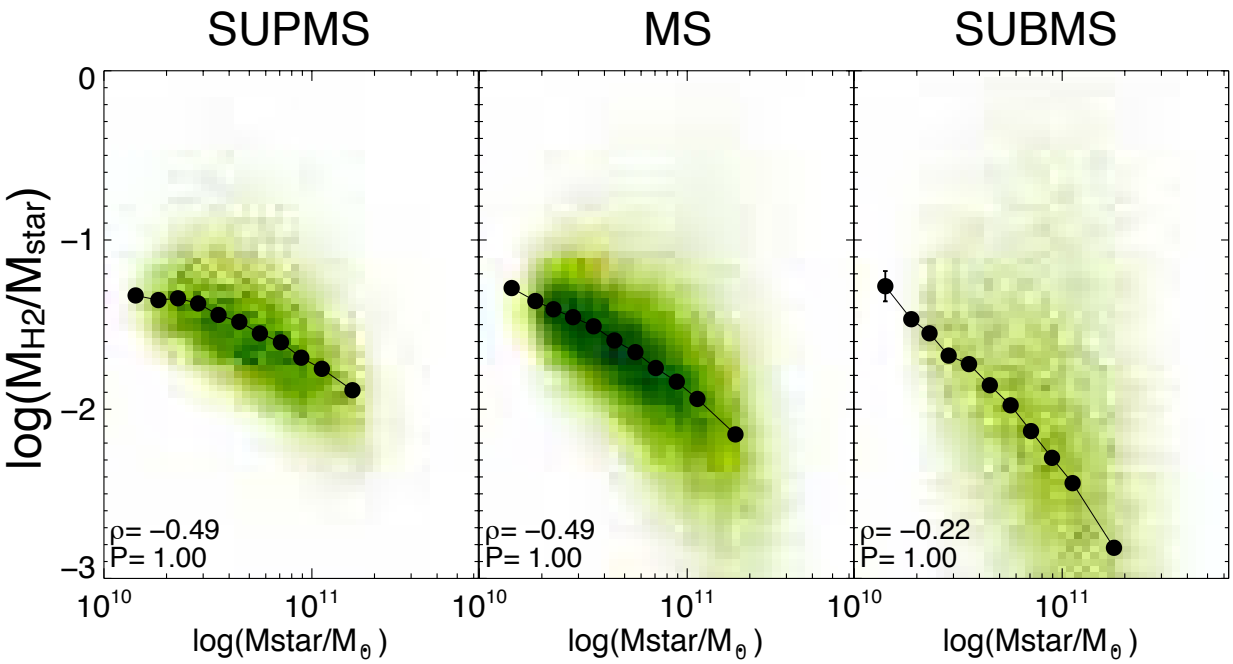


Figure 6.10: Molecular gas mass fraction, $f_{H2} = M_{H2}/M\star$ as a function of stellar mass, M$\star$, for central galaxies located above (SUPMS), along (MS) and below (SUBMS) the Main Sequence of star forming galaxies (defined as the median indicator in previous section, see Popesso, Concas et al. 2018a), left, middle and right panel, respectively. The black points are the averaged $\log(f_{H2})$ values in bin of stellar mass. In each panel, the Spearman correlation coefficient of the $\log(f_{H2}) - \log(M\star)$ relation ($\rho$) is shown. The $f_{H2}$ clearly decrease with the stellar mass in all the three samples.

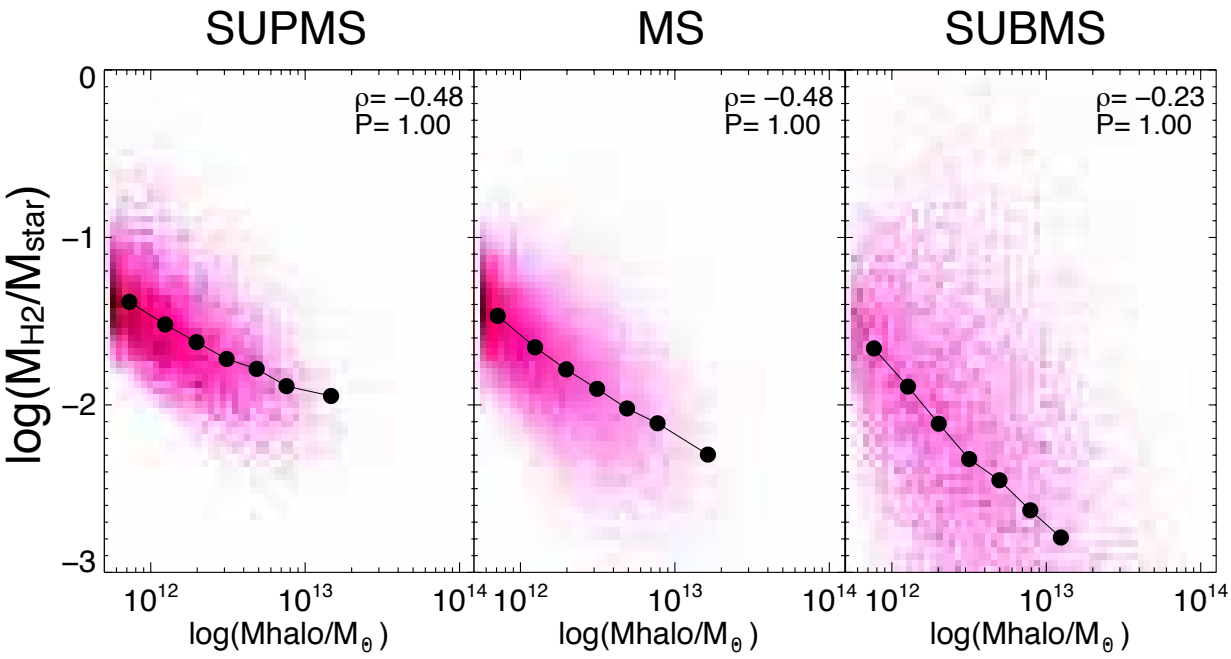


Figure 6.11: Molecular gas mass fraction, $f_{H2} = M_{H2}/M\star$ as a function of halo mass, $M_{halo}$, for central galaxies located above (SUPMS), along (MS) and below (SUBMS) the Main Sequence of star forming galaxies (defined as the median indicator in previous section, see Popesso, Concas et al. 2018), left, middle and right panel, respectively. The black points are the averaged $\log(f_{H2})$ values in bin of halo mass. In each panel, the Spearman correlation coefficient of the $\log(f_{H2}) - \log(M_{halo})$ relation ($\rho$) is shown. The $f_{H2}$ clearly decrease with the increasing of the halo mass in all the three samples.

the variation $f_{H2}$ across the MS as a function of the $\Delta MS$ in several bin of stellar mass. The figure shows the results obtained from the mean Balmer decrement in each cell. This is fully consistent with the $f_{H2}$ indirectly obtained from the stacked spectra. We clearly see a positive correlation with $f_{H2}$ increasing from below to above the MS as found also by Saintonge et al. (2016) and at much higher redshift by Scoville et al. (2014, 2015, 2017). The higher the stellar mass the steeper the increase of the molecular gas fraction from the lower to the upper envelope of the MS.

The Figure 6.12 shows also very clearly that $f_{H2}$ decreases along the MS (dashed line in the panel) at increasing stellar mass, by more than on order of magnitude from $10^{10}$ $M_\odot$ to $10^{11}$ $M_\odot$. Even more interesting, we observe that $f_{H2}$ decreases only by a factor of 2 from $10^{10}$ $M_\odot$ to $10^{10.5}$ $M_\odot$, with a more rapid drop of 1 dex between $10^{10.5}$ $M_\odot$ to $10^{11}$ $M_\odot$, where Popesso, Concas et al. (2018) observe most of the bending of the relation. Such decrease is at least 3 times larger than the scatter of the Balmer decrement-$M_{H2}$ relation. Thus, the decrease in molecular mass fraction in the bending region is not ascribable to the error in the molecular gas mass estimates, but it is physical. We conclude that the bending of the MS towards high stellar masses is due to a dramatic decrease of the availability of molecular gas to the massive central galaxies, which dominate numerically such region

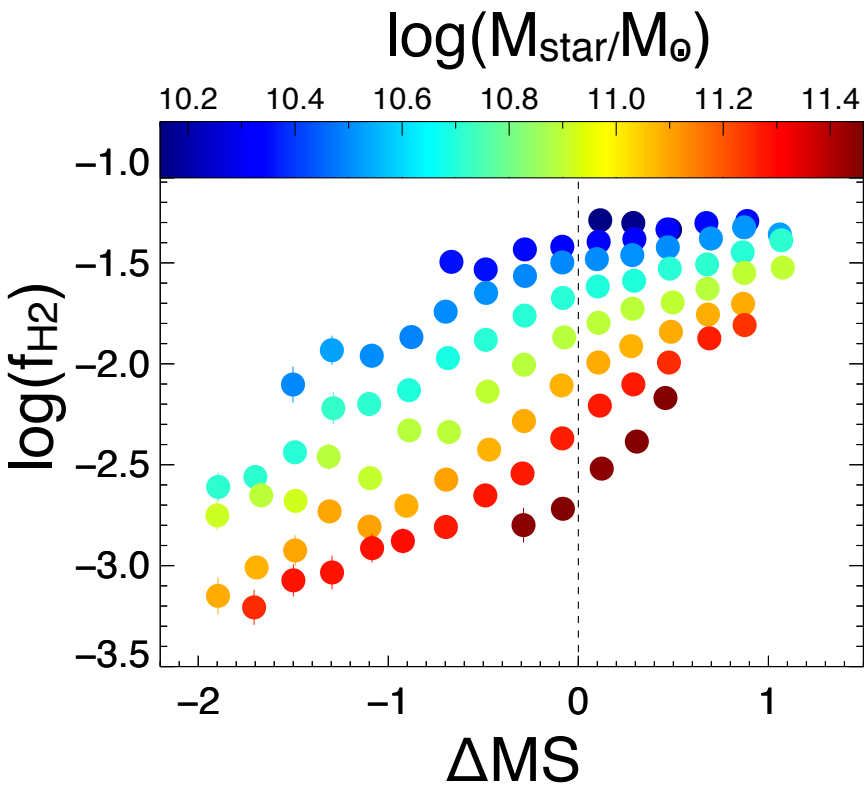


Figure 6.12: Molecular gas mass fraction, $f_{H2}$, as a function of distance from the MS, $\Delta MS$, in different stellar mass bins. The different bins of stellar mass are indicated with different colours, as defined in the color bar. The dotted vertical lines indicate the position of the MS defined as in Popesso, Concas et al., 2018. Error bars are the error in the median values.

of the SFR-$M\star$ plane. In addition, once we did the same analysis as a function of the host halo mass, as shown in Fig. 6.13, we clearly observe the same dramatic decrease of the molecular gas mass along the MS as a function of the halo mass, with the largest decrease above $10^{12-12.5}$ $M_{\odot}$. This clearly points to a close relationship between the galaxy molecular gas mass content and the environment.

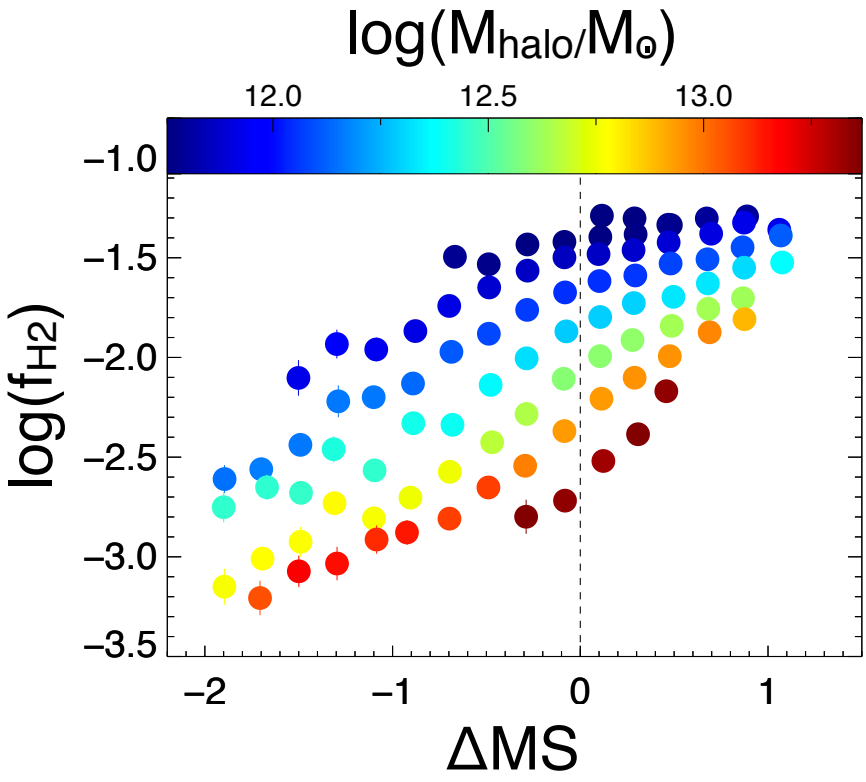


Figure 6.13: Molecular gas mass fraction, $f_{H2}$, as a function of distance from the MS, $\Delta MS$, in different halo mass bins. The different bins of halo mass are indicated with different colours, as defined in the color bar. The dotted vertical lines indicate the position of the MS. Error bars are the error in the median values.

## 6.4 Discussion

What can cause such rapid drop of the cold gas mass fraction?

One possible explanation is the change of the galaxy morphology along the MS. Indeed, several works in the literature show that galaxies along the MS tend to be purely disks at low masses and turn into more bulge dominated systems as the stellar mass increases (e.g., Wuyts et al., 2011; Whitaker et al., 2014; Erfanianfar et al., 2016; Morselli et al., 2017). Since bulges tend to have colors and star formation activity quite similar to the massive quiescence spheroidal, the increases in the bulge prominence could explain a drop in the cold gas content as a function of stellar mass along the MS. To explore this possibility, we match our galaxy sample with the morphology catalog of Simard et al. (2011). Such catalog provides an estimate of the bulge percentage through the Bulge over Total luminosity ratio (B/T, see Chapter 2 for more details). We use such estimate to analyze how the B/T is changing as a function of the stellar mass, across and along the MS. This is shown in Fig. 6.14. We do not due here the analysis of the variation of the B/T across that MS, that is fully analyzed in Morselli et al. (2017). We focus more on the variation of the B/T along the MS at increasing stellar masses. As visible in the figure, the mean B/T of galaxies

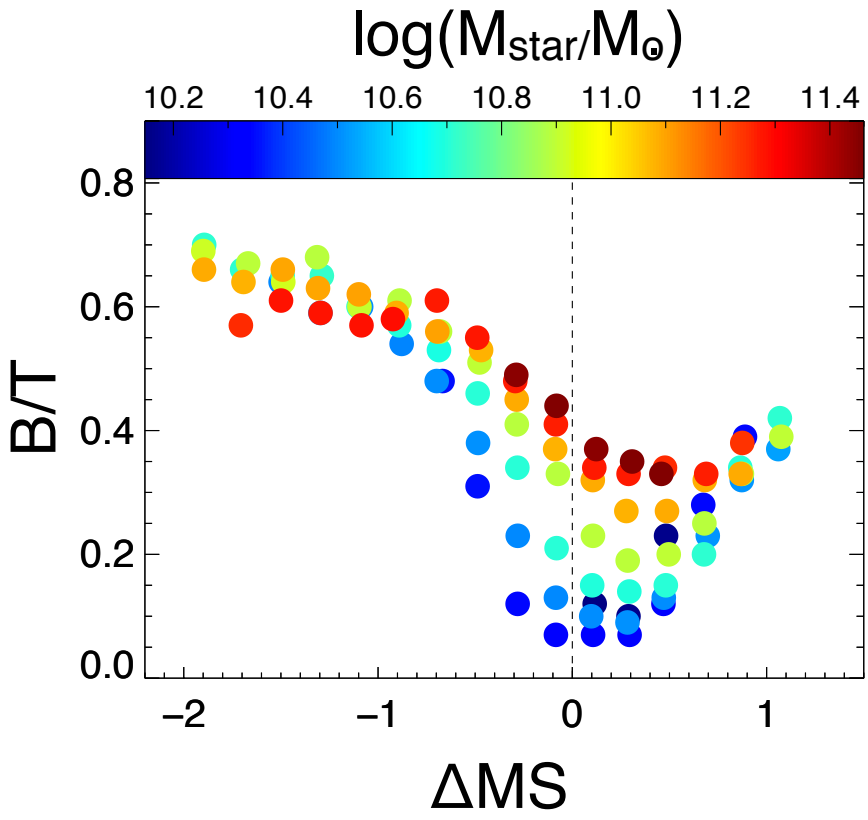


Figure 6.14: Bulge over Total luminosity ratio, B/T, as a function of distance from the MS, $\Delta MS$, in different stellar mass bins. The different bins of stellar mass are indicated with different colours, as defined in the color bar. The dotted vertical line indicate the position of the MS defined as in Popesso, Concas et al., 2018. Error bars are the error in the median values.

on the MS (dashed line at $\Delta MS = 0$) is increasing from 0.1 at $\sim 10^{10}$ $M_{\odot}$ to 0.35 above $\sim 10^{11}$ $M_{\odot}$.

Under the assumption that the central bulge component is red and dead, this would imply a $\sim 25\%$ decrease of the gas-rich region (from 10% to 35% of stellar mass located in the bulge) involved in the star formation activity. This is clearly not sufficient to explain a drop of more than 1 dex in the fraction of molecular gas mass.

There are few possible explanations for the depletion of the cold gas in the disk: (1) the cold gas is removed from the galactic disk; (2) the cold gas is heated, loosing the possibility to form new stars; and-or, (3) the cold gas reservoir is consumed without replenishment.

The common physical processes advocated to explain the lack of cold gas in galaxies via point (1) and (2) are the feedback from active galactic nuclei (AGN), and star formation activity (SF). According to simulations, both mechanisms are supposed to be able to swipe away the cold gas supply, and/or to heat the cold gas and so prevent the formation of new stars. The massive and energetic outflows powered by the AGN are routinely detected at low and high redshift (see Chapter 1 and the recent review of Harrison 2017). Despite the

amount of such detections, from a pure empirical point of view it is not fully understood if and how the presence of such winds can be related to the gas reservoir and so to the star formation activity of the host galaxy (Woo et al., 2017; Cresci & Maiolino, 2018). On the other hand, the formation of massive stars can reduce the availability of the cool gas to fuel further star formation episodes via large-scale outflows due to multiple Supernovae explosions (e.g., Chevalier, 1977; Murray et al., 2005a; Hopkins et al., 2014). However, while the role of SF feedback in the models seems to be crucial for dwarf galaxies, it is not very clear for massive systems (Hopkins et al., 2008).

Nevertheless, as it is shown in Chapter 3 and 4 (Concas et al. 2017b and 2018a), in the local galaxies both the the SF- and AGN-induced winds are characterized by very low velocity (lower than the escape velocity of the galaxy), suggesting that the outflowing gas remains bound to the galaxy and likely falls back to the disk, as suggested by the "galaxy fountain" scenario (e.g., Shapiro & Field, 1976; Fraternali & Binney, 2006; Fraternali, 2017). The gas might cool down and fall back onto the galactic disk, leading to the replenishment of cold gas and triggering further episodes of SF activity. Thus, SF- and AGN-induced outflows in the local Universe cannot be considered as the main mechanism for driving the molecular gas away from the galactic disk.

Here we propose that the environment might play a crucial role. Indeed, the fact that MS is bending where the galaxy population is dominated by central galaxies of group and cluster sized halos, and the molecular gas fraction is decreasing along the MS as a function of the halo mass, would suggest a close relationship between the availability of cold gas and the environment.

From a theoretical point of view, this is established in the mass accretion theory, as already pointed out in Chapter 1. Indeed, the $10^{12} - 10^{12.5}$ $M_{\odot}$ host halo mass, which in terms of central galaxy stellar mass corresponds roughly to $10^{10.5}$ $M_{\odot}$, is considered to be the mass threshold for the transition between two distinct channels of gas accretion: the so called "cold" and "hot" accretion modes (Katz et al., 2003; Kereš et al., 2005, 2009; Birnboim & Dekel, 2003; Dekel & Birnboim, 2006; Dekel et al., 2009). According to the cosmological simulation, at low halo masses, below $10^{12-12.5}$ $M_{\odot}$, the growth of the central galaxy is expected to be dominated by the "cold mode" accretion, which occurs through cold gas streams coming from the cosmic filaments. Instead, above the same halo mass threshold the intra-group and intra-cluster medium is shock-heated to the virial temperature at $10^6 - 10^7$ K during the gravitational collapse. In such hot atmosphere, the cold gas streams are disrupted and are no longer feeding the star formation process of the central galaxy, taking the galactic disk to a regime of cold gas starvation (e.g., Birnboim & Dekel, 2003; Dekel & Birnboim, 2006; Dekel et al., 2009; Kereš et al., 2009).

The reduced molecular gas mass fraction observed in this work would be consistent with such scenario. However, if the hot atmosphere of the massive halos induce a substantial gas starvation, the local MS should appear nearly gas empty in the high stellar mass end. Indeed, the molecular gas depletion time at the SFR observed in the local Universe is about 1 Gyr (Saintonge et al., 2016). Why do we observe so many massive galaxies still in the MS region and well above the MS at very high SFR?

A possible explanation can be provided by the interaction between the hot gas around

the central galaxy (hot corona) and the ejected material from the galactic disk, as proposed by fountain-driven accretion model (e.g., Shapiro & Field, 1976; Fraternali & Binney, 2006). As point out by Fraternali (2017) in a recent review, the outflow of cold and metal rich material ejected from the galaxy through SF feedback would interact with the hot coronal gas leading to its cooling. According to Fraternali (2017), the ejected material would mix with the hot gas, and the mixture would cool down through metal emission lines. The gas would eventually fall back to the galactic disk with a ballistic trajectory. Such cold gas accretion mechanism would be a valuable way to sustain the SF activity also in central galaxies of massive halos and to maintain a non empty MS at very high masses. In addition, if the coronal temperature is assumed to be of order of the virial temperature of the dark matter halo in which the galaxy is located, then we can relate it to the virial mass of the halo (see Fraternali 2017). Under this assumption, the ability of a galaxy to cool its own corona decreases for increasing halo mass (Armillotta et al., 2016). The fountain-driven condensation is high for $M_{halo} \lesssim 3 \times 10^{12}$ $M_\odot$, and it becomes less and less efficient for larger halo masses, until $M_{halo} \gtrsim 10^{13}$ $M_\odot$ when the gas accretion stops completely (Armillotta et al., 2016). This is consistent with the halo mass distribution observed in the SFR-M$\star$ plane. This accretion deficiency seem to be perfectly in agreement with the observed reduction of cold gas fraction at high halo mass regime ($M_{halo} > 10^{12}$ $M_\odot$). In addition, galaxies inhabiting host halos with masses above $10^{13.5}$ $M_\odot$ tend to lie below the MS or in a region where the MS is no longer visible.

However, we point out that the gas starvation induced by the gravitational heating in massive halos is not sufficient to guarantee the complete shut-down of the SF activity in the central galaxy. Indeed, as showed by Binney & Fraternali (2012) hot galactic coronae can cool efficiently at their very center, replenish the galaxy of cold gas and triggering central episodic of star formation and AGN activity. In this respect, all simulations advocate once again the effect of the central AGN to prevent the cooling of the gas by dumping large quantity of energy into the circum-galactic medium through radio jets and lobes (see Croton et al., 2006; Schaye et al., 2015; Genel, 2016).

### 6.4.1 Summary and Conclusions

In this work, the distribution of molecular hydrogen gas mass, $M_{H2}$, for the very fist time, is analyzed in a statistically significant sample of sample of $\sim 160,000$ central massive (at stellar mass above $10^{10}$ $M_\odot$) galaxies at redshift $z < 0.2$ drawn from Sloan Digital Sky Survey (SDSS, DR7). By using the Balmer decrement-molecular gas mass relation, $M_{H2}$-BD presented in Chapter 5, the $M_{H2}$ are derived for all our galaxies. Thanks to our exquisite statistics, we are able to investigate the molecular gas fraction, $f_{H2} = M_{H2}/M\star$, in a very large range of physical galaxies properties, as the stellar mass (M$\star$), distance from the Main Sequence of star forming galaxies ($\Delta$MS)and the host halo mass ($M_{halo}$).

The main results of the paper may be summarized as follows.

1. In central massive galaxies, the molecular gas fraction decreases with the increase of the stellar mass (Fig. 6.10). We find that statistically, the central less massive

galaxies are molecular gas-richer than the more massive ones. This anti-correlation is found in all galaxy subsample, on, above and below the Main Sequence (MS) of star forming galaxies. This result is in good agreement with the previous scaling relations obtained with the xCOLD GASS sample (512 galaxies) by Saintonge et al. (2017).

2. We investigate how the molecular gas content varies along and across the MS. We find that the position of the galaxies in the SFR-M$\star$ plane is statistically dictated by the cold gas reservoir. The molecular gas fraction $f_{H2}$ increases from below to above the MS at fixed stellar mass. In other words, the galaxies located above the MS which exhibit the strongest episodes of star formation are also characterized by the higher gas fraction at each mass level.

3. By splitting galaxies according with their host dark matter halo mass, we found that the average $H2$ gas fraction also decreases as a function of the halo mass (Fig. 6.11). The central galaxies located in large halos ($> 10^{12.5}$ M$_\odot$) show a clear gas depletion in comparison to the less massive counterparts. This is the first study to show that there is a clear connection between the galaxy molecular hydrogen gas reservoir and their environment. This finding is in agreement with HI-deficiency observed in massive halos galaxies by Catinella et al. (2013). The central massive galaxies located in massive group and cluster are then characterized by both molecular and atomic hydrogen gas depletion.

4. Looking at the properties of galaxies along the MS, we find that the molecular gas fractions decline steadily whit the stellar mass by more than on order of magnitude from $10^{10}$ $M_\odot$ to $10^{11}$ $M_\odot$ (Fig. 6.12). In particular, we observe that $f_{H2}$ slightly decreases from $10^{10}$ $M_\odot$ to $10^{10.5}$ $M_\odot$, while it shows a more rapid drop between $10^{10.5}$ $M_\odot$ to $10^{11}$ $M_\odot$, where Popesso, Concas et al. (2018) observe most of the bending of the MS relation.

5. When B/T of our galaxy sample is taken into account, we find that the bulge component only increases by $\sim$25 percent (from 0.1 to 0.35) from $10^{10}$ to $10^{11}$ M$_\odot$ (see Fig. 6.14). This value is clearly not sufficient to explain the observed drop of more than 1 dex in the molecular gas fraction.

We therefore conclude that the bending of the MS towards high stellar masses is due to a dramatic decrease of the availability of molecular gas in the disk of central massive galaxies. We discuss that the environment might play a crucial role in this respect. Indeed, the region of the MS bending and the largest decrease of the molecular gas fraction is dominated by central galaxies of group and cluster sized halos. We argue that the cold gas starvation induced by the fall of galaxies in the massive halos and the consequent inability of the hot corona to cool efficiently might be responsible for the observe trends.

# Chapter 7

# Conclusions and future prospects

In this chapter I summarize the main results of this Ph.D thesis and the methodology adopted to reach them. The main objective of this work was to identify the key physical process that removes gas from a galaxy and/or prevent gas from condensing into new stars in the local galaxies, commonly known as "quenching" mechanism. Two main aspects of the quenching scenario are put under examination:

- (i) the so called "internal quenching", related to the effect of the star formation (SF) feedback and to the Active Galactic Nuclei (AGN) on the host galaxy properties;
- (ii) the "external quenching" due to the environment in which the galaxies live.

For both purposes, a depth analysis of spectroscopic data is performed, with particular attention to few spectral absorption and emission features observable in the rest-frame optical wavelength range. We explore the effect of internal processes in Chapter 3 and 4 by investigating the presence and the effect of galactic winds in the bulk of the galaxy population in the local Universe. In Chapter 5 and 6 the we examine the role of the environment on regulating the galaxy gas reservoir and so its SF activity.

## 7.1 Summary of the present work

In Chapter 3, we investigate the presence of ionized galactic winds in a large spectroscopic sample of $\sim 600,000$ local galaxies drawn from the spectroscopic SDSS DR7 database (fully described in Chapter 2). In particular, we use any deviation of the forbidden [OIII]$\lambda$5007 emission line profile from a Gaussian as diagnostics for the presence of galactic outflows. The spectral stacking technique is used to increase the signal-to-noise ratio (SNR) of the spectra and to determine how the average [OIII]$\lambda$5007 profile changes as a function of the key galaxy physical parameters, such as star formation rate (SFR) and stellar mass (M$\star$).

In the global galaxy population, we do not find evidence of a second Gaussian broader component in most of the SFR-M$\star$ plane. A marginal detection, at the $\sim 2\sigma$ level, is obtained only at stellar masses $> 10^{10.5} M_{\odot}$ in a large range of SFR. This is confirmed by

the observation of a line width parameter slightly larger (again at the $\sim 2\sigma$ level) than the value predicted for a pure Gaussian line profile in the same region of the plane. The line profile appears to be always symmetric, even when a second broader component might contribute. The flux percentage enclosed in the broader component, when detected, is approximately 10% in most of the plane and reaches values of 20-25% at very high masses and SFRs and in the valley between the the Main Sequence (MS) of star forming galaxies (MS) and the quiescent region.

The comparison of the line width of the [OIII] with the velocity dispersion obtained from the absorption stellar features reveals a good agreement in most of the plane, indicating that the [OIII] traces the underlying galaxy potential well as the stellar component. Only in few very low SFR and M$\star$ bins we observe a disagreement, that we ascribe to spectral resolution issues and differences in the stellar and gas kinematics in purely disk galaxies.

We also explore how the line profiles relate to the particular photoionization mechanisms: SF or AGN activity.

The analysis of the [OIII] line profile shows that for "pure" SF galaxies, the ionized interstellar gas traced by the [OIII]$\lambda$5007 line never appears to be outflowing. The line profile is perfectly fitted by a single Gaussian without need for a second component. This holds in all the regions of the SFR-stellar mass plane dominated by SF galaxies, such as the MS.

The significance of a second broader Gaussian component increases with a clear trend with the increase of the AGN contribution to the galaxy spectrum, with a maximum for the AGN TYPE 1. The flux enclosed in the second component rises steadily from 0% in "pure" SF galaxies to $\sim$48% in the TYPE1 AGNs. The analysis of the [OIII] line profile of each BPT class in the SFR-stellar mass diagram shows that galaxies with an increasing AGN contribution occupy preferentially the region of the diagram where the global population shows a marginal deviation from the Gaussian line profile: at high mass and SFR and in the valley between the MS and the quiescent region. If AGN hosts are removed from the global sample, such deviations disappear in any locus of the SFR-M$\star$ diagram. The preferential location of AGN hosts, distinguished in different BPT classes, is also analyzed by performing the BPT analysis on the stacked spectra. We clearly observe a preferential location of galaxies in the diagram as a function of their nuclear activity. In particular, SF-AGN galaxies occupy the region at high stellar mass and SFR, while AGN-SF and LINERs are located preferentially in the valley between the MS and the quiescent region.

The comparison of the velocity dispersion obtained from the [OIII] line width with the velocity dispersion derived from the absorption features imprinted by the stellar component shows that the ionized gas traces the galaxy potential well as the stellar component for the "pure" SF galaxies. The ratio between the two velocity dispersions increases with the increase of the AGN contribution at any bin of stellar velocity dispersion. This, once again, confirms the role of the AGN contribution in leading to a larger [OIII] line width, and so to the presence of winds, independently of the galaxy mass or SFR.

These results clearly indicate that, when using the low-density ionized gas emission lines as wind indicators, the SF activity itself, in the local Universe, is not capable of driving galactic winds at any value of the instantaneous SFR or stellar mass. Our results

confirm the role of AGN feedback in leading to galactic winds, at least of ionized gas, in the local Universe, in agreement with many recent findings in a large redshift window.

On average, we did not observe large velocity line shift or width. The observed average velocity shift with respect to the systemic redshift is below the SDSS instrumental resolution $\Delta V < 70$ km s$^{-1}$, and the line width of the second Gaussian component is only of the order of 350-400 km s$^{-1}$ also in the BPT classes, which include an AGN contribution. Thus, rather than galactic wind, the overall population of AGN hosts in the local Universe undergo a phase of *light breeze*. Since the AGN hosts are located in the high-mass region of the SFR-M$\star$ diagram at stellar masses $\geq 10^{10.5}$ M$_\odot$, and are found to be in dark matter halos larger than $10^{12-12.5}$ M$_\odot$, such velocities are at least one order of magnitude lower than the galaxy escape velocity. Therefore, the gas entrained in the wind is very unlikely to escape the galaxy potential well and thus affecting the galaxy gas content and SF activity.

These results are presented in Concas et al. (2017), A&A, 606, A36

In Chapter 4, the same galaxy sample is used to study the interstellar NaI $\lambda$5890, 5895 (NaD) resonant line in order to look for evidence of cold-gas outflows in the local Universe. This is the first time that doppler blue-shifts of the NaD absorption feature have been investigated as a tracer of cold gas kinematics (T < 1000 K) with a statistically significant sample that includes passive, star-forming and starburst galaxies. Also in this case, we make use of the stacking technique. As for the [OIII] line profile analysis, the SDSS spectra are stacked together in bins of SFR and M$\star$ to reach a much higher SNR than in the individual spectra and, study the neutral gas wind occurrence as a function of the galaxy position in the SFR-M$\star$ diagram.

After carefully subtracting the stellar continuum, we find that galaxies at very high stellar masses M$\star > 10^{10.5} M_\odot$, in the passive and starburst regions show a clear residual sodium absorption component. While for passive galaxies this is found consistent with the systemic velocity of the galaxy, for starburst galaxies (at SFR $> 12.5 M_\odot$/yr), the residual component is clearly blue-shifted, by more than the instrumental resolution. In the former case it is still unclear whether the residual component is due to the ISM or to an extra sodium abundance in the stars or an effect of a bottom-heavy IMF in the ETGs. In the latter case, instead, the clear blue-shift suggests the presence of outflowing gas.

We find that the incidence of NaD blue-shifted line seems to be independent to the AGN presence in the galaxy host. The AGN population follows the same trend in the SFR-M$\star$ plane as the bulk of the galaxy population.

We perform an in depth analysis of the galaxies in the starburst region (SFR $> 12.5 M_\odot/yr$) at very high mass to study the geometry of the outflow and to identify the most likely ejecting mechanism, SF and/or AGN feedback. We find that the ISM NaD absorption lines show a clear transition from a clear Gaussian doublet, perfectly centered at the systemic velocity in the edge-on systems (inclination $i > 50°$ of the disk rotation axis), to an outflow, blue-shifted, component in face-on galaxies ($i < 50°$). The peak and the maximum velocity shift are of $\sim 200$ km s$^{-1}$ and $\sim 460$ km s$^{-1}$ in the face-on galaxies, while they decrease to zero in edge-on systems. This would suggest that the outflow direction is perpendicular to the disk or it exhibits a large opening angle.

These trends are observed in both "purely" star-forming and AGN dominated galaxies. These results would suggest that the blue-shifted Na D component is outflowing from the galactic disk and it is likely powered by the local star formation activity of the disk itself in both pure SF systems and AGN, in agreement with Sarzi et al. (2016).

We compare the line profile of Na D residual component with the [OIII] line profile to check for the co-existence of neutral and ionized gas outflow. We find that, even at the highest SFRs, purely SF galaxies do not show evidence of outflow in the [OIII] profile, which is perfectly fitted by a single Gaussian component, consistently with the results showed in Chapter 3.

For the AGN population in the same highest SFR region, instead, the [OIII] emission line exhibits an asymmetric profile, consistent with the presence of an extra broad and blue-shifted component. Thus, we observe both neutral and ionized phase gas outflow only in the AGN population with very high SFR.

In conclusion, we find that, in the local Universe, galactic winds show two "faces" which are related to two different ejection mechanisms, namely the neutral outflowing gas phase related to the star formation rate in the galaxy disk and the ionized winds related to the AGN feedback.

The low outflow velocities, also in this case, suggest that the neutral and ionized phases of the outflowing gas remain bound to the galaxy and likely fall back to the disk, consistently with the "gas circulation" scenario proposed by Fraternali & Binney (2006).

These results are presented in Concas et al. (2018a), submitted to A&A.

In Chapter 5, we propose a new methodology aimed to deriving indirectly the cold gas reservoir of star-forming galaxies. By using a sample of 333 local massive galaxies drawn from the xCOLD GASS survey (Saintonge et al., 2017), we investigate the empirical correlation between the dust reddening and the total molecular gas mass. In particular, the ratio between the H$\alpha$ and H$\beta$ emission lines, namely Balmer Decrement (BD), are used as a tracer of dust reddening in the optical galaxy spectra. This value is then compared with the CO(1-0) line luminosity, $L_{CO}$ observations and, the derived molecular mass $M_{H2}$ provided for the same objects. We find a strong correlation between the two observables, BD and $L_{CO}$ and the derived $M_{H2}$, with a similar scatter of 0.33, 0.34 dex, respectively.

The correlation disappear if the atomic gas phase is taken in account, as a demonstration that the atomic hydrogen mass ($M_{HI}$) is not tracing the star formation regions in local galaxies, but likely a much larger region. This is likely due to the fact that the region traced by the BD, the stellar disk, is much smaller than the HI disk.

We test the $L_{CO}-M_{H_2}$-BD correlation against galaxy inclination, metallicity, adopted $\alpha_{CO}$ conversion factor, to look for possible sources of scatter and bias. The slope and the scatter of the correlation do not depend on any of the considered parameters in our sample. We find, instead, that the main source of bias is the selection effect due to the SDSS fiber aperture. Indeed, for very nearby extended galaxies, the 3" fiber aperture samples only the very central region of the system, where the Balmer decrement value is likely driven mainly by the central bulge component. Thus, this provides a biased, reduced level of dust extinction with respect to the observed amount of molecular gas in the IRAM

xCOLD GASS sample. In order to use the Balmer decrement as an unbiased proxy of the molecular gas mass, this method can be applied only to SDSS galaxies with $r50$ radius (the radius encapsulating 50% of the galaxy light) at least less than twice the fiber aperture radius.

These results will appear in Concas & Popesso (2018) in preparation.

Finally in Chapter 6, we investigate the relation between star formation (SF) activity of local massive galaxies and their environment.

We first analyse the slope and shape of the MS of star-forming galaxies in the local Universe by using several dataset. For all SFR indicators, the MS relation flattens progressively at high stellar masses ($M\star > 10^{10}$ $M_\odot$) with respect to the linear relation found by Renzini & Peng (2015) at lower stellar masses ($M\star < 10^{10.5}$ $M_\odot$). The significance of such bending depends, though, on the SFR indicator and on the MS indicator used in the analysis.

The analysis of the mean Bulge over Total ratio (B/T) in the MS region along and across the relation shows that the B/T increase from 0.1 to 0.35 from $10^{10}$ to $10^{11}$ $M_\odot$ is not sufficient to explain the bending of the MS at very high masses. In addition to the increase of the bulge component we observed also indication for a decrease of the SF activity of the disk along the MS. While the quiescence of the bulge component could be due to the effect of central AGN feedback, the lower SFR of the disk at high masses could be due, instead, to the gas starvation induced by the gravitational heating in massive halos. Indeed, we observed that above $10^{10.5}$ $M_\odot$, where the bending is most significant, the totality of the galaxies in the MS region are central galaxies of group and cluster sized halos.

To test this possibility we explore the relation between the molecular gas mass fraction ($f_{H2} = M_{H2}/M\star$) of galaxies and the host halo mass. By using the BD-$M_{H2}$ correlation studied in Chapter 5, we investigate if the environment acts in reducing the availability of cold molecular gas, which is the fuel for the star formation process.

We find that, in central massive galaxies, which dominate the MS region, the molecular gas fraction decreases with the increase of the stellar mass. Statistically, the low mass galaxies are molecular gas-richer than the more massive ones. This anti-correlation is found in all galaxy subsamples, on, above and below the MS of star forming galaxies, in good agreement with the previous scaling relations obtained with the xCOLD GASS sample (512 galaxies) by Saintonge et al. (2017).

We investigate how the molecular gas content varies along and across the MS. Our results indicate that the position of the galaxies in the SFR-M$\star$ plane is statistically dictated by the cold gas reservoir. The molecular gas fraction, $f_{H2}$, increases from below to above the MS at fixed stellar mass. In other words, the galaxies located above the MS which exhibit the strongest episodes of star formation are also characterized by the highest gas fraction at each stellar mass.

By splitting galaxies according to their host dark matter halo mass, we find that the average $f_{H2}$ also decreases as a function of the halo mass. The central galaxies, located in large halos ($M_{halo} > 10^{12.5}$ $M_\odot$), show a clear gas depletion in comparison to the systems

in less massive halos. This is the first study that show the existence of a clear connection between the galaxy molecular hydrogen gas reservoir and the environment. This finding is in agreement with the HI-deficiency observed in massive halos galaxies by Catinella et al. (2013). The central massive galaxies located in massive group and cluster are then characterized by both molecular and atomic hydrogen gas depletion.

Looking at the properties of galaxies along the MS, we find that the molecular gas fraction declines steadily with the stellar mass by more than on order of magnitude from $10^{10}$ $M_{\odot}$ to $10^{11}$ $M_{\odot}$. In particular, we observe that $f_{H2}$ slightly decreases from $10^{10}$ $M_{\odot}$ to $10^{10.5}$ $M_{\odot}$, while it shows a more rapid drop between $10^{10.5}$ $M_{\odot}$ to $10^{11}$ $M_{\odot}$, where we observe most of the bending of the MS relation.

We therefore concluded that the bending of the MS towards high stellar masses is due to a dramatic decrease of the availability of molecular gas in the disk of massive central galaxies. We discussed that the environment might play a crucial role in this respect. Indeed, the region of the MS bending and the largest decrease of the molecular gas fraction is dominated by central galaxies of group and cluster sized halos. We argued that the cold gas starvation induced by the fall of galaxies in the massive halos and the consequent inability of the hot corona to cool efficiently might be responsible for the observe trends. These results will appear in Concas & Popesso (2018) in preparation and in Popesso, Concas et al. (2018), submitted to A&A.

## 7.2 Future work

The future developments of the present work will focus on two main aspects: (i) applying the tools presented here to available Integral-Field-Unit (IFU) data to spatially resolve the effect of "internal" and "external" quenching in nearby galaxies, and (ii) extending this study to high-redshift galaxy samples to evaluate the effect of such quenching mechanisms across the cosmic time.

The new generation of IFU surveys, CALIFA (Sánchez et al., 2012), SAMI (Croom et al., 2012), and MaNGA (Bundy et al., 2015) provide an optimal dataset for galaxies in the local Universe. By using state-of-the-art spectral fit technique, such as the new FIREFLY code (Wilkinson et al., 2017), we will be able to extract the main stellar physical parameters (age, metallicity, SFH, SFR and stellar mass), dust extinction, and the residual spectrum characterized by interstellar features.

We already started a preliminary analysis of the MaNGA data in particular to apply an approach similar to the one proposed in Chapter 3 and 4 (Concas et al. 2017b, 2018a) to study the occurrence of gas outflows in different gas phases. We aim at using the same tracers of cold and ionized gas outflows in the UV-optical range (e.g. [OII], balmer lines, [OIII], NaD, etc..) to spatially resolve the ongoing outflow, determine its geometry as a function of the powering source and establish its effect on the galaxy SF activity. The data reduction of the first thousand of MaNGA galaxies already started during a visit at the Institute of Cosmology and Gravitation of the Portsmouth University in the group of Prof. Maraston. The same group developed the FIRERFLY code for the analysis of the

stellar continuum in SDSS spectra. We are currently analyzing the reduced MaNGA maps to resolve cold and ionized outflows in purely SF and AGN host galaxies.

The same dataset will also allows to analyze the spatial distribution of the dust mass and the cold gas content in galaxies by using the Balmer-decrement-$M_{H2}$ relation studied in Chapter 5. This will be calibrated in few very nearby galaxies where similar high resolution archival ALMA CO maps are available.

With such dataset in hand we will be able to study the occurence of galactic wind and the distribution of molecular mass in relation to several global galaxies properties (M$\star$, SFR, age, metallicity, disk inclination, BPT classification, etc.) but also in relation to local properties like stellar surface density, SFR surface density, age and metallicity gradients. Such information will be used to test different scenarios of gas accretion and depletion, so shedding light on the effect of the SF/AGN feedback and environment on regulating the galaxy life.

As a further necessary steps, we will extend such analysis to high redshift by taking advantage of the ESO archive. Indeed, several deep fields, such as COSMOS, GOODS-S and HDFS have been observed during the MUSE (Multi Unit Spectroscopic Explorer) Guaranteed Time Observations (GTO) program and their observations will soon be available in the archive. The advent of the Multi Object Optical and Near-infrared Spectrograph for the VLT (MOONS) will, then, allow performing the same analysis at the peak of the cosmic star formation history at redshifts 1.5−2.

The combination of MaNGA, CALIFA, SAMI, MUSE observations together with the revolutionary observing facilities in the near future, as MOONS, James Webb Space Telescope (JWST), the Square Kilometer Array (SKA) and, the Atacama Large Millimeter Array (ALMA), will make possible to follow the evolution of the galaxy baryon cycle from z$\sim$ 0 to $\sim$ 2, revolutionizing our understanding of how galaxies evolve and quench as a function of the cosmic time.

# Bibliography


Abazajian, K. N., et al. 2009, ApJS, 182, 543

Abell, G. O. 1965, ARA&A, 3, 1

Abraham, R. G., van den Bergh, S., Glazebrook, K., et al. 1996, ApJS, 107, 1

Accurso, G., Saintonge, A., Catinella, B., et al. 2017, MNRAS, 470, 4750

Adelman-McCarthy, J. K., Agüeros, M. A., Allam, S. S., et al. 2006, ApJS, 162, 38

Alloin, D., & Bica, E. 1989, A&A, 217, 57

Armillotta, L., Fraternali, F., & Marinacci, F. 2016, MNRAS, 462, 4157

Arribas, S., Colina, L., Bellocchi, E., Maiolino, R., & Villar-Martín, M. 2014, A&A, 568, A14

Baldry, I., Glazebrook, K., & Driver, S. 2008, MNRAS, 388, 945

Baldry, I. K., Balogh, M. L., Bower, R. G., et al. 2006, MNRAS, 373, 469

Baldry, I. K., Glazebrook, K., Brinkmann, J., et al. 2004, ApJ, 600, 681

Baldry, I. K., Driver, S. P., Loveday, J., et al. 2012, MNRAS, 421, 621

Baldwin, J. A., Phillips, M. M., & Terlevich, R. 1981, PASP, 93, 5

Balogh, M. L., Baldry, I. K., Nichol, R., et al. 2004, ApJ, 615, L101

Balogh, M. L., Schade, D., Morris, S. L., et al. 1998, ApJ, 504, L75

Barnes, D. G., Staveley-Smith, L., de Blok, W. J. G., et al. 2001, MNRAS, 322, 486

Barnes, J. E., & Hernquist, L. 1996, ApJ, 471, 115

Baugh, C. M., Cole, S., & Frenk, C. S. 1996, MNRAS, 283, 1361

Behroozi, P. S., Conroy, C., & Wechsler, R. H. 2010, ApJ, 717, 379

Behroozi, P. S., Wechsler, R. H., & Conroy, C. 2013, ApJ, 770, 57

Bell, E. F., McIntosh, D. H., Katz, N., & Weinberg, M. D. 2003a, ApJ, 585, L117

—. 2003b, ApJS, 149, 289

Bellocchi, E., Arribas, S., Colina, L., & Miralles-Caballero, D. 2013, A&A, 557, A59

Bennett, C. L., Halpern, M., Hinshaw, G., et al. 2003, ApJS, 148, 1

Bennett, S. M., & Moss, C. 1998, A&AS, 132, 55

Benson, A. J., Frenk, C. S., Baugh, C. M., Cole, S., & Lacey, C. G. 2001, MNRAS, 327, 1041

Best, P. N., & Heckman, T. M. 2012, MNRAS, 421, 1569

Bica, E., & Alloin, D. 1986, A&A, 166, 83

Bicay, M. D., & Giovanelli, R. 1987, ApJ, 321, 645

Binney, J., & Fraternali, F. 2012, in European Physical Journal Web of Conferences, Vol. 19, European Physical Journal Web of Conferences, 08001

Birnboim, Y., & Dekel, A. 2003, MNRAS, 345, 349

Biviano, A., Katgert, P., Mazure, A., et al. 1997, A&A, 321, 84

Blanton, M. R., Eisenstein, D., Hogg, D. W., Schlegel, D. J., & Brinkmann, J. 2005, ApJ, 629, 143

Blanton, M. R., Hogg, D. W., Bahcall, N. A., et al. 2003, ApJ, 594, 186

Boquien, M., Boselli, A., Buat, V., et al. 2013, A&A, 554, A14

Bordoloi, R., Lilly, S. J., Hardmeier, E., et al. 2014, ApJ, 794, 130

Boselli, A., Gavazzi, G., Lequeux, J., et al. 1997, A&A, 327, 522

Boselli, A., Eales, S., Cortese, L., et al. 2010, PASP, 122, 261

Bothun, G. D. 1984, ApJ, 277, 532

Boulanger, F., Baud, B., & van Albada, G. D. 1985, A&A, 144, L9

Bourne, N., Dunne, L., Maddox, S. J., et al. 2016, MNRAS, 462, 1714

Bower, R. G., Benson, A., Malbon, R., et al. 2006, MNRAS, 370, 645

Boyle, B. J., & Terlevich, R. J. 1998, MNRAS, 293, L49

Braine, J., Combes, F., Casoli, F., et al. 1993, A&AS, 97, 887

Brinchmann, J., Charlot, S., Kauffmann, G., et al. 2013, MNRAS, 432, 2112

Brinchmann, J., Charlot, S., White, S., et al. 2004, MNRAS, 351, 1151

Brusa, M., Bongiorno, A., Cresci, G., Perna, M., et al. 2015, MNRAS, 446, 2394

Brusa, M., Perna, M., Cresci, G., et al. 2016, A&A, 588, A58

Bruzual, G., & Charlot, S. 2003, MNRAS, 344, 1000

Bundy, K., Bershady, M. A., Law, D. R., et al. 2015, ApJ, 798, 7

Cano-Díaz, M., Maiolino, R., Marconi, A., et al. 2012, A&A, 537, L8

Cappellari, M., & Emsellem, E. 2004, PASP, 116, 138

Carniani, S., Marconi, A., Maiolino, R., et al. 2015, A&A, 580, A102

Carter, D., Visvanathan, N., & Pickles, A. J. 1986, ApJ, 311, 637

Catinella, B., Schiminovich, D., Kauffmann, G., et al. 2010, MNRAS, 403, 683

Catinella, B., Schiminovich, D., Cortese, L., et al. 2013, MNRAS, 436, 34

Catinella, B., Saintonge, A., Janowiecki, S., et al. 2018, MNRAS, 476, 875

Cazzoli, S., Arribas, S., Colina, L., et al. 2014, A&A, 569, A14

Cazzoli, S., Arribas, S., Maiolino, R., & Colina, L. 2016, A&A, 590, A125

Chabrier, G. 2003, PASP, 115, 763

Chary, R., & Elbaz, D. 2001, ApJ, 556, 562

Chen, Y.-M., Tremonti, C., Heckman, T., et al. 2010, AJ, 140, 445

Chevalier, R. A. 1977, ARA&A, 15, 175

Chevalier, R. A., & Clegg, A. W. 1985a, Nature, 317, 44

—. 1985b, Nature, 317, 44

Christlein, D., & Zabludoff, A. I. 2005, ApJ, 621, 201

Cicone, C., Maiolino, R., & Marconi, A. 2016, A&A, 588, A41

Cicone, C., Maiolino, R., Sturm, E., et al. 2014, A&A, 562, A21

Cimatti, A., Brusa, M., Talia, M., et al. 2013, ApJ, 779, L13

Ciotti, L. 1991, A&A, 249, 99

Cole, S., Lacey, C. G., Baugh, C. M., & Frenk, C. S. 2000, MNRAS, 319, 168

Concas, A., Popesso, P., Brusa, M., et al. 2017, A&A, 606, A36

Conroy, C., & Wechsler, R. H. 2009, ApJ, 696, 620

Conselice, C. J. 2006, ApJ, 638, 686

Conselice, C. J., Wilkinson, A., Duncan, K., & Mortlock, A. 2016, ApJ, 830, 83

Cortese, L., Ciesla, L., Boselli, A., et al. 2012, A&A, 540, A52

Cresci, G., & Maiolino, R. 2018, Nature Astronomy, 2, 179

Cresci, G., et al. 2015, ApJ, 799, 82

Croom, S. M., Lawrence, J. S., Bland-Hawthorn, J., et al. 2012, MNRAS, 421, 872

Croton, D., J., et al. 2006, MNRAS, 365, 11

Daddi, E., Dickinson, M., Morrison, G., et al. 2007, ApJ, 670, 156

Dale, D. A., & Helou, G. 2002, ApJ, 576, 159

Dale, D. A., Aniano, G., Engelbracht, C. W., et al. 2012, ApJ, 745, 95

Dame, T. M., Hartmann, D., & Thaddeus, P. 2001, ApJ, 547, 792

Davé, R., Finlator, K., & Oppenheimer, B. D. 2011, MNRAS, 416, 1354

Davis, T. A., Krajnović, D., McDermid, R. M., et al. 2012, MNRAS, 426, 1574

De Lucia, G., Springel, V., White, S., Croton, D., & Kauffmann, G. 2006, MNRAS, 366, 499

de Vaucouleurs, G. 1948, Annales d'Astrophysique, 11, 247

Dekel, A., & Birnboim, Y. 2006, MNRAS, 368, 2

Dekel, A., Sari, R., & Ceverino, D. 2009, ApJ, 703, 785

Dekel, A., & Silk, J. 1986, ApJ, 303, 39

Di Matteo, T., Springel, V., & Hernquist, L. 2005, nature, 433, 604

Doi, M., Tanaka, M., Fukugita, M., et al. 2010, AJ, 139, 1628

Donas, J., Buat, V., Milliard, B., & Laget, M. 1990, A&A, 235, 60

Dopita, M. A., & Sutherland, R. S. 2003, Astrophysics of the diffuse universe

Draine, B. T., Dale, D. A., Bendo, G., et al. 2007, ApJ, 663, 866

Dressler, A. 1980, ApJ, 236, 351

Dunne, L., Gomez, H. L., da Cunha, E., et al. 2011, MNRAS, 417, 1510

Eales, S., Smith, M. W. L., Auld, R., et al. 2012, ApJ, 761, 168

Eales, S. A., Smith, M. W. L., Wilson, C. D., et al. 2010, A&A, 518, L62

Elbaz, D., Daddi, E., Le Borgne, D., et al. 2007, A&A, 468, 33

Elbaz, D., Dickinson, M., Hwang, H. S., et al. 2011, A&A, 533, A119

Erb, D. 2015, Nature, 523, 169

Erb, D. K., Quider, A. M., Henry, A. L., & Martin, C. L. 2012, ApJ, 759, 26

Erb, D. K., Steidel, C. C., Shapley, A. E., et al. 2006, ApJ, 646, 107

Erfanianfar, G., Popesso, P., Finoguenov, A., et al. 2016, MNRAS, 455, 2839

Fabian, A. 2012, ARAA, 50, 455

Ferrarese, L., & Merritt, D. 2000, ApJ, 539, L9

Feruglio, C., Maiolino, R., Piconcelli, E., et al. 2010, A&A, 518, L155

Feruglio, C., Fiore, F., Carniani, S., et al. 2015, A&A, 583, A99

Förster Schreiber, N. M., Genzel, R., Newman, S. F., et al. 2014, ApJ, 787, 38

Franceschini, A., Hasinger, G., Miyaji, T., & Malquori, D. 1999, MNRAS, 310, L5

Fraternali, F. 2017, in Astrophysics and Space Science Library, Vol. 430, Astrophysics and Space Science Library, ed. A. Fox & R. Davé, 323

Fraternali, F., & Binney, J. J. 2006, MNRAS, 366, 449

Freedman, W. L., Madore, B. F., Mould, J. R., et al. 1994, Nature, 371, 757

Fukugita, M., Ichikawa, T., Gunn, J. E., et al. 1996, AJ, 111, 1748

Galametz, M., Kennicutt, R. C., Calzetti, D., et al. 2013, MNRAS, 431, 1956

García-Burillo, S., Combes, F., Usero, A., et al. 2015, A&A, 580, A35

Gavazzi, G., Boselli, A., & Kennicutt, R. 1991, AJ, 102, 1569

Gavazzi, G., Boselli, A., Pedotti, P., Gallazzi, A., & Carrasco, L. 2002, A&A, 396, 449

Gavazzi, G., Boselli, A., van Driel, W., & O'Neil, K. 2005, A&A, 429, 439

Gavazzi, G., Catinella, B., Carrasco, L., Boselli, A., & Contursi, A. 1998, AJ, 115, 1745

Genel, S. 2016, ApJ, 822, 107

Genzel, R., Newman, S., Jones, T., et al. 2011, ApJ, 733, 101

Genzel, R., Förster Schreiber, N. M., Rosario, D., et al. 2014, ApJ, 796, 7

Genzel, R., Tacconi, L. J., Lutz, D., et al. 2015, ApJ, 800, 20

Gerke, J. R., Kochanek, C. S., Prieto, J. L., Stanek, K. Z., & Macri, L. M. 2011, ApJ, 743, 176

Giovanelli, R., & Haynes, M. P. 1985, ApJ, 292, 404

Gómez, P. L., Nichol, R. C., Miller, C. J., et al. 2003, ApJ, 584, 210

Greene, J., & Ho, L. 2005, ApJ, 627, 721

Greene, J. E., Zakamska, N., & Smith, P. 2012, ApJ, 746, 86

Groves, B., Brinchmann, J., & Walcher, C. J. 2012, MNRAS, 419, 1402

Gruppioni, C., Pozzi, F., Rodighiero, G., et al. 2013, MNRAS, 432, 23

Gunn, J. E., & Gott, III, J. R. 1972, ApJ, 176, 1

Gunn, J. E., Carr, M., Rockosi, C., et al. 1998, AJ, 116, 3040

Gunn, J. E., Siegmund, W. A., Mannery, E. J., et al. 2006, AJ, 131, 2332

Guo, Q., White, S., Li, C., & Boylan-Kolchin, M. 2010, MNRAS, 404, 1111

Guo, Q., White, S., Boylan-Kolchin, M., et al. 2011, MNRAS, 413, 101

Harrison, C. 2014, PhD thesis, Durham University

Harrison, C., Alexander, D. M., Mullaney, J. R., & Swinbank, A. M. 2014, MNRAS, 441, 3306

Harrison, C. M. 2017, Nature Astronomy, 1, 0165

Harrison, C. M., Alexander, D. M., Swinbank, A. M., et al. 2012, MNRAS, 426, 1073

Harrison, C. M., Alexander, D. M., Mullaney, J. R., et al. 2016, MNRAS, 456, 1195

Hashimoto, Y., Oemler, Jr., A., Lin, H., & Tucker, D. L. 1998, ApJ, 499, 589

Haynes, M. P., & Giovanelli, R. 1984, AJ, 89, 758

Haynes, M. P., Giovanelli, R., Martin, A. M., et al. 2011, AJ, 142, 170

Heavens, A., Panter, B., Jimenez, R., & Dunlop, J. 2004, Nature, 428, 625

Heckman, T., Armus, L., & Miley, G. 1990, ApJS, 74, 833

Heckman, T. M., & Best, P. N. 2014, ARA&A, 52, 589

Heckman, T. M., Kauffmann, G., Brinchmann, J., et al. 2004, ApJ, 613, 109

Heckman, T. M., Lehnert, M. D., Strickland, D. K., & Armus, L. 2000, ApJS, 129, 493

Heckman, T. M., & Thompson, T. A. 2017, ArXiv e-prints, arXiv:1701.09062

Henriques, B. M. B., White, S. D. M., Thomas, P. A., et al. 2017, MNRAS, 469, 2626

Hill, M. J., & Zakamska, N. 2014, MNRAS, 439, 2701

Hogg, D. W., Blanton, M. R., Brinchmann, J., et al. 2004, ApJ, 601, L29

Hopkins, P., et al. 2006, ApJS, 163, 50

Hopkins, P. F., Hernquist, L., Cox, T. J., & Kereš, D. 2008, ApJS, 175, 356

Hopkins, P. F., Kereš, D., Oñorbe, J., et al. 2014, MNRAS, 445, 581

Hopkins, P. F., Quataert, E., & Murray, N. 2011, MNRAS, 417, 950

Hubble, E., & Humason, M. L. 1931, ApJ, 74, 43

Hubble, E. P. 1925, Popular Astronomy, 33

—. 1936, Realm of the Nebulae

Ilbert, O., Salvato, M., Le Floc'h, E., et al. 2010, ApJ, 709, 644

Ilbert, O., McCracken, H. J., Le Fèvre, O., et al. 2013, A&A, 556, A55

Ilbert, O., Arnouts, S., Le Floc'h, E., et al. 2015, A&A, 579, A2

Israel, F. P. 1997, A&A, 317, 65

—. 2005, A&A, 438, 855

Israel, F. P., Bontekoe, T. R., & Kester, D. J. M. 1996, A&A, 308, 723

James, A., Dunne, L., Eales, S., & Edmunds, M. G. 2002, MNRAS, 335, 753

Janowiecki, S., Catinella, B., Cortese, L., et al. 2017, MNRAS, 466, 4795

Jeong, H., Yi, S. K., Kyeong, J., et al. 2013, ApJS, 208, 7

Jiang, F., & van den Bosch, F. C. 2014, MNRAS, 440, 193

Juneau, S., Glazebrook, K., Crampton, D., et al. 2005, ApJ, 619, L135

Kannappan, S. J. 2004, ApJ, 611, L89

Katz, N., Keres, D., Dave, R., & Weinberg, D. H. 2003, in Astrophysics and Space Science Library, Vol. 281, The IGM/Galaxy Connection. The Distribution of Baryons at z=0, ed. J. L. Rosenberg & M. E. Putman, 185

Kauffmann, G., Charlot, S., & White, S. D. M. 1996, MNRAS, 283, L117

Kauffmann, G., Colberg, J. M., Diaferio, A., & White, S. D. M. 1999, MNRAS, 303, 188

Kauffmann, G., Li, C., & Heckman, T. M. 2010, MNRAS, 409, 491

Kauffmann, G., White, S. D. M., Heckman, T. M., et al. 2004, MNRAS, 353, 713

Kauffmann, G., Heckman, T. M., White, S. D. M., et al. 2003a, MNRAS, 341, 54

Kauffmann, G., Heckman, T. M., Tremonti, C., et al. 2003b, MNRAS, 346, 1055

Kay, S. T., Pearce, F. R., Frenk, C. S., & Jenkins, A. 2002, MNRAS, 330, 113

Kenney, J. D. P., van Gorkom, J. H., & Vollmer, B. 2004, AJ, 127, 3361

Kennicutt, R. C., Calzetti, D., Aniano, G., et al. 2011, PASP, 123, 1347

Kennicutt, Jr., R. C. 1983, AJ, 88, 483

—. 1998, ARA&A, 36, 189

Kennicutt, Jr., R. C., Bothun, G. D., & Schommer, R. A. 1984, AJ, 89, 1279

Kereš, D., Katz, N., Fardal, M., Davé, R., & Weinberg, D. H. 2009, MNRAS, 395, 160

Kereš, D., Katz, N., Weinberg, D. H., & Davé, R. 2005, MNRAS, 363, 2

Kewley, L., Dopita, M., Sutherland, R., Heisler, C., & Trevena, J. 2001, ApJ, 556, 121

Kewley, L., Groves, B., Kauffmann, G., & Heckman, T. 2006, MNRAS, 372, 961

King, A., & Pounds, K. 2015, ARA&A, 53, 115

Kodaira, K., Watanabe, T., Onaka, T., & Tanaka, W. 1990, ApJ, 363, 422

Koopmann, R. A., & Kenney, J. D. P. 1998, ApJ, 497, L75

Kormendy, J., & Ho, L. C. 2013, ARA&A, 51, 511

Kroupa, P. 2001, MNRAS, 322, 231

Larson, R. B., Tinsley, B. M., & Caldwell, C. N. 1980, ApJ, 237, 692

Lee, S.-K., Im, M., Kim, J.-W., et al. 2015, ApJ, 810, 90

Lehnert, M. D., & Heckman, T. M. 1996, ApJ, 472, 546

Leitherer, C., Robert, C., & Drissen, L. 1992, ApJ, 401, 596

Leroy, A. K., Bolatto, A., Bot, C., et al. 2009, ApJ, 702, 352

Leroy, A. K., Bolatto, A., Gordon, K., et al. 2011, ApJ, 737, 12

Leroy, A. K., Walter, F., Martini, P., et al. 2015, ApJ, 814, 83

Leslie, S. K., Kewley, L. J., Sanders, D. B., & Lee, N. 2016, MNRAS, 455, L82

Lewis, I., Balogh, M., De Propris, R., et al. 2002, MNRAS, 334, 673

Liddle, A. R. 2007, MNRAS, 377, L74

Lilly, S., Le Fevre, O., Hammer, F., & Crampton, D. 1996, ApJ, 460, L1

Liu, G., Zakamska, N., Greene, J., Nesvadba, N., & Liu, X. 2013, MNRAS, 436, 2576

Lundmark, K. 1926, Arkiv for Matematik, Astronomi och Fysik, 19, 1

—. 1927, Nova Acta Regiae Soc. Sci. Upsaliensis Ser. V

Lynds, C. R., & Sandage, A. R. 1963, AJ, 68, 284

Mac Low, M.-M., & Ferrara, A. 1999, ApJ, 513, 142

Madau, P., & Dickinson, M. 2014, ARAA, 52, 415

Madau, P., Ferguson, H. C., Dickinson, M., et al. 1996, MNRAS, 283, 1388

Madau, P., Pozzetti, L., & Dickinson, M. 1998, ApJ, 498, 106

Magdis, G. E., Elbaz, D., Daddi, E., et al. 2010, ApJ, 714, 1740

Magdis, G. E., Daddi, E., Sargent, M., et al. 2012, ApJ, 758, L9

Magdis, G. E., Rigopoulou, D., Hopwood, R., et al. 2014, ApJ, 796, 63

Magnelli, B., Lutz, D., Saintonge, A., et al. 2014, A&A, 561, A86

Magorrian, J., Tremaine, S., Richstone, D., et al. 1998, AJ, 115, 2285

Maiolino, R., Gallerani, S., Neri, R., et al. 2012, MNRAS, 425, L66

Maiolino, R., Russell, H. R., Fabian, A. C., et al. 2017, Nature, 544, 202

Mamon, G. 1996, in Third Paris Cosmology Colloquium, ed. H. J. de Vega & N. Sánchez, 95

Marasco, A., Fraternali, F., & Binney, J. J. 2012, MNRAS, 419, 1107

Marcillac, D., Elbaz, D., Chary, R. R., et al. 2006, A&A, 451, 57

Marconi, A., & Hunt, L. K. 2003, ApJ, 589, L21

Martin, C. 2005, ApJ, 621, 227

—. 2006, ApJ, 647, 222

Martin, C., et al. 2012a, ApJ, 760, 127

Martin, C. L., Shapley, A. E., Coil, A. L., et al. 2012b, ApJ, 760, 127

Martini, P., Leroy, A. K., Mangum, J. G., et al. 2018, ApJ, 856, 61

McKeith, C. D., Greve, A., Downes, D., & Prada, F. 1995, A&A, 293, 703

McNamara, B. R., & Nulsen, P. E. J. 2012, New Journal of Physics, 14, 055023

Merloni, A., & Heinz, S. 2007, MNRAS, 381, 589

Mihos, J. C. 2004, in IAU Symposium, Vol. 217, Recycling Intergalactic and Interstellar Matter, ed. P.-A. Duc, J. Braine, & E. Brinks, 390

Milne, E. A. 1933, MNRAS, 93, 668

Moore, B., Ghigna, S., Governato, F., et al. 1999, ApJ, 524, L19

Moore, B., Governato, F., Quinn, T., Stadel, J., & Lake, G. 1998, ApJ, 499, L5

Morselli, L., Popesso, P., Erfanianfar, G., & Concas, A. 2017, A&A, 597, A97

Moss, C., & Whittle, M. 1993a, ApJ, 407, L17

—. 1993b, ApJ, 407, L17

—. 2005, MNRAS, 357, 1337

Moster, B. P., naab, T., & White, S. 2013, MNRAS, 428, 3121

Moster, B. P., Somerville, R., Maulbetsch, C., et al. 2010, ApJ, 710, 903

Moustakas, J., Coil, A. L., Aird, J., et al. 2013, ApJ, 767, 50

Mullaney, J. R., Alexander, D. M., Fine, S., et al. 2013, MNRAS, 433, 622

Murray, N., Quataert, E., & Thompson, T. 2005a, ApJ, 618, 569

Murray, N., Quataert, E., & Thompson, T. A. 2005b, ApJ, 618, 569

Mutchler, M., Bond, H. E., Christian, C. A., et al. 2007, PASP, 119, 1

Muzzin, A., Marchesini, D., Stefanon, M., et al. 2013, ApJ, 777, 18

Nedelchev, B., Sarzi, M., & Kaviraj, S. 2017, ArXiv e-prints, arXiv:1705.07994

Newman, S. F., Genzel, R., Förster-Schreiber, N. M., et al. 2012a, ApJ, 761, 43

—. 2012b, ApJ, 761, 43

Noeske, K. G., Weiner, B. J., Faber, S. M., et al. 2007, ApJ, 660, L43

Noll, S., Burgarella, D., Giovannoli, E., et al. 2009, A&A, 507, 1793

Nordon, R., Lutz, D., Shao, L., et al. 2010, A&A, 518, L24

Nordon, R., Lutz, D., Genzel, R., et al. 2012, ApJ, 745, 182

O'Connell, R. W. 1976, ApJ, 206, 370

Oemler, Jr., A. 1974, ApJ, 194, 1

Osterbrock, D. E., & Ferland, G. J. 2006, Astrophysics of gaseous nebulae and active galactic nuclei

Pannella, M., Carilli, C. L., Daddi, E., et al. 2009, ApJ, 698, L116

Pearce, F. R., Jenkins, A., Frenk, C. S., et al. 2001, MNRAS, 326, 649

Peng, Y.-j., Lilly, S, J., K., K., et al. 2010, ApJ, 721, 193

Perna, M., Brusa, M., Salvato, M., et al. 2015, A&A, 583, A72

Perna, M., Lanzuisi, G., Brusa, M., Cresci, G., & Mignoli, M. 2017a, ArXiv e-prints, arXiv:1705.08388

Perna, M., Lanzuisi, G., Brusa, M., Mignoli, M., & Cresci, G. 2017b, A&A, 603, A99

Peterson, R. C. 1976, ApJ, 210, L123

Pettini, M., Steidel, C., Adelberger, K., Dickinson, M., & Giovalisco, M. 2000, ApJ, 528, 96

Pimbblet, K. A., Smail, I., Edge, A. C., et al. 2006, MNRAS, 366, 645

Planck Collaboration, Adam, R., Ade, P. A. R., et al. 2016a, A&A, 594, A1

Planck Collaboration, Ade, P. A. R., Aghanim, N., et al. 2016b, A&A, 594, A13

Popesso, P., Biviano, A., Romaniello, M., & Böhringer, H. 2007, A&A, 461, 411

Popesso, P., Biviano, A., Finoguenov, A., et al. 2015, A&A, 579, A132

Pozzetti, L., Bolzonella, M., Lamareille, F., et al. 2007, A&A, 474, 443

Pozzetti, L., Bolzonella, M., Zucca, E., et al. 2010, A&A, 523, A13

Prochaska, J. X., Kasen, D., & Rubin, K. 2011, ApJ, 734, 24

Puech, M., Hammer, F., Flores, H., et al. 2010, A&A, 510, A68

Quilis, V., Bower, R. G., & Balogh, M. L. 2001, MNRAS, 328, 1091

RemyRuyer, A., Madden, S. C., Galliano, F., et al. 2013, A&A, 557, A95

Renzini, A., & Peng, Y.-j. 2015, ApJ, 801, L29

Roberts, M. S. 1969, AJ, 74, 859

Rodighiero, G., Renzini, A., Daddi, E., et al. 2014, MNRAS, 443, 19

Rodríguez Zaurín, J., Tadhunter, C. N., Rose, M., & Holt, J. 2013, MNRAS, 432, 138

Roman-Duval, J., Israel, F. P., Bolatto, A., et al. 2010, A&A, 518, L74

Rubin, K. H. R., Prochaska, J. X., Koo, D. C., et al. 2014, ApJ, 794, 156

Rupke, D., Gültekin, K., & Veilleux, S. 2017, ArXiv e-prints, arXiv:1708.05139

Rupke, D., & Veilleux, S. 2011, ApJL, 729, L27

—. 2013, ApJ, 768, 75

Rupke, D., Veilleux, S., & Sanders, D. 2002, ApJ, 570, 588

—. 2005a, ApJ, 160, 87

—. 2005b, ApJ, 160, 115

—. 2005c, ApJ, 632, 751

Rupke, D. S. N., & Veilleux, S. 2015, ApJ, 801, 126

Saintonge, A., Kauffmann, G., Kramer, C., et al. 2011, MNRAS, 415, 32

Saintonge, A., Catinella, B., Cortese, L., et al. 2016, MNRAS, 462, 1749

Saintonge, A., Catinella, B., Tacconi, L. J., et al. 2017, ApJS, 233, 22

Salak, D., Nakai, N., Miyamoto, Y., Yamauchi, A., & Tsuru, T. G. 2013, PASJ, 65, 66

Salim, J., et al. 2007, ApJS, 173, 267

Salim, S., Charlot, S., Rich, R. M., et al. 2005, ApJ, 619, L39

Salim, S., Lee, J. C., Janowiecki, S., et al. 2016, ApJS, 227, 2

Sánchez, S. F., Kennicutt, R. C., Gil de Paz, A., et al. 2012, A&A, 538, A8

Sanders, D. B., Soifer, B. T., Elias, J. H., Neugebauer, G., & Matthews, K. 1988, ApJ, 328, L35

Santini, P., Maiolino, R., Magnelli, B., et al. 2014, A&A, 562, A30

Sarzi, M., Kaviraj, S., Nedelchev, B., et al. 2016, MNRAS, 456, L25

Sarzi, M., et al. 2006, MNRAS, 366, 1151

Scarlata, C., & Panagia, N. 2015, ApJ, 801, 43

Scarlata, C., Carollo, C. M., Lilly, S. J., et al. 2007, ApJS, 172, 494

Schaaf, R., Pietsch, W., Biermann, P. L., Kronberg, P. P., & Schmutzler, T. 1989, ApJ, 336, 722

Schawinski, K., Urry, C. M., Simmons, B. D., et al. 2014, MNRAS, 440, 889

Schaye, J., Crain, R. A., Bower, R. G., et al. 2015, MNRAS, 446, 521

Schlegel, D., Finkbeiner, D., & Davis, M. 1998, ApJ, 500, 525

Schreiber, C., Pannella, M., Elbaz, D., et al. 2015, A&A, 575, A74

Schwartz, C. M., & Martin, C. L. 2004, ApJ, 610, 201

Scoville, N., Aussel, H., Sheth, K., et al. 2014, ApJ, 783, 84

Scoville, N., Sheth, K., Aussel, H., et al. 2015, ArXiv e-prints, arXiv:1505.02159

Scoville, N., Lee, N., Vanden Bout, P., et al. 2017, ApJ, 837, 150

Seaquist, E. R., & Clark, J. 2001, ApJ, 552, 133

Sérsic, J. L. 1963, Boletin de la Asociacion Argentina de Astronomia La Plata Argentina, 6, 41

Shapiro, K. L., Genzel, R., Quataert, E., et al. 2009, ApJ, 701, 955

Shapiro, P. R., & Field, G. B. 1976, ApJ, 205, 762

Shapley, A., Steidel, C., Pettini, M., & Adelberger, K. 2003, ApJ, 588, 65

Simard, L., Mendel, J. T., Patton, D. R., Ellison, S. L., & McConnachie, A. W. 2011, ApJS, 196, 11

Simard, L., Willmer, C. N. A., Vogt, N. P., et al. 2002, ApJS, 142, 1

Smoot, G. F., Bennett, C. L., Kogut, A., et al. 1992, ApJ, 396, L1

Somerville, R. S., Hopkins, P. F., Cox, T. J., Robertson, B. E., & Hernquist, L. 2008, MNRAS, 391, 481

Somerville, R. S., & Primack, J. R. 1999, MNRAS, 310, 1087

Soto, K. T., & Martin, C. L. 2012, ApJS, 203, 3

Soto, K. T., Martin, C. L., Prescott, M. K. M., & Armus, L. 2012, ApJ, 757, 86

Speagle, J. S., Steinhardt, C. L., Capak, P. L., & Silverman, J. D. 2014, ApJS, 214, 15

Spearman, C. 1904, The American Journal of Psychology, 15, 72

Spiniello, C., Trager, S. C., Koopmans, L. V. E., & Chen, Y. P. 2012, ApJ, 753, L32

Spitzer, Jr., L. 1978, JRASC, 72, 349

Springel, V., & Hernquist, L. 2003, MNRAS, 339, 289

Stasinska, G., Cid Fernandes, R., et al. 2006, MNRAS, 371, 972

Steidel, C. C., Erb, D. K., Shapley, A. E., et al. 2010, ApJ, 717, 289

Strateva, I., Ivezić, Ž., Knapp, G. R., et al. 2001, AJ, 122, 1861

Strauss, M. A., et al. 2002, AJ, 124, 1810

Strickland, D. K., & Heckman, T. M. 2009, ApJ, 697, 2030

Struck, C., & Smith, D. C. 1999, ApJ, 527, 673

Sturm, E., González-Alfonso, E., Veilleux, S., et al. 2011, ApJ, 733, L16

Tacconi, L. J., Neri, R., Genzel, R., et al. 2013, ApJ, 768, 74

Talia, M., Brusa, M., Cimatti, A., et al. 2017, MNRAS, 471, 4527

Thomas, D., Maraston, C., & Bender, R. 2003, MNRAS, 343, 279

Thomas, D., Maraston, C., Schawinski, K., Sarzi, M., & Silk, J. 2010, MNRAS, 404, 1715

Thornton, K., Gaudlitz, M., Janka, H.-T., & Steinmetz, M. 1998, ApJ, 500, 95

Tomczak, A. R., Quadri, R. F., Tran, K.-V. H., et al. 2016, ApJ, 817, 118

Tremonti, C. A., Moustakas, J., & Diamond-Stanic, A. 2007, ApJ, 663, L77

Tremonti, C. A., Heckman, T. M., Kauffmann, G., et al. 2004, ApJ, 613, 898

Valiante, E., Smith, M. W. L., Eales, S., et al. 2016, MNRAS, 462, 3146

van Dokkum, P. G., & Conroy, C. 2010, Nature, 468, 940

—. 2012, ApJ, 760, 70

van Gorkom, J. H. 2004, Clusters of Galaxies: Probes of Cosmological Structure and Galaxy Evolution, 305

Veilleux, S., Cecil, G., & Bland-Hawthorn, J. 2005, ARAA, 43, 769

Veilleux, S., Kim, D.-C., Sanders, D. B., Mazzarella, J. M., & Soifer, B. T. 1995, ApJS, 98, 171

Veilleux, S., & Osterbrock, D. E. 1987, ApJS, 63, 295

Verdes-Montenegro, L., Yun, M. S., Williams, B. A., et al. 2001, A&A, 377, 812

Villar-Martín, M., Humphrey, A., Delgado, R. G., Colina, L., & Arribas, S. 2011, MNRAS, 418, 2032

Voit, G. M., Bryan, G. L., Balogh, M. L., & Bower, R. G. 2002, ApJ, 576, 601

Vollmer, B., Cayatte, V., Balkowski, C., & Duschl, W. J. 2001, ApJ, 561, 708

Walter, F., Weiss, A., & Scoville, N. 2002, ApJ, 580, L21

Westmoquette, M. S., Clements, D. L., Bendo, G. J., & Khan, S. A. 2012, MNRAS, 424, 416

Westmoquette, M. S., Gallagher, J. S., Smith, L. J., et al. 2009, ApJ, 706, 1571

Whitaker, K. E., Franx, M., Leja, J., et al. 2014, ApJ, 795, 104

Whitaker, K. E., Franx, M., Bezanson, R., et al. 2015, ApJ, 811, L12

White, S. D. M., & Frenk, C. S. 1991, ApJ, 379, 52

White, S. D. M., & Rees, M. J. 1978, MNRAS, 183, 341

Wilkinson, D. M., Maraston, C., Goddard, D., Thomas, D., & Parikh, T. 2017, MNRAS, 472, 4297

Wolfire, M. G., Hollenbach, D., McKee, C. F., Tielens, A. G. G. M., & Bakes, E. L. O. 1995, ApJ, 443, 152

Woo, J.-H., Son, D., & Bae, H.-J. 2017, ApJ, 839, 120

Wood, C. M., Tremonti, C. A., Calzetti, D., et al. 2015, MNRAS, 452, 2712

Worthey, G. 1998, PASP, 110, 888

Worthey, G., Faber, S. M., Gonzalez, J. J., & Burstein, D. 1994, ApJS, 94, 687

Worthey, G., Ingermann, B. A., & Serven, J. 2011, ApJ, 729, 148

Wuyts, S., et al. 2011, ApJ, 742, 96

Yang, X., Mo, H. J., & van den Bosch, F. C. 2009, ApJ, 695, 900

Yang, X., Mo, H. J., van den Bosch, F. C., & Jing, Y. P. 2005, MNRAS, 356, 1293

Yang, X., Mo, H. J., van den Bosch, F. C., et al. 2007, ApJ, 671, 153

Yang, X., Mo, H. J., van den Bosch, F. C., Zhang, Y., & Han, J. 2012, ApJ, 752, 41

York, D. G., et al. 2000, Aj, 120, 1579

Yoshida, N., Stoehr, F., Springel, V., & White, S. D. M. 2002, MNRAS, 335, 762

Zakamska, N., & Greene, J. 2014, MNRAS, 442, 784

Zhang, W., Li, C., Kauffmann, G., et al. 2009, MNRAS, 397, 1243

Zhang, X., & Buta, R. J. 2012, ArXiv e-prints, arXiv:1203.5334